Modelling of the heating and evaporation of fuel droplets

Tarsisius Kristyadi

Ph.D. **2007**

Modelling of the heating and evaporation of fuel droplets

Tarsisius Kristyadi

A thesis submitted in partial fulfilment of the requirements of the University of Brighton for the degree of Doctor of Philosophy

October 2007

School of Engineering
University of Brighton

COPYRIGHT

ABSTRACT

The results of a comparative analysis of liquid and gas phase models for fuel droplets heating and evaporation, suitable for implementation into computational fluid dynamics (CFD) codes, are presented. Among liquid phase models, the analysis is focused on the model based on the assumption that the liquid thermal conductivity is infinitely large, and the so called effective thermal conductivity model. Seven gas phase models are compared. These are six semi-theoretical models, based on various assumptions, and a model based solely on the approximation to experimental data. It is pointed out that the gas phase model, taking into account the finite thickness of the thermal boundary layer around the droplet, predicts the evaporation time closest to the one based on the approximation to experimental data.

The values of the absorption coefficients of gasoline fuel (BP Pump Grade 95 RON ULG), 2,2,4-trimethylpentane $(CH_3)_2CHCH_2C(CH_3)_3$ (iso-octane) and 3-pentanone $CH_3CH_2COCH_2(CH_3)_3$ have been measured experimentally in the range of wavelengths between 0.2 μm and 4 μm. The values of the average absorption efficiency factor for all fuels have been approximated by a power function aR_d^b, where R_d is the droplet radius. a and b in turn have been approximated by piecewise quadratic functions of the radiation temperature, with the coefficients calculated separately in the ranges 2 - 5 μm, 5 - 50 μm, 50 - 100 μm and 100 - 200 μm for all fuels. This new approximation is shown to be more accurate compared with the case when a and b are approximated by quadratic functions or fourth power polynomials of the radiation temperature, with the coefficients calculated in the full range of 2 - 200 μm.

Results of experimental studies of heating and evaporation of monodisperse ethanol and acetone droplets in two regimes are compared with the results of modelling. It is pointed out that for relatively small droplets the experimentally measured droplet temperatures are close to the predicted average droplet temperatures, while for larger droplets the experimentally measured droplet temperatures are close to the temperatures predicted at the centre of droplets.

All the developed models have been implemented into the KIVA-2 CFD code and validated against available in-house experimental data referring to spray penetration and ignition delay in Diesel engines.

CONTENTS

APPENDICES

LIST OF FIGURES

LIST OF TABLES

ACKNOWLEDGEMENTS

I would like to thank my supervisors Prof. Sergei Sazhin, Prof. Morgan Heikal and Dr. Cyril Crua for their assistance and support.

I wish to express my gratitude to Dr. Walid Abdelgaffar and Dr. Serguei Martynov, their constant support and help.

I am grateful to Prof. S.V. Mikhalovsky, Dr. S.T. Meikle, Dr. O.Al-Hanbali and Dr. Steve Begg for their help in performing the experiments described in Chapter 4, useful discussions and support.

I am grateful to Dr. G. Castanet and Prof. F. Lemoine for providing experimental data and useful discussions of the results presented in Chapter 5.

I want to thank Romain Demory and Kurosh Kamini for useful discussions and support.

I acknowledge the financial help provided by the Indonesian Government via TPSDP Batch III project at Institut Teknologi Nasional (ITENAS) Bandung Indonesia.

Finally I would like to thank my family for their constant affection and support.

DECLARATION

I hereby certify that this thesis is my own work except where otherwise indicated. I have identified my sources of information, and in particular have put in quotation marks and identified the origins of any passages that have been quoted word for word.

Signed: Date:

NOMENCLATURE

a	coefficient introduced in Equation (2.1.28) ($\mathrm{m}^{-\mathrm{b}}$), acceleration in Equation (6.2.12)
a_{λ}	liquid fuel absorption coefficient (1/m)
$a_{0,1,2,3,4}$	coefficients introduced in Equation (2.1.28) ($\mathrm{m}^{-\mathrm{b}}$, $1/(\mathrm{K\ m}^{\mathrm{b}})$, $1/(\mathrm{K}^2\ \mathrm{m}^{\mathrm{b}})$, $1/(\mathrm{K}^3\mathrm{m}^{\mathrm{b}})$, $1/(\mathrm{K}^4\ \mathrm{m}^{\mathrm{b}})$)
a_{mr}	integral stoichiometric coefficients for reaction *r* in Equation (6.2.18)
A	area of droplet (m^2)
A_{f1}, A_{f2}, A_{f3}, A_{f4},	pre exponential factors in Arrhenius form in Equations (2.3.15)-(2.3.18)
b	coefficient introduced in Equation (2.1.28)
$b_{0,1,2,3,4}$	coefficients introduced in Equation (2.1.28) (1, 1/K, $1/\mathrm{K}^2$, $1/\mathrm{K}^3$, $1/\mathrm{K}^4$)
b_{mr}	integral stoichiometric coefficients for reaction *r* in Equation (6.2.18)
B	branching agent
B_1	breakup time constant
Bi	Biot number
B_{f}	parameter introduced in Equation (2.2.5)
B_{M}	Spalding mass number
B_{T}	Spalding heat transfer number
B_{λ}	Planck function ($\mathrm{W}/(\mathrm{m}^2\ \mu\mathrm{m})$)
B_o	model constant for Equation (6.2.9)
c	specific heat capacity (J/(kg K))
C	distance parameter
$C_{1,2}$	coefficients in the Planck function ($\mathrm{W}\ \mu\mathrm{m}^3/\mathrm{m}^2$, $\mu\mathrm{m\ K}$)
C_D	drag coefficient
C_f, C_k, C_d	dimensionless constant in Equation (6.2.2)
CN	contraction coefficient
D	binary diffusion coefficient (m^2/s)
d	parameter introduced in Equation (6.2.1)
E_{f1}, E_{f2}, E_{f3}, E_{f4}	activation energies in Equations (2.3.15)-(2.3.18) (J)
E_{fr}	activation temperature in Equation (6.2.21) (J)
E_{br}	activation temperature in Equation (6.2.22) (J)
F	parameter introduced in Equation (6.2.1) (J)
f_1,f_2,f_3,f_4	the rate constant in Equations (2.3.9) – (2.3.12) defined by Equations (2.3.15) –(2.3.18)
$F_{\mathrm{T,M}}$	correction factors: $\delta_{\mathrm{T}}/\delta_{\mathrm{T0}}$; $\delta_{\mathrm{M}}/\delta_{\mathrm{M0}}$
Fo	Fourier number: $k_{\mathrm{l}}t/\rho_{\mathrm{l}}c_{\mathrm{l}}R^2_{\mathrm{d}}$
h	convection heat transfer coefficient($\mathrm{W}/(\mathrm{m}^2\ \mathrm{K})$)
h_{m}	mass transfer coefficient (m/s)
h_0	$(hR_{\mathrm{d}}/k_{\mathrm{l}})$-1
$I_{\lambda}^{0(\mathrm{ext})}$	spectral intensity of external radiation integrated over all angles ($\mathrm{W}/(\mathrm{m}^2\ \mu\mathrm{m})$)
k	thermal conductivity (W/(m K))
k_b	rate coefficient of branching reaction in Shell autoignition model

k_p	rate coefficient of branching reaction in Shell autoignition model
k_q	rate coefficient of branching reaction in Shell autoignition model
k_t	rate coefficient of branching reaction in Shell autoignition model
k_{br}	coefficient on Equation (6.2.22)
k_{fr}	coefficient on Equation (6.2.22)
L	specific heat of evaporation (J/kg)
Le	Lewis number: $k_g/(c_{pg}\rho_g D)$
m	mass (kg), molar concentration (mole/m^3)
$\dot{m}$	evaporation rate (kg/s)
m_λ	complex index of refraction: n_λ-iκ_λ
M	molar mass (kg/kmol), species
n	index of refraction (does not depend on λ)
n_λ	index of refraction (depends on λ)
n_0	1.46
Nu	Nusselt number
p	pressure (Pa), parameter introduced in Equation (2.3.14)
p_n	coefficients introduced in Equation (2.1.22) (K/s)
$p_\lambda(R)$	spectral distribution of radiative power density (W/(m^3 μm))
$P(R)$	radiative term in Equation (2.1.21) (K/s)
P_{total}	total amount of radiation absorbed in a droplet (K/s)
Pe	Peclet number
Pr	Prandtl number
q	parameter introduced in Equation (2.3.14)
$\dot{q}$	heat flux (W/m^2)
Q	intermediate agent
Q_a	efficiency factor of absorption
Q_K	the total heat release rate defined in Equation (2.3.21) (W)
Q_L	heat loss through the boundary walls defined by Equation (2.3.22) (W)
R	distance from the droplet centre (m)
R_g	gas constant (J/(kg K))
R_u	universal gas constant (J/(kmol K))
R_{eq}	radius of equilibrium Equation (6.2.9) (m)
R^*	radical
RH	hydrocarbon fuel
Re	Reynolds number
s	coefficient introduced in Equation (2.2.12)
Sc	Schmidt number
Sh	Sherwood number
t	time (s)
T	temperature (K), Taylor number in Equations (6.2.7) and (6.2.8)
T_D	doppler period (s)
T_{phase}	period between the zero crossings of the signal (s)
$\tilde{T}_0(R)$	parameter introduced in Equation (2.1.5) (K)
$\mathbf{u}$	fluid velocity (m/s)
U	value of the net velocity of the mixture (m/s)
$\mathbf{v}$	molecular velocities (m/s)
V	volume of droplet (m^3)
$\lVert v_n \rVert$	parameter introduced in Equation (2.1.5)

$w_\lambda\,(R)$	normalised absorbed spectral power density of radiation
W	molecular weight (kg/mole)
We	Weber number
x_1, x_2, x_3, x_4	kinetic rate parameters on Shell autoignition model defined in Equations (2.3.15)-(2.3.18)
X	molar fraction
x_λ	size parameter: $2\pi R_d/\lambda$
y_1, y_2, y_3, y_4	kinetic rate parameters on Shell autoignition model defined in Equations (2.3.15)-(2.3.18)
Y	mass fraction
y	dimensionless parameter on Equation (6.2.3)
z	parameter introduced in Equation (2.2.24)
Z	Dimensionless number defined as : $\sqrt{We_l / Re_l}$

Greek symbols

α	angle between the two beams
β	wedge angle
β_c	coefficients introduced in Equation (2.1.12)
β_m	evaporation or condensation coefficient
δm_{RBQ}	total change in mass of R*, B and Q over time step (kg/s)
ε	emissivity
ε / k_B	parameter used in Equation (C5) (K)
f	frequency (1/s)
γ	coefficient of autoignition model introduced in Equation (2.3.14)
$\bar{\gamma}$	parameter introduced in Equation (2.1.37)
$\delta_{T,M}$	film thickness (m)
θ_R	radiative temperature (K)
Φ	parameter introduced in Equation (2.5.2)
Φ_{ij}	function introduced in Equation (C3)
κ	$k_l/(c_l\rho_l R^2_d)$ (1/s)
κ_λ	index of absorption
λ	wavelength (m or μm)
λ_m	3.4 μm
λ_n	eigen values obtained from the solution of Equation (2.1.6)
λ_{st}	evaporation rate constant in Equation (2.2.2)
Λ_0	function introduced in Equation (2.1.28)
Ψ	parameter introduced in Equation (2.1.8)
ϕ	parameter introduced in Equation (2.2.52)
Φ	phase shift
μ	dynamic viscosity (kg/(m s))
μ_*	$\sqrt{1-\left(1/n(R/R_d)\right)^2}$
μ_c	$\sqrt{1-\left(1/n^2\right)}$
$\mu_0(t)$	$(hT_g(t)R_d/k_l)$ (K)
ν	kinematic viscosity (m^2/s)
ζ	parameter introduced in Equation (2.1.9)
ξ	parameter introduced in Equation (2.1.38)
ξ	parameter introduced in Equation (2.3.24)

ρ	density (kg/m^3)
σ	Stefan–Boltzmann constant (W/(m^{2}K^4))
σ_s	interfacial surface tension (N/m)
τ_e	evaporation time (s)
τ_λ	$a_\lambda R$
τ_0	$a_\lambda R_d$
χ	k_{eff}/k_l (see Equation (2.1.11))
Ω	collision integral, frequency (1/s)
ω	frequency (1/s)
Λ	wavelength (m)
τ_{bu}	breakup time (s)

Subscripts

b	boiling
abs	absorbed
amb	ambient
c	centre or convection
cr	critical
d	droplet
eff	effective
eq	equilibrium
ext	external
f	film surrounding droplets or fuel
F	fuel vapour
g	gas
inj	injection
iso	isolated
l	liquid
lg	from liquid to gas
m	type of species in the liquid phase
mix	mixture
0	initial or non-evaporating
p	constant pressure, pump
R	radiation
ref	reference
s	surface
S	Stokes
sv	saturated fuel vapour
t	time dependent
u	universal
v	fuel vapour
- 0	inner side of the droplet surface
+0	outer side of the droplet surface
∞	infinitely far from the droplet surface

Superscripts

—	average
~	normalised

1. INTRODUCTION

1.1 Background

Diesel engines are widely used due to their high efficiency and cost effectiveness. This has increased the demand for higher output, lower noise and emission performance from these engines. In meeting these demands, an in-depth understanding of the processes in these engines, and their modelling is crucial. One of these processes is droplet heating and evaporation. In Diesel engines, fuel droplet heating and evaporation play an important role in determining spray penetration, air/fuel mixing and autoignition.

Experimental analysis of monodisperse droplets heating and evaporation have been presented by Castanet e al. (2002, 2005). The droplet temperatures, velocities and radii in monodisperse streams were measured accurately using two colour laser induced fluorescence and particle dynamic analyser technique. The authors suggested a correction factor to take into account the drop-drop interaction effect on the heat and mass transfer number. Crua (2002) studied some processes in realistic Diesel engines.

Droplet heating and evaporation in a hot ambient gas are driven by convective and radiative processes. In the case of convective heating and evaporation, the processes in the liquid phase control the heat transfer from the droplet surface to its centre. The processes in the gas phase control heat and mass transfer from the surrounding gas to the droplet surface. In the case of radiative heating, the droplets are assumed to be opaque and grey or semi transparent. Considerable progress has been achieved in developing the models for convective and radiative heating of droplets and the results have been reported in a number of papers (Abramzon and Sirignano, 1989; Aggarwal, 1998; Sirignano, 1999; Dombrovsky, 2000, 2002b; Sazhin et al., 2001a, 2004a,b,c; Dombrovsky and Sazhin, 2003b, 2004; Sazhin, 2006).

Sazhin et al. (2004b) suggested a new numerical scheme for the analysis of droplet heating and evaporation based on the analytical solution of the heat conduction equation inside the droplet. This scheme takes into account the effect of temperature gradient inside the droplet. This model turned out to be attractive for implementation into CFD codes (see Sazhin et al., 2005a,b). The analysis of the results of implementation of this scheme for non-coupled solutions and a simple gas phase model showed that it is more accurate and computer efficient than the scheme based on a numerical solution of the heat conduction equation inside droplets (Sazhin et al., 2005a). It remained uncertain whether this conclusion is valid for more realistic cases (coupled solutions) and other gas phase models.

A simplified yet accurate model describing the thermal radiation absorption in semi-transparent Diesel fuel droplets was developed by Dombrovsky et al. (2001) and Sazhin et al. (2004a). In this model, detailed Mie calculations were replaced by the approximation of the absorption efficiency factor for droplets with an analytical formula aR_d^b, where R_d is the droplet radius and a and b are polynomials (quadratic functions in most cases) of the radiation temperature. The coefficients of these polynomials were found by comparison with rigorous computations for realistic Diesel fuel droplets, assuming that these droplets are irradiated by black-body thermal radiation.

In this thesis the results of further in-depth numerical analysis of fuel droplet convective and radiative heating and evaporation are presented. These results are compared with experimental data where appropriate.

1.2 Objectives of the project

The objectives of the project are:

1. Comparative numerical analysis of convective and radiative heating of individual droplets and their evaporation using various gas and liquid phase models.
2. Further development of the model of radiative absorption in semi-transparent fuel droplets
3. Comparison of the results predicted by the numerical analysis with available experimental data.
4. The implementation of the numerical scheme, developed for the analysis of heating and evaporation of individual droplets, into a customised version of the KIVA-2 CFD code. The most up-to-date droplet break-up models were implemented into this version of the KIVA-2 code as a result of work on a separate project.

5. The comparison of the prediction of the new customised version of the KIVA-2 CFD code with available in-house experimental data.

1.3 Structure of the thesis

The thesis comprises the following main parts. The literature review on spray modelling and experimental studies with a view of applications to Diesel engines is presented in Chapter 2. A comparative analysis of droplet heating and evaporation models is given in Chapter 3. In Chapter 4, further development of the droplet radiative heating model is presented. The experimental validation of the model of droplet heating and evaporation is presented and discussed in Chapter 5. The result of implementation of the model into the KIVA-2 CFD code and the application of the new customised version of this code to the analysis of the processes in Diesel engines is discussed in Chapter 6. The conclusions drawn from this thesis and recommendations for further work are presented in Chapter 7. The appendices contain additional information relating to various part of the thesis.

2. LITERATURE REVIEW

During the Diesel cycle, the air at close-to-atmospheric pressure and temperature is inducted to the combustion chamber and then compressed to a pressure of about 4 MPa and temperature of about 800 K during the compression stroke (Heywood, 1988). Liquid fuel is injected by the fuel injection system into the engine cylinder at the end of the compression stroke. The fuel atomises into small droplets and penetrates into the combustion chamber. Fuel injection pressures in the range from 20 to 170 MPa are used, depending on engine size and type of combustion system employed (Heywood, 1988). Then, the liquid fuel is heated and evaporates and fuel vapour mixes with the high-temperature high-pressure air. Since the air temperature and pressure are above the fuel's ignition point, spontaneous ignition (autoignition) of portions of the already-mixed fuel vapour and air occurs after a delay period. The details of the process depend on the characteristics of the fuel, the design of the engine's combustion chamber, fuel injection system, and the engine's operating conditions. It is an unsteady and heterogeneous combustion process. This thesis will focus on modelling and experimental studies of these sprays. The analysis will start with an overview of droplet heating models without taking into account the effects of evaporation.

2.1 Models of droplet heating without evaporation

The droplets in the combustion chamber are heated by convection and radiation by the surrounding gas. The problem of modelling the heating and evaporation of droplets has been widely discussed in the literature (Lefebvre, 1989; Sirignano, 1999; Sazhin, 2006). The models of convective heating of droplets include 2 components: modelling of the processes in the liquid phase, and modelling of heat transfer from surrounding gas to the droplet surface. In most studies it is assumed that droplets retain their spherical forms and the temperature over the whole droplet surface remains the same, although it can vary with time. This assumption effectively allows the separation of the analysis of heat transfer in gaseous and liquid phases. In the case of radiative heating of droplets the processes in the gas phase are usually ignored and the gas is assumed to be transparent for thermal radiation. In the following sections the models for convective and radiative heating of droplets will be considered separately.

2.1.1 Convective heating

2.1.1.1 Liquid phase analysis

Sirignano (1999) suggested the following classification of the models for heat transfer inside droplets, in order of increasing complexity: 1) models based on the assumption that the droplet surface temperature is uniform and does not change with time; 2) models based on the assumption that there is no temperature gradient inside droplets (infinite thermal conductivity (ITC) models); 3) models taking into account finite liquid thermal conductivity, but not the re-circulation inside droplets (conduction limit); 4) models taking into account both finite liquid thermal conductivity and the re-circulation inside droplets via the introduction of a correction factor to the liquid thermal conductivity (effective thermal conductivity (ETC) models); 5) models describing the re-circulation inside droplets in terms of vortex dynamics (vortex models); 6) models based on the full solution of the Navier-Stokes equation.

The first group of models allows the reduction of the dimension of the system via the complete elimination of the equation for droplet temperature. This appears to be particularly attractive for the analytical studies of droplet evaporation and the thermal ignition of fuel vapour/air mixture (Sazhin et al., 2001a). This group of models, however, appears to be too simplistic for most practically important applications. Groups (5) and (6) have not been used and are not expected to be used in most applications, including computational fluid dynamics (CFD) codes, in the foreseeable future due to their complexity. These models are widely used for the validation of more basic models of droplet heating, or for in-depth understanding of the underlying physical processes (e.g. Abramzon and Sirignano, 1989; Abramzon and Sazhin, 2005, 2006). The focus of this analysis will be on Groups (2)–(4), as these are the ones which are actually used in most practical applications, including CFD codes, or their incorporation in them is feasible.

For the second group of models (no temperature gradient inside droplets) the droplet temperature can be found from the energy balance equation:

$$\frac{4}{3}\pi R_{\mathrm{d}}^{3}\rho_{\mathrm{l}}c_{\mathrm{l}}\frac{dT_{\mathrm{d}}}{dt} = 4\pi R_{\mathrm{d}}^{2}h\left(T_{\mathrm{g}\infty} - T_{\mathrm{d}}\right), \tag{2.1.1}$$

where R_d is the droplet radius, ρ_l and c_l are the liquid density and specific heat capacity respectively, $T_{g\infty}$ and T_d are the ambient gas and droplet temperatures respectively, t is time, h is the convection heat transfer coefficient. Approximations for h depend on the processes in the gas phase, as discussed in the next section. Equation (2.1.1) merely indicates that all the heat supplied from the gas to the droplet is spent on raising the temperature of the droplet. It has a straightforward solution:

$$T(t) = T_{\mathrm{d}}(t) = T_{\mathrm{g}\infty} + \left(T_{\mathrm{d0}} - T_{\mathrm{g}\infty}\right)\exp\left(-\frac{3ht}{c_{\mathrm{l}}\rho_{\mathrm{l}}R_{\mathrm{d0}}}\right), \qquad (2.1.2)$$

where $T_d(t = 0) = T_{d0}$.

Equation (2.1.2) shows that the value of droplet temperature does not depend on R although this temperature is time varying. In this model, it is assumed that internal resistance of the droplet is negligible in comparison with the external resistance due to convection heat transfer. In a steady state case this could be justified when the Biot number is less than 0.1 ($Bi<0.1$) (Holman, 2002), where $Bi=h(V/A)/k_l$, V and A are volume and area of the droplet respectively, k_l is liquid thermal conductivity. Equation (2.1.1) and its solution (2.1.2) are widely used in various applications. Equation (2.1.1) was used to determine experimentally the heat transferred by convection to droplets (Castanet et al., 2001). Solution (2.1.2) is widely used in most CFD codes.

The application of this model is sometimes justified by the fact that liquid thermal conductivity is much higher than that of gas. However, the main parameter which controls droplet transient heating is not its conductivity, but its diffusivity. In the case of Diesel engine sprays, the diffusivity for liquid is more than an order of magnitude less than that for gas (Sazhin, 2006). This raises the question of whether the second group of models is applicable to modelling transient fuel droplet heating in these engines. The only reasonable way to answer this question is to consider the third group of models, which takes into account the effect of finite liquid thermal conductivity.

If the liquid thermal conductivity is not infinitely large then the effects of temperature gradient inside droplets need to be taken into account. As the first approximation, the effects of convection inside droplets can be ignored and the conduction limit can be considered (Group 3). The application of the third group of models can be based on the solution of the heat conduction equation inside the droplet which can be written as (Luikov, 1968; Carslaw and Jaeger, 1986):

$$c_1\rho_1\frac{\partial T}{\partial t}=k_1\left(\frac{\partial^2 T}{\partial R^2}+\frac{2}{R}\frac{\partial T}{\partial R}\right) \tag{2.1.3}$$

with the following boundary condition at the droplet surface:

$$h\left(T_{\mathrm{g}}-T_{\mathrm{s}}\right)=k_1\frac{\partial T}{\partial R}\Big|_{R=R_{\mathrm{d}}}, \tag{2.1.4}$$

and the corresponding condition at the centre of the droplet: $\frac{\partial T}{\partial R}\Big|_{R=0}=0$. The initial condition is taken in the form: $T(t=0)=T_{\mathrm{d}0}(R)$, $T(R_{\mathrm{d}})=T_{\mathrm{s}}=T_{\mathrm{s}}(t)$ is droplet's surface temperature, $T_{\mathrm{g}}=T_{\mathrm{g}}(t)$ is the ambient gas temperature, the subscript ∞ has been omitted.

Sazhin et al. (2004b) suggested analytical solutions of Equation (2.1.3). At first an explicit solution of the problem with constant heat transfer coefficient was obtained. Arbitrary initial temperature distributions inside droplets were taken into account. Also a general solution for the case of time dependent convection heat transfer coefficient was obtained. In this case the solution of the original differential equation was reduced to the solution of the Volterra integral equation of the second kind. Finally a solution for the case of almost constant convection heat transfer coefficient was obtained. In this case the problem has been solved using the perturbation theory. All three solutions were implemented into a zero dimensional CFD code, describing droplet heating and evaporation (Sazhin et al., 2005a).

In the case when $h(t)=h=$const, the solution of Equation (2.1.3) can be presented as (Sazhin et al., 2004b):

$$T(R,t)=\frac{R_{\mathrm{d}}}{R}\sum_{n=1}^{\infty}\left\{q_n\exp\left[-\kappa\lambda_n^2 t\right]-\frac{\sin\lambda_n}{\|v_n\|^2\lambda_n^2}\mu_0(0)\exp\left[-\kappa\lambda_n^2\right]-\frac{\sin\lambda_n}{\|v_n\|^2\lambda_n^2}\int_0^t\frac{d\mu_0(\tau)}{d\tau}\exp\left[-\kappa\lambda_n^2(t-\tau)\right]d\tau\right\}\sin\lambda_n\left(\frac{R}{R_{\mathrm{d}}}\right)+T_{\mathrm{g}}(t) \tag{2.1.5}$$

where:

$$\kappa = \frac{k_1}{c_1 \rho_1 R_\mathrm{d}^2}, \quad h_0 = \left(hR_\mathrm{d}/k_1\right) - 1, \quad \|v_n\|^2 = \frac{1}{2}\left(1 + \frac{h_0}{h_0^2 + \lambda_n^2}\right), \mu_\mathrm{o}(t) = hT_\mathrm{g}(t)R_\mathrm{d}/k_1,$$

$$\widetilde{T}_0(R) = RT_{\mathrm{d}0}(R)/R_\mathrm{d}, \quad q_n = \frac{1}{R_\mathrm{d}\|v_n\|^2}\int_0^{R_\mathrm{d}} \widetilde{T}_0(R)\sin\left[\lambda_n\left(\frac{R}{R_\mathrm{d}}\right)\right]dR,$$

a set of eigenvalues λ_n, numbered in ascending order (n=1, 2,..) is found from the solution of the following equation:

$$\lambda \cos\lambda + h_0 \sin\lambda = 0. \tag{2.1.6}$$

The solution based on the assumption of constant convective heat transfer coefficient was shown to be the most efficient for the implementation into numerical codes (Sazhin et al., 2005a). Initially, this solution was applied at the first time step, using initial distribution of temperature inside the droplet. The results of the analytical solution over this time step were used as the initial condition for the second time step etc. Detailed discussion of this analytical solution and its application are performed in Sazhin et al. (2004b). A number of other analytical solutions for specific heat source distribution in a sphere and various boundary conditions are presented in several well known monographs (e.g. Luikov, 1968; Carslaw and Jaeger, 1986).

Bertoli and Migliaccio (1999) suggested that numerical solution of the heat conduction equation inside the droplets (conduction limit) is incorporated it into CFD code KIVA-2, to relax the assumption of infinitely high thermal conductivity of liquid. This approach was shown to increase the accuracy of calculations but the additional computational cost might be too high.

Dombrovsky and Sazhin (2003a) suggested a model for convective heating of droplets based on the assumption of the parabolic temperature profile inside the droplets. Effect of temperature gradient inside droplets has been taken into account without solving the heat conduction equation. The temperature profile predicted by this model does not satisfy Equation (2.1.3), but satisfies the equation of thermal balance at droplet surfaces. The temperature profile in the droplet is approximated as:

$$T(R,t) = T_\mathrm{c}(t) + \left[T_\mathrm{s}(t) - T_\mathrm{c}(t)\right]\left(R/R_\mathrm{d}\right)^2, \tag{2.1.7}$$

where T_c is the temperature in the centre of the droplet, T_s is the surface temperature of the droplet. This presentation of *T(R,t)* takes into account the difference between the temperature in the centre and on the surface of the droplet. The boundary condition at *R=0* is satisfied. The boundary condition at $R=R_d$ and the condition for thermal balance of the droplet leads to the following equation (Dombrovsky and Sazhin, 2003a):

$$T_s = \left(\overline{T} + 0.2\zeta T_g\right) / \psi \, , \tag{2.1.8}$$

where $\psi = 1 + 0.2\zeta,\ \zeta = 0.5 Nu k_g / k_l,\ ,\overline{T} = \frac{3}{R_d^3} \int_0^{R_d} R^2 T(R) dR$ is the average droplet temperature.

In the limiting case when *Nu*=const, introducing dimensionless temperature $\theta = \frac{(T - T_0)}{(T_g - T_0)}$ and Fourier number $Fo = \frac{k_l t}{\rho_l c_l R_d^2}$, Equation (2.1.8) can be presented as:

$$\theta_s = \frac{\overline{\theta} + 0.2\zeta}{\psi}, \tag{2.1.9}$$

where $\overline{\theta} = 1 - \exp(-3\zeta Fo / \psi)$.

The predictions of this model were shown to be more accurate when compared with the predictions of the infinite thermal conductivity model except at the very initial stage of droplet heating. Application of this model in CFD codes requires very small additional CPU time.

Equation (2.1.9) is expected to introduce noticeable errors for small *Fo*. Hence correction factor is needed to improve the accuracy of the model in the whole range of *Fo*. The corrected form of Equation (2.1.9) was suggested by Dombrovsky and Sazhin (2003a) in the form:

$$\theta_s = \frac{\left(\overline{\theta} + 0.2\zeta\right)\left[1 - \exp(-\xi Fo)\right]}{\psi}, \tag{2.1.10}$$

where $\xi = 100\sqrt{\zeta}$.

Sazhin et al. (2005a) performed a comparative analysis of the performances of the infinite thermal conductivity model, model based on the parabolic temperature profile inside the droplets, numerical solution of the discretised heat conduction equation inside droplets and the model based on the analytical solution of the heat conduction equation. The values of parameters typical for Diesel engines were used. Methods of numerical solution of the discretised heat conduction equation based on the finite volume method have been widely discussed in the literature (e.g. Patankar, 1980; Versteeg and Malalasekera, 1995). The predictions of the algorithm based on the numerical solution of the discretised heat conduction equation and the algorithm using the analytical solution of this equation almost coincided for both the surface temperature and droplet radius. Both these solutions differed noticeably from the prediction of the model based on the assumption of no temperature gradient inside the droplet. The predictions of the parabolic model were between the abovementioned solutions. As shown by Sazhin et al. (2005a), the error and CPU time requirement of calculations based on the algorithm using analytical solution were consistently lower when compared with the errors of calculations based on the numerical solution of the discretised heat transfer equation. The errors of the numerical algorithm based on the parabolic temperature profile were less than the errors of numerical algorithm based on the assumption of no temperature gradient inside the droplets. The CPU time requirements of the parabolic temperature profile model were slightly larger than those of the model based on the assumption of no temperature gradient inside droplets. Note, that comparative analysis performed by Sazhin et al. (2005a) was under the assumption that gas parameters are fixed (non-coupled solution).

Abramson and Sirignano (1989) have developed a model of droplet heating and evaporation which takes into account effects of internal recirculation. This model was based on the solution of the two dimensional equation of convective heat transfer within a vaporizing droplet. This complex 'extended' model is believed to be very complicated and unpractical for implementation into CFD codes. A simplified model, called effective thermal conductivity model (ETC) (Group 4), was shown to be more practical than the extended model. In the effective thermal conductivity model, the thermal conductivity of liquid is multiplied by the factor χ which takes into account the effect of internal circulation on heat transfer within the droplet: $k_{\mathrm{eff}} = \chi k_{\mathrm{l}}$. The factor χ varies within 1 to 2.72 depending on the instantaneous liquid Peclet number

($Pe_l=Re_lPr_l$), it has been approximated by the following expression (Abramzon and Sirignano, 1989):

$$\chi = 1.86 + 0.86\ \tanh\left[2.225\log_{10}\left(Pe_l/30\right)\right]. \qquad (2.1.11)$$

This model does not allow the correct description of temperature distribution inside droplets, but gives accurate prediction of droplet surface temperature and vaporization rate. Comparative analysis presented by the authors has shown that both extended and effective thermal conductivity models predict similar evaporation times. Hence using the effective conductivity model can be justified. This model is particularly important for many practical engineering applications, where the details of temperature distribution inside droplets are generally not important. This model reduces the problem's dimension, which leads to considerable saving of the computer cost. Further analysis of this model, taking into account the effects of thermal radiation has been performed by Abramzon and Sazhin (2005; 2006). Comparative analysis of ETC and ITC model has been performed by Sazhin et al. (2005b). In general, the ETC model predicts quicker rise of surface temperature compared with ITC model. This was related to the fact that the heat reaching the surface of the droplet is spent on heating the whole droplet in ITC model, and heating of a relatively thin layer near the droplet surface in the ETC model. Then the surface temperature predicted by ETC model becomes lower than the predicted by the ITC model, due to the reduction of convective heating.

2.1.1.2 Gas phase analysis

Analysis of convective heat transfer in the gas phase is generally based on the analysis of the Nusselt number ($Nu=2R_dh/k_g$). Investigation of various methods to calculate Nu has been presented in many well known text books (e.g. Kreith, 1988; Incropera and DeWitt, 1996; Holman, 1997).

If it is assumed that the surface temperature of the droplet is fixed, the Nusselt number (Nu) depends on the Reynolds and Prandtl numbers ($Re_d=2R_d\left|\mathbf{v}_d-\mathbf{v}_g\right|/\nu_g$ and $Pr_d=c_{pg}\mu_g/k_g$, where $\mathbf{v}_d$ and $\mathbf{v}_g$ are droplet and gas velocities, ν_g and μ_g are gas kinematic and dynamic viscosities, c_{pg} and k_g are gas specific heat capacity at constant pressure and thermal conductivity respectively). In the case of stagnant non-evaporating droplet, ($Re=0$), $Nu=2$. The quantitative analysis of moving droplets shows that Nu is expected to be proportional to $Re^{1/2}Pr^{1/3}$ (Fuchs, 1959). Thus the general formula for *Nu* can be written as:

$$Nu = 2 + \beta_{\mathrm{c}}\, Re_{\mathrm{d}}^{1/2}\, Pr_{\mathrm{d}}^{1/3} \tag{2.1.12}$$

where the coefficient β_c cannot be derived from the simplified analysis. It should be obtained either from experimental or from rigorous numerical analysis.

A number of approximations for the Nusselt number of moving droplets, related to Equation (2.1.12), have been suggested. The most popular correlation for non-evaporating droplet has been presented as (Bird et al., 2002):

$$Nu = 2 + 0.6\, Re_{\mathrm{d}}^{1/2}\, Pr_{\mathrm{d}}^{1/3}\,. \tag{2.1.13}$$

The factor 0.6 in the equation above was sometimes replaced by 0.552, to give (Abramzon and Sirignano, 1989):

$$Nu = 2 + 0.552\, Re_{\mathrm{d}}^{1/2}\, Pr_{\mathrm{d}}^{1/3}\,. \tag{2.1.14}$$

Abramzon and Sirignano (1989) drew attention to the fact that Equation (2.1.14) over estimates heat transfer at low Reynolds number ($Re_{\mathrm{d}} \leq 10$) and suggested an alternative correlation in the form:

$$Nu = 1 + \left(1 + Re_{\mathrm{d}}\, Pr_{\mathrm{d}}\right)^{1/3} f\left(Re_{\mathrm{d}}\right), \tag{2.1.15}$$

where

$$f\left(Re_{\mathrm{d}}\right) = \begin{cases} 1 & \text{when } Re_{\mathrm{d}} \leq 1 \\ Re_{\mathrm{d}}^{0.077} & \text{when } 1 < Re_{\mathrm{d}} \leq 400. \end{cases} \tag{2.1.16}$$

Equation (2.1.15) approximated the results obtained by a number of authors for $0.25<Pr_{\mathrm{d}}<100$ with an error less than 3% (Abramzon and Sirignano, 1989).

Melissari et al. (2005) suggested a mathematical model to describe the heat transfer process when a melting sphere is immersed in a moving fluid. Based on this model, the following correlation for *Nu* was obtained

$$Nu = 2 + 0.47\, Re_{\mathrm{d}}^{\;0.5}\, Pr_{\mathrm{d}}^{\;0.36}\,. \tag{2.1.17}$$

This correlation is applicable to fluids with a wide range of Prandtl numbers. The lower end of this range includes the Prandtl number for liquid sodium ($Pr \approx 0.003$), whereas the upper end includes the Prandtl number for water ($Pr_{\mathrm{d}} \approx 10$). The analysis was performed for $10^2 \leq Re_{\mathrm{d}} \leq 5\text{x}10^4$. This model was validated against various experimental results involving metals and water. *Nu* predicted by Equation (2.1.17) is reasonably close to *Nu* predicted by Equation (2.1.14).

2.1.2 Radiative heating

2.1.2.1 Early models

The theory of radiative exchange between particulates and gas has been developed by a number of authors (e.g. Siegel and Howell, 1992; Modest, 1993). The simplest model for radiative heating of droplets could be based on the assumption that droplets are opaque grey spheres characterised by the surface emissivity ε (Sazhin et al., 2000). In this case, the heat flux into the droplets can be described by the following expression:

$$|\dot{q}| = h\left(T_{g\infty} - T_s\right) + \sigma\varepsilon\left(\theta_R^4 - T_s^4\right), \qquad (2.1.18)$$

where σ is the Stefan-Boltzmann constant and θ_R is the so called radiative temperature. For optically thick gas θ_R can be identified with the ambient temperature T_g while for optically thin gas it can be identified with the external temperature T_{ext} (Modest, 1993). The value of ε could be specified based on experimental data or rigorous calculations. This approach, however, has a number of important limitations. For example, it does not take into account the dependence of ε on droplet radius and external temperature. A more physically consistent approach to modelling the radiative heating of droplets is based on the assumption that droplets are semi-transparent. This is discussed in the next section.

2.1.2.2 Analysis of semi-transparent droplets

In the case of semi transparent droplets, the radiative heating of the droplets takes place not at their surfaces but via the absorption of thermal radiation penetrating inside the droplets. In the case of the infinite thermal conductivity liquid model (Group 2) and in the presence of thermal radiation, Equation (2.1.1) can be generalized to:

$$\frac{4}{3}\pi R_d^3 \rho_l c_l \frac{dT_d}{dt} = 4\pi R_d^2 h\left(T_g - T_d\right) + \rho_l c_l P_{total}, \qquad (2.1.19)$$

where

$$P_{\text{total}} = 4\pi \int_0^{R_{\text{d}}} P(R) R^2 dR \tag{2.1.20}$$

is the total amount of thermal radiation absorbed in a droplet, P_{total} is measured in K/s.

In the case of finite thermal conductivity and effective thermal conductivity models (Groups 3 and 4), the heat conduction equation for semi transparent droplets in the presence of thermal radiation can be written as:

$$c_1 \rho_1 \frac{\partial T}{\partial t} = k_1 \left(\frac{\partial^2 T}{\partial R^2} + \frac{2}{R} \frac{\partial T}{\partial R} \right) + c_1 \rho_1 P(R), \tag{2.1.21}$$

where *P(R)* accounts for the radiative heating of droplets, measured in K/s. This equation can be solved subject to the same boundary condition (2.1.4) as before.

Analytical solution of Equation (2.1.21) is a straightforward generalisation of solution (2.1.5) and can be written as (Sazhin et al., 2004b):

$$\begin{aligned} T(R,t) = \frac{R_d}{R} \sum_{n=1}^{\infty} \Bigg\{ & \frac{p_n}{\kappa \lambda_n^2} + \exp\left[-\kappa \lambda_n^2 t\right] \left(q_n - \frac{p_n}{\kappa \lambda_n^2} \right) - \frac{\sin\lambda_n}{\|v_n\|^2 \lambda_n^2} \mu_o(0) \exp\left[-\kappa \lambda_n^2 t\right] - \\ & \frac{\sin\lambda_n}{\|v_n\|^2 \lambda_n^2} \int_0^t \frac{d\mu_0(\tau)}{d\tau} \exp\left[-\kappa \lambda_n^2 (t-\tau)\right] d\tau \Bigg\} \sin \lambda_{\text{n}} \left(\frac{R}{R_d} \right) + T_g(t), \end{aligned} \tag{2.1.22}$$

where

$$p_n = \frac{1}{R_{\text{d}}^2 \|v_n\|^2} \int_0^{R_d} R P(R) \sin\left(\lambda_n \left(\frac{R}{R_{\text{d}}} \right) \right) dR. \tag{2.1.23}$$

The value of thermal radiation power can be calculated based on the equation:

$$P(R) = \frac{1}{\rho_1 c_1} \int_0^{\infty} p_\lambda(R) d\lambda, \tag{2.1.24}$$

where $p_\lambda(R)$ is the distribution of thermal radiation power density absorbed inside the droplet. The value of $p_\lambda(R)$ can be calculated based on the Mie theory, but these calculations are very complicated and are beyond the scope of this review. Various approximations for *P(R)* will be considered in the next section.

2.1.2.2.1 Radiative heating of the whole droplets

In most cases, the thermal radiation constitutes only a relatively small part of droplet's thermal balance. Hence the thermal radiation model needs to be kept simple (Sazhin et al., 2000). A widely used approach to characterise the absorption of thermal radiation in droplets is based on the application of the efficiency factor of absorption Q_{a}, defined as the ratio of radiation power absorbed in a droplet to the power of thermal radiation illuminating this droplet. Dombrovsky et al. (2003) suggested a simple approximation for calculation the efficiency factor of absorption for radiation absorbed by the whole droplet:

$$Q_{\mathrm{a}} = \frac{4n}{(n+1)^2}\left[1-\exp(-4\kappa_\lambda x)\right], \tag{2.1.25}$$

where n is the index of refraction, κ_λ is the index absorption and x is the diffraction parameter that can be calculated as $x = 2\pi R_{\mathrm{d}} / \lambda$, where λ is the wave length of radiation. The value of n was calculated based on subtractive Kramers-Krönig analysis and the measurement of n_0 at one particular wavelength. It was shown that the results of these calculations for typical Diesel fuel used in cars can be accurately approximated by the following relationship (Dombrovsky et al., 2002):

$$n = n_0 + 0.02\frac{\lambda - \lambda_{\mathrm{m}}}{(\lambda - \lambda_{\mathrm{m}})^2 + 0.001}, \tag{2.1.26}$$

where λ_{m}=3.6 μm, n_0 = 1.46. For practical calculations of κ_λ, the dependence of n on λ can be ignored, and n can be put equal to 1.46 (Dombrovsky et al., 2002).

Assuming that the thermal radiation illuminating the droplet is that of a black body and n is constant, the average efficiency factor of absorption of thermal radiation in the range of λ from λ_1 to λ_2 was found as (Dombrovsky et al., 2001; Sazhin et al., 2004a):

$$\overline{Q_{\mathrm{a}}} = \frac{4n}{(n+1)^2}\left\{1-\left[\frac{\left[\displaystyle\int_{\lambda_1}^{\lambda_2}\frac{\exp\left(-\frac{8\pi\kappa_\lambda R_{\mathrm{d}}}{\lambda}\right)}{\lambda^5\left[\exp\left(C_2/(\lambda T_{\mathrm{ext}})\right)-1\right]}d\lambda\right]}{\left[\displaystyle\int_{\lambda_1}^{\lambda_2}\frac{d\lambda}{\lambda^5\left[\exp\left(C_2/(\lambda T_{\mathrm{ext}})\right)-1\right]}\right]}\right]\right\}, \tag{2.1.27}$$

where C_2=1.439 x 10^4µm K.

It can be seen that Equation (2.1.27) is rather complicated for implementation into CFD codes. Hence, a simple but accurate approximation of $\overline{Q_{\mathrm{a}}}$ is needed. Taking into account the experimentally measured values of κ_λ for various Diesel fuels it was found that the best approximation for $\overline{Q_{\mathrm{a}}}$ in the ranges 5 µm ≤ R_{d} ≤ 50 µm and temperature 1000 K ≤ T_{ext} ≤ 3000 K is provided by the function:

$$\Lambda = aR_{\mathrm{d}}^{b}, \tag{2.1.28}$$

where a and b are quadratic functions of T_{ext} approximated as:

$$\left.\begin{aligned} a &= a_0 + a_1\left(\frac{T_{\mathrm{ext}}}{1000}\right) + a_2\left(\frac{T_{\mathrm{ext}}}{1000}\right)^2 \\ b &= b_0 + b_1\left(\frac{T_{\mathrm{ext}}}{1000}\right) + b_2\left(\frac{T_{\mathrm{ext}}}{1000}\right)^2 \end{aligned}\right\}, \tag{2.1.29}$$

gas was assumed to be optically thin. The values of a_0, a_1, a_2, b_0, b_1, and b_2 depend on the type of Diesel fuel used. For low sulphur ESSO AF 1313 un-boiled Diesel fuel in the range of 5 µm ≤ R_{d} ≤ 50µm and 1000 K ≤ T_{ext} ≤ 3000 K, the values of a_0, a_1, a_2, b_0, b_1, and b_2 were found to be 0.10400, -0.054320, 0.008000, 0.49162, 0.098369 and -0.007857 respectively (Sazhin et al., 2004a).

The contribution of thermal radiation for T_{ext} <1000 K is negligibly small in most cases. As can be seen from Equation (2.1.29), a decreases about five times when T_{ext} increases from 1000 to 3000 K. The dependence of b on T_{ext} is much slower: it increases from about 0.51 to about 0.65 when T_{ext} increases from 1000 to 3000 K (Dombrovsky et al., 2001).

Similar approach was used by Sazhin et al. (2004a) to analyse various Diesel fuels (boiled and un-boiled BP Ford reference Diesel fuel, boiled low sulphur ESSO AF1313 Diesel fuel), for droplet radii in the range 2 μm ≤ R_d ≤ 200 μm and external temperature in the range 500 K ≤ T_{ext} ≤ 3000 K. The boiling simulated the ageing process of fuels. From these analyses it can be concluded that Approximation (2.1.28) with a and b defined by Equations (2.1.29) is applicable for all four types of fuel in the range 2 μm ≤ R_d ≤ 200 μm and 1000 K ≤ T_{ext} ≤ 3000 K, although it becomes less accurate for droplets with radii greater than 50 μm. For 500 K ≤ T_{ext} ≤ 3000 K Equations (2.1.29) appeared to be poor for all types of fuel under consideration. To achieve better accuracy, Sazhin et al., (2004a) suggested the following approximations:

$$\left.\begin{aligned} a &= a_0 + a_1\left(\frac{T_{\mathrm{ext}}}{1000}\right) + a_2\left(\frac{T_{\mathrm{ext}}}{1000}\right)^2 + a_3\left(\frac{T_{\mathrm{ext}}}{1000}\right)^3 + a_4\left(\frac{T_{\mathrm{ext}}}{1000}\right)^4 \\ b &= b_0 + b_1\left(\frac{T_{\mathrm{ext}}}{1000}\right) + b_2\left(\frac{T_{\mathrm{ext}}}{1000}\right)^2 + b_3\left(\frac{T_{\mathrm{ext}}}{1000}\right)^3 + b_4\left(\frac{T_{\mathrm{ext}}}{1000}\right)^4 \end{aligned}\right\}. \qquad (2.1.30)$$

The values of a_0, a_1, a_2, a_3, a_4, b_0, b_1, b_2, b_3 and b_4, depend on the type of Diesel fuel used. For un-boiled low sulphur ESSO AF 1313 Diesel fuel in the range of 5μm ≤ R_d ≤ 50μm and 500 K ≤ T_{ext} ≤ 3000 K the values of a_0, a_1, a_2, a_3, a_4, b_0, b_1, b_2, b_3 and b_4 were found to be -0.0417, 0.28362, -0.26836, 0.09526, -0.011767, 0.9671, -0.9761, 0.84533,-0.28534, and 0.034233 respectively (Sazhin et al., 2004a). The contribution of thermal radiation at temperatures close to 500 K are expected be small.

2.1.2.2.2 Effect of the distribution of radiation absorption inside droplets.

A simplified model to calculate the distribution of radiation absorption inside droplets was suggested by Dombrovsky and Sazhin (2003b). The model was based on the assumption that the diffraction parameter x is much greater than unity and the geometric optics analysis is applicable (Dombrovsky, 2000). Remembering the definition of Q_a (the ratio of radiation power absorbed in a droplet to the power of thermal radiation illuminating the droplet) we can write (Dombrovsky, 1996):

$$\rho_l c_l P_{\mathrm{total}} = \pi R_d^2 \int_0^\infty Q_a I_\lambda^{0(\mathrm{ext})} d\lambda, \qquad (2.1.31)$$

where $I_\lambda^{0(\mathrm{ext})}$ is the intensity of external thermal radiation, P_{total} is defined by Equation (2.1.20)

Presentation of the results for differential absorption of thermal radiation is simplified if the following normalised function is introduced (Dombrovsky and Sazhin, 2003b):

$$w(R)=\frac{p_\lambda(R)}{\left[\frac{3}{R_{\mathrm{d}}^3}\int_0^{R_d} p_\lambda(R)R^2 dR\right]}, \tag{2.1.32}$$

where $p_\lambda(R)$ is the spectral radiation power absorbed per unit volume.

In this case, the value of thermal radiation power absorbed per unit volume inside the droplet can be calculated based on the following equation (Dombrovsky and Sazhin, 2003b):

$$P(R)=\int_0^\infty p_\lambda(R)d\lambda=\frac{0.75}{\rho_1 c_1 R_d}\int_0^\infty Q_a w(R) I_\lambda^{0(\mathrm{ext})} d\lambda. \tag{2.1.33}$$

If the external thermal radiation is that of a black body at temperature T_{ext} then $I_\lambda^{0(\mathrm{ext})}=4\pi B_\lambda(T_{\mathrm{ext}})$ and Equation (2.1.33) can be written as:

$$P(R)=\frac{3\pi}{\rho_1 c_1 R_{\mathrm{d}}}\int_0^\infty Q_{\mathrm{a}} w(R) B_\lambda(T_{\mathrm{ext}}) d\lambda, \tag{2.1.34}$$

where the Plank function $B_\lambda\,(T_{\mathrm{ext}})$ is defined as (Modest, 1993):

$$B_\lambda(T_{\mathrm{ext}})=\frac{C_1}{\pi\lambda^5\left[\exp\left(C_2/(\lambda T_{\mathrm{ext}})\right)-1\right]}, \tag{2.1.35}$$

C_1=3.742 x 10^8 Wμm^4/m^2, and C_2 is the same as in Equation (2.1.27).

As follows from Equation (2.1.34), the problem of approximate calculation of the radiation power absorbed per unit volume inside droplets reduces to the problem of finding an approximation for *w(R)*. Dombrovsky and Sazhin (2003b) suggested the approximations in the form:

$$w(R)=\frac{\left[1-\mu_*\Theta\left(\frac{R}{R_{\mathrm{d}}}-\left(\frac{1}{n}\right)\right)\right]\left[\left(\frac{R}{R_{\mathrm{d}}}\right)^2+\bar{\gamma}\right]}{\left[0.6\left(1-\mu_{\mathrm{c}}^5\right)-\mu_{\mathrm{c}}^3/n^2\right]+\bar{\gamma}\left(1-\mu_{\mathrm{c}}^3\right)}, \tag{2.1.36}$$

where $\bar{\gamma} = (1.5/\tau_0)^2 - (0.6/n)^2$, $\tau_0 = a_\lambda R_{\mathrm{d}}$, $\mu_{\mathrm{c}} = \sqrt{1-\left(\frac{1}{n}\right)^2}$, $\mu_* = \sqrt{1-\left(\frac{1}{n(R/R_{\mathrm{d}})}\right)^2}$,

$$\Theta(x) = \begin{cases} 0 & \text{when } x < 0 \\ 1 & \text{when } x \geq 0 \end{cases}$$

and

$$w(R) = \frac{\xi^2 \tau_0^3}{3} \frac{\exp[-\xi(\tau_0 - \tau)]}{\tau_0(\xi\tau_0 - 2) + (2/\xi)[1 - \exp(-\xi\tau_0)]}, \tag{2.1.37}$$

where $\xi = 2/(1+\mu_{\mathrm{c}})$. Equation (2.1.36) was used when $\tau_0 < \sqrt{2.5}$. Otherwise Equation (2.1.37) was used. The generalisation of this model to the case of asymmetrically illuminated droplet was reported by Dombrovsky and Sazhin (2004).

From above consideration, there are two different approaches to modelling the effects of thermal radiation on heating and evaporation of droplets. If the distribution of thermal radiation absorption inside droplets is needed, the term of *P(R)* in Equation (2.1.21) as defined by Equation (2.1.34) is used. If the distribution of thermal radiation absorption inside droplet is ignored then a much simpler approach can be used as suggested by Dombrovsky et al. (2001) and Sazhin et al. (2004a):

$$P(R) = \frac{3 \text{ x } 10^6 \, a\sigma R_{\mathrm{d}(\mu\mathrm{m})}^{b-1} \, T_{\mathrm{ext}}^4}{\rho_1 c_1} \tag{2.1.38}$$

When Equation (2.1.38) is applied, the expression for p_n, used in Equation (2.1.23), can be simplified to (Sazhin et al., 2005a):

$$p_n = \frac{1}{\rho_1 c_1 \|v_n\|^2} \int_0^1 3x10^6 \, aR_{\mathrm{d}}^{b-1} T_{\mathrm{ext}}^4 \left(\frac{R}{R_{\mathrm{d}}}\right) \sin\left(\lambda_n \left(\frac{R}{R_{\mathrm{d}}}\right)\right) dR. \tag{2.1.39}$$

Expression (2.1.34) is certainly more accurate than Expression (2.1.38), but its application requires much more CPU time than application of Expression (2.1.38). Most of the CPU time is actually spent on calculation of the integral over λ in Equation (2.1.34).

2.2 Models of droplet heating and evaporation

In Diesel engines, fuel evaporation plays an important role in determining air/fuel mixing. Evaporation of droplets involves simultaneous heat and mass transfer processes. The heat required for evaporation is transferred to the droplet surface by convection and radiation from surrounding hot gases while fuel vapour is transferred by convection and diffusion back into gas stream. Lefebvre (1989) has considered steady state and unsteady state evaporation. Steady state analysis is used to describe the stage in the droplet evaporation process where the drop surface has attained its wet-bulb temperature and all the heat supplied to its surface is spent to provide the latent heat of vaporisation. In many practical applications, a number of simplified assumptions are made: the droplets are assumed to be spherical, radiation is neglected, droplet temperature is assumed to be uniform and the fuel is assumed to be a pure liquid having a well-defined boiling point. In the case of unsteady heating and evaporation, effects of the heat-up period in the evaporation process cannot be neglected. Several methods of calculation of temperature and evaporation rate during the heat-up period have been suggested (Lefebvre, 1989).

In the most general case, the droplet evaporation includes two main phases: detachment of fuel molecules from the surface of the droplet into gas in the immediate vicinity of droplet surface and diffusion of fuel vapour from this surface into the ambient gas. The mathematical modelling of the first process is described by kinetic models (Kryukov et al., 2004; Shishkova and Sazhin, 2006) and that of the second one is described by hydrodynamic models. In most CFD applications the kinetic effects near the droplet surface are ignored and the fuel vapour is assumed to be saturated in this region. This section will be focused on the hydrodynamic models which are universally used in CFD codes. Before the analysis of advanced hydrodynamic models, I will start with analysis of classical D^2-law and empirical correlations.

In a similar way as the convection heat transfer coefficient was introduced to describe droplet heating, the mass transfer coefficient h_m is used to describe their mass transfer. In the general case, the dimensionless mass transfer number, the Sherwood number has been introduced:

$$Sh = \frac{2R_\mathrm{d} h_\mathrm{m}}{D_\mathrm{g}}, \qquad (2.2.1)$$

where D_g is the binary diffusion coefficient of fuel vapour in gas. In the case of stationary non evaporating droplets Sh=2.

2.2.1 Classical D^2-law

The classical D^2- law was formulated in the 1950s by Godsave and Spalding (e.g. Lefebvre, 1989; Sirignano, 1999). It was derived for an isolated, single component droplet, burning in a quiescent, oxidizing environment. The term D^2-law indicates that the square of the droplet diameter decreases linearly with time. For constant droplet surface temperature the evaporation rate λ_{st} is introduced as the surface regression rate defined as:

$$\lambda_{\mathrm{st}} = -\frac{dD^2}{dt}. \tag{2.2.2}$$

In order to obtain the evolution of droplet diameter, Equation (2.2.2) is integrated with the initial condition $D(t=0)= D_0$ (Lefebvre, 1989):

$$D^2(t) = D_0^2 - \lambda_{\mathrm{st}} t. \tag{2.2.3}$$

The result is the well-known D^2-law, stating that the square of the droplet diameter decreases linearly with time during droplet evaporation. In addition to the evaporation rate, another important parameter in droplet evaporation is the life time of the droplet, also called evaporation time τ_e, which can be determined from Equation (2.2.3) with $D(t=\tau_e)=0$:

$$\tau_{\mathrm{e}} = \frac{D_0^2}{\lambda_{\mathrm{st}}}. \tag{2.2.4}$$

The applicability of the D^2-law is limited since it is based the assumption that droplet temperature is constant.

2.2.2 Empirical correlations

Early empirical correlations for evaporating droplets were suggested by Renksizbulut et al. (1983). The authors suggested the correlation for the Nusselt number for moving and evaporating droplets in the form:

$$Nu = \frac{2 + 0.57\, Re_{\mathrm{f}}^{1/2}\, Pr_{\mathrm{f}}^{1/3}}{\left(1 + B_{\mathrm{f}}\right)^{0.7}}, \tag{2.2.5}$$

where

$$B_{\mathrm{f}} = \frac{c_{\mathrm{pv}}\left(T_{\mathrm{g}} - T_{\mathrm{s}}\right)}{L}\left(1 - \frac{|\dot{q}_{\mathrm{d}}|}{|\dot{q}_{\mathrm{c}}|} + \frac{|\dot{q}_{\mathrm{R}}|}{|\dot{q}_{\mathrm{c}}|}\right), \tag{2.2.6}$$

$|\dot{q}_{\mathrm{d}}|$ is the heat rate spent on raising the temperature of a liquid droplet, $|\dot{q}_{\mathrm{c}}|$ and $|\dot{q}_{\mathrm{R}}|$ are the rates supplied to droplets by convection and radiation respectively, $Re_{\mathrm{f}}=2R_{\mathrm{d}}\rho_{\mathrm{g}}|\mathrm{v_g}-\mathrm{v_d}|/\mu_{\mathrm{gf}}$, subscript f indicates that the values of parameters are taken inside the film surrounding the droplet, subscript ∞ in the term T_{g} is omitted. It was assumed that the film temperature is equal to:

$$T_{\mathrm{f}} = \frac{T_{\mathrm{g}} + T_{\mathrm{s}}}{2}, \tag{2.2.7}$$

the fuel vapour mass fraction is equal to:

$$Y_{\mathrm{f}} = \frac{Y_{\mathrm{fs}} + Y_{\mathrm{f}}}{2}, \tag{2.2.8}$$

and the droplets can be treated as grey bodies with emissivities equal to 0.95. Equation (2.2.5) was obtained in the following range of parameters $0.07 \le B_{\mathrm{f}} \le 2.79$ and $24 \le Re_{\mathrm{f}} \le 1974$. Note that in the absence of evaporation $|\dot{q}_{\mathrm{d}}| = |\dot{q}_{\mathrm{c}}| + |\dot{q}_{\mathrm{R}}|$ and $B_{\mathrm{f}} = 0$.

Similarly to Equation (2.2.5), the correlation for Sh for moving evaporating droplets was obtained experimentally in the form (Haywood et al., 1989):

$$Sh = \frac{2 + 0.87\, Re_{\mathrm{f}}^{1/2}\, Sc_{\mathrm{f}}^{1/3}}{\left(1 + B_{\mathrm{M}}\right)^{0.7}}, \tag{2.2.9}$$

where $Sc_{\mathrm{f}} = \upsilon_{\mathrm{f}}/D_{\mathrm{f}}$ is the Schmidt number determined in the film region, B_{M} is the Spalding mass number that be defined as:

$$B_{\mathrm{M}} = \frac{Y_{\mathrm{vs}} - Y_{\mathrm{v\infty}}}{\left(1 - Y_{\mathrm{vs}}\right)} = \frac{\rho_{\mathrm{vs}} - \rho_{\mathrm{v\infty}}}{\rho_{\mathrm{gs}}}, \tag{2.2.10}$$

Y_{vs} is fuel vapour mass fraction at the droplet surface and $Y_{\mathrm{v\infty}}$ is air (gas) mass fraction away from the droplet surface, ρ_{vs} and $\rho_{\mathrm{v\infty}}$ are densities of fuel vapour in the vicinity of droplets and away from them (ambient gas). Y_{vs} can be obtained from the following relation (Lefebvre, 1989):

$$Y_{\mathrm{vs}} = \left[1 + \left(\frac{p_{\mathrm{gas}}}{p_{\mathrm{fs}}} - 1\right)\frac{M_{\mathrm{a}}}{M_{\mathrm{f}}}\right]^{-1}, \tag{2.2.11}$$

where

$$p_{\mathrm{fs}} = \exp\left[s_{\mathrm{f}} - \frac{x_{\mathrm{f}}}{T_{\mathrm{s}} - 43} \right], \tag{2.2.12}$$

and p_{gas} are partial pressure of fuel vapour and the total gas pressure respectively, s_{f} and x_{f} are constants to be specified for specific fuels, M_{a} and M_{f} are air and fuel molar masses respectively. Equation (2.2.9) was obtained for $20 \le Re_{\mathrm{f}} \le 2000$.

Renksizbulut et al. (1989) suggested accurate mathematical and numerical model to analyse evaporation process of an isolated n-heptane droplet. Various grids and time steps both in liquid and gas phase were used. The authors concluded that the correlations for the Nusselt number and the Sherwood number are close to those predicted by experimental studies (see Equations (2.2.5) and (2.2.9)).

2.2.3 Hydrodynamic models

Hydrodynamic models of droplet evaporation are related to the diffusion model of fuel vapour from the surface of the droplet into the ambient gas. These models are usually based on the assumption that fuel vapour in the vicinity of the droplet surface is saturated. Hence, the rate of fuel evaporation is equal to the rate of fuel diffusion from the droplet surface to ambient gas. Ignoring the effect of ambient air we can write:

$$\dot{m}_{\mathrm{d}} = -4\pi R_{\mathrm{d}} D_{\mathrm{v}} \left(\rho_{\mathrm{vs}} - \rho_{\mathrm{v}\infty} \right), \qquad 2.2.13)$$

where D_{v} is the diffusion coefficient of the fuel vapour, ρ_{vs} and $\rho_{\mathrm{v}\infty}$ are the same as in Equation (2.2.10). Equation (2.2.13) is known as the Maxwell equation (Sazhin, 2006). Its limitation lies in the fact that it takes into account only the diffusion process, but ignores the effect of convective flow of the mixture of air and fuel vapour away from the surface of the droplet. To take into account this effect (Stefan flow), the droplet evaporation rate could be based on the following expression:

$$\dot{m}_{\mathrm{d}} = 4\pi R^2 \left(D_{\mathrm{v}} \frac{d\rho_{\mathrm{v}}}{dR} - D_{\mathrm{g}} \frac{\rho_{\mathrm{v}}}{\rho_{\mathrm{g}}} \frac{d\rho_{\mathrm{g}}}{dR} \right), \tag{2.2.14}$$

where ρ_{v} and ρ_{g} are fuel vapour and gas densities, D_{g} is the diffusion coefficient of ambient gas (air). It is generally assumed that $D_{\mathrm{g}}=D_{\mathrm{v}}$ and the total density of the mixture of gas and fuel vapour in the vicinity of the droplet surface is constant ($\rho_{\mathrm{total}}=\rho_{\mathrm{g}}+\rho_{\mathrm{v}}$). In this case the rearrangement and integration of Equation (2.2.14) from $R=R_{\mathrm{d}}$ to $R=\infty$

gives the following expression for $\dot{m}_\mathrm{d}$:

$$\dot{m}_\mathrm{d} = -4\pi R_\mathrm{d} D_\mathrm{g} \rho_\mathrm{total} \ln(1 + B_\mathrm{M}). \tag{2.2.15}$$

This model is widely use for stationary evaporating droplets. Remembering the definition of h_m we can write:

$$\dot{m}_\mathrm{d} = 4\pi R_\mathrm{d}^2 h_\mathrm{m} (\rho_\mathrm{vs} - \rho_{\mathrm{v}\infty}). \tag{2.2.16}$$

Combining Equations (2.2.15) and (2.2.16) we obtained the following expression for *Sh* (Lefebvre, 1989):

$$Sh = \frac{2\ln(1 + B_\mathrm{M})}{B_\mathrm{M}}. \tag{2.2.17}$$

Equation (2.2.17) can be presented in a more general form:

$$Sh = Sh_0 \frac{\ln(1 + B_\mathrm{M})}{B_\mathrm{M}}, \tag{2.2.18}$$

where $Sh_0 = 2$ for stationary droplets.

Similarly, the following expression for the Nusselt number was obtained (Lefebvre, 1989):

$$Nu = Nu_0 \frac{\ln(1 + B_\mathrm{M})}{B_\mathrm{M}}, \tag{2.2.19}$$

where Nu_0 is the Nusselt number for non-evaporating droplets (Nu_0=2 for stationary droplets).

An alternative expression for *Nu* can be found taking into account the effect of vapour superheating (raising of fuel vapour temperature from T_s to T_g). The energy balance equation for a droplet taking into account this effect can be written as (Sirignano, 1978):

$$4\pi R_\mathrm{d}^2 k_\mathrm{g} \frac{dT}{dR} = -\dot{m}_\mathrm{d} c_\mathrm{pv} (T - T_\mathrm{s}) - \dot{m}_\mathrm{d} L(T_\mathrm{s}) + |\dot{q}_\mathrm{d}| \tag{2.2.20}$$

The left hand side of this equation shows the heat supplied from the surrounding gas to the droplet. The first term in the right hand side shows the heat required to heat fuel vapour from T_s to $T=T(R)$ (gas temperature at the distance R from centre of the droplet). The second and third terms in the right hand side show the heat spent on droplet evaporation and raising its temperature, respectively. Equation (2.2.20) can be rearranged to:

$$4\pi k_{\mathrm{g}} \frac{dT}{c_{\mathrm{pv}}(T-T_{\mathrm{s}})+L(T_{\mathrm{s}})-(|\dot{q}_{\mathrm{d}}|/\dot{m}_{\mathrm{d}})} = -\frac{\dot{m}_{\mathrm{d}}dR}{R^2}. \tag{2.2.21}$$

Introducing the Spalding heat transfer number B_{T} (Abramzon & Sirignano, 1989):

$$B_{\mathrm{T}} = \frac{c_{\mathrm{pv}}(T_{\mathrm{g}}-T_{\mathrm{s}})}{L(T_{\mathrm{s}})-(|\dot{q}_{\mathrm{d}}|/\dot{m}_{\mathrm{d}})} \tag{2.2.22}$$

and integrating both parts of Equation (2.2.21) from T=T_{s} to T=T_{g} and from R=R_{d} to R=∞ respectively, we obtain:

$$\dot{m}_{\mathrm{d}} = -\frac{4\pi k_{\mathrm{g}} R_{\mathrm{d}}}{c_{\mathrm{pv}}} \ln(1+B_{\mathrm{T}}). \tag{2.2.23}$$

For practical calculations, widely used in CFD applications, El Wakil et al. (1954) suggested a correction for the Nusselt number to take into account the effect of super heating in the form (see also Sazhin, 2006):

$$Nu = \frac{z}{e^z-1} Nu_0, \tag{2.2.24}$$

where

$$z = -\frac{\dot{m}_{\mathrm{d}} c_{\mathrm{pv}}}{4\pi k_{\mathrm{g}} R_{\mathrm{d}}} = \frac{\dot{m}''_{\mathrm{d}} R_{\mathrm{d}} c_{\mathrm{pv}}}{k_{\mathrm{g}}}, \tag{2.2.25}$$

where $\dot{m}''_d$ is the mass flux.

For the heat which reaches the surface of a droplet, we can write the following expression:

$$|\dot{q}_{\mathrm{s}}| = -\dot{m}_{\mathrm{d}} L + |\dot{q}_{\mathrm{d}}| = 4\pi R_{\mathrm{d}}^2 h(T_{\mathrm{g}}-T_{\mathrm{s}}) = 4\pi R_{\mathrm{d}}^2 \frac{Nu k_{\mathrm{g}}}{2R_{\mathrm{d}}}(T_{\mathrm{g}}-T_{\mathrm{s}}). \tag{2.2.26}$$

Combining Equations (2.2.22), (2.2.23) and (2.2.26) we obtain the following equation for Nu:

$$Nu = \frac{\ln(1+B_{\mathrm{T}})}{B_{\mathrm{T}}} Nu_0, \tag{2.2.27}$$

which is obviously different from Equation (2.2.19) (but equivalent to Equation (2.2.24)). For a stationary evaporating droplet, Equation (2.2.27) reduces to:

$$Nu = \frac{2\ln(1+B_{\mathrm{T}})}{B_{\mathrm{T}}}. \tag{2.2.28}$$

The Sherwood number for evaporating moving droplets depends on *Re* and *Sc*. The well known correlation for Sh_0 can be presented as (Bird et al., 2002):

$$Sh_0 = 2 + 0.6\,Re_{\mathrm{d}}^{1/2}\,Sc_{\mathrm{d}}^{1/3}. \tag{2.2.29}$$

For evaporating moving droplets the expression for the Nusselt number and the Sherwood number can be presented as:

$$Sh = \frac{\ln(1+B_{\mathrm{M}})}{B_{\mathrm{M}}}\left(2 + 0.6\,Re_{\mathrm{d}}^{1/2}\,Sc_{\mathrm{d}}^{1/3}\right) \tag{2.2.30}$$

$$Nu = \frac{\ln(1+B_{\mathrm{T}})}{B_{\mathrm{T}}}\left(2 + 0.6\,Re_{\mathrm{d}}^{1/2}\,Pr_{\mathrm{d}}^{1/3}\right). \tag{2.2.31}$$

The factor 0.6 in the equations above can be replaced by 0.552. Hence, Correlations (2.2.30) and (2.2.31) become (Abramzon and Sirignano, 1989):

$$Sh = \frac{\ln(1+B_{\mathrm{M}})}{B_{\mathrm{M}}}\left(2 + 0.552\,Re_{\mathrm{d}}^{1/2}\,Sc_{\mathrm{d}}^{1/3}\right) \tag{2.2.32}$$

$$Nu = \frac{\ln(1+B_{\mathrm{T}})}{B_{\mathrm{T}}}\left(2 + 0.552\,Re_{\mathrm{d}}^{1/2}\,Pr_{\mathrm{d}}^{1/3}\right). \tag{2.2.33}$$

Alternatively, remembering Equation (2.1.15), we can write (Abramzon and Sirignano, 1989):

$$Nu = \frac{\ln(1+B_{\mathrm{T}})}{B_{\mathrm{T}}}\left(1 + (1 + Re_{\mathrm{d}}\,Pr_{\mathrm{d}})^{1/3} f(Re_{\mathrm{d}})\right) \tag{2.2.34}$$

$$Sh = \frac{\ln(1+B_{\mathrm{M}})}{B_{\mathrm{M}}}\left(1 + (1 + Re_{\mathrm{d}}\,Sc_{\mathrm{d}})^{1/3} f(Re_{\mathrm{d}})\right). \tag{2.2.35}$$

Abramzon and Sirignano (1989) refined the classical model above by taking into account the effect of convective transport caused by the droplet motion relative to the gas by introducing so called ‘film’ theory. The film theory assumes that the resistance to heat or mass exchange between a surface and a gas flow may be modelled by introducing the concept of gas films of thicknesses: δ_{T} and δ_{M}. Subscripts T and M refer to the heat and mass transfer respectively. For a non-evaporating droplet, the thickness of the thermal and diffusion films δ_{T} and δ_{M} are calculated as (Abramzon and Sirignano, 1989):

$$\delta_{\mathrm{T0}} = \frac{2R_{\mathrm{s}}}{Nu_0 - 2} \qquad (2.2.36)$$

and

$$\delta_{\mathrm{M0}} = \frac{2R_{\mathrm{s}}}{Sh_0 - 2}\,. \qquad (2.2.37)$$

The effect of Stefan flow was taken into account by introducing the correction factors:

$F_{\mathrm{T}}=\delta_{\mathrm{T}}/\delta_{\mathrm{T0}}$ (2.2.38)

and

$F_{\mathrm{M}}=\delta_{\mathrm{M}}/\delta_{\mathrm{M0}}$. (2.2.39)

To find the correction factors F_{M} and F_{T} for the film thickness, they considered a model problem of the laminar boundary layer developed for a flow past a vaporising wedge. The range of parameters was the following: $0 \le (B_{\mathrm{T}}, B_{\mathrm{M}}) \le 20$; $1 \le (Sc, Pr) \le 3$; $0 \le \beta \le 2\pi$ (β is wedge angle). In the case of an isothermal surface and constant physical properties of fluid, the problem has a self similar solution and the correction factors F_{T} and F_{M} do not depend on the local Reynolds number. It was found that values of F_{M} and F_{T} are practically insensitive to Schmidt and Prandtl numbers and the wedge angle variations, and can be approximated as:

$F_{\mathrm{M}}=F(B_{\mathrm{M}})$, $F_{\mathrm{T}}=F(B_{\mathrm{T}})$, (2.2.40)

where $F(B_{\mathrm{M,T}})$ is the universal function:

$$F(B_{\mathrm{M,T}}) = (1 + B_{\mathrm{M,T}})^{0.7}\,\frac{\ln(1 + B_{\mathrm{M,T}})}{B_{\mathrm{M,T}}} \qquad (2.2.41)$$

Note that $F(B)$ increases from 1 to 1.285 as B grows from 0 to 8. In the interval $8 \le B \le 20$, the values of $F(B)$ remain practically constant.

To take into account the effect of film thickness, they suggested modified Nusselt and Sherwood numbers to Nu^* and Sh^* defined as:

$$Nu^* = 2 + \frac{Nu_0 - 2}{F(B_{\mathrm{T}})}\,, \qquad (2.2.42)$$

$$Sh^* = 2 + \frac{Sh_0 - 2}{F(B_{\mathrm{M}})}\,. \qquad (2.2.43)$$

In practical implementations into CFD codes the actual Sherwood number (*Sh*) and Nusselt number (*Nu*) need to be used. These parameters can be found from the following equations:

$$Nu = Nu^* \frac{\ln(1+B_\mathrm{T})}{B_\mathrm{T}} \tag{2.2.44}$$

$$Sh = Sh^* \frac{\ln(1+B_\mathrm{M})}{B_\mathrm{M}}. \tag{2.2.45}$$

Taking into account film theory, the correlations for *Nu* and *Sh* should be modified and Equations (2.2.30)-(2.2.35) become:

$$Sh = 2\frac{\ln(1+B_\mathrm{M})}{B_\mathrm{M}}\left[1+0.3\frac{Sc_\mathrm{d}^{1/3}\,Re_\mathrm{d}^{1/2}}{F(B_\mathrm{M})}\right] \tag{2.2.46}$$

$$Nu = 2\frac{\ln(1+B_\mathrm{T})}{B_\mathrm{T}}\left[1+0.3\frac{Pr_\mathrm{d}^{1/3}\,Re_\mathrm{d}^{1/2}}{F(B_\mathrm{T})}\right] \tag{2.2.47}$$

$$Sh = 2\frac{\ln(1+B_\mathrm{M})}{B_\mathrm{M}}\left[1+0.276\frac{Sc_\mathrm{d}^{1/3}\,Re_\mathrm{d}^{1/2}}{F(B_\mathrm{M})}\right] \tag{2.2.48}$$

$$Nu = 2\frac{\ln(1+B_\mathrm{T})}{B_\mathrm{T}}\left[1+0.276\frac{Pr_\mathrm{d}^{1/3}\,Re_\mathrm{d}^{1/2}}{F(B_\mathrm{T})}\right] \tag{2.2.49}$$

$$Sh = 2\frac{\ln(1+B_\mathrm{M})}{B_\mathrm{M}}\left[1+\frac{(1+Sc_\mathrm{d}\,Re_\mathrm{d})^{1/3} f(Re)-1}{2F(B_\mathrm{M})}\right] \tag{2.2.50}$$

$$Nu = 2\frac{\ln(1+B_\mathrm{T})}{B_\mathrm{T}}\left[1+\frac{(1+Pr_\mathrm{d}\,Re_\mathrm{d})^{1/3} f(Re)-1}{2F(B_\mathrm{T})}\right]. \tag{2.2.51}$$

Introducing the new parameter ϕ:

$$\phi = \left(\frac{c_{pv}}{c_{pg}}\right)\left(\frac{Sh^*}{Nu^*}\right)\frac{1}{Le} \tag{2.2.52}$$

The following relation can be obtained (Abramzon and Sirignano, 1989):

$$B_\mathrm{T} = (1+B_\mathrm{M})^{\phi} - 1 \tag{2.2.53}$$

An alternative model was suggested by Yao et al. (2003) in which the following relations were used:

$$Sh = 2\frac{\ln(1+B_{\mathrm{M}})}{B_{\mathrm{M}}}\left(1+\frac{R_{\mathrm{d}}}{\delta_{\mathrm{M}}}\right) \qquad (2.2.54)$$

and

$$Nu = 2\frac{\ln(1+B_{\mathrm{T}})}{B_{\mathrm{T}}}\left(1+\frac{R_{\mathrm{d}}}{\delta_{\mathrm{T}}}\right). \qquad (2.2.55)$$

The analytical solution suggested by Sazhin et al. (2004b) and described in Section 2.1.1 can be generalised to take into account the effect of evaporation on gas temperature (T_{g}) in Equations (2.1.5) and (2.1.22). This is achieved by replacing T_{g} by the so-called effective temperature defined as:

$$T_{\mathrm{eff}} = T_{\mathrm{g}} + \frac{\rho_{\mathrm{l}} L \dot{R}_{\mathrm{d}}}{h}, \qquad (2.2.56)$$

where the value of $\dot{R}_{\mathrm{d}}$ can be taken from the previous time step during numerical calculations.

The models described by Equations (2.2.30)-(2.2.35) and Equations (2.2.46)-(2.2.51) will be used in our analysis in the next chapter. These models need to be compared with the model based on the experimental analysis. The model based on Equations (2.2.30) and (2.2.31) but with B_{T} is replaced by B_{M} will be referred to as Model 0. The model based on Equations (2.2.30) and (2.2.31) will be referred to as Model 1. The model based on Equations (2.2.46) and (2.2.47) will be referred to as Model 2. The model based on Equations (2.2.34) and (2.2.35) will be referred to as Model 3. The model based on Equations (2.2.50) and (2.2.51) will be referred to as Model 4. The model based on Equations (2.2.48) and (2.2.49) will be referred to as Model 5. The model based on the empirical correlations described by Equations (2.2.5) and (2.2.9) will be referred to as Model 6. The summary of the models is presented in Table 2.1:

Model 0	$Sh = \frac{\ln\left(1+B_{\mathrm{M}}\right)}{B_{\mathrm{M}}}\left(2+0.6\,Re_{\mathrm{d}}^{1/2}\,Sc_{\mathrm{d}}^{1/3}\right)$ $Nu = \frac{\ln\left(1+B_{\mathrm{M}}\right)}{B_{\mathrm{M}}}\left(2+0.6\,Re_{\mathrm{d}}^{1/2}\,Pr_{\mathrm{d}}^{1/3}\right)$
Model 1	$Sh = \frac{\ln\left(1+B_{\mathrm{M}}\right)}{B_{\mathrm{M}}}\left(2+0.6\,Re_{\mathrm{d}}^{1/2}\,Sc_{\mathrm{d}}^{1/3}\right)$ $Nu = \frac{\ln\left(1+B_{\mathrm{T}}\right)}{B_{\mathrm{T}}}\left(2+0.6\,Re_{\mathrm{d}}^{1/2}\,Pr_{\mathrm{d}}^{1/3}\right)$
Model 2	$Sh = 2\frac{\ln\left(1+B_{\mathrm{M}}\right)}{B_{\mathrm{M}}}\left[1+0.3\frac{Sc_{\mathrm{d}}^{\;1/3}\,Re_{\mathrm{d}}^{\;1/2}}{F\left(B_{\mathrm{M}}\right)}\right]$ $Nu = 2\frac{\ln\left(1+B_{\mathrm{T}}\right)}{B_{\mathrm{T}}}\left[1+0.3\frac{Pr_{\mathrm{d}}^{\;1/3}\,Re_{\mathrm{d}}^{\;1/2}}{F\left(B_{\mathrm{T}}\right)}\right]$
Model 3	$Nu = \frac{\ln\left(1+B_{\mathrm{T}}\right)}{B_{\mathrm{T}}}\left(1+\left(1+Re_{\mathrm{d}}\,Pr_{\mathrm{d}}\right)^{1/3} f\left(Re_{\mathrm{d}}\right)\right)$ $Sh = \frac{\ln\left(1+B_{\mathrm{M}}\right)}{B_{\mathrm{M}}}\left(1+\left(1+Re_{\mathrm{d}}\,Sc_{\mathrm{d}}\right)^{1/3} f\left(Re_{\mathrm{d}}\right)\right)$
Model 4	$Sh = 2\frac{\ln\left(1+B_{\mathrm{M}}\right)}{B_{\mathrm{M}}}\left[1+\frac{\left(1+Sc_{\mathrm{d}}\,Re_{\mathrm{d}}\right)^{1/3} f\left(Re\right)-1}{2F\left(B_{\mathrm{M}}\right)}\right]$ $Nu = 2\frac{\ln\left(1+B_{\mathrm{T}}\right)}{B_{\mathrm{T}}}\left[1+\frac{\left(1+Pr_{\mathrm{d}}\,Re_{\mathrm{d}}\right)^{1/3} f\left(Re\right)-1}{2F\left(B_{\mathrm{T}}\right)}\right]$
Model 5	$Sh = 2\frac{\ln\left(1+B_{\mathrm{M}}\right)}{B_{\mathrm{M}}}\left[1+0.276\frac{Sc_{\mathrm{d}}^{\;1/3}\,Re_{\mathrm{d}}^{\;1/2}}{F\left(B_{\mathrm{M}}\right)}\right]$ $Nu = 2\frac{\ln\left(1+B_{\mathrm{T}}\right)}{B_{\mathrm{T}}}\left[1+0.276\frac{Pr_{\mathrm{d}}^{\;1/3}\,Re_{\mathrm{d}}^{\;1/2}}{F\left(B_{\mathrm{T}}\right)}\right]$
Model 6	$Sh = \frac{2+0.87\,Re_{\mathrm{f}}^{1/2}\,Sc_{\mathrm{f}}^{1/3}}{\left(1+B_{\mathrm{M}}\right)^{0.7}}$ $Nu = \frac{2+0.57\,Re_{\mathrm{f}}^{1/2}\,Pr_{\mathrm{f}}^{1/3}}{\left(1+B_{\mathrm{f}}\right)^{0.7}}$

Table 2.1 Summary of the gas phase model

2.3 Autoignition modelling

Autoignition of Diesel sprays is usually described in terms of ignition delay and ignition sites location. Although the autoignition may be considered as a continuous process (Dec and Espey, 1998) it is widely accepted that autoignition is the beginning of the thermal explosion that follows the physical processes (mixing of fuel with ambient gas) and chemical reactions leading to the onset of a flame (Aggarwal, 1998). Modelling of the autoignition is essential for predicting the initiation of combustion in Diesel engines (Griffiths and Barnard, 1995). Two main parameters characterize the autoignition process: the initial temperature at which the autoignition can develop and the time delay before the start of autoignition (Brady, 1996). Detailed kinetic mechanism of the autoignition process is very complicated as it includes many chemical reactions and species. The chemical part of the autoignition process can be described in terms of chain reactions that occur as initiating reactions, chain propagating reactions, chain branching reactions and terminating reactions (Borman and Ragland, 1998).

A simplified description of these processes was suggested by the group of researcher from Shell research Ltd. This mechanism is known as the Shell model. In the Shell model the autoignition chemistry is reduced to eight-step chain branching reaction scheme incorporated into four processes (Halstead et al.,1977)

Initiation :

$RH + O2 \rightarrow 2R^*$ Rate coefficient k_q (2.3.1)

Propagation

$R^* \rightarrow R^*+P$ Rate coefficient k_p (2.3.2)

$R^* \rightarrow R^*+B$ Rate coefficient $f_1 k_p$ (2.3.3)

$R^* \rightarrow R^*+Q$ Rate coefficient $f_4 k_p$ (2.3.4)

$R^*+Q \rightarrow R^*+B$ Rate coefficient $f_2 k_p$ (2.3.5)

Branching

$B \rightarrow 2R^*$ Rate coefficient k_q (2.3.6)

Termination

$R^* \rightarrow out$ Rate coefficient $f_2\, k_p$ (2.3.7)

$2R^* \rightarrow out$ Rate coefficient $f_2\, k_p$, (2.3.8)

where RH represents hydrocarbon fuel (C_nH_{2m}), R^* is radical, B is the branching agent, Q is the intermediate agent and P is the product, consisting of H_2O, CO_2 and CO. The intermediate species can be generally related to aldehydes (RCHO) while the branching agent is related to hydroperoxide (RO_2H) at low temperature and to hydrogen peroxide (H_2O_2) at high temperature (Benson, 1981). The main assumption of the Shell autoignition model is that the radicals R^* entering into the scheme are treated as one type of radical using the steady-state hypothesis. The time variations of species concentrations are described by the following equations (Halstead et al.,1977):

$$\frac{d[R^*]}{dt} = 2\left(k_q[RH][O_2] + k_b[B] - k_t[R^*]^2\right) - f_3 k_p[R^*] \tag{2.3.9}$$

$$\frac{d[B]}{dt} = f_1 k_p[R^*] + f_2 k_p[Q][R^*] - k_b[B] \tag{2.3.10}$$

$$\frac{d[Q]}{dt} = f_4 k_p[R^*] + f_2 k_p[Q][R^*] \tag{2.3.11}$$

$$\frac{d[O_2]}{dt} = -pk_p[R^*] \tag{2.3.12}$$

$$[RH] = \frac{[O_2] - [O_2](t=0)}{pm} + [RH](t=0), \tag{2.3.13}$$

where m is the molar concentration of the various species. The parameter p is obtained from the overall product path (Schäpertöns and Lee, 1985):

$$C_{n/m}H_2 + pO_2 \rightarrow qP, \tag{2.3.14}$$

where

$$P = \left[(n/m)(\gamma CO + (1-\gamma)CO_2) + H_2O\right]/q$$

$$p = \left(n(2-\gamma) + m\right)/2m$$

$$q = \frac{n}{m} + 1$$

The coefficient γ determines the burned products mixture via $[CO]/[CO_2] = \gamma/(1-\gamma)$

The rate constants in Equations (2.3.9) – (2.3.13) are defined by the following expressions (Halstead et al.,1977; Schäpertöns and Lee,1985):

$$f_1 = A_{f1}\exp\left(-E_{f1}/R_uT\right)[O_2]^{x1}[RH]^{y1} \tag{2.3.15}$$

$$f_2 = A_{f2}\exp\left(-E_{f2}/R_uT\right) \tag{2.3.16}$$

$$f_3 = A_{f3}\exp\left(-E_{f3}/R_uT\right)[O_2]^{x3}[RH]^{y3} \tag{2.3.17}$$

$$f_4 = A_{f4}\exp\left(-E_{f4}/R_uT\right)[O_2]^{x4}[RH]^{y4} \tag{2.3.18}$$

$$k_i = A_i\exp\left(-E_i/R_uT\right) \tag{2.3.19}$$

where i stands for p_1, p_2, p_3, q, B and t, R is the universal gas constant, A_f, E_f, x and y are the kinetic rate parameters fitted for each particular fuel,

$$k_p = \left[\frac{1}{k_{p1}[O_2]} + \frac{1}{k_{p2}} + \frac{1}{k_{p3}[RH]}\right]^{-1}$$

The Shell autoignition model uses the following equation for the temperature (Halstead et al., 1977):

$$\frac{dT}{dt} = \frac{1}{c_v n_{tot}}\left(Q_k - Q_L - \frac{n_{tot}R_uT}{V}\frac{dV}{dt}\right), \tag{2.3.20}$$

where c_v is the specific heat capacity at constant volume, n_{tot} is the total number of moles in the volume V, Q_k is the chemical heat release defined as:

$$Q_K = k_p qV[R^*], \tag{2.3.21}$$

q is the exothermicity per cycle, Q_L is latent heat loss through the boundary walls defined as:

$$Q_L = \phi V(T - T_w), \tag{2.3.22}$$

where $\phi = hS/V$, S/V is the ratio of surface to volume.

The last term on the right hand side of Equation (2.3.20) accounts for the work due to the piston motion. This term, as well as the term Q_L, is accounted for by the enthalpy transport equation in CFD codes. In this case, the change in temperature must be based only on the contribution of the chemical reaction. Equation (2.3.20) is simplified to (Sazhin et al., 1999):

$$\frac{dT}{dt} = \frac{1}{c_v n_{tot}} k_p q V \left[R^*\right] \tag{2.3.23}$$

The development of the Shell model followed two main directions. The first direction is focused on the modifications of the coefficients without changing the overall structure by adjusting the kinetic rates to fit experimental data (Schäpertöns and Lee, 1985; Theobald, 1986). The second direction is focused on modifying the equations to better reflect the underlying chemistry and this leads to change in the overall structure of model.

Sazhin et al. (1999) suggested a new mathematical formulation for the Shell model. This is particularly important for implementation in CFD codes. The authors replaced the time as an independent variable by the fuel depletion, which is the difference between the initial fuel concentration and current one. This allowed reducing the original system of equations used in the model to only two coupled first-order ordinary differential equation for the concentration of radicals and branching agent. Then these two equations were reduced to one second order differential equation for the concentration of radicals:

$$\begin{aligned} & d_R\left[R^*\right]\left[R^*\right]'' + d_R\left(\left[R^*\right]'\right)^2 + \left(-\left(d_R' - d_R f_B\right)\left[R^*\right] - d_R b_R - 2 d_R c_R \left[R^*\right]\right)\left[R^*\right]' = \\ & \left(d_R b'_R - b_R\left(d_R' - d_R f_B\right)\right)\left[R^*\right] + \left(d_R c_R' - c_R\left(d_R' - d_R f_B\right)\right)\left[R^*\right]^2 \\ & \qquad + d_B a_R' + d_R^2 g_B - a\left(d_R' - d_R f_B\right), \end{aligned} \tag{2.3.24}$$

where :

$$a_R = 2m \frac{k_q\left(\left[RH\right]_0 - \xi\right)\left(\left[O_2\right]_0 - pm\xi\right)}{k_p},$$

$$b_R = -mf_3,\ c_R = -2m\frac{k_t}{k_p},\ d_R = 2m\frac{k_B}{k_p},\ f_B = \frac{mk_B}{k_p\left[R^*\right]},$$

$$g_B = mA_{f1}\exp\left[-\frac{E_{f1}}{R_u\left(T_0+\frac{mq}{C_v[N]}\xi\right)}\right]\left([O_2]_0-pm\xi\right)^{x1}\left([RH]_0-\xi\right)^{y1}$$

$$+mA_{f2}\exp\left[-\frac{E_{f2}}{R_u\left(T_0+\frac{mq}{C_v[N]}\xi\right)}\right][Q].$$

Once the concentration of radicals is obtained, the concentration of the intermediate agent, temperature and time can be obtained from the following equations:

$$[Q]=e^{-F}\int_0^{\xi} g_Q e^F d\xi \tag{2.3.25}$$

$$T=T_0+\frac{mq}{C_v[N]}\xi \tag{2.3.26}$$

$$t=t_0+\sqrt{\frac{m\xi_1}{k_p k_q [RH]_0[O_2]_0}}+\int_{\xi_1}^{\xi}\frac{d\xi}{\frac{k_p}{m}\left[R^*\right]}, \tag{2.3.27}$$

where $\xi=[RH]_0-[RH],[RH]_0=[RH](t=0),F=\int_0^{\xi} f_Q d\xi,T_0=T(t=0)$.

This formulation of the Shell model saves CPU time by about 40-60 % per step for typical problem (Sazhin et al., 1999).

Sazhina et al. (1999, 2000) considered the application of the Shell model to modeling of the autoignition of Diesel fuel sprays. This takes place at a wide range of equivalence ratios, pressures and temperatures, in contrast to the autoignition in premixed gasoline fuel. It was necessary to impose flammability limits to restrict the range of equivalence ratios for which the autoignition is active. They suggested flammability limits is the range of equivalence ratios from 0.5 to 3.2 as a starting point and this limit increases linearly with increasing pressure. The Shell autoignition model does not predict autoignition for end compression temperature lower than 570 K and is inhibited if the temperature increases higher than 1100 K or very sharp temperature rise ($>10^7$) K/s occurs. The authors showed that the autoignition chemical delay for Diesel fuel is much less than physical delay due to droplet transit time, atomisation, heating, evaporation and mixing for droplet radii. This justifies the application of less accurate than detail kinetic mechanism, but more computer efficient Shell model. The values of the A_{f4} in the Shell model for n-heptane were taken equal to 3 x 10^6 and 6 x 10^6.

Sazhina et al. (2000) followed the Schäpertöns and Lee (1985) and Theobald (1986) idea that increase in mass of R^*, B and Q originates in fuel and oxygen consumption. They suggested calculating the total change in mass of R^*, B and Q over time step as:

$$\delta m_{RBQ} = \delta m_R + \delta m_B + \delta m_Q \tag{2.3.28}$$

where δm_R, δm_B, δm_Q are changes in mass of R^*, B and Q respectively in a given cell over a time step of integration. δm_{RBQ}, is shared stoichiometrically between the reactants, C_nH_{2m} and O_2, so that the decrement of fuel mass is estimated as δm_{RBQ} where S is the stoichiometric oxygen-fuel ratio by mass in the main propagation path:

$$1\,(\text{kg})\,C_nH_{2m} + S\,(\text{kg})\,O_2 \rightarrow (1+S)(kg)P \tag{2.3.29}$$

In this case the O_2 consumption will increase by $\delta m_{RBQ}\,S/(1+S)$ and the termination reactions convert the R^* radicals into fuel and oxygen.

2.4 The KIVA CFD code

KIVA is a multidimensional CFD code designed for the numerical calculation of transient, two and three dimensional chemically reactive flows with sprays. The code is capable to calculate such flows in internal combustion engine cylinders with arbitrary shaped piston geometries, taking into account the effects of turbulence and wall heat transfer. KIVA solves the transient equations of motion of a turbulent, chemically reactive mixture of ideal gases, coupled to the equations of motions for single component vaporising fuel sprays. The solution procedure is based on the finite volume method called the Arbitrary Lagrangian Eulerian (ALE) method. In addition to the chemical reaction model, several other models related to sprays are used in this code. These include models for droplet aerodynamics, droplet collisions and coalescences, break-up and evaporation. Two turbulence models are available; standard version of k-ε

turbulence model and a modified version of this model (sub-grid scale model). Spray break-up is modelled using the Taylor Analogy Break-up (TAB) model based on the analogy between an oscillating and distorting droplet and a spring mass system.

The change in droplet radius due to vaporisation is described by hydrodynamic model with the following equation (Amsden et al., 1989):

$$\frac{dR}{dt} = \frac{\rho_{\mathrm{g}} D_{\mathrm{g}}}{2\rho_{\mathrm{l}} R_{\mathrm{d}}} B_{\mathrm{M}} Sh \tag{2.4.1}$$

where Sh is described in Equation (2.2.30). This equation is equivalent to Equation (2.2.15). The rate of droplet temperature change is determined by the energy balance equation in such a way that the energy supplied to the droplet either increases the droplet temperature or supplies heat for its vaporisation. These are described by the following equation (Amsden et al., 1989):

$$-\dot{m}_{\mathrm{d}} L + \rho_{\mathrm{l}} c_{\mathrm{l}} \frac{4}{3} \pi R_{\mathrm{d}}^2 \frac{dT}{dt} = 4\pi R_{\mathrm{d}}^2 \frac{Nu k_{\mathrm{g}}}{2R_{\mathrm{d}}} \left(T_{\mathrm{g}} - T_{\mathrm{s}}\right), \tag{2.4.2}$$

where the Nusselt number is described in Equation (2.2.31) with B_{T} replaced by B_{M} (similarly to Model 0). The latter equation takes into account the effect of vapour superheating.

Several versions of this code have been developed by Los Alamos National Laboratory. These are KIVA, KIVA-2, KIVA-3 and KIVA-3V. KIVA-2 is an improved version of KIVA that has better computational efficiency, numerical accuracy and physical sub-models. It is more user friendly and versatile than KIVA (Amsden et al., 1989). KIVA-3 is an extension of KIVA-2. It uses the same numerical solution procedure, and solves the same set of equations. KIVA-3 is applicable to laminar or turbulent flows, subsonic or supersonic flows and single-phase or dispersed two-phase flows. In contrast to KIVA-2, KIVA-3 uses a block structured mesh with connectivity defined through indirect addressing. KIVA-3V is an extended version of KIVA-3, can model any number of vertical valves in the cylinder head. Other new features developed in KIVA-3V are particle based liquid wall film model, improved sorting subroutine, mixing-controlled turbulent combustion model and an optional RNG k-ε turbulence model (Amsden, 1997).

2.5 Experimental studies

Experimental studies are used to investigate phenomena in an engine combustion chamber. Fuel spray structure, fuel atomisation, spray penetration, droplet size distribution, spray evaporation and autoignition are some of many phenomena that can be investigated experimentally. The structure of Diesel sprays is very important for understanding the atomisation, vaporisation and mixing processes that take place in an engine cylinder. The droplet size distribution in a spray is directly related to spray atomisation and vaporisation processes. Different spray configurations are used in different Diesel combustion systems. Various techniques have been developed to investigate the above phenomena. These are optical, electrical/electronic and mechanical ones (Lefebvre, 1989). The optical technique can be subdivided into two groups; direct imaging and non-imaging techniques. These are widely used in Diesel spray characterisation, as both are non intrusive methods. Direct imaging techniques have been focused on measuring spray geometry such as spray cone angle, break-up length and length of penetration. Non direct imaging techniques are usually focused on droplet velocities, droplet size and density.

High speed photography with charge coupled device (CCD) camera is the simplest tool for direct imaging. CCD cameras have been used to capture images of sprays or sprays particle, with the aid of mercury vapour lamp, flash light or laser pulses to create a high intensity light source. This technique requires analysis of the captured images. For high density sprays, the droplet images may become very closely packed or even overlap. Crua (2002) used a high speed CCD video camera operating at 27000 frames per second with a resolution 126 x 64 x 256 pixels to record spray injections in the Ricardo Proteus Engine. Using these tools, visualisation and spray patterns of Diesel sprays in various conditions were obtained. Analysis of images of spray patterns have been used to determined spray penetration lengths (Sazhin et al., 2003).

Phase Doppler Anemometry (PDA) is a tool based on a non direct imaging principle that is widely used for determination of droplet sizes and velocities. PDA is a non-intrusive optical technique used to simultaneously determine the droplet size and velocity at a specific point in the spray. PDA consists of four main elements. These are laser source, beam splitter, photomultiplier and receiving optics. The optical configuration of a PDA system is showed in figure 2.5.1 below.

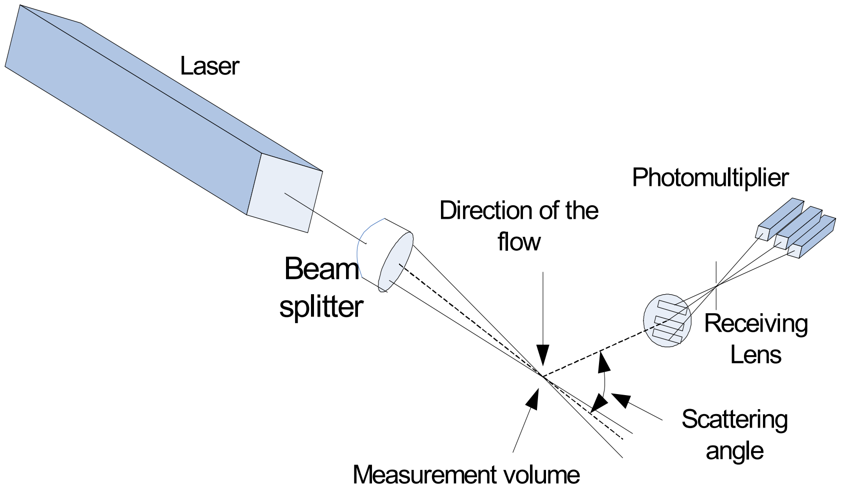

Figure 2.5.1 Schematic of the optical configuration system of a PDA (Dust et al., 1981)

The output beam from the laser is split into two or more components of equal intensity. A lens is used to change the direction of the beams causing them to cross at a point where they are focused. Interference of the light beams in the measurement volume creates a set of equally spaced fringes. Velocity and size measurements are made when a particle carried by the flow passes through the fringes. When a particle traverses the control volume, the amount of light scattered fluctuates with the fringes. This is then collected by another lens and focussed onto a photo detector which converts the fluctuations of light intensity into fluctuations in voltage signal. The frequency of this fluctuation is proportional to the velocity of the particle (Dust et al., 1981):

$$f = \frac{2U \sin(\alpha / 2)}{\lambda} \tag{2.5.1}$$

where U is the velocity component of particle normal to the fringes, α is the angle between the two beams and λ is the wavelength of the laser light.

The doppler frequency f can be determined by measuring the period of the doppler signal. If the laser wavelength and the angle of intersection of the two beams are known, the droplet velocity can be calculated. To determine the droplet size of particle, it is necessary to measure the spatial frequency of the interference fringe pattern produced by the scattered light. Bachalo and Houser (1984) showed that this could be achieved by using a second photo detector to collect light simultaneously from a different part of the interference pattern. A doppler signal is produced by each detector but with a phase shift between them. The signal from the two detectors have the same doppler frequency f and similar amplitude, but are separated by a phase shift Φ given by:

$$\Phi = \frac{T_{\text{phase}}}{T_{\text{D}}} 360^{o}, \tag{2.5.2}$$

where T_{D} is the doppler period and T_{phase} is the period between the zero crossings of the signals from detectors 1 and 2. The phase shift is directly related to the droplet size by a linear calibration curve.

Phase doppler anemometers are among the most accurate flow measurement devices. There are, however limitations of this technique:

a. The refractive index of air in the combustion chamber may change during the test, and the incident laser beams will be defocused, affecting the position of the measuring volume.

b. Velocities of particles are measured only when particles pass through the measurement volume. Sometimes such a sample set is biased as more particles pass through the measuring volume in a given time. This has an affect on the estimated velocity variance.

c. During the injection, the shape of spray varies according to in-cylinder conditions. Therefore spherical droplets can be deformed to generate irregular-shape particles that cannot produce reliable results, as the light reflected from these particles creates uneven light scattering patterns.

Laser Doppler Anemometry is another tool to measure droplet velocity. Two laser beams intersect at a point to form a fringe pattern. Particles passing the fringe pattern reflect the laser light at each fringe. Provided the fringe spacing is known, local velocities can be determined by analysing the doppler shift of scattered light (Crua, 2002).

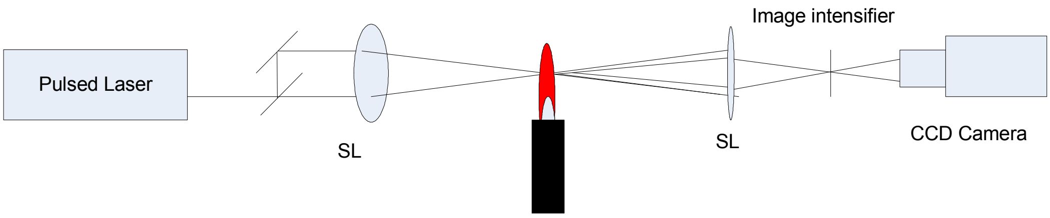

Figure 2.5.2 An illustration of the Laser Doppler Anemometry principle (Watrasiewicz and Rudd, 1977).

It is difficult to use LDA when the gas temperature and/or density variations are large and cause significant differences in refractive indices. If the refractive index of the gases through which the two laser beams enter the system are not the same, the possibility arises that the laser beams will not cross. Under these conditions measurements are not possible (Jeffrey, 1976)

2.6 Conclusions to Chapter 2

Finite thermal conductivity of fuel droplets and the effect of radiation need to be taken into account when modelling droplet heating and evaporation in Diesel engines. The liquid phase model of convective heating, based on the analytical solution of heat conduction equation, suggested by Sazhin et al. (2004b), was shown to be more effective (from the points of view of the balance of accuracy and CPU requirements) than the approach based on the numerical solution of the discretised heat conduction equation inside the droplet. This result was obtained based on fix gas parameters. No coupling between liquid and gas phases was taken into account at this stage. Hence, the performance of the model based on the analytical solution, suggested by Sazhin et al. (2004b), should be investigated taking into account the coupling of liquid and gas phases. Regarding the gas phase models, six semi-theoretical models and one model based on the approximation of experimental data were described. Further analysis of both liquid and gas phase models need to be performed for realistic Diesel engine parameters, taking into account the effect of break-up, ignition, dynamic of droplets and related processes.

The contribution of thermal radiation is relatively small in the droplet heating process. Hence thermal radiation models need to be kept simple. They need to take into account the semi-transparency of the droplets, but can ignore the spatial variations of radiation absorption inside the droplets. Models of radiative heating in Diesel engines have been suggested by a number authors (Dombrovsky, 2000; Dombrovsky et al., 2001; Dombrovsky and Sazhin, 2003c; Sazhin et al., 2004a). However, further analysis of these models and their applications are needed.

Various methods used to investigate spray and combustion characterisation in Diesel engine experimentally have been reviewed.

3. COMPARATIVE ANALYSIS OF THE MODELS FOR FUEL DROPLET HEATING AND EVAPORATION

As mentioned in Chapter 2, the importance of the development of accurate and computer efficient models, describing fuel droplet heating and evaporation in engineering and environmental applications, is widely recognised (for example, Lefebvre, 1989; Sirignano, 1999; Sazhin, 2006). In most of these applications, the processes of droplet heating and evaporation have to be modelled alongside the effects of turbulence, combustion, droplet break-up and related phenomena in complex three-dimensional enclosures (for example, Bertoli and Migliaccio, 1999; Sazhina et al., 2000). This has led to a situation where finding a compromise between the complexity of the models and their computational efficiency becomes the essential precondition for successful modelling. Several simplified models for droplet heating and evaporation have been developed (Sazhin, 2006). In these models the sophisticated underlying physics was described using relatively simple mathematical tools. Some of these models, including those taking into account the effects of the temperature gradient inside droplets, recirculation inside them and their radiative heating, were implemented into numerical codes focused on simulating droplet convective and radiative heating, evaporation and the ignition of fuel vapour/air mixture (Sazhin et al., 2005a,b). These are discussed in Chapter 2.

Although the results reported by Sazhin et al. (2005a,b) have clearly demonstrated the usefulness of the new numerical model for droplet heating, based on the analytical solution of the heat conduction equation inside a droplet, a number of important issued had to be addressed. Firstly, the comparison between the accuracy and CPU efficiency of the new model and the one based on the numerical solution of the discretised heat conduction equation inside the droplet was performed under the assumption that gas parameters are fixed (non-coupled solution). Secondly, the predictions of the new model were studied based on one of the simplest models for the gas phase. The sensitivity of the results to the choice of the gas phase model was not investigated.

The main objective of this chapter is to extend further the analysis reported by Sazhin et al. (2005a,b) with a view to clarifying the above mentioned two issues. The performance of the new model, developed by Sazhin et al. (2005a,b), will be investigated taking into account the coupling of liquid and gas phases, and using various models for the gas phase. The models used in the analysis are discussed in Chapter 2. The numerical procedure and properties of the fuels and mixture are presented in Appendices A, B, C and D. The main results of this chapter are presented in the paper by Sazhin, Kristyadi et al. (2006).

3.1 Monodisperse spray: Effect of gas phase models

This section is focused on the investigation of the effects of the choice of a gas phase model on fuel droplet heating and evaporation. The break-up processes and chemical reactions in the gas phase are ignored. The temperature gradient inside droplets and recirculation in them are taken into account based on the effective thermal conductivity (ETC) model and the analytical solution (2.1.22) (Sazhin et al., 2005b). The physical properties of fuel, except radiation properties were taken as for n-dodecane (see Appendix A). The radiation properties of fuel were based on the results of the measurements of the absorption coefficient of low sulphur ESSO AF1313 Diesel fuel used in cars (Sazhin et al., 2004a). Following Sazhin et.al. (2005b) it was assumed that droplets were injected at room temperature (T_d = 300 K) into air at temperature of 880 K and gas pressure of 3 MPa. The relatively low gas pressure for Diesel engine conditions was chosen to avoid the analysis of supercritical heating and evaporation. The overall volume of injected liquid fuel was taken equal to 1 mm^3, and the volume of air, where the fuel was injected, was taken equal to 883 mm^3. In this case, provided that all fuel is evaporated without combusting, the fuel vapour/ air mixture is expected to become close to stoichiometric (Sazhin et al., 2005b).

At first the radiation effects are ignored. The initial droplet radius and velocity are assumed to be equal to 10 μm and 1 m/s, respectively. The plots of droplet radius R_d and surface temperature T_s versus time for gas phase Models 0-6 are shown in Figure 3.1.1. As follows from this figure, the effect of the choice of the gas model on time evolution of T_s is relatively small, especially at the very initial stage of heating. However, this effect on time evolution of R_d is clearly visible. The difference in the evaporation times predicted by various models can reach almost 15%. If we assume that Model 6 is the most accurate one, as the one based merely on experimental data, then we can conclude that the most accurate semi-theoretical models are Models 3 and 4, and the least accurate is Model 0 used by Sazhin et al. (2005b). Interestingly, the prediction of Model 3 is closer to the prediction of Model 6 than the prediction of Model 4, although Model 4 is expected to be more accurate than Model 3.

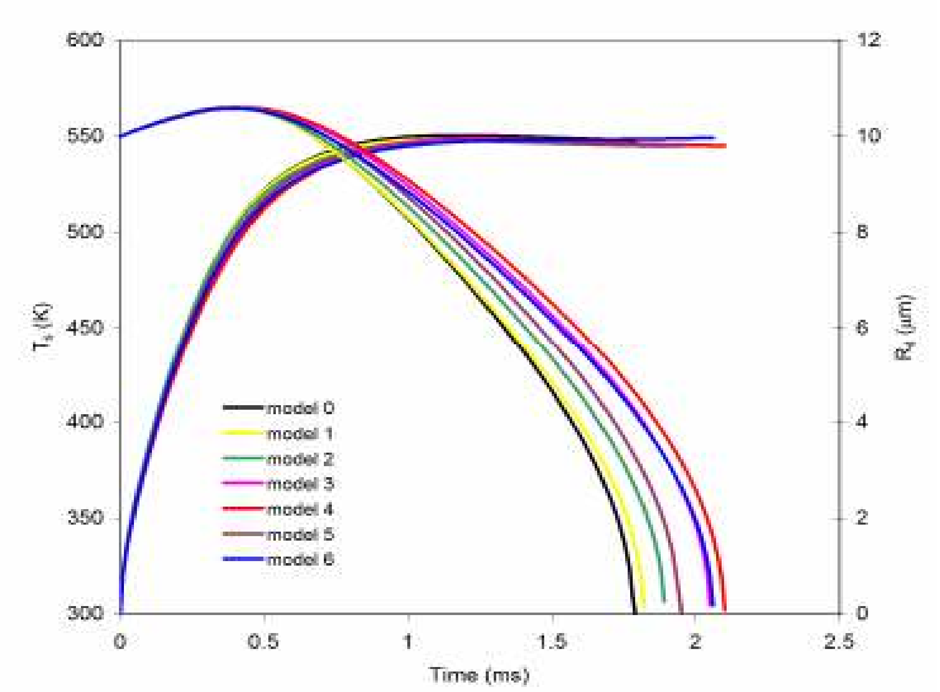

Figure 3.1.1 Plots of T_s and R_d versus time for the initial gas temperature T_{g0} = 880 K, gas pressure P_{g0} = 3 MPa, initial droplet temperature T_{d0} = 300 K, initial droplet radius R_{d0} = 10 μm and velocity $\mathbf{v}_{d0}$ = 1 m/s. The overall volume of injected liquid fuel was taken equal to 1 mm^3, and the volume of air, where the fuel was injected, was taken equal to 883 mm^3. The results were obtained based on the effective thermal conductivity (ETC) model, the analytical solution of the heat conduction equation, and using seven gas phase models. The effects of thermal radiation are ignored. The saturation temperature is 553 K (Poling et. al., 2000)

The same plots as in Figure 3.1.1 but for the droplet initial velocity 10 m/s, are shown in Figure 3.1.2. The closeness between temperature curves in Figure 3.1.2 is about the same as in the case shown in Figure 3.1.1, but the deviation of the plots for the droplet radii is noticeably greater in this case than in the case shown in Figure 3.1.1. The difference in the evaporation times predicted by various models in this case can reach about 20%. As in the case shown in Figure 3.1.1, the evaporation time predicted by Model 4 is close to the one predicted by Model 6. In contrast to the case shown in Figure 3.1.1, however, the evaporation times predicted by Models 3 and 6 are noticeably different. The difference in Models 3 and 4 lies in the values of $F(B_{\mathrm{M}})$ and $F(B_{\mathrm{T}})$ (see Equations (2.2.50) and (2.2.51)). The contribution of the terms containing these functions in Equations (2.2.50) and (2.2.51) is proportional to $\sqrt{Re_{\mathrm{d}}}$. Hence the accuracy of calculating these terms is more important in the case of the droplet with the initial velocity 10 m/s (Figure 3.1.2) than in the case of the droplet with the initial velocity 1 m/s (Figure 3.1.2).

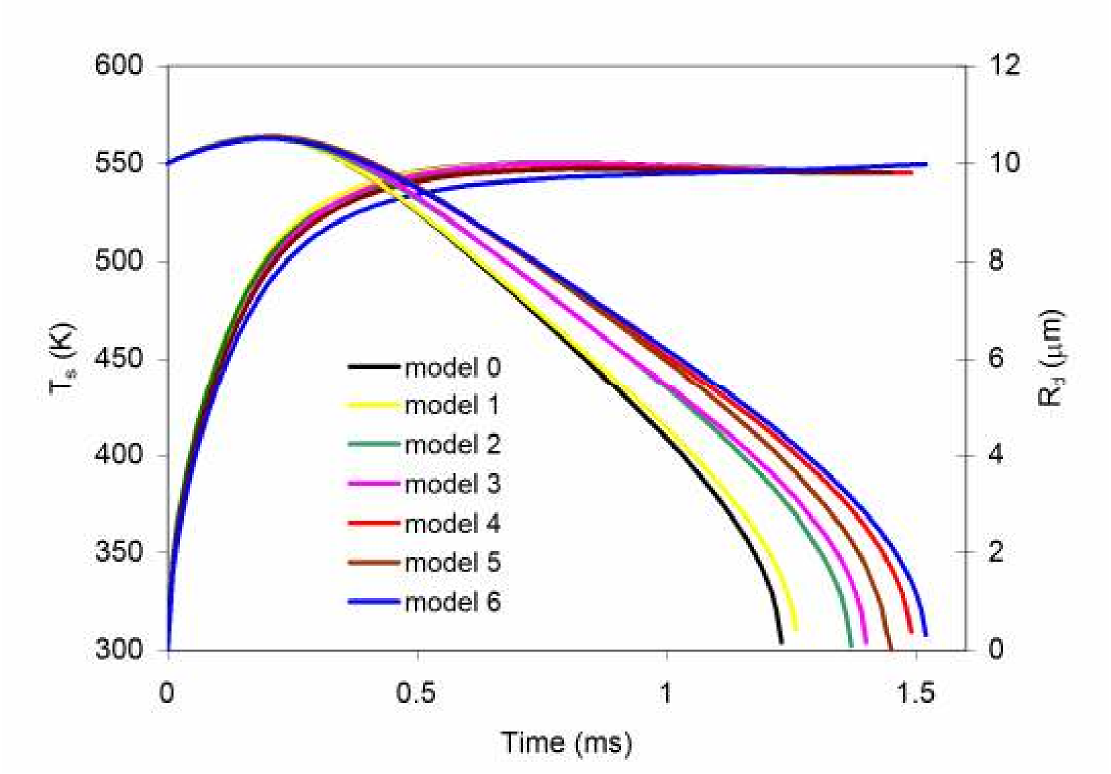

Figure 3.1.2 The same as Figure 3.1.1 but for the initial droplet velocity equal to 10 m/s

In Figures 3.1.3 and 3.1.4 the same plots as in Figures 3.1.1 and 3.1.2 are shown, but for the droplets with the initial radii equal to 50 μm. The same closeness between the plots for R_{d} predicted by Models 4 and 6 as in Figures 3.1.1 and 3.1.2, can be clearly seen in Figures 3.1.3 and 3.1.4. Note that in the case of Figures 3.1.3 and 3.1.4, the values of $\sqrt{Re_d}$ are $\sqrt{5}$ larger than in the case of Figures 3.1.1 and 3.1.2. Hence the contribution of the terms $F(B_{\mathrm{M}})$ and $F(B_{\mathrm{T}})$ is expected to be more important in the cases shown in Figures 3.1.3 and 3.1.4 than in the cases shown in Figures 3.1.1 and 3.1.2.

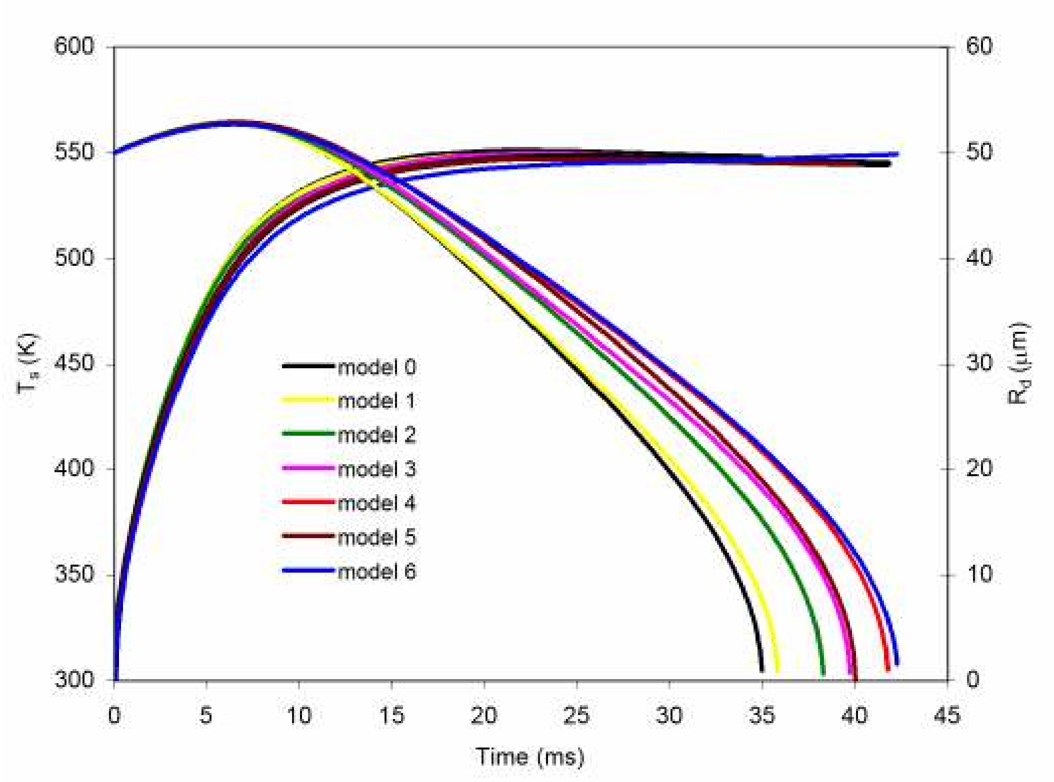

Figure 3.1.3 The same as Figure 3.1.1 but for the initial droplet radius equal to 50 μm

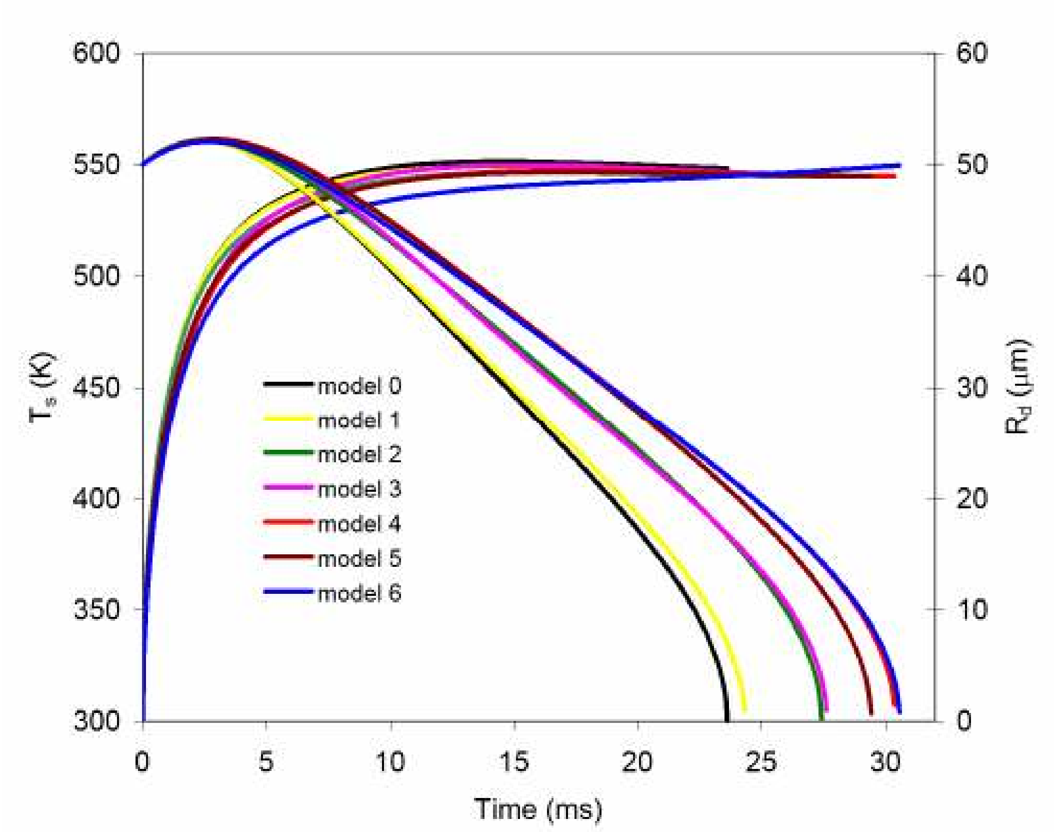

Figure 3.1.4 The same as Figure 3.1.2 but for the initial droplet radius equal to 50 μm

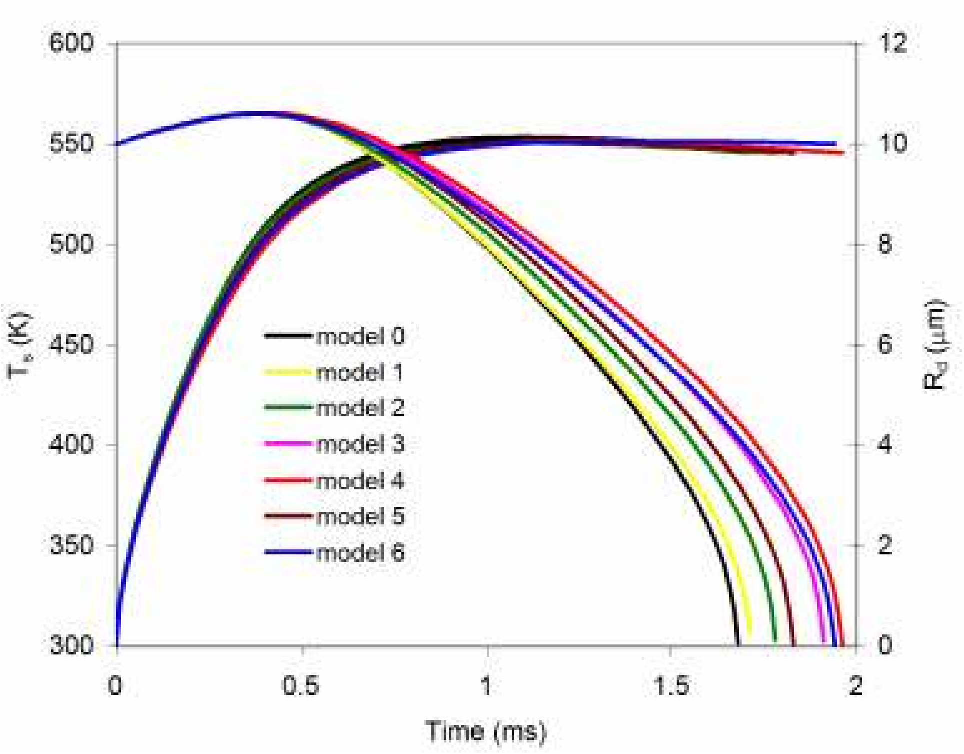

Figure 3.1.5 The same as Figure 3.1.1 but taking into account the effects of thermal radiation assuming that $T_{ext} = 2000$ K

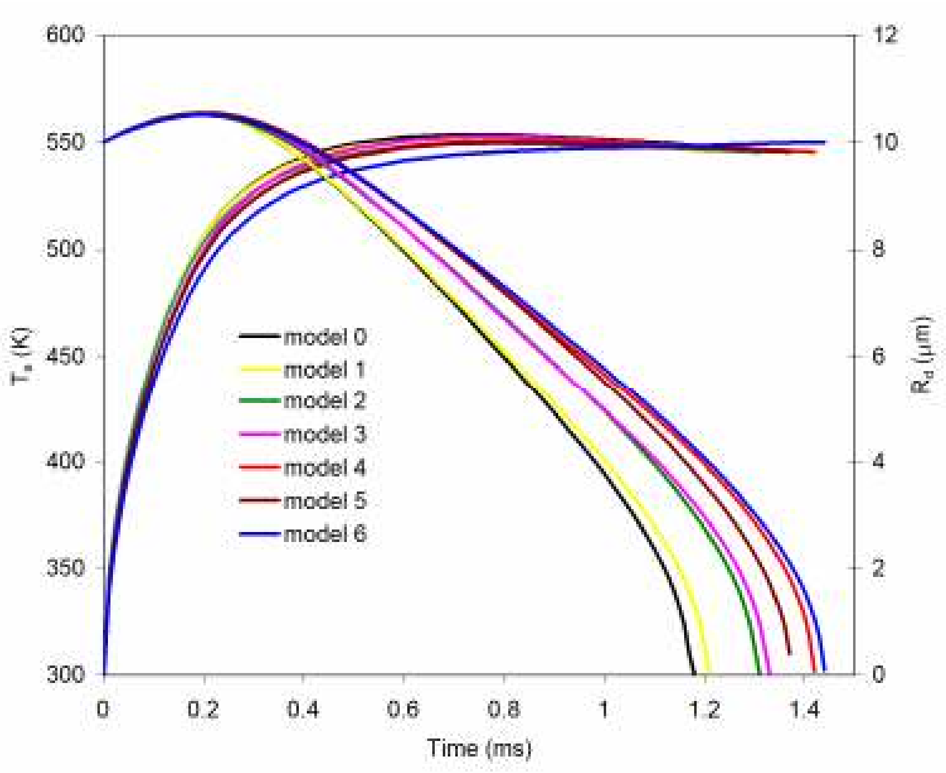

Figure 3.1.6 The same as Figure 3.1.2 but taking into account the effects of thermal radiation assuming that $T_{ext} = 2000$ K

In Figures 3.1.5 and 3.1.6 the same plots as in Figures 3.1.1 and 3.12 are shown but for the case when the radiative heating of droplets is taken into account. We assumed that the gas is optically thin and the radiative heating is performed by the external source (remote flame) with temperature $T_{\text{ext}} = 2000$ K. This value of T_{ext} is realistic for Diesel engines (Flynn et al., 1999; Sazhina et al., 2000). Comparing Figures 3.1.1 and 3.1.5 we can see that the effect of thermal radiation leads to a reduction in the evaporation time by about 5%.

In the cases shown in Figures 3.1.2 and 3.1.6 this reduction of the evaporation time due to thermal radiation is much smaller than in the cases shown in Figures 3.1.1 and 3.1.5. This can be related to the fact that in the cases shown in Figures 3.1.2 and 3.1.6, the convective heating of droplets is larger than in the cases shown in Figures 3.1.1 and 3.1.5, due to larger initial droplet velocities. Hence, the relative contribution of the radiative heating is smaller in the cases shown in Figures 3.1.2 and 3.1.6 than in the cases shown in Figures 3.1.1 and 3.1.5. As in the cases shown in Figures 3.1.1 - 3.1.4, the temperature plots shown in Figures 3.1.5 and 3.1.6 predicted by all seven models are rather close, at least at the initial stage of droplet heating and evaporation. In contrast to the cases shown in Figures 3.1.1 - 3.1.4, the maxima on the temperature plots can be seen. The physical meaning of these maxima is discussed by Abramzon and Sazhin (2005, 2006).

As pointed out in Abramzon and Sazhin (2006), in the absence of thermal radiation, the droplet temperature approaches some equilibrium or ‘wet-bulb’ temperature, at which all of the heat coming to the droplet surface from the gas is spent on evaporation (latent heat), and the net heat penetrating to the liquid phase becomes zero. In the presence of radiation, however, the droplet surface temperature continues to rise above that wet-bulb temperature, due to radiation energy supplied to the droplet interior. As the surface droplet temperature grows, the heat coming to the droplet surface by convection decreases, but the heat spent on evaporation increases. As a result, the direction of the net heat flux inside the droplet becomes negative (heat flows from droplet centre to droplet surface). During the process of evaporation, the total radiative power absorbed by the droplet (droplet volume times $P(R)$) decreases approximately proportionally to $R_d^{2.6}$ (see Equation (2.1.38) in which $b \approx 0.6$). The power lost by the droplets during the conduction heat transfer from the droplet centre to the droplet surface is approximately proportional to droplet surface area divided by droplet radius (proportional to R_d). Hence, at a certain radius, the power lost by the droplet during the conduction heat transfer becomes equal to the radiative power absorbed by the droplet. This corresponds to the maximum droplet average temperature. The moment this happens is expected to be close to the moment when the maximum droplet surface temperature is reached. For smaller droplet radii, the power loss is expected to dominate over the radiative power absorbed by the droplet, and the droplet average and surface temperatures are expected to decrease. This is consistent with predictions of at least some of the models shown in Figures 3.1.5 and 3.1.6. As in the case of Figures 3.1.1 – 3.1.4, the closeness between the plots for R_d predicted by Models 4 and 6 is clearly seen.

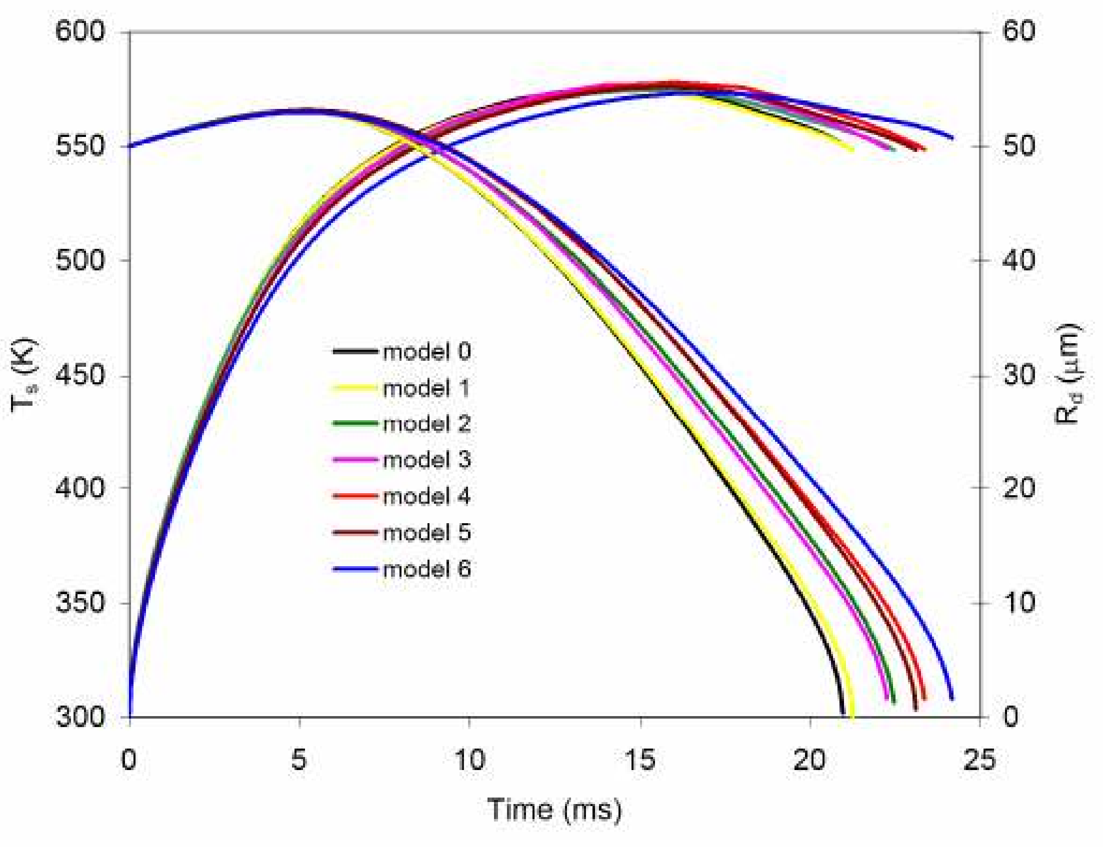

Figure 3.1.7 The same as Figure 3.1.3 but taking into account the effects of thermal radiation assuming that $T_\mathrm{ext} = 2000$ K

In Figures 3.1.7 and 3.1.8 the same plots as in Figures 3.1.5 and 3.1.6 are shown, but for the droplets with the initial radii equal to 50 μm. Comparing Figures 3.1.3 and 3.1.7, we can see that the reduction of the evaporation time due to the effect of thermal radiation in the case of large droplets, is much more significant than in the case of small droplets, as would be expected (see Abramzon and Sazhin, 2005, 2006). The same significant reduction of the evaporation time can be seen in the case when the droplet initial velocity is equal to 10 m/s (compare Figures 3.1.4 and 3.1.8). The maxima in the temperature plots are more clearly seen in Figures 3.1.7 and 3.1.8 than in Figures 3.1.5 and 3.1.6. As in the case of Figures 3.1.1 – 3.1.6, the closeness of the R_d curves predicted by Models 4 and 6 is clearly seen in Figures 3.1.7 and 3.1.8.

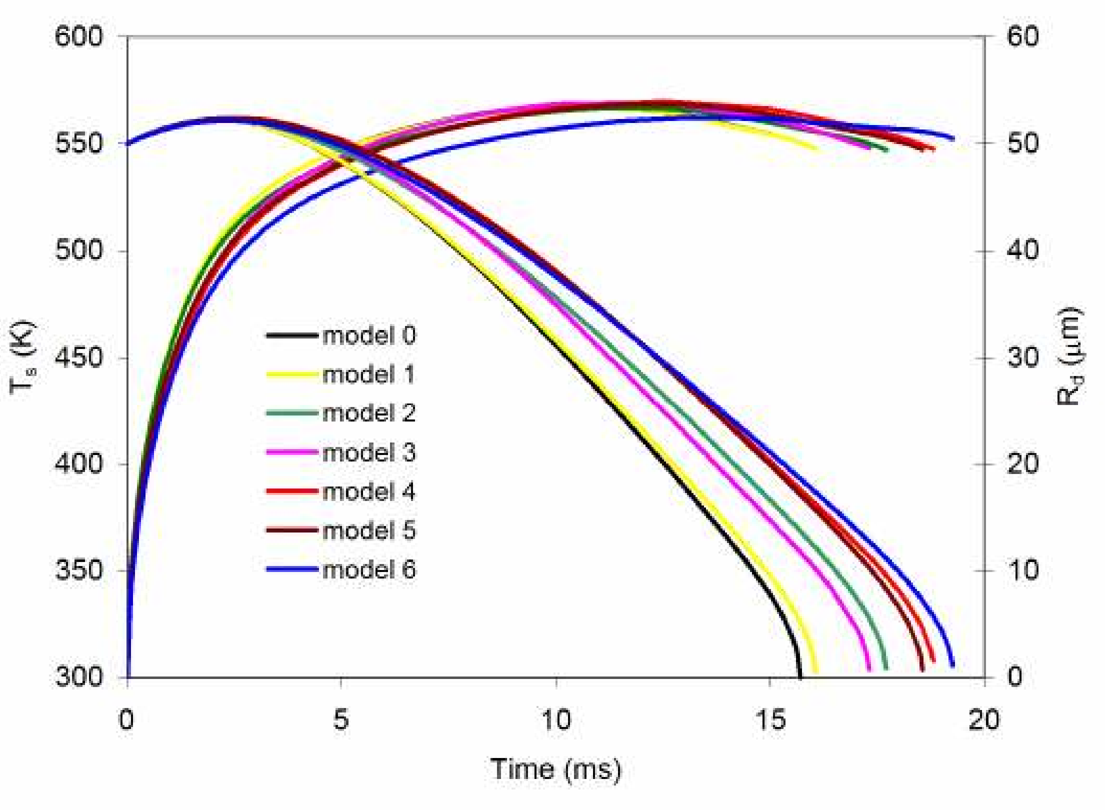

Figure 3.1.8 The same as Figure 3.1.4 but taking into account the effects of thermal radiation assuming that $T_{ext} = 2000$ K

The same closeness between the predictions of Models 4 and 6 was observed when the pressure was reduced to 2 MPa. Also this result remained the same when the data for n-dodecane molecules reported by Hirschfelder et al. (1967) rather than by Paredes et al. (2000) were used, or the reference temperature and fuel vapour mass fraction in Model 6 were calculated similarly to Models 0-5. The summary of the evaporation time errors predicted by Models 0 – 5 relative to Model 6 for gas pressure 2 MPa are presented in Figures 3.1.9 and 3.1.10. These errors were calculated based on the comparison of evaporation times predicted by Model 0 to Model 5 relative to Model 6 (for example, the error of evaporation time predicted by Model 0 : 100% x (evaporation time of Model 6 – evaporation time of Model 0)/evaporation time of Model 6).

As can be seen from Figures 3.1.9 and 3.1.10, Model 4 has consistently the lowest evaporation time error relative to Model 6. Hence, our recommendation is to use gas Model 4 for the analysis of fuel droplet heating and evaporation rather than Model 0 as used by Sazhin et al. (2005b).

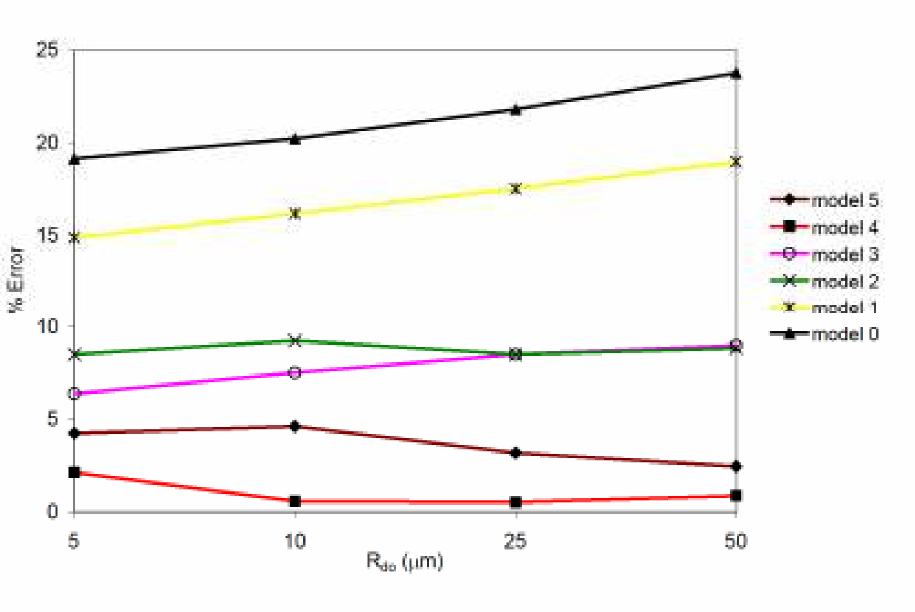

Figure 3.1.9 Errors of evaporation time predicted by various models relative to Model 6 versus the initial droplet radius, using the initial droplet velocity 1 m/s and gas pressure 2 MPa. The effects of radiation are ignored

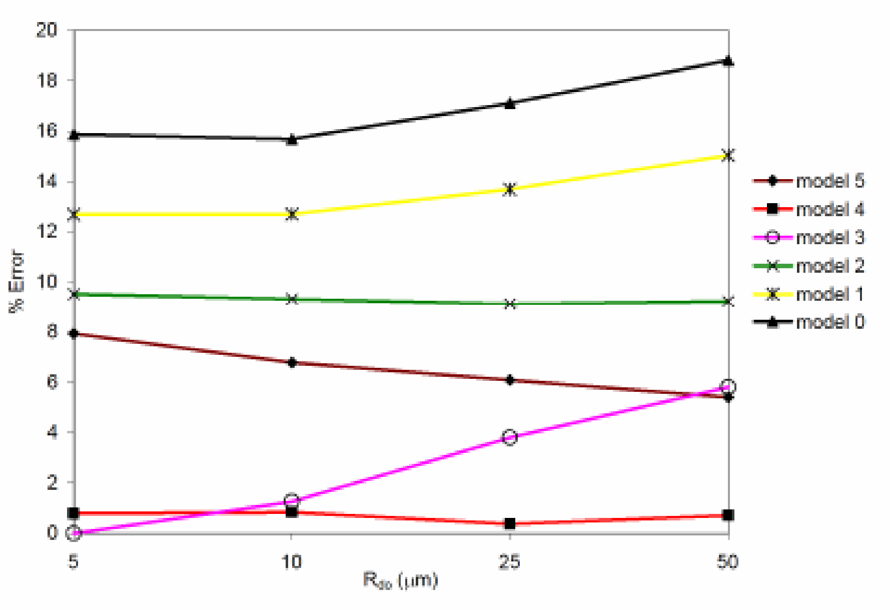

Figure 3.1.10 The same as Figure 3.1.9 but for the initial droplet velocity 10 m/s

The main advantage of Model 4 compared with Model 6 is that the former takes into account the underlying physics more accurately than the latter. For example, Equation (2.2.5) predicts that

$$\frac{\partial Nu}{\partial Re_{\mathrm{d}}} \propto \frac{1}{\sqrt{Re_{\mathrm{d}}}} \to \infty$$

when $Re_{\mathrm{d}} \to 0$, which is clearly unphysical (cf. analysis of Models 1 and 2 by Abramzon and Sirignano, 1989).

3.2 Monodisperse spray: Effect of liquid phase models

Results of preliminary analysis of the effects of liquid phase models on droplet heating and evaporation are presented by Sazhin et al. (2005a,b). In the first paper, a one way process of droplet heating was considered, assuming that the gas parameters were fixed. In the second paper, a more in-depth analysis was performed, taking into account the coupling between droplets and gas. However, this analysis was based on only one gas model (Model 0) and no investigation of the effects of various gas models was performed. As follows from the analysis of the previous section, the most reliable semi-theoretical gas model is Model 4. Hence, we repeated the analysis of Sazhin et al. (2005b), but using Model 4. The result was essentially the same as reported by Sazhin et al. (2005b). Namely, the numerical algorithms taking into account temperature gradients inside droplets, based on the analytical solution of the heat conduction equation and its numerical solution, predict practically the same results in a wide range of parameters typical for Diesel engines. In both cases the time step was taken as 0.001 ms. For the numerical solution of the heat conduction equation inside the droplets, 100 cells along the radius were used.

The evaporation time predicted by both these algorithms was close to the evaporation time predicted by the model, based on the assumption of no temperature gradient inside the droplets (ITC model or liquid phase Model 2). However, a noticeable difference in temperatures was observed at the initial stage of droplet heating and evaporation. This is illustrated in Figure 3.2.1 for the droplets with the initial radius equal to 10 μm and initial velocity 1 m/s injected into the gas with the same parameters as in the case shown in Figure 3.1.1.

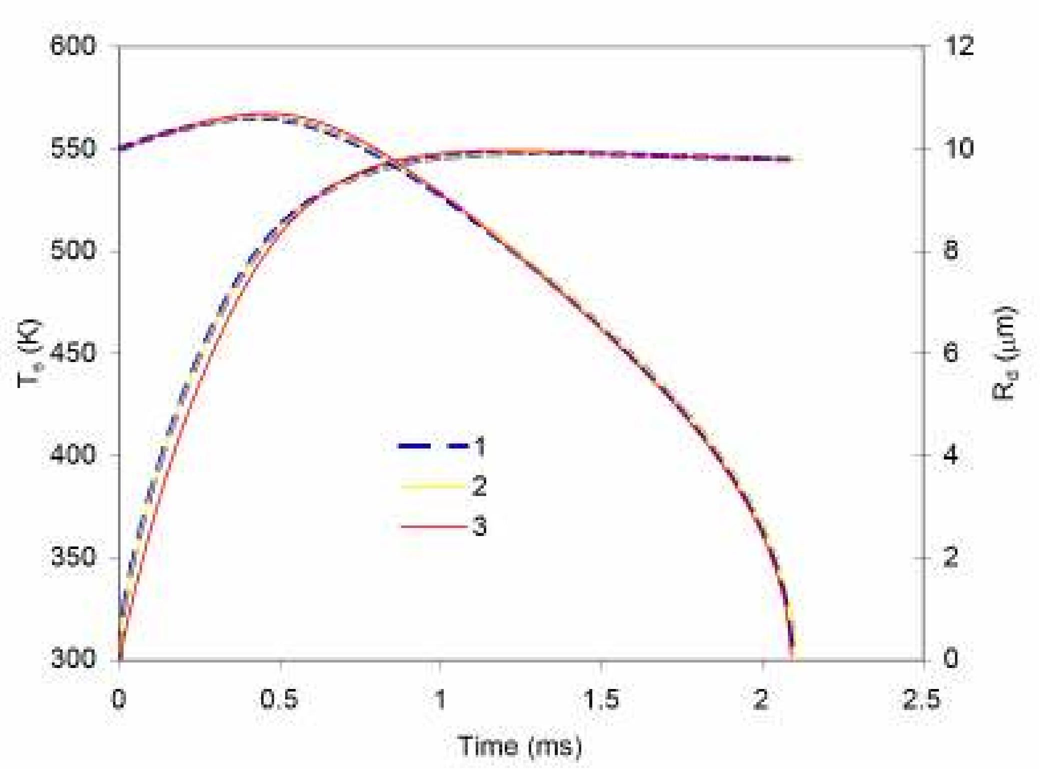

Figure 3.2.1 The same as Figure 3.1.1 but using three liquid phase numerical algorithms: the algorithm based on the analytical solution of the heat conduction equation inside the droplet (1), the algorithm based on the numerical solution of the heat conduction equation inside the droplet (2), the algorithm based on the assumption that the thermal conductivity inside droplets is infinitely large (3)

Comparing Figures 3.1.1 and 3.2.1, one can see that the differences in evaporation time due to the choice of the liquid phase model are negligible, compared with the differences due to the choice of the gas phase model. However, the differences in the estimate of the droplet surface temperature at the initial stages of droplet heating and evaporation due to the choice of the gas phase model are negligible, compared with the differences due to the choice of the liquid phase model. Hence, to predict accurately the time evolution of both droplet radius and surface temperature, accurate modelling of both gas and liquid phase is required.

The same conclusion could be inferred from the plots for droplet initial velocity 10 m/s, and for both these velocities and the initial droplet radius 50 μm. For this initial radius, the effects produced by the choice of the liquid phase model were more pronounced than in the case of the initial droplet radius equal to 10 μm. The curves for the parabolic temperature profile model in most cases lay between the curves for the model, based on the assumption of the infinite thermal conductivity of droplets, and the effective thermal conductivity model.

As can be seen from Figure 3.2.1, for the sufficiently small time step and large number of cells along the radius (in the case of the numerical solution of the heat conduction equation), predictions of the numerical algorithms based on the analytical solution of the heat conduction equation, and its numerical solution, practically coincide. In most practical applications, however, the choice of numerical algorithms is based not merely on their accuracy, but also on a reasonable compromise between accuracy and computer efficiency. Assuming that gas parameters are fixed, it was shown in Sazhin et al. (2005a) that for the time steps in the range between 1 μs and 0.1 ms, the numerical algorithm based on the analytical solution of the heat conduction equation is always more accurate and less CPU intensive than the algorithm based on the numerical solution of this equation.

The analysis of Sazhin et al. (2005a) was repeated taking into account the coupling between droplets and gas and using gas Model 4. The same gas and droplet parameters as in Figure 3.2.1 were used. The results are shown in Figure 3.2.2. This figure essentially confirms the conclusion made by Sazhin et al. (2005a) regarding the accuracy and CPU efficiency of the numerical algorithm based on the analytical solution of the heat conduction equation.

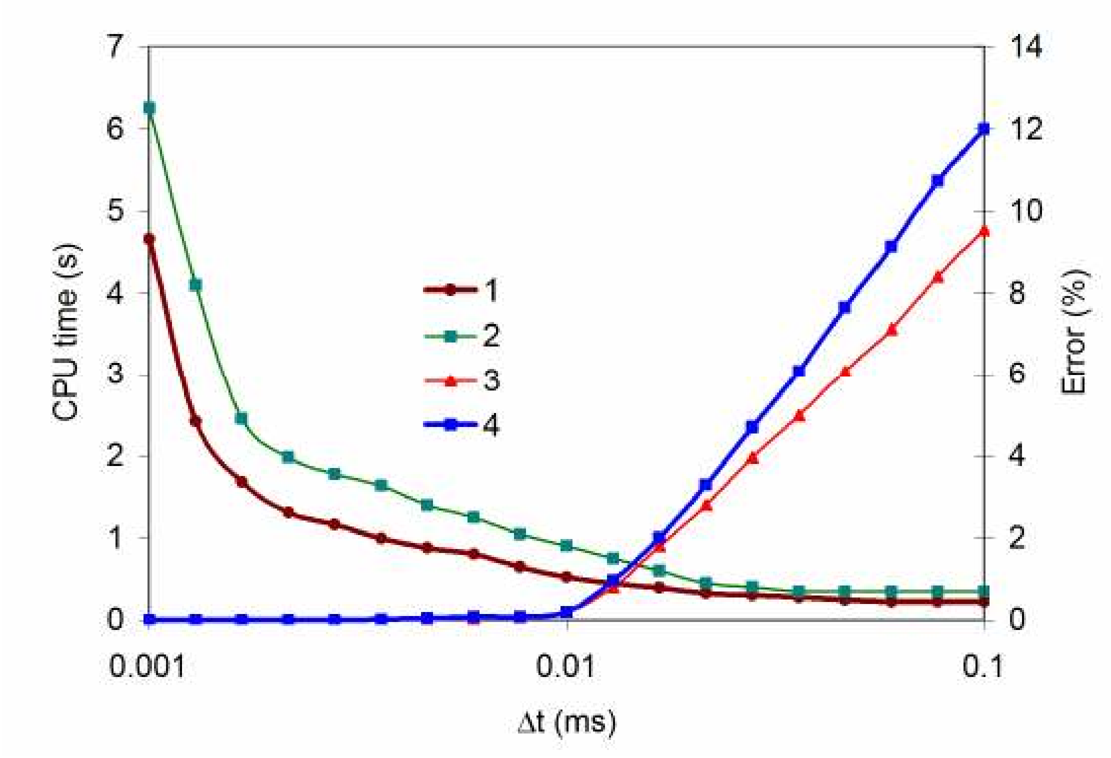

Figure 3.2.2 Plots of error and CPU times of the calculations of the evaporation time versus time step for the same set of parameters as in Figure 3.2.1. The errors were calculated relative to the predictions of the numerical solution of the discretised heat conduction equation with $\Delta t = 10^{-6}$ s and using 1000 nodes along the droplet radius. Curves (1) and (2) refer to CPU times required by the numerical algorithms based on the analytical and numerical solutions of the heat conduction equation inside the droplet respectively. Curves (3) and (4) refer to errors in predictions of the numerical algorithms based on the analytical and numerical solutions of the heat conduction equation inside the droplet respectively

3.3 Modelling versus experiments

As in Sazhin et al. (2005b), the experimental results reported by Belardini et al. (1992) and Nomura et al. (1996) were used for comparison with predictions of the model. In the experiment conducted by Belardini et al. (1992), 10^{-9} g of tetradecane was injected at a temperature of 300 K and an initial velocity of 6 m/s through a hole of 0.28 mm diameter into a 100 cm^3 chamber. The chamber was filled with air at 1 bar, and the initial temperatures were in the range from 473 K to 673 K. The evolution of droplet diameter during the evaporation process was measured starting with droplet diameter equal to 72 μm. The results of measurements were presented in the form of a plot of $(R_d/R_{d0})^2$ versus time t and are shown in Figure 3.3.1. In the same figure, the time evolution of this variable, predicted by algorithms described in Chapter 2, are presented. The calculations were performed using the effective thermal conductivity (ETC) model for the liquid phase and Model 4 for the gas phase (Curve 1), ETC model for the liquid phase and Model 0 for the gas phase with the same values of parameters as used by Sazhin et al. (2005b) (Curve 2), infinite thermal conductivity (ITC) model for the liquid phase and Model 4 for the gas phase (Curve 3), ETC model for the liquid phase and Model 4 for the gas phase, using the parameters reported by Hirschfelder et al. (1967) for tetradecane molecules (used for calculation of the binary diffusion coefficient) (Curve 4). The parameters reported by Paredes et al. (2000) for tetradecane molecules were used for Curves 1-3. The physical properties of tetradecane, used in the calculations, are given in Appendix A. The effect of thermal radiation was taken into account assuming that the radiation temperature is equal to the gas temperature.

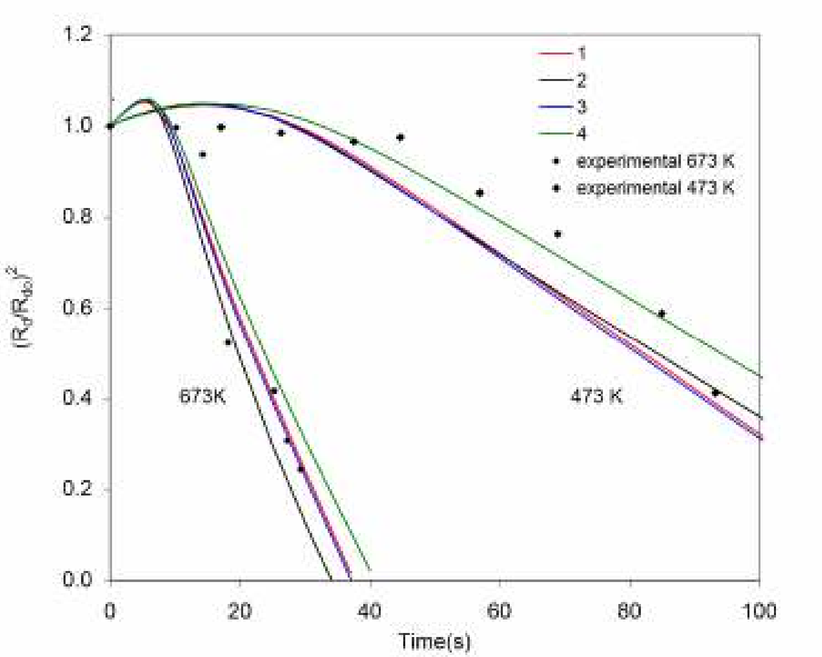

Figure 3.3.1 The values of $(R_d/R_{d0})^2$ for evaporating tetradecane droplets versus time, as measured by Belardini et al. (1992), and the results of calculations based on algorithms described in Chapter 2. The values of the initial gas temperatures are indicated near the curves

As follows from Figure 3.3.1, gas Models 0 and 4 predict slightly different time evolution of the droplet radius, but both of them seem to show qualitative agreement with experimental data. The agreement of the prediction of Model 4 with experimental data is better than that of Model 0 for the initial gas temperature 673 K, but is marginally worse for the initial gas temperature 473 K. The predictions of ETC and ITC models (Curves 1 and 3) are practically the same, in agreement with the earlier result reported by Sazhin et al. (2005b). The visible difference between Curves 1 and 4 indicates rather strong dependence of the prediction of gas Model 4 on the values of the binary diffusion coefficient. There is still much uncertainty regarding the latter values and this is translated into uncertainty of the prediction of the droplet evaporation models.

The experimental data reported by Nomura et al. (1996) were obtained for suspended $n-$heptane droplets in nitrogen atmosphere at pressures in the range between 0.1 and 1 MPa and temperatures in the range between 400 K and 800 K. Droplet initial radii varied from 300 μm to 350 μm. The experiments were performed under microgravity conditions. The experimentally observed values of $(R_d/R_{d0})^2$ versus t for pressure 0.1 MPa, initial gas temperatures 471 K, 555 K, 648K, 741 K, and the initial droplet radii equal to 300 μm, are shown in Figure 3.3.2. Also, the results of calculations for the same values of parameters are shown. The calculations were based on the same models as used in Figure 3.3.1. The physical properties of n-heptane are given in Appendix A.

As follows from Figure 3.3.2, for the initial gas temperature 471 K, the predictions of all models under consideration are practically the same. For higher initial temperatures, however, the agreement between the experimental data and the prediction of Model 4 appears to be consistently worse than with the prediction of Model 0. As in the case reported by Sazhin et al. (2005b), taking into account the finite thermal conductivity of droplets and recirculation in them, slightly improves the agreement of prediction of the model with experimental data. The effect of binary diffusion coefficient on the values of R_d is relatively small in this case.

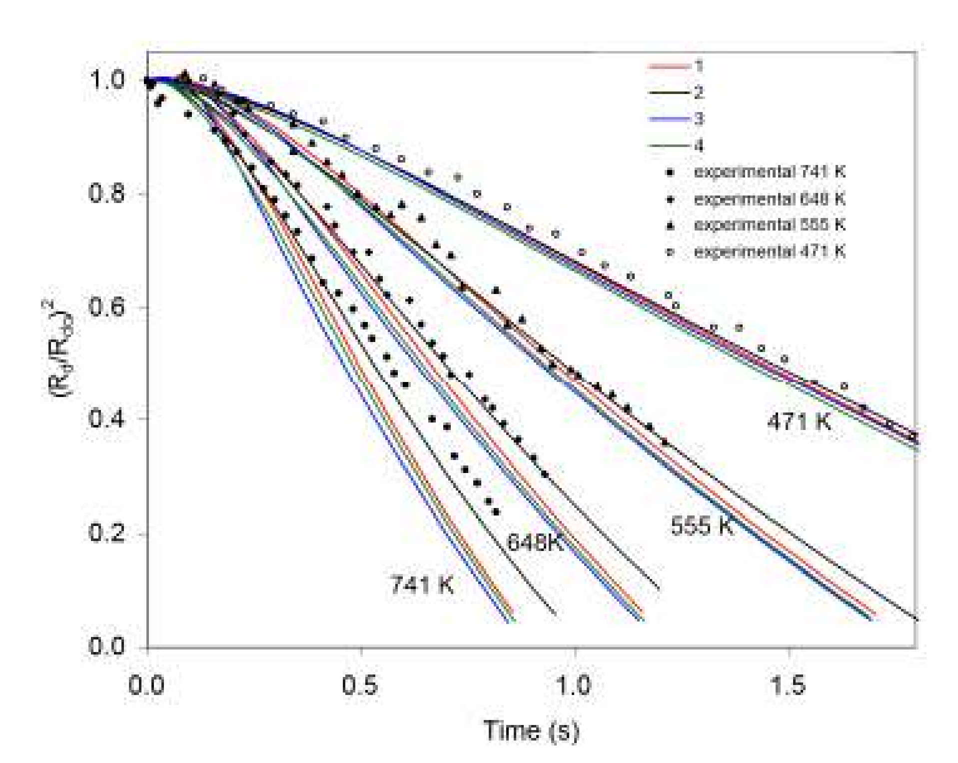

Figure 3.3.2 The values of $(R_d/R_{d0})^2$ for evaporating n-heptane droplets versus time for the initial pressure of 0.1 MPa, as measured by Nomura et al. (1996), and the results of calculations for the same combination of liquid and gas models as in Figure 3.3.1. The values of the initial gas temperatures are indicated near the curves

Plots of droplet surface temperature T_s versus t for the same parameters as in Figure 3.3.2 are shown in Figures 3.3.3 and 3.3.4. As can be seen in Figure 3.3.4, at the very initial stage of droplet heating and evaporation, the values of T_s are relatively insensitive towards the choice of gas phase model (Curves 1, 2 and 4 are rather close), but depend strongly on the choice of the liquid phase model (cf. Curves 1 and 3). The values of T_s predicted by the ITC model are much less than those predicted by the ETC model at the very initial stage of droplet heating regardless of the choice of the gas phase model.

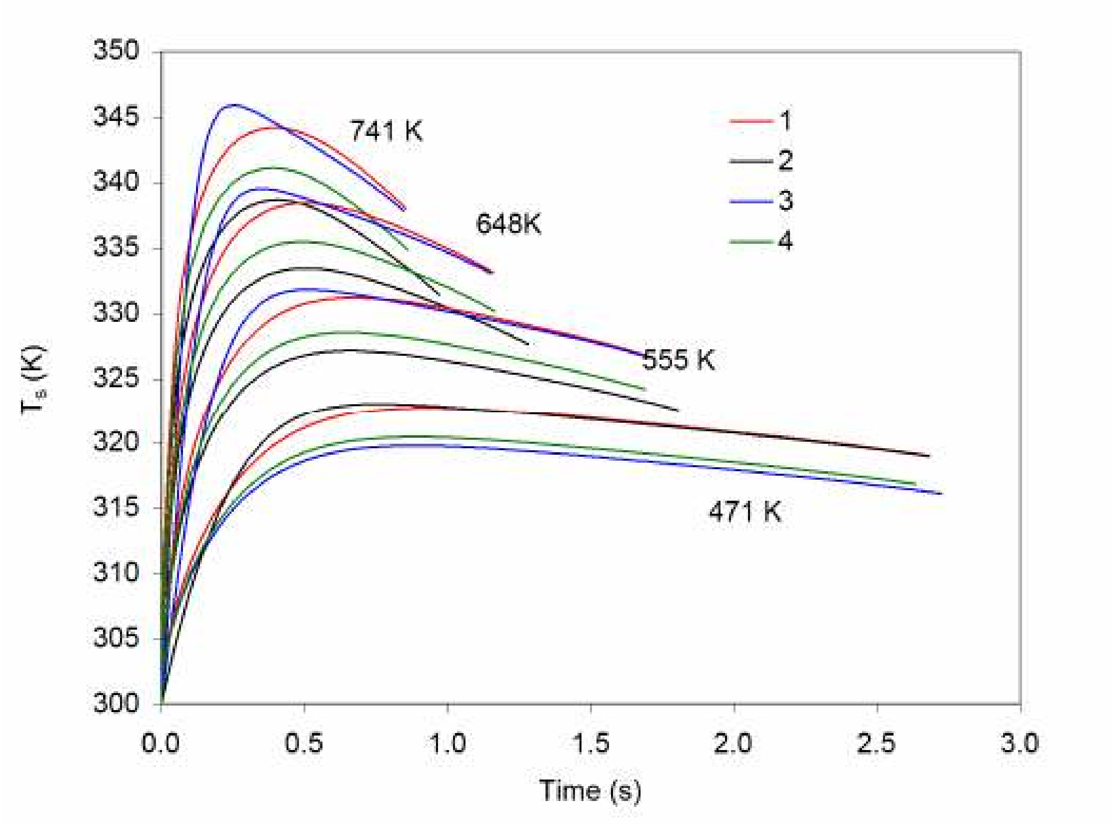

Figure 3.3.3 The plots of T_s versus time for the same values of parameters as in Figure 3.3.2, calculated using the same liquid and gas phase models as in this figure

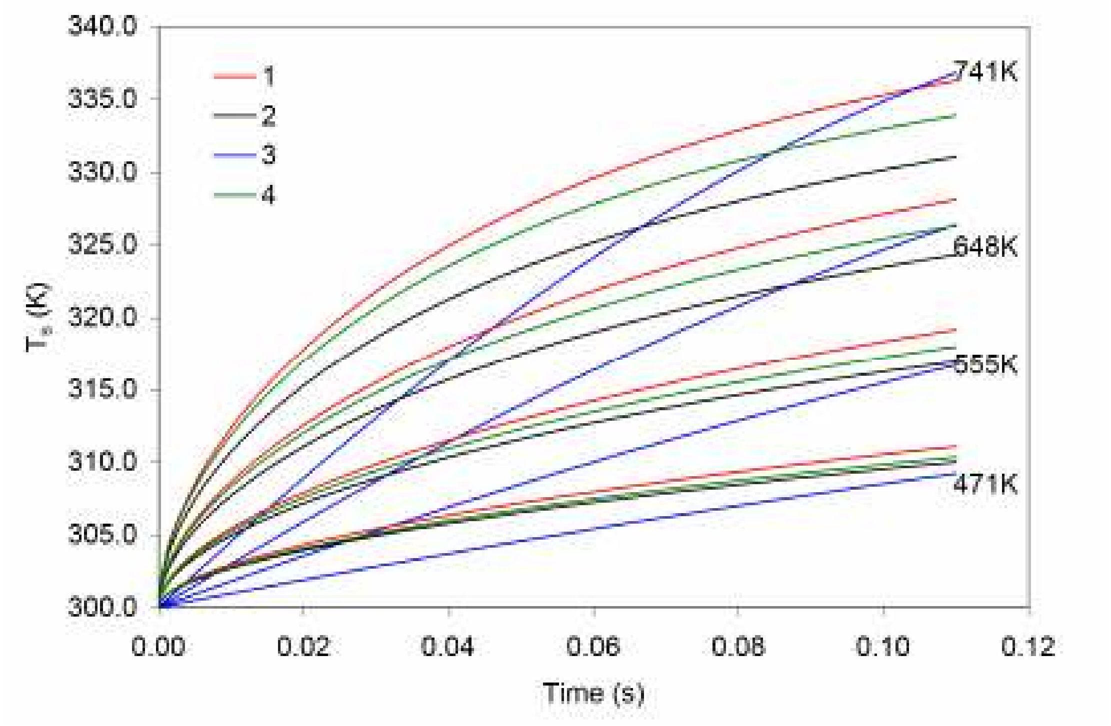

Figure 3.3.4 Zoomed part of Figure 3.3.3 referring to the very initial stage of evaporation

At intermediate times both liquid and gas phase models affect the values of T_s (see Figure 3.3.3). During longer times the effects of liquid phase model on the values of T_s are negligible in most cases, and the predicted values of this temperature depend mainly on the choice of the gas phase model (see Figure 3.3.3). Note that, as in the cases shown in Figures 3.1.5 – 3.1.8, all models predict the maximal values of droplet surface temperature at certain moments of time. These maxima are related to the contribution of thermal radiation, as discussed earlier (cf. Figures 3.1.5 – 3.1.8).

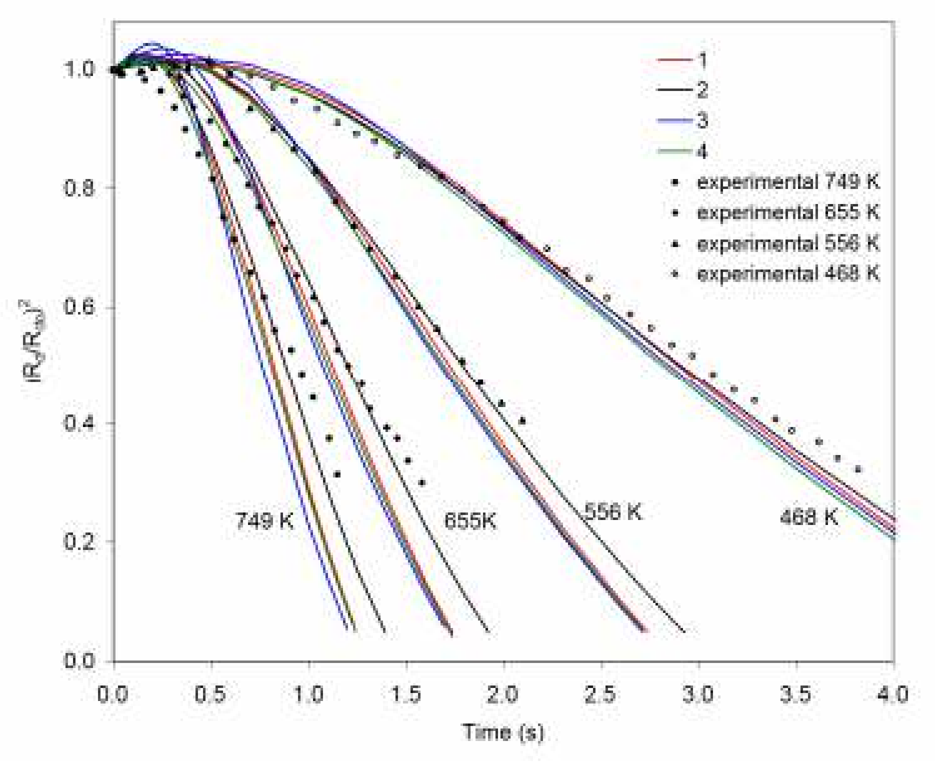

Figure 3.3.5 The same as in Figure 3.3.2 but for the initial gas pressure of 0.5 MPa

The plots similar to those shown in Figure 3.3.2 but for pressure 0.5 MPa, and various initial gas temperatures, are shown in Figure 3.3.5. As follows from this figure, for the initial gas temperature 468 K, the predictions of all models are close, as in the case shown in Figure 3.3.2. At larger initial temperatures, the predictions of gas Model 4 are marginally closer to the experimental data at the initial stages of evaporation. However, during longer times the predictions of gas phase Model 0 with parameters used by Sazhin et al. (2005b) seem to be in better agreement with experimental data than the predictions of gas phase Model 4. The effect of the binary diffusion coefficient on the values of R_d is relatively small in this case, as shown in Figure 3.3.2. In agreement with the results reported by Sazhin et al. (2005b), the ETC model predicts marginally more accurate results compared with the ITC one, similar to the case of lower pressure (see Figure 3.3.2). The comparison of the experimental results and the predictions of the models for the initial gas pressure 1 MPa and various initial gas temperatures is shown in Figure 3.3.6. The conclusions, which are obtained from the observation of this figure, are essentially the same as those which follow from Figure 3.3.5. The corresponding plots of T_s versus t have properties similar to those shown in Figures 3.3.3 and 3.3.4 for pressure 0.1 MPa.

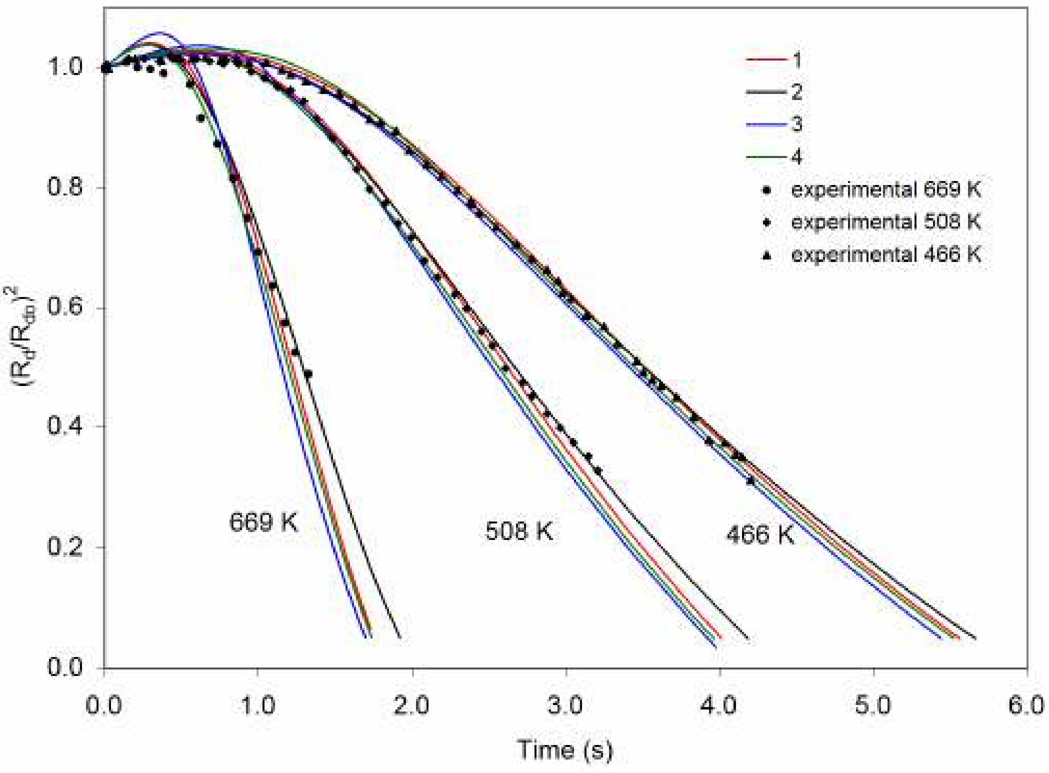

Figure 3.3.6 The same as in Figure 3.3.2 but for the initial gas pressure of 0.1 MPa

To summarise the results presented in this section, the comparison between the predictions of the models and experimental data reported by Belardini et al. (1992) and Nomura et al. (1996), is rather inconclusive. Namely, these data cannot support any of the gas phase models under consideration. The effect of liquid phase models is relatively small in the general case, and it leads to marginally better agreement between the predictions of the models and experimental data.

3.4 Effects of droplet break-up and autoignition

The models and experimental results considered so far did not take into account the effects of autoignition of fuel vapour/ air mixture, and the effects of droplet break-up. In this section both these effects are taken into account. As in Sazhin et al. (2005b), the Shell autoignition model and the bag/ stripping droplet break-up models are used. These models are described in Sazhin et al. (2005b).

As in Sazhin et al. (2005b), we use the experimental data on the total ignition delay times reported by Tanabe et al. (1995), for comparison with the prediction of some of the models described in Chapter 2. In the experiment described by Tanabe et al. (1995), n-heptane droplets with the initial radii of 350 μm were suspended in air at pressure 0.5 MPa. The droplets diameters were measured within ± 50 μm. A furnace able to generate almost uniform gas temperature (from room temperature to 1100 K) was constructed and used for this experiment. The igniting droplets were observed by a Michelson interferometer so that the time-dependent temperature distribution around them could be estimated. Interferometric images were stored on an 8 mm video tape with a frame rate of 50 s^{-1} and were analysed by computer image processing. The experiment was performed under microgravity conditions by using a 110 m drop tower. This enabled the authors to observe spherically symmetrical phenomenon, that could be compared with the one-dimensional theoretical analysis (Tanabe et al., 1995).

The volume of air used in the experiment was not specified, but it can be assumed that this volume was rather large. As in Sazhin et al. (2005b), lean ignition limit was taken when the equivalence ratio is equal to 0.5 for the initial gas temperature T_{g0} = 600 K. This corresponds to the case when the volume of air is equal to that of a sphere with the radius equal to 19.1 radii of droplets. The observed total ignition delay times (physical + chemical ignition delays) versus initial gas temperatures are shown in Figure 3.4.1. In the same figure, the total ignition delay times predicted by the same models as used in Figures 3.3.1 –

3.3.6 are shown. The calculations were based on the Shell model with $A_{f4} = 3 \times 10^6$ (Sazhina et al., 1999, 2000).

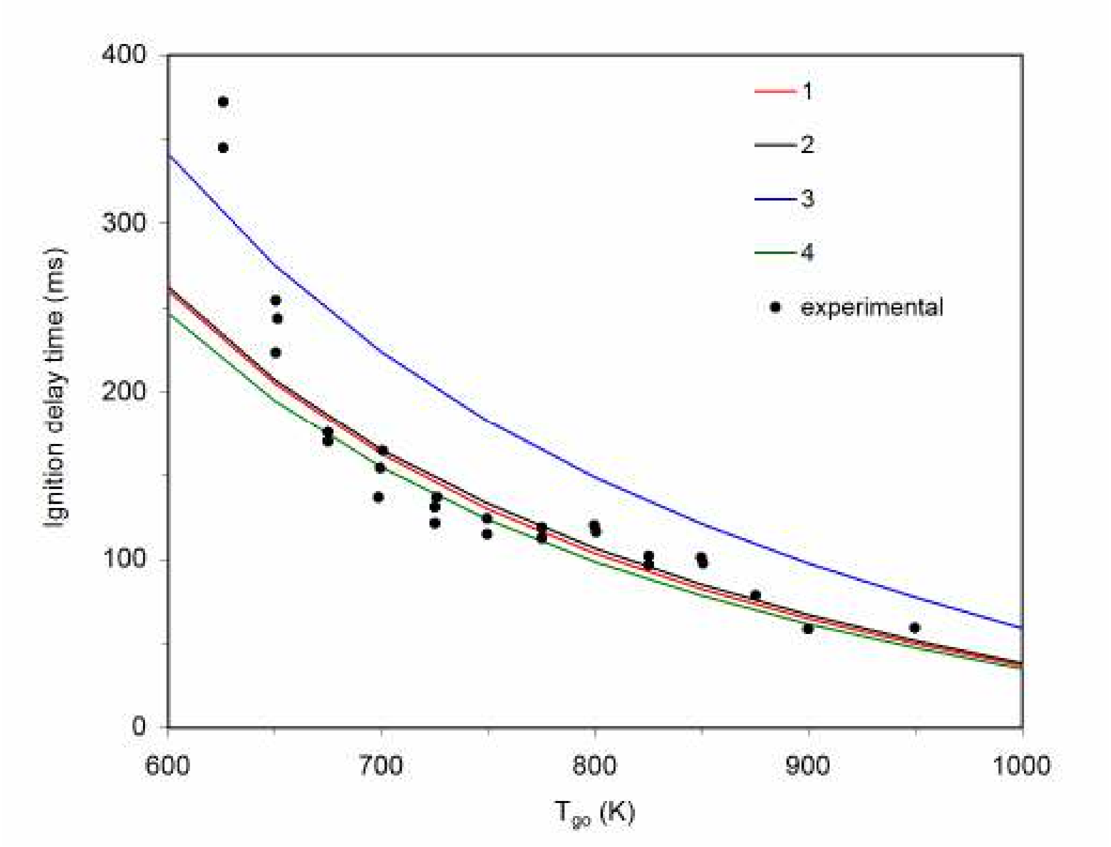

Figure 3.4.1 The values of the total ignition delay time for evaporating n-heptane droplets versus initial gas temperature, as measured by Tanabe et al. (1995), and the results of calculations based on the same combination of liquid and gas phase models as in the cases shown in Figures 3.3.1 – 3.3.6. The version of the Shell autoignition model described by Sazhina et al. (1999, 2000) was used with the coefficient $A_{f4} = 3 \times 10^6$. The ratio of the volumes of air and liquid droplets was taken equal to $19.1^3 = 6967.871$ to provide the equivalence ratio 0.5 for $T_{g0} = 600$ K

As follows from Figure 3.4.1, Curves 1, 2 and 4 are very close to each other. This means that the predicted total ignition delay is practically independent of the choice of the gas phase model. At the same time, the visible difference between these curves and Curve 3 indicates a strong effect of the finite thermal conductivity of the droplets and recirculation in them on the total ignition delay. This result is similar to the one reported by Sazhin et al. (2005b) and shows the need of taking into account the effects in the liquid phase in modelling of the ignition delay. Note that the agreement between the predictions of the ETC model with experimental data for initial gas temperatures greater than about 650 K, shown in this figure, cannot be interpreted as the experimental validation of the model, due to the uncertainty of the parameters of the Shell model.

The rest of this section will focus on the investigation of the effects of various liquid and gas models on droplet heating and evaporation, and the ignition of fuel vapour/ air mixture in a monodisperse spray, taking into account the droplet break-up effect. The effect of thermal radiation is ignored. The fuel is approximated by n-dodecane (see Appendix A). Gas and liquid parameters are the same as in the cases shown in Figures 3.1.1 – 3.1.8 and 3.2.1- 3.2.2. The autoignition process is assumed to be completed when the fuel vapour/ air temperature reached 1100 K.

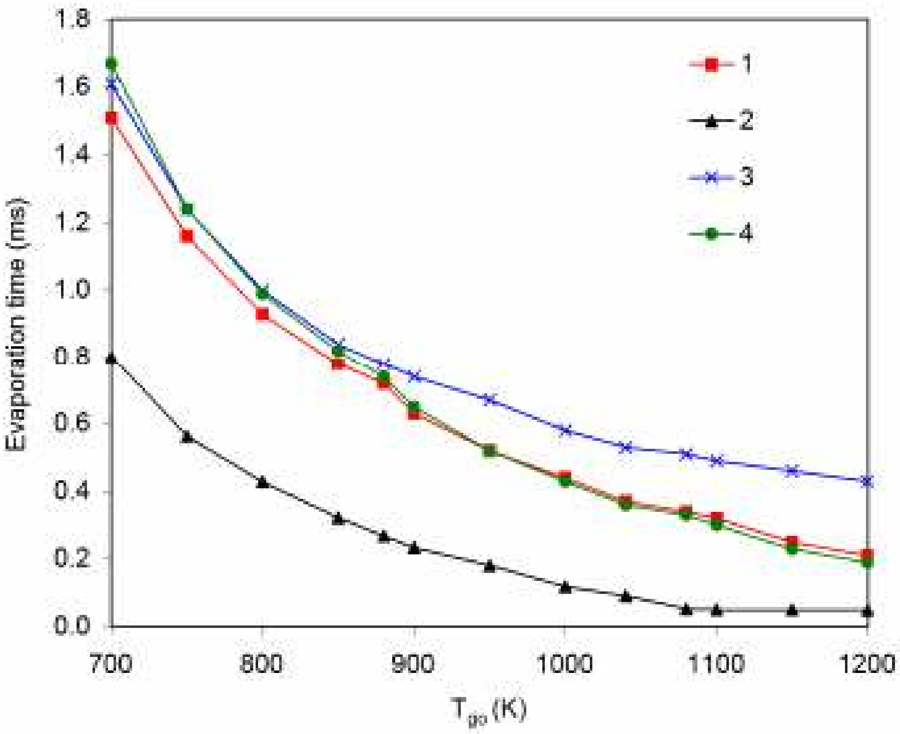

Figure 3.4.2 The values of the evaporation time versus initial gas temperature calculated based on the same combination of liquid and gas models as in the cases shown in Figures 3.3.1-3.3.6 and 3.4.1. Bag and stripping droplet break-ups were taken into account. The initial droplet diameter and velocity are taken equal to 50 μm and 50 m/s respectively. Symbols indicate the values of gas temperatures for which the evaporation times were calculated

Figure 3.4.2 illustrates the effect of various gas and liquid models on droplet evaporation time at various initial gas temperatures in the presence of break-up, but without taking into account chemical reactions in the gas phase. The initial droplet diameter and velocity are assumed equal to 50 μm and 50 m/s respectively. Symbols in the figure indicate the values of the initial gas temperatures for which calculations of the evaporation time were performed. As one can see from Figure 3.4.2, in the presence of break-up, the contribution of gas and liquid models to the values of evaporation time are of the same order of magnitude. This situation is different from the one presented in Figures 3.1.1 – 3.1.8 where it was shown that in the absence of break-up the contribution of the liquid phase models to the evaporation time is negligible. In all cases shown in Figure 3.4.2, taking into account the effects of finite thermal conductivity in droplets and recirculation in them, leads to a prediction of shorter evaporation times in agreement with the results reported by Sazhin et al. (2005b). At small initial gas temperatures (less than about 900 K) this predicted increase in the evaporation time is relatively small. At larger initial gas temperatures, however, this effect becomes noticeably stronger. At T_{g0} = 1200 K the evaporation time predicted by the ITC model is approximately twice as large compared with the one predicted by the ETC model. The effect of the binary diffusion coefficient on the evaporation time is relatively small. The discussion about the physical background of some of these effects is given in Sazhin et al. (2005b).

The plots of the total ignition delay versus the initial gas temperature T_{g0} in the presence of break-up for the same droplets as used in Figure 3.4.2, are shown in Figure 3.4.3. The Shell autoignition model with $A_{f4} = 3 \times 10^6$ was used (Sazhina et al. 1999, 2000). As in Figure 3.4.2, symbols indicate the values of the initial gas temperatures for which the calculations were performed. As can be seen from Figure 3.4.3, in all cases the ignition delay decreases with increasing T_{g0}. As in the case of the evaporation time shown in Figure 3.4.2, the total ignition delay depends on the choices of both gas and liquid phase models. At T_{g0} close to 950 K the time delays predicted by gas Models 4 and 0 almost coincide. This result agrees with the one shown in Figure 3.4.1. For the initial gas temperatures greater than about 890 K, the ITC model predicts longer total ignition delays compared with the ETC model in agreement with the result reported by Sazhin et al. (2005b). The effect of the binary diffusion coefficient on the total ignition delay is visible but not dominant.

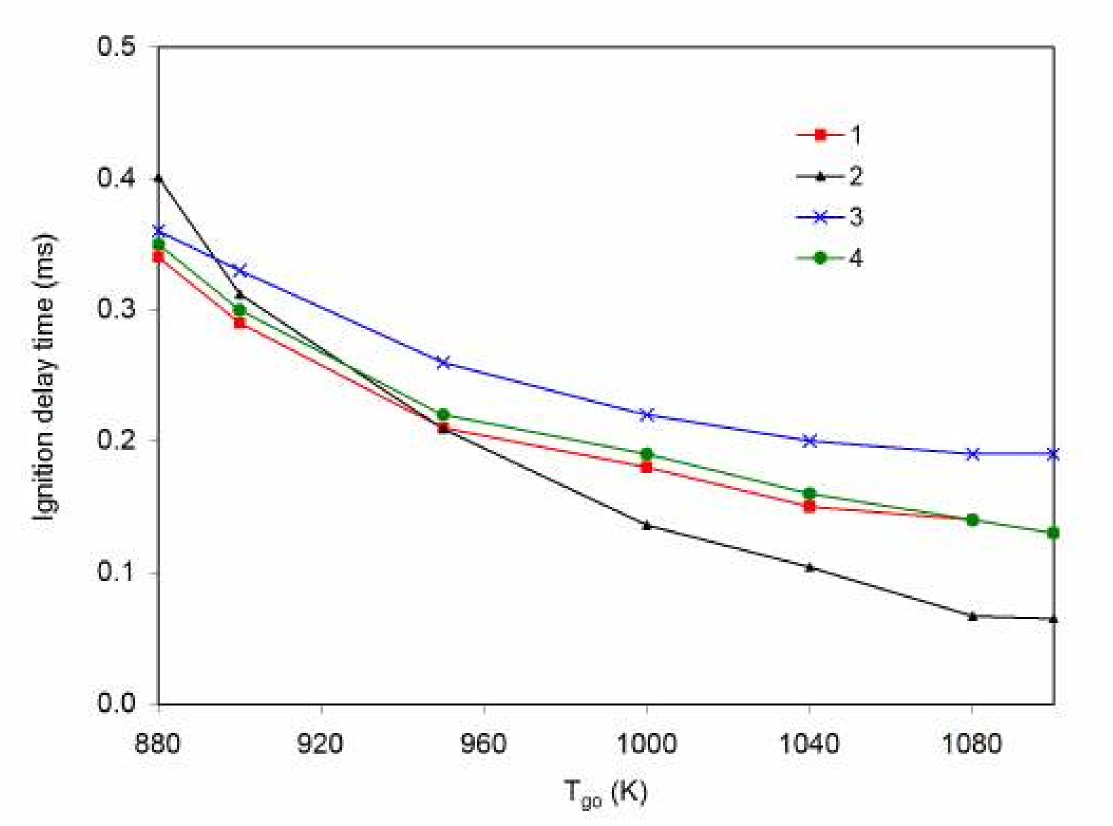

Figure 3.4.3 The plots of the total ignition delay versus the initial gas temperature T_{g0} in the presence of the break-up for the same droplets as used in Figure 3.4.2, calculated based on the same models as in the cases shown in Figures 3.3.1-3.3.6 and Figures 3.4.1-3.4.2. The Shell autoignition model with $A_{f4} = 3 \times 10^6$ was used (see Sazhina et al., 1999, 2000). Symbols indicate the values of gas temperature for which the ignition delay times were calculated

To summarise the results presented in this section, we can conclude that the choices of gas and liquid models are equally important for the correct estimate of droplet evaporation and the ignition of fuel vapour/air mixture in the presence of droplet break-up. Ignoring the effects of finite thermal conductivity of droplets and recirculation in them in this case (as typically done in most commercial CFD codes) could lead to unacceptably big errors in predictions of these parameters.

3.5 Conclusions to Chapter 3

A comparative analysis of liquid and gas phase models for fuel droplet heating and evaporation, suitable for implementation into computational fluid dynamics (CFD) codes, is presented. The analysis is focused on the liquid phase model based on the assumption that the liquid thermal conductivity is infinitely large (infinite thermal conductivity (ITC) model), and the so called effective thermal conductivity (ETC) model suggested by Abramzon and Sirignano (1999). Seven gas phase models are compared. These are six semi-theoretical models based on various assumptions and a model based on the approximation of experimental data. It is pointed out that the gas phase model, taking into account the finite thickness of the thermal boundary layer around the droplet, in the form suggested by Abramzon and Sirignano (1999), predicts the evaporation time closest to the one based on the approximation of experimental data. This gas phase model is recommended for practical applications in CFD codes. In most cases, the predicted droplet evaporation time depends strongly on the choice of the gas phase model. The dependence of this time on the choice of the liquid phase model, however, is weak if the droplet break-up processes are not taken into account. On the other hand, the dependence of the droplet surface temperature at the initial stage of heating and evaporation, on the choice of the gas phase model is weak, while its dependence on the choice of the liquid phase model is strong. The direct comparison of the predictions of various gas models with experimental data for droplet evaporation in the absence of break-up reported by Belardini et al. (1992) and Nomura et al. (1996) leads to inconclusive results. None of gas phase models under consideration can be supported by all experimental data presented. The ETC model leads to a marginally better agreement with experimental data than the ITC model.

Several liquid and gas phase models were used for modelling droplet heating and evaporation, together with the autoignition of the mixture of air and fuel vapour produced by evaporating droplets. The chemical part of the autoignition process was modelled based on the Shell model in the form suggested by Sazhina et al. (1999). The results were compared with experimental data reported by Tanabe et al. (1995). It is pointed out that the predicted total ignition delay (physical and chemical delays) depends weakly on the choice of the gas phase model for the values of parameters used by Tanabe et al. (1995). Its dependence on the choice of the liquid phase model turned out to be strong, in agreement with the earlier results presented by Sazhin et al. (2005b). In the presence of droplet break-up processes, the evaporation time and the total ignition delay depend both on the choice of gas and liquid phase models.

4. APPROXIMATE ANALYSIS OF THERMAL RADIATION ABSORPTION IN FUEL DROPLETS

As mentioned in Chapter 2, more advanced models for radiation absorption in Diesel fuel droplets have been developed by Dombrovsky (2004), Dombrovsky and Sazhin (2003c, 2004). These take into account the distribution of absorption inside droplets. None of these models, however, seem to be suitable for implementation into CFD codes due to excessive CPU requirements (Sazhin, 2006; Sazhin et al., 2004a, 2005a; Abramzon and Sazhin, 2005, 2006). Therefore in practical applications, implementing the distribution of radiation absorption inside droplets seems to be of limited potential. Simplified but accurate models have been developed by Dombrovsky et al. (2001) and Sazhin et al. (2004a) (see Equation (2.1.38)). There are two main shortcomings in the model developed by Dombrovsky et al. (2001) and Sazhin et al. (2004a). Firstly, the analysis in these papers was focused only on Diesel fuels (although various types of these fuels were considered). Secondly, the accuracy of the aforementioned approximation of the absorption efficiency factor was shown to be poor when the range of droplet radii was large (typical values of droplet radii in Diesel engines are in the range 2 μm – 200 μm). The focus of this chapter is mainly to address these matters.

The analysis of this chapter is started with analysis of experimental studies of the optical properties of gasoline fuel (BP Pump Grade 95 RON ULG), 3-pentanone and 2,2,4-trimethylpentane (iso-octane). These are presented and discussed in Section 4.1. The results are compared with the results for Diesel fuel reported earlier by Sazhin et al. (2004a). A new approximation for the efficiency factor of absorption of all these fuels in a wide range of droplet radii is suggested and discussed in Section 4.2. The results predicted by various approximations are compared in Section 4.3. In Section 4.4 the new approximation for the efficiency factor of absorption is applied to simulate heating and evaporation of fuel droplets. The main results of this chapter are summarised in Section 4.5.

4.1 Optical properties of fuels

Three fuels (i) gasoline fuel (BP Pump Grade 95 RON ULG), (ii) iso-octane $(CH_3)_2CHCH_2C(CH_3)_3$ and (iii) 3-pentanone $CH_3CH_2COCH_2CH_3$ were used for the analyses. Iso-octane and 3-pentanone are most often used in experimental studies of gasoline fuel sprays and mixture preparation: iso-octane is 100 RON gasoline and 3-pentanone is used as a fluorescent dopant for laser induced fluorescence (LIF). The results were compared with the earlier results for low sulphur ESSO AF1313 Diesel fuel, hereafter referred to as Diesel fuel. The absorption coefficients of fuels were measured in the ranges 0.2 μm – 0.8 μm and 0.4 μm – 4 μm. Ultraviolet – visible spectra (0.2 μm – 0.8 μm) were obtained using a UV-Visible spectrophotometer Shimadzu, model 1601. The spectra were recorded in a 1 cm quartz cell for samples diluted with n-hexane. In the range (0.4 μm – 4 μm) the absorption coefficients were measured using a Fourier transform infrared (FTIR) spectrometer, (Nicolet FT-IR Avatar). A resolution of 8 cm^{-1} was used, recording 32 scans in a NaCl cell with an optical path length of 0.025 mm. The background was recorded as the empty NaCl cell. All samples were diluted with chloroform and all measurements were carried out at room temperatures. In all cases, the dilution was used when the value of the absorption coefficient exceeded the measuring limit of the instrument. The corrections for dilutions were made. In contrast to the case previously reported by Sazhin et al. (2004a), infrared spectra (4 μm – 6 μm) could not be measured, as the FTIR spectrometer (Nicolet FT-IR Nexus) was not operational for significant period during the course of this work. The measurement error for the absorption coefficient was approximately 5% across the whole range of wavelengths.

In the range 0.4 μm to 0.8 μm the difference between the results obtained using these methods was generally small. Over this range the results obtained using a UV-Visible spectrophotometer were considered to be more reliable than those obtained using a Fourier transform infrared spectrometer. The reason for this is that as one approaches the upper and lower measurement limits of the spectrometer the signal to noise ratio decreases, leading to incorrect readings.

Results of the calculation of the indices of absorption for all three fuels, based on the measurements of the corresponding absorption coefficient, are presented in Figure 4.1.1. On the same figure, the previously reported plots by Sazhin et al. (2004a) of κ versus λ for Diesel fuel are reproduced. About 2300 individual measurements were used for presenting each of these plots.

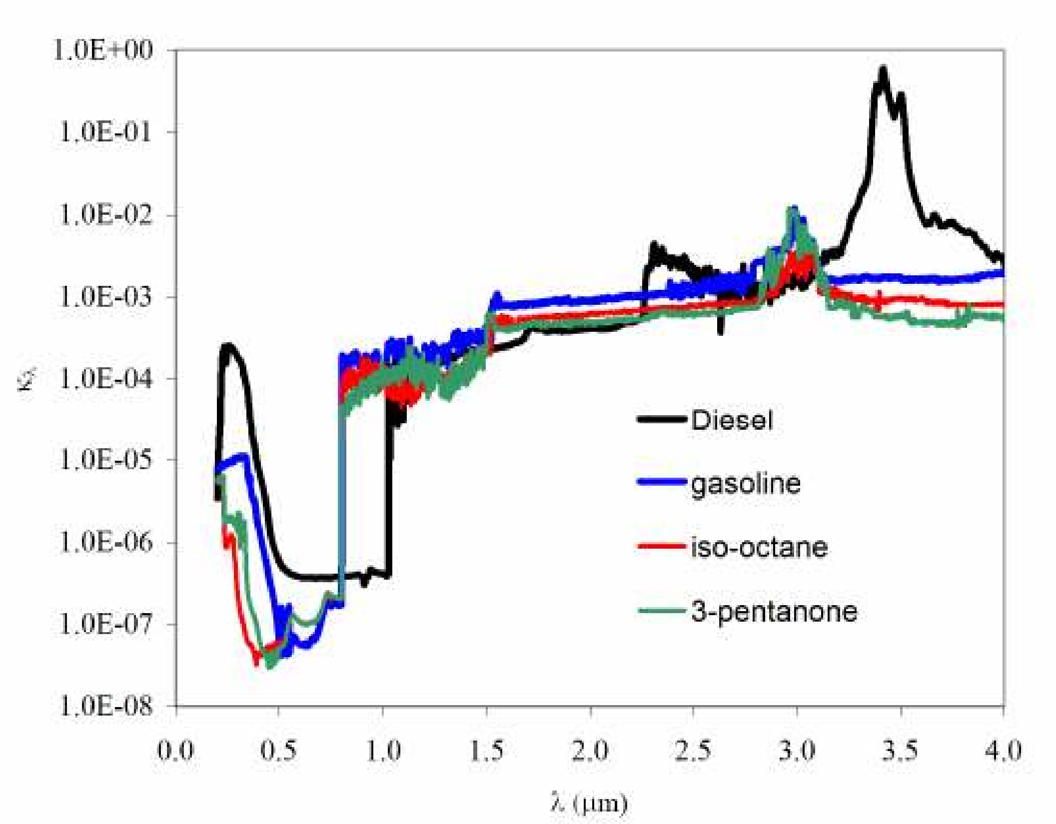

Figure 4.1.1 Indices of absorption of four types of fuel: low sulphur ESSO AF1313 Diesel fuel, gasoline fuel (BP Pump Grade 95 RON ULG), 2,2,4-trimethylpentane (iso-octane) and 3-pentanone versus wavelength λ. The results for Diesel fuel are reproduced from Sazhin et al. (2004a)

As can be seen in Figure 4.1.1, the dependence of κ on the type of fuel is noticeable, and there are a number of similarities between the plots. For all fuels, the region of semi-transparency in the range 0.5 μm < λ < 1 μm is evident. The index of absorption increases by approximately 3 orders of magnitude when λ increases from 0.5 μm to 1.5 μm. At the same time, some noticeable differences between the indices of absorption of the fuels can be identified. For example, the peak of absorption of Diesel fuel at $\lambda \approx 3.4$ μm is much more pronounced than the corresponding peaks of absorption of the other fuels. Also the value of λ when this peak is observed is shifted from 3.4 μm for Diesel fuel to approximately 3.0 μm for other fuels. Strong peaks at around 3.5 μm are related to C-H stretch vibrations of non-aromatic molecules, occurring in the range of 3.3 μm - 3.5 μm. Less intense peaks at around 3.0 μm are most likely due to the presence of aromatic hydrocarbons, in which C-H stretch vibrations from benzene rings are expected. This is supported by the absorbance at around 0.25 μm which is characteristic of the π-π electron transitions in the aromatic benzene ring. Aromatic hydrocarbons are added to gasoline to increase its octane number. The differences in the optical properties of the fuels shown in Figure 4.1.1 are expected to produce 4 different values of the average absorption efficiency factors of fuel droplets.

Index of refraction measurements were conducted using the ABBE 60 direct reading refractometer at room temperature. This index was measured by turning a dual prism combination through an angle, which is proportional to the refractive index of liquid placed between the two prisms. The light source was white. It was emitted from a tungsten lamp. The angle of light emerging from the combination of prisms was measured using a telescope that moved over a calibrated refractive index scale. The telescope was focused on the edge of the light beam, which showed up as a dark edge in the field of view. The values of refractive indices for the three fuels were: gasoline ($n = 1.394 \pm 0.001$); iso-octane ($n = 1.389 \pm 0.001$) and 3- pentanone ($n = 1.390 \pm 0.001$). The measurement of the index of refraction for Diesel fuel was $n = 1.460$ with similar error except in the region of strong absorption ($\lambda \approx 3.4$ μm) (Dombrovsky et al., 2003). The relatively weak dependence of n on λ for Diesel fuel has only a minor effect on the efficiency factor of absorption of this fuel (Dombrovsky et al., 2003). Therefore, this dependence can be ignored when this factor is calculated for Diesel fuel (Sazhin et al., 2004a). We assume that this conclusion remains valid for other fuels.

4.2 Average efficiency factor of absorption

Following Dombrovsky (2002) and Dombrovsky et al. (2003) the absorption efficiency factor of droplets Q_a at a given wavelength λ, obtained using detailed Mie calculations, is approximated as Equation (2.1.25). This equation gives a better approximation for Q_a when compared with that used in (Dombrovsky et al., 2001). Dombrovsky et al. (2001) and Sazhin et al. (2004a) assumed that the dependence of the incoming radiation intensity on λ is close to that of a black body. Using Equation (2.1.25) the averaged (over wavelengths) absorption efficiency factor of droplets is calculated from Equation (2.1.27).

The accuracy of Equation (2.1.27) increases with the increased separation between λ_1 and λ_2. The separation is limited by the available experimental facilities. In our case this range is between 0.2 μm and 4 μm. This, however, is not the major limitation of the model; over the range of the most important radiation temperatures for Diesel engine applications (1000 K – 3000 K), the values of λ at which the intensity of black body radiation is maximum ($\lambda_{\max}$), lie in the range between 0.97 μm and 2.90 μm. Since these values of $\lambda_{\max}$ lie in the range of wavelengths at which the measurements were performed and the intensity of thermal radiation decreases rapidly when $|\lambda - \lambda_{\max}|$ increases, it can be assumed that limits 0.2 μm and 4 μm for λ provide reasonably accurate values of $\overline{Q}_a$ as predicted by Equation (2.1.27).

To illustrate the effect of the range of λ on the value of $\overline{Q}_a$, the calculations have been performed for low sulphur ESSO AF1313 Diesel fuel in the range 0.2 μm – 4 μm, using data for κ shown in Figure 4.1.1 and for the same fuel in the range 0.2 μm – 6 μm, using data for κ reported by Sazhin et al. (2004a). The results of these calculations are shown in Figure 4.2.1 in the form of the plots of $\overline{Q}_a$ versus droplet radius, for three radiation temperatures: 1000 K, 2000 K and 3000 K. The curves calculated in these ranges are close for all three temperatures. Except for the smallest droplet radii, the deviation between these curves does not exceed 10%. This is comparable with the errors introduced by a number of other assumptions in the model. These include errors introduced by approximation (2.1.25) (see Dombrovsky et al. (2001) for the analysis of the accuracy of this approximation) and errors introduced by the assumption that the external radiation is that of a black body.

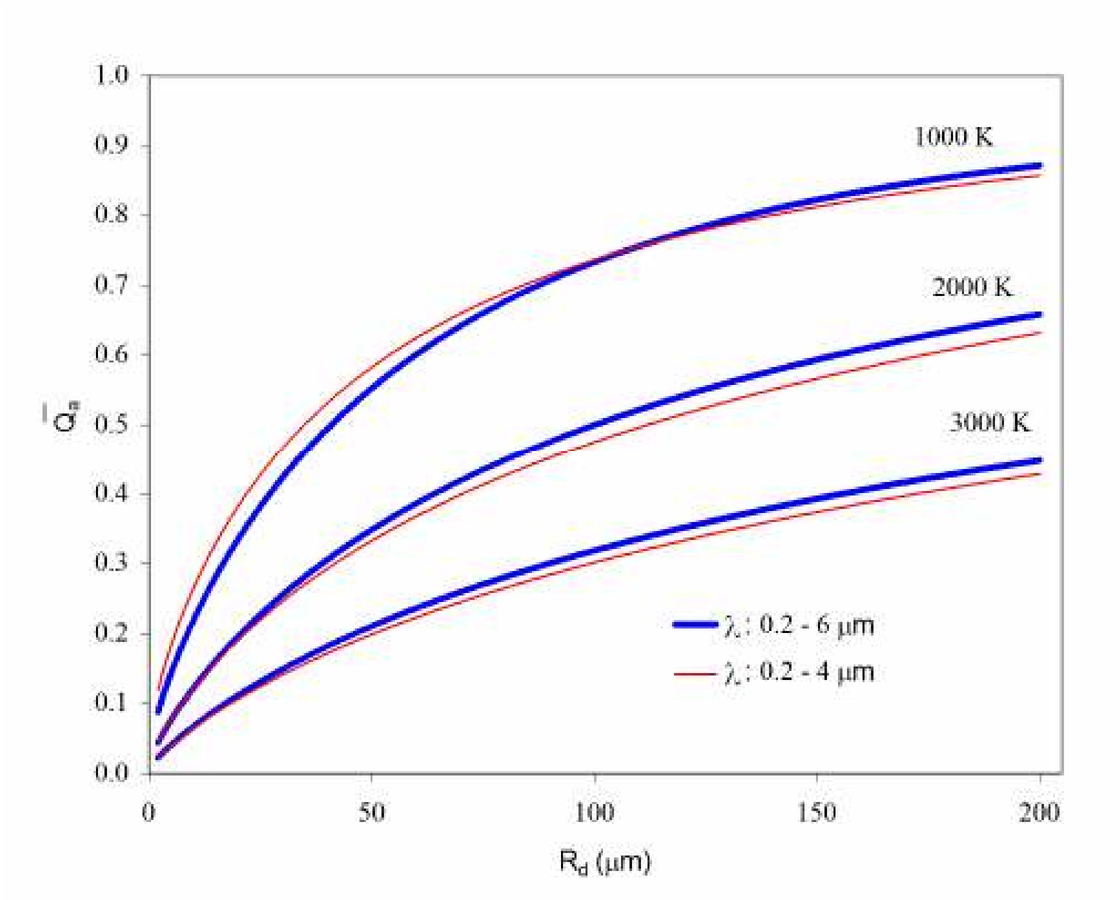

Figure 4.2.1 Plots $\overline{Q}_a$ versus droplet radius for Diesel fuel and three radiation temperature: 1000 K, 2000 K and 3000 K (indicated near curves), as calculated from Equation (2.1.27). Blue thick curves are based on the values of κ in the range 0.2 μm – 6 μm, as reported in Sazhin et al. (2004a). Red thin curves are based on the values of κ in the range 0.2 μm – 4 μm, as shown in Figure 4.1.1

The contribution of thermal radiation absorption at $\lambda < 0.2$ μm can be safely ignored for all three temperatures (it is well below 0.03%). The maximal possible contribution of thermal radiation absorption at $\lambda > 6$ μm (assuming that all external radiation at these wavelengths is absorbed in droplets) is expected to be 26% for θ_R = 1000 K, 5% for θ_R = 2000 K and 2% for θ_R = 3000 K. A more realistic contribution of thermal radiation absorption at in this range of λ is expected only from a strong absorption band in the 6.8 μm – 7.5 μm region. In the case of θ_{R} = 1000 K, θ_{R} = 2000 K and θ_{R} = 3000 K, the maximal contribution from the later range is estimated to be 3.8%, 0.9% and <0.3% respectively (Silverstein et. al., 2005). This is well below the errors shown in Figure 4.2.1. Hence, the application of data presented in Figure 4.1.1 for calculation of $\overline{Q}_{\mathrm{a}}$ based on Equation (2.1.27) can be justified.

Following Dombrovsky et al. (2001) and Sazhin et al. (2004a) the results of the calculation of $\overline{Q}_{\mathrm{a}}$ based on Equation (2.1.27) are approximated by the following expression (see Equation (2.1.28)):

$$\Lambda = aR_{\mathrm{d}}^{b}$$

where

$$a = \sum_{i=0}^{N} a_i \left(\frac{\theta_{\mathrm{R}}}{1000} \right)^i \tag{4.2.1}$$

$$b = \sum_{i=0}^{N} b_i \left(\frac{\theta_{\mathrm{R}}}{1000} \right)^i \tag{4.2.2}$$

θ_{R} is in K, R_{d} is in μm, a_i is in $\mu\mathrm{m}^{-b}\mathrm{K}^{-i}$, b_i is in K^{-i}.

In Dombrovsky et al. (2001), it was assumed that $N = 2$. In Sazhin et al. (2004a) both $N = 2$ and $N = 4$ were considered and it was shown that the fourth order approximation is particularly important when the radiation temperatures are less than 1000 K (when the overall contribution of the thermal radiation in the process of droplet heating is small). For radiation temperatures equal or greater than 1000 K, approximations (4.2.1) and (4.2.2) with $N = 2$ were used.

The coefficients a_i and b_i in Equations (4.2.1) and (4.2.2) were obtained by curve fitting and direct comparison of the values of Λ predicted by Equation (2.1.28) and $\overline{Q}_{\mathrm{a}}$ predicted by Equation (2.1.27). Approximation (2.1.28) for $N = 2$ shows good agreement with (2.1.27) for R_{d} in the range 5 μm – 50 μm, but less so for R_{d} in the range 2 μm – 200 μm.

Here, in contrast to Dombrovsky et al. (2001) and Sazhin et al. (2004a), approximations (4.2.1) and (4.2.2) are not used for the entire range of droplet radii (2 μm – 200 μm), but in sub-ranges over R_d. Taking $N = 2$, the values of coefficients a_i and b_i in various sub-ranges over R_d and various fuels have been calculated. The results are shown in Table 4.1.

Type of fuel	R_{min} (μm)	R_{max} (μm)	a_0	a_1	a_2	b_o	b_1	b_2
Diesel (low sulphur ESSO AF1313)	2	5	0.177537	-0.111821	0.019098	0.340153	0.163354	-0.020202
	5	50	0.181243	-0.117208	0.020356	0.299978	0.232538	-0.032668
	50	100	0.358073	-0.243320	0.043437	0.070587	0.308590	-0.043973
	100	200	0.635142	-0.440123	0.079431	-0.075184	0.339893	-0.048833
Gasoline (BP Pump Grade 95 RON ULG)	2	5	0.020400	-0.005650	0.000450	0.957600	0.011450	-0.001450
	5	50	0.029100	-0.009300	0.000900	0.771800	0.052950	-0.005850
	50	100	0.092600	-0.038400	0.004800	0.455900	0.096050	-0.008350
	100	200	0.276800	-0.125450	0.016550	0.215500	0.108950	-0.006950
2,3,4-Trimethylpentane	2	5	0.010310	-0.001990	0.000090	0.985320	0.002500	-0.002990
	5	50	0.013100	-0.003150	0.000150	0.874900	0.023450	-0.002250
	50	100	0.030500	-0.009750	0.000850	0.650100	0.050350	-0.003150
	100	200	0.076900	-0.027300	0.002600	0.451000	0.055600	-0.000100
3-Pentanone	2	5	0.013100	-0.004000	0.000370	0.940590	0.022660	-0.003220
	5	50	0.019200	-0.007250	0.000850	0.736400	0.092500	-0.012800
	50	100	0.038400	-0.016450	0.002150	0.537500	0.125010	-0.015700
	100	200	0.065100	-0.024950	0.002750	0.440200	0.088950	-0.006850

Table 4.1 The coefficients of a_i and b_i calculated for various ranges of R_d and various fuels, assuming that N=2.

For $N = 4$, approximations (4.2.1) and (4.2.2) with the same coefficients a_i and b_i were used in the entire range of droplet radii 2 μm – 200 μm. The corresponding values of coefficients a_i and b_i are shown in Table 4.2. Finally, approximations (4.2.1) and (4.2.2) for $N = 2$ with the same coefficients a_i and b_i were used in the entire range of droplet radii 2 μm – 200 μm. The corresponding values of coefficients a_i and b_i are shown in Table 4.3. Note that the values of these coefficients for Diesel fuel differ slightly from the values given by Sazhin et al. (2004a). This is attributed to different ranges of λ used in the current analysis. The values of Λ predicted by Equation (2.1.28) and $\overline{Q}_a$ predicted by Equation (2.1.27) for various approximations of a and b are compared in the next section.

Coefficients \ Fuel	Diesel (low sulphur ESSO AF1313)	Gasoline (BP 95 RON ULG)	2,2,4 -Trimethylpentane	3-Pentanone
a_0	0.143452	0.074546	0.035479	0.045995
a_1	-0.016510	-0.049511	-0.034435	-0.047760
a_2	-0.058531	0.023057	0.023033	0.029250
a_3	0.027674	-0.006836	-0.007777	-0.009075
a_4	-0.003661	0.000829	0.000964	0.001065
b_0	0.482037	0.406702	0.429499	0.327158
b_1	-0.249135	0.334640	0.625147	0.686807
b_2	0.286669	-0.208455	-0.462004	-0.463508
b_3	-0.094873	0.068515	0.152989	0.147149
b_4	0.010658	-0.008410	-0.018322	-0.017281

Table 4.2 The coefficients of a_i and b_i calculated for R_d in the range 2 μm – 200 μm and various fuels, assuming that $N = 4$.

Coefficients \ Fuel	Diesel (low sulphur ESSO AF1313)	Gasoline (BP 95 RON ULG)	2,2,4-Trimethylpentane	3-Pentanone
a_0	0.252827	0.05220	0.02010	0.02590
a_1	-0.167207	-0.020890	-0.00610	-0.010400
a_2	0.029404	0.002710	0.000500	0.001290
b_0	0.160138	0.575405	0.721815	0.620380
b_1	0.274847	0.081630	0.048190	0.112250
b_2	-0.038919	-0.008300	-0.005300	-0.015710

Table 4.3 The coefficients of a_i and b_i calculated for R_d in the range 2 μm – 200 μm and various fuels, assuming that $N = 2$.

4.3 Comparison of the results

The plots of $\overline{Q}_a$ and three approximations Λ for Diesel fuel versus R_d are shown in Figure 4.3 for the range 2 μm – 200 μm. As can be seen from this figure, the piecewise quadratic approximation for coefficients *a* and *b* accurately predicts the values of Λ. The values of Λ based on quadratic and fourth power approximations over the whole range of R_d are noticeably different from $\overline{Q}_a$. The piecewise quadratic approximation for coefficients *a* and *b* is therefore expected to be of use in practical engineering applications, including computational fluid dynamics (CFD) codes.

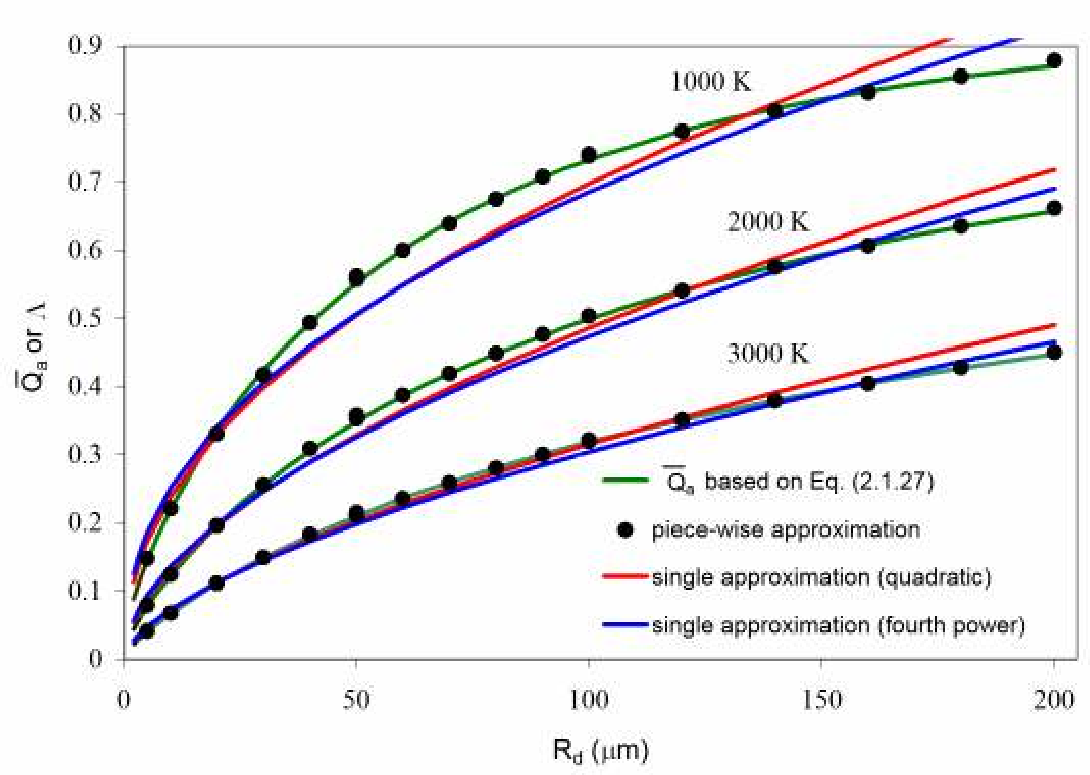

Figure 4.3.1 Plots of $\overline{Q}_a$ and its three approximations Λversus droplet radius for Diesel fuel. Three radiation temperature: 1000 K, 2000 K and 3000 K (indicated near curves) were considered. Green solid curve refer to $\overline{Q}_a$ as calculated from Equation (2.1.27). Black dots refer to piecewise approximation for Λ, as calculated from Equation (2.1.28). Red solid curved refer to a single quadratic approximation for Λ. Blue solid curves refer to a single fourth power approximation for Λ

The same conclusion was drawn for gasoline (Figure 4.3.2), iso-octane (Figure 4.3.3) and 3-pentanone (Figure 4.3.4). Note that the temperature effect on $\overline{Q}_a$ is greatest for Diesel fuel. The maximum values of $\overline{Q}_a$ are greater for Diesel and gasoline fuels than for iso-octane and 3-pentanone. For all fuels, the values of $\overline{Q}_a$ decrease with increasing external temperature in agreement with the results reported earlier by Dombrovsky (2001) and Sazhin et al. (2004a).

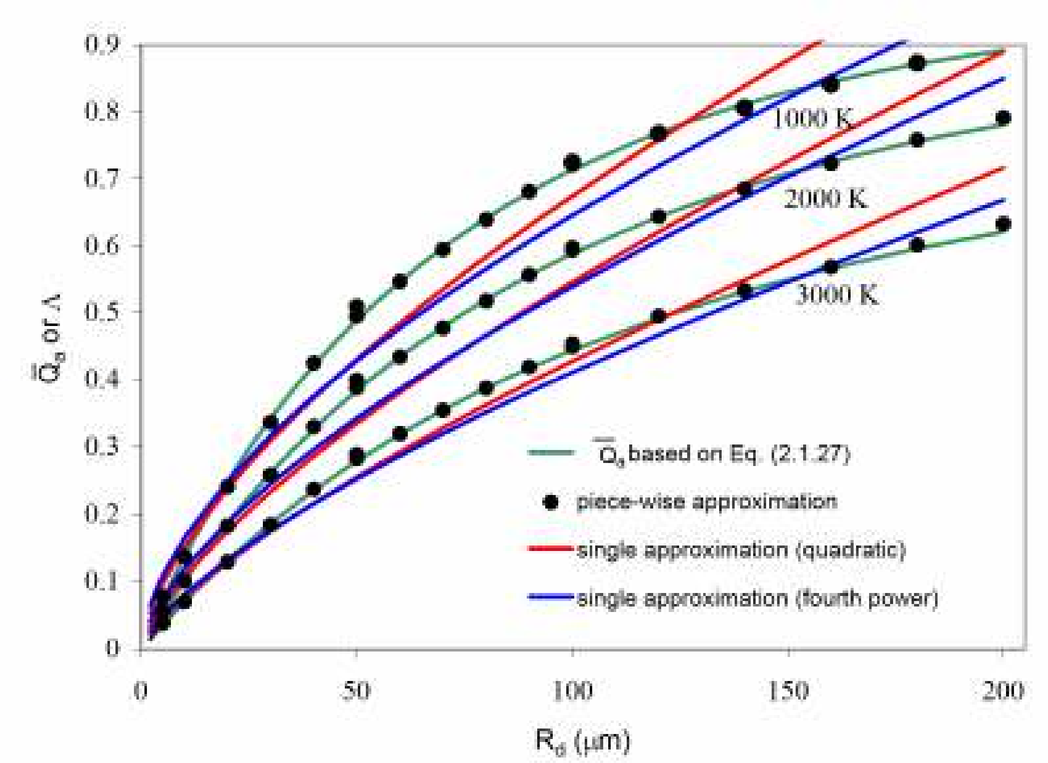

Figure 4.3.2 The same as Figure 4.4.1 but for gasoline fuel

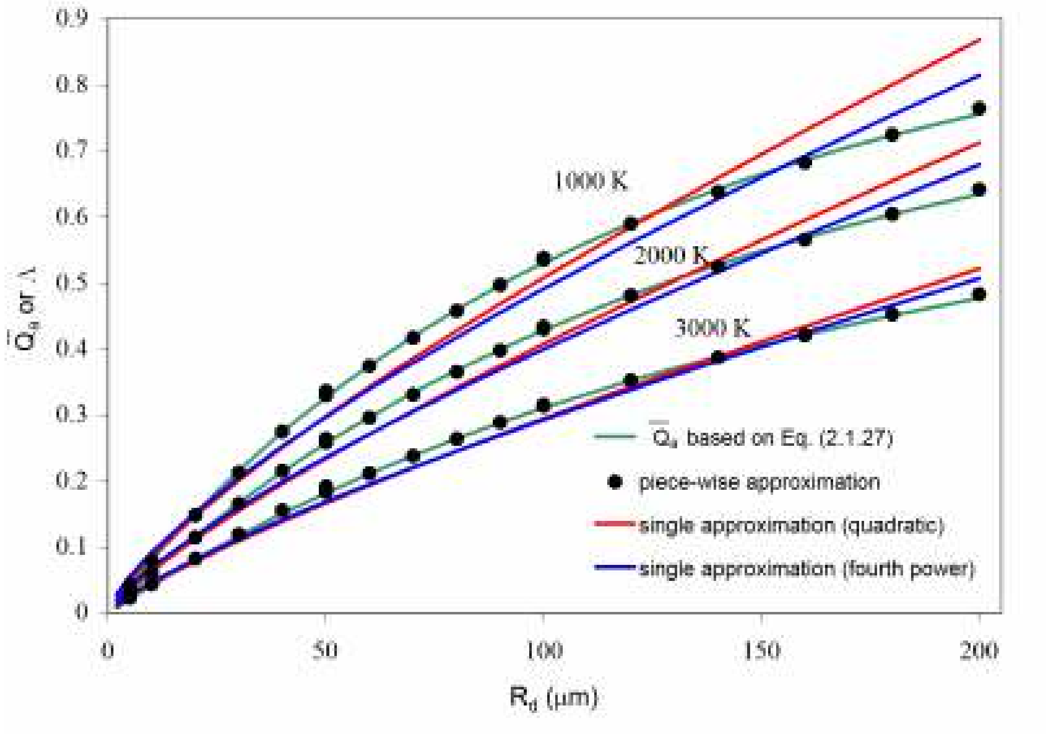

Figure 4.3.3 The same as Figure 4.3.1 but for iso-octane

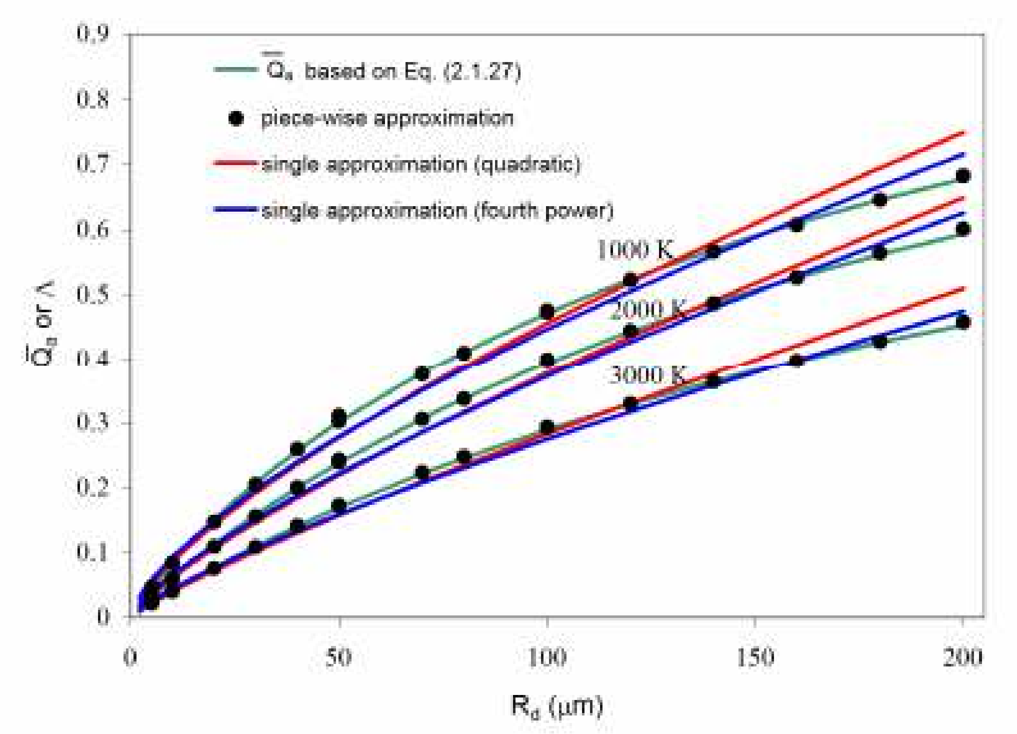

Figure 4.3.4 The same as Figure 4.3.1 but for 3-pentanone

4.4 Applications

To illustrate the effect of thermal radiation on Diesel fuel droplet heating and evaporation, the time evolution of radius and surface temperature of a droplet was considered. A droplet at room temperature (T_{d0} = 300 K) and with initial radius equal to 10 μm was injected into air with ambient temperature of 600 K and pressure of 3 MPa (Sazhin et. al., 2005b). The initial velocity of the droplet was taken to be 1 m/s. The overall volume of injected liquid fuel was taken as 1 mm^3. The volume of air, where the fuel was injected, was taken equal to 639 mm^3. This volume was calculated using the assumption that Diesel fuel can be approximated as n-dodecane ($C_{12}H_{26}$) and that the initial gas temperature is equal to 600 K. In this case, provided that all fuel is evaporated without combusting, the fuel vapour/air mixture is expected to become close to stoichiometric (Sazhin et al., 2006). The temperature dependence of all transport coefficients and density was taken into account. The relevant approximations are presented and discussed in Sazhin et al.

(2006). The droplet was irradiated homogeneously from all directions by external thermal radiation from a source at temperatures in the range from 1000 K to 3000 K.

This is a rather idealised case, as in Diesel engines the droplets are likely to be irradiated from one side only (Flynn et al., 1999) (a detailed mathematical analysis of this case is presented by Dombrovsky and Sazhin (2004)). To take into account the effect of asymmetrical irradiation of droplets, the actual power absorbed by droplets could be halved, compared with the case of homogeneous irradiation. Alternatively, this effect can be accounted for by the corresponding adjustment of the radiation temperature. The integral effect of symmetrical radiative heating of droplets by the source at temperature θ_R is approximately equivalent to the effect of asymmetrical droplet heating by a source at temperature $\theta_{R(eff)} = 2^{1/4}\theta_R = 1.19\theta_R$. As pointed out in (Sazhin et al., 2005a; Abramzon and Sazhin, 2005, 2006) the effect of non-homogeneous, but spherically symmetrical, distribution of the radiative heating inside a droplet is insignificant when the radiative heating of droplets takes place simultaneously with convective heating. We anticipate that this conclusion is valid in the case of asymmetrical droplet radiative heating.

The effect of thermal radiation was taken into account using the new model based on the piecewise approximation of the coefficients a and b in Equation (2.1.28) (see Table 4.1) for T_{ext} = 1000 K, 2000 K and 3000 K, and the model based on the single quadratic approximations of these coefficients (see Table 4.3) for T_{ext} = 3000 K. The predictions of the model based on the single fourth power approximations are expected to lie between the predictions of these two models. The liquid and gas phase models used in the analysis are summarised in Chapter 2. The solutions in both these phases are fully coupled (see Chapter 3).

The plots of T_s and R_d for Diesel fuel versus time with and without taking into account the effect of thermal radiation are shown in Figure 4.4.1. The droplet radius initially increases due to thermal expansion of liquid fuel, until the effect of evaporation dominates. In the case at T_{ext} =1000 K, the effect of thermal radiation on droplet evaporation is small. This effect visibly increases when the external temperature increases to 2000 K and 3000 K (the lifetime of a droplet becomes shorter). In the case without radiation, the droplet surface temperature monotonically increases until it reaches the wet bulb temperature. When the effect of thermal radiation is taken into account, the surface temperature reaches a maximum value before it reduces to the same wet bulb temperature. This effect was discussed in detail by Abramzon and Sazhin (2006).

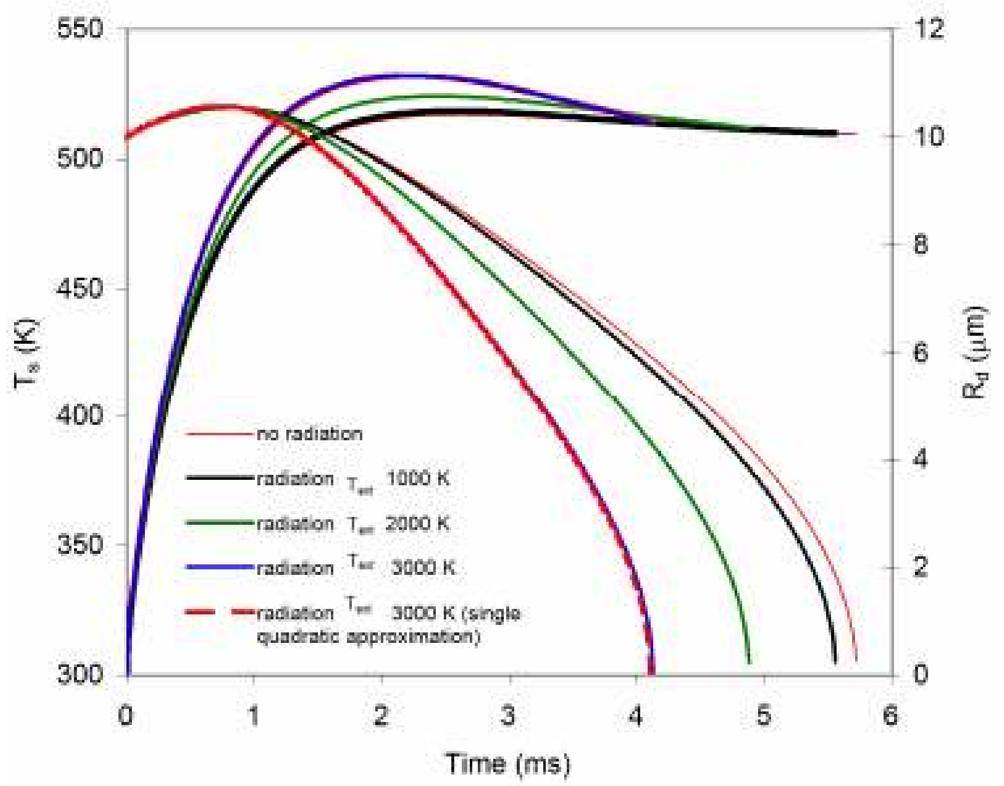

Figure 4.4.1 Plots of T_s and R_d for a Diesel fuel droplet versus time for an initial air temperature T_{g0} = 600 K, air pressure P_{g0} = 3 MPa, droplet initial temperature T_{d0} = 300 K, radius R_{d0}= 10 μm and velocity v_{d0} = 1 m/s. The overall volume of injected liquid fuel was taken equal to 1 mm^3, and the volume of air was equal to 639 mm^3. The results were obtained based on the effective thermal conductivity (ETC) model and the analytical solution of the heat conduction equation inside the droplet. Red solid curves refer to the case when effects of radiation are ignored. Black, green and blue solid curves refer to the case when thermal radiation is generated by a source with external temperatures 1000 K, 2000 K and 3000 K respectively and calculated using the model based upon a piecewise approximation of the coefficients *a* and *b* in Equation (2.1.28). Red dashed curves refer to the case when thermal radiation is generated by a source with external temperature of 3000 K and the model based on single quadratic approximation for these coefficients (Sazhin et. al., 2004a)

The plots calculated using the model based on the piecewise approximation of the coefficients *a* and *b* in Equation (2.1.28) and the model based on the single quadratic approximations of these coefficients are nearly coincident for $T_{\text{ext}} = 3000$ K. These curves are expected to be even closer for lower external temperatures. This happens despite the fact that the values of the average absorption efficiency factors predicted by these models are visibly different (see Figure 4.3.1). Thus, in many practical applications, including modelling of heating and evaporation of droplets, the high accuracy of the approximation of the average absorption efficiency factor, provided by the model based on a piecewise approximation of the coefficients *a* and *b*, is not always required. However, since the computer requirements of the implementation of this new model are all but the same as those of the model based on the single quadratic approximations of these coefficients, the application of the new model is recommended in all cases.

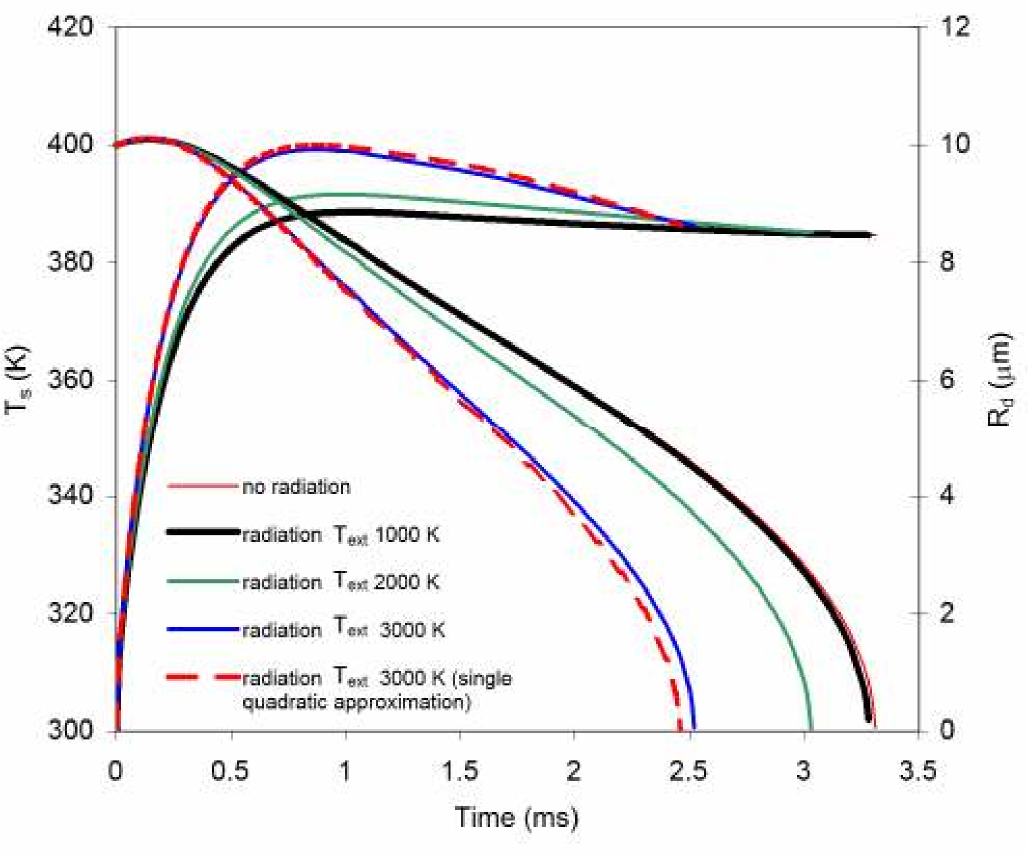

Figure 4.4.2 The same as Figure 4.4.1 but for gasoline fuel, injected into a gas volume equal to 620 mm^3

Plots similar to those shown in Figure 4.4.1, but for gasoline fuel are presented in Figure 4.4.2. The physical properties of the gasoline fuel used in our study are shown in Appendix 2. In contrast to Diesel fuel, gasoline fuel is injected into a gas volume of 620 mm^3. The volume was calculated under the assumption that gasoline fuel can be approximated as $C_{7.9}H_{17.8}$. In this case, provided that all gasoline fuel is evaporated without combusting, the fuel vapour/ air mixture is expected to become close to stoichiometric, as in the case of Diesel fuel. The general shapes of the curves shown in Figures 4.4.1 and 4.4.2 are rather similar, except that the difference between the curves calculated using the model based on the piecewise approximation of the coefficients *a* and *b* in Equation (2.1.28) and the model based on the single quadratic approximations of these coefficients, is more pronounced in the case of Figure 4.4.2 than Figure 4.4.1. This justifies the application of the new model in the case of gasoline.

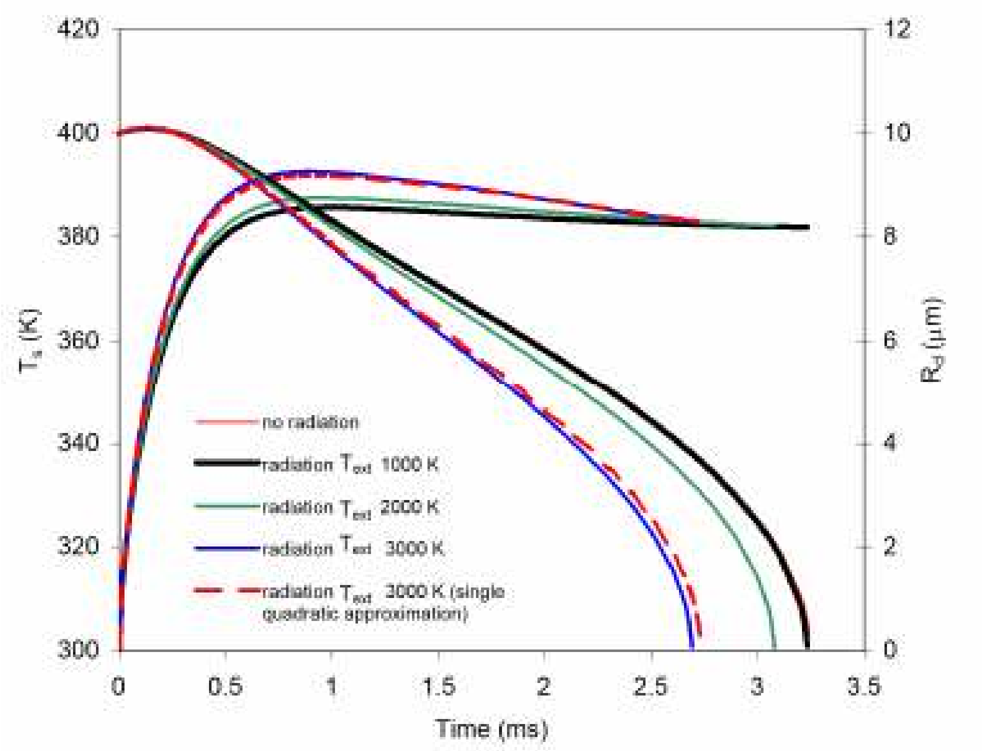

Figure 4.4.3 The same as Figure 4.4.1 but for iso-octane, injected into gas volume equal to 625 mm^3

The iso-octane and 3-pentanone cases are presented in Figures 4.4.3 and 4.4.4 respectively. The physical properties of iso-octane and 3-pentanone are shown in Appendix A. These fuels were injected into gas volumes of 625 mm^3 and 712 mm^3 respectively. Comparison of Figures 4.4.3 and 4.4.4, and Figures 4.4.1 and 4.4.2 shows that the effect of radiation on heating and evaporation of iso-octane and 3-pentanone is noticeably weaker than in the case of Diesel fuel and gasoline. This agrees with the results presented in Figures 4.3.1 - 4.3.4. Also, the choice of the approximation of the average absorption efficiency factor is more important for iso-octane than for 3-pentanone.

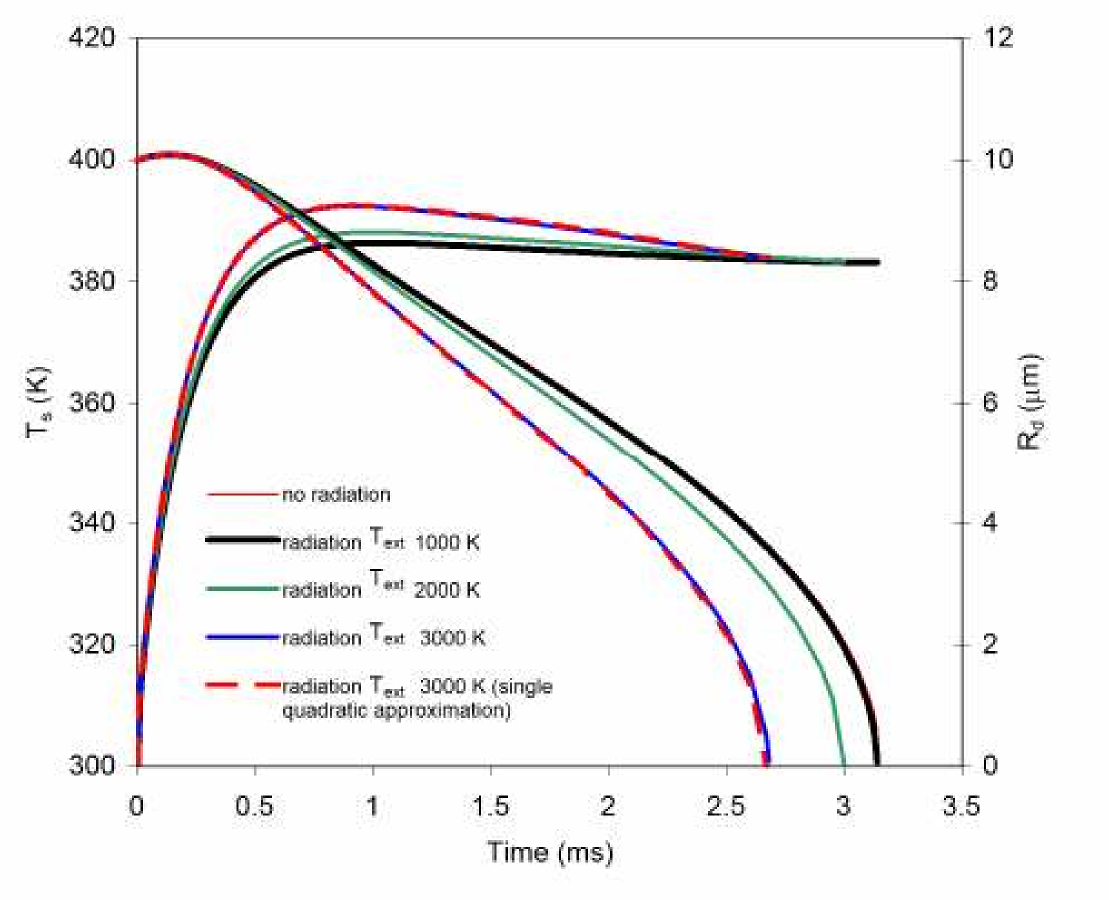

Figure 4.4.4 The same as Figure 4.4.1 but for 3-pentanone, injected into a gas volume equal to 712 mm^3

Returning to our problem of finding an approximation for the absorption efficiency factor we can say that the relatively weak dependence of droplet heating and evaporation on the accuracy of this approximation gives us an additional argument in favour of using an approximate formula (2.1.25) instead of the detailed Mie calculations of the distribution of thermal radiative absorption inside droplets. In contrast to the model described in this chapter, the implementation of the model, based on Mie calculations, into CFD codes would be infeasible.

4.5 Conclusions to Chapter 4

The values of absorption coefficients of gasoline fuel (BP Pump Grade 95 RON ULG), 2,2,4-trimethylpentane (iso-octane) and 3-pentanone have been measured experimentally in the range of wavelengths 0.2 μm – 4 μm. Ultraviolet – visible spectra (0.2 μm – 0.8 μm) have been obtained using a UV-Visible spectrophotometer Shimadzu, model 1601. In the range 0.4 μm – 4 μm the absorption coefficients have been measured using a Fourier transform infrared spectrometer (Nicolet FTIR Avatar). The values of the indices of absorption calculated based on these coefficients have been shown to be similar to those obtained earlier for low sulphur ESSO AF1313 Diesel fuel. For all fuels, the region of semi-transparency in the range 0.5 μm $< \lambda <$ 1 μm is illustrated. The index of absorption increases by approximately 3 orders of magnitude when λ increases from 0.5 μm to 1.5 μm. At the same time, noticeable differences between the indices of absorption of the fuels can be identified. For example, the peak of absorption of Diesel fuel at $\lambda \approx 3.4$ μm is much more pronounced than the corresponding peaks of absorption of other fuels. Also, the value of λ when this peak is observed is close to 3.4 μm for Diesel fuel, and close to approximately 3.0 μm for other fuels. The values of this index tend to be lower for pure substances (e.g. iso-octane and 3-pentanone) than for Diesel and gasoline fuels.

It has been shown that the main contribution to the average absorption efficiency factor is expected to come from radiation at wavelengths less than 4 μm for the range of external temperatures between 1000 K and 3000 K. The value of this factor has been approximated by a power function aR_{d}^{b}, where R_{d} is the droplet radius. Coefficients a and b are approximated by piecewise quadratic functions of the radiation temperature, with the coefficients calculated separately in the ranges of radii 2 µm – 5 µm, 5 µm – 50 µm, 50 µm – 100 µm and 100 µm – 200 µm for all fuels. This new approximation has been shown to be more accurate when compared with the case when a and b are approximated by quadratic functions or fourth power polynomials of the radiation temperature, with the coefficients calculated over the entire range 2 µm – 200 µm suggested by Sazhin et. al. (2004a). This difference in the approximations of a and b, however, have been shown to have little effect on the modelling of fuel droplet heating and evaporation in conditions typical for internal combustion engines, especially in the case of Diesel fuel and 3-pentanone.

5. MONODISPERSE DROPLETS HEATING AND EVAPORATION: EXPERIMENTAL STUDY AND MODELLING

So far our analysis has been focused on single isolated droplets. In practical situations, however, many droplets are present in a spray and the average distance between them can be less than a few droplet diameters. A typical droplet therefore will not behave as an isolated droplet, rather than as part of droplet arrays that take into account droplet to droplet interaction phenomena. These interaction phenomena are particularly important near the fuel injection devices, where the droplet concentration is high.

The importance of sprays in various engineering and environmental applications is well known (Sirignano, 1999). Heating, evaporation and combustion models for isolated droplets are widely available in the literature (for example, Sirignano, 1999; Abramzon and Sirignano, 1989; Michaelides, 2003; Sazhin, 2006). Although there are a number of publications where these processes in droplet clusters have been studied (for example, Dwyer et al., 2000; Harstad and Bellan, 2001), the present understanding of droplet-to-droplet interaction is still limited. These processes have been mainly studied based on simplified configurations. Although it is possible to construct full-scale experimental facilities that enable the control of injection and environmental conditions over wide range, it is often difficult to separate the relative influences of these parameters on the observed behaviour of a spray. These problems are not encountered for linearly streamed monodisperse droplets. The size, velocity, temperature and spacing of the droplets can be adjusted separately at the injection, where the ambient conditions can be controlled (Frohn and Roth, 2000). This kind of droplet stream is therefore an interesting tool for investigating droplet-to-droplet interactions and it has already been used in previous numerical and experimental studies.

Sangiovanni and Kesten (1976) were perhaps the first to investigate the effects of droplet interaction on the ignition time for droplet streams injected into a hot gas environment. They noticed that a closer spacing of the droplets enhances the strength of the heat and mass diffusion from the flame region. Sangiovanni and Labowsky (1982) reported measurements of the droplet lifetime under similar conditions. They found that the classical "D^2-Law" is not strictly applicable to interacting droplets due to the transient nature of that interaction. Brzustowski et al. (1979) studied the combustion of two motionless droplets of arbitrary size by solving the Laplace equation for vapour concentration. They quantified the reduction in the burning rate when droplets approach one another, almost to come into contact. Labowsky (1980) and Marberry et al. (1984) used the point sources method to determine the burning rates of stagnant droplets in finite arrays containing up to eight symmetrically arranged monodisperse droplets. Later, the effect of droplet motion was taken into account by Chiang and Sirignano (1993a,b) who performed a comprehensive numerical study of two and three evaporating droplets moving together. Their computation included: the effects of variable thermophysical properties; transient heating and internal circulation in the liquid phase; boundary-layer blowing; moving interfaces due to surface regression; and the relative motion between droplets.

More recently, two experimental studies of droplet interactions in monodisperse streams were reported by Castanet et al. (2002, 2005). The two-colour laser induced fluorescence technique was used by the authors to measure droplet temperature. This technique was combined with the measurement of droplet sizes using either Phase Doppler Anemometry or interferometry on light scattered by the droplets in a forward direction. Knowledge of the size, velocity and temperature of the droplets enabled the authors to estimate the heat fluxes acting on the evaporating droplets. Results were obtained for a relatively large set of data corresponding to droplets moving into a flame or within the thermal boundary layer of a vertical heated plate. The distance parameter, defined as the droplet spacing divided by the droplet diameter, was increased up to almost 20 by removing electrically charged droplets with an applied electrostatic field. For the case of combusting droplets, the authors suggested a correction factor that should be applied to the Nusselt and Sherwood numbers for isolated droplets to take onto account interaction between them. This correction is a function of the distance parameter. For distance parameters larger than 9, the interaction effects were shown to be negligible.

In the present chapter, the results of further experimental and numerical studies of the dynamic heating and evaporation of fuel droplet arrays are reported. The measurements were performed for two different conditions: heating and evaporation of droplets in a hot air flow of given temperature and heating and evaporation in a flame. Ethanol and acetone fuels were chosen for the experimental study since these fuels have rather different volatilities. The space-averaged temperature of the droplets was measured using the two-colour laser induced fluorescence technique. For meaningful comparisons between simulations and measurements, the comparative sizes of the droplets and the measurement volume were taken into account. When the droplets were larger than the probe volume of the optics, the probe was unable to detect the whole of the fluorescence signal produced by a single droplet; this introduced a bias to the calculation of average temperature.

In the first set of experiments, the ambient gas temperature was measured by a K-type thermocouple. In the case of heating and evaporation of fuel droplets in a flame produced by previously injected droplets, this parameter is deduced from measurements performed by CARS thermometry (Coherent Anti-stokes Raman Scattering). This technique, which is based on pioneering investigations by Druet and Taran (1981), has received considerable attention from those studying combustion during the last two decades.

The model used for the analysis of experimental data is essentially based on the one originally developed by Abramzon and Sirignano (1989) and further adapted for numerical simulation of droplet heating and evaporation, taking into account the effect of thermal radiation (see Chapters 2 - 4). The recirculation inside droplets is considered via the introduction of the effective thermal conductivity of droplets (effective thermal conductivity (ETC) model). In the gas phase, the model takes into account the effect of finite thickness of the thermal boundary layer around droplets (Model 4). The radiative heating of droplets is calculated taking into account their semi-transparency. This model has been further developed to capture the effect of the finite distance parameter, introduced earlier in this section.

The experimental set-up is described in Section 5.1. In Section 5.2, the numerical model used in the analysis is discussed. In Section 5.3, experimental and numerical results are compared and discussed. The main results of this chapter are summarised in Section 5.4.

5.1 Experimental setup

5.1.1 The monodispersed droplet stream

The experimental were conducted at Laboratoire D'energetique et de Macanique Theorique et Appliquee (LEMTA), ENSEM, France. Linear monodisperse droplet streams were generated by Rayleigh disintegration of a liquid jet undergoing vibrations which were obtained by a piezoceramic actuator (Castanet et. al., 2002, 2005). The voltage applied to the piezoceramic is a square wave, the amplitude of which determines the position of the break-up zone for a given fuel at a given temperature. The fuel is pre-heated in the injector body by means of an external heated water circulation. The temperature of the fuel is measured exactly at the injection point with a K type thermocouple. For specific frequencies of the forced mechanical vibrations, the liquid jet breaks up into equally spaced and monosized droplets (Frohn, 2000). By adjusting the liquid flow rate and the piezoceramic frequency, it is possible to increase the droplet spacing up to about 6 times the droplet diameter. This, however, is accompanied by a modification of droplet sizes.

A device, enabling the electrostatic deviation of the droplets, has been used to increase further the droplets spacing without changing the droplet diameter (Castanet et al., 2002). This device, called deviator, is mounted at the injector exit. When droplets pass through the ring (positioned just at the break-up location of the cylindrical jet), they are negatively charged by electrical impulses transmitted by the ring. The frequency of the impulses can be controlled in such a way that only a fraction of the droplets acquire charges. Afterwards, a high intensity electrostatic field is applied to droplets when they enter the gap between the two electrodes. The charged droplets are deviated from their vertical trajectory and picked up, whereas the remaining droplets form a stream with increased spacing.

Two liquids were tested: ethanol and acetone, which have significantly different volatilities. To investigate pure evaporation, droplets are injected in a hot co-flowing air stream, released from two electrical heaters, arranged symmetrically relative to the droplet streaming axis (Maqua et al., 2006). The air velocity, as measured by Laser Doppler Anemometry (LDA), was about 2 m/s in the vicinity of the droplet injection point (Figure 5.1.1c). The air temperature field, measured by a thermocouple, decreased from 550°C at the injection point to about 100°C at z=60 mm (Figure 5.1.1a,b).

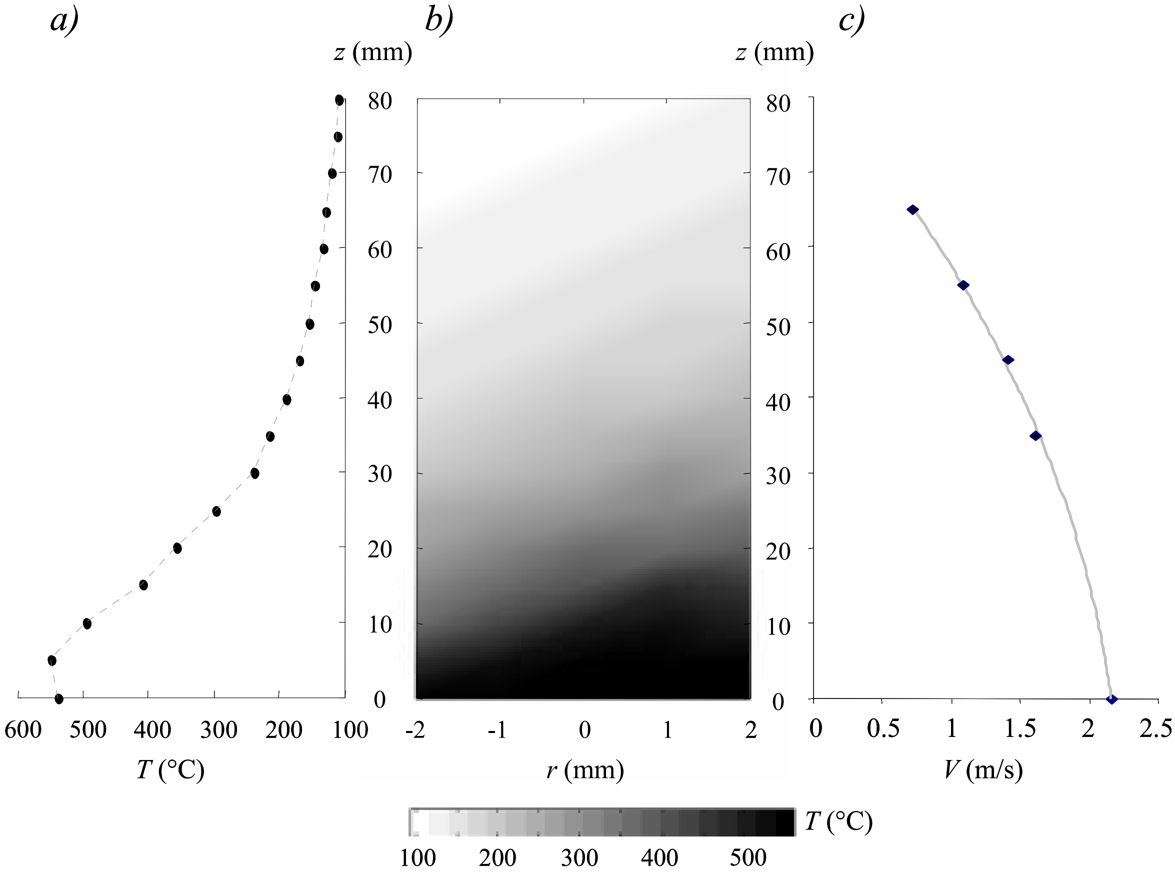

Figure 5.1.1 Temperature and air velocity in the hot air plume (a: profile of the temperature along the z-axis at r = 0, b: spatial distribution of the temperature within the air plume and c: profile of the gas velocity along the z-axis at r = 0)

To study droplets heating and evaporation in a flame, an electrically heated coil is positioned just after the break-up zone of the liquid jet and a laminar flame with a column shape is obtained (Castanet et al., 2005). The temperature field within the flame was characterized by CARS. The outlines of these measurements will be presented in the following section.

5.1.2 Measurement of the gas temperature in the flame by CARS thermometry

A detailed description of CARS theory, including the derivation of expressions for the signal intensity and description of numerous technical approaches in practical measurement systems is described in numerous textbooks and papers (for example, Eckbreth, 1996; Grisch et al., 2004). In what follows, a brief overview of this technique is given. CARS is a four wave parametric process in which three waves, two at the pump frequency (ω_P) and one at the Stokes frequency (ω_S) are focused to the measurement point in the sample to produce a new coherent beam at the anti-Stokes frequency ($\omega_{AS}=2\omega_P - \omega_S$). The strength of the interaction depends on the nonlinear third-order susceptibility of the medium, which is greatly enhanced when the frequency difference ($\omega_P - \omega_S$) matches a Raman active vibrational resonance in the medium. The nonlinear susceptibility is density and temperature-dependent providing the basis of diagnostics. Measurements of medium properties are performed from the shape of the spectral signatures and/or intensity of the CARS radiation. Temperature information is based on the fact that the intensity distributions of the transitions in a CARS spectrum are relative to the populations of the rotational and vibrational levels of the studied molecules and consequently, the thermodynamic temperature of the system. The collisional line-broadening parameters used to analyze the N_2 spectra in the whole temperature range were taken from the modified energy gap law of Bonamy et al. (1977). The CARS system consists of an optical bench which simultaneously produces the pump and Stokes beams.

The laser beams are focused on the monodispersed droplet flame by means of a single 160 mm-focal-length achromat yielding a 0.5 mm-long and 30 μm-diameter probe volume. For each location in the flame, 400 single-shot N_2 CARS spectra were recorded for the temperature determination. For each single-shot measurement, the experimental CARS spectrum was fitted, using a least-square minimisation routine, to theoretical spectra simulated using the CARS modelling described above. Typically, the accuracy of temperature measurements, which were found to be sensitive to collisonal narrowing and nitrogen linewidths, is equal to 5 %, i.e. ± 15 K at room temperature and then decreases progressively to 2 % at 1700 K (i.e. ± 30 K). Figure 5.1.2 shows a typical radial profile of the temperature within a flame surrounding pure ethanol droplets. The droplet diameter is symbolised by *D* and distance from the stream axis is symbolised by *r*. The flame front can be clearly seen since it corresponds to a maximum of about 2000 K.

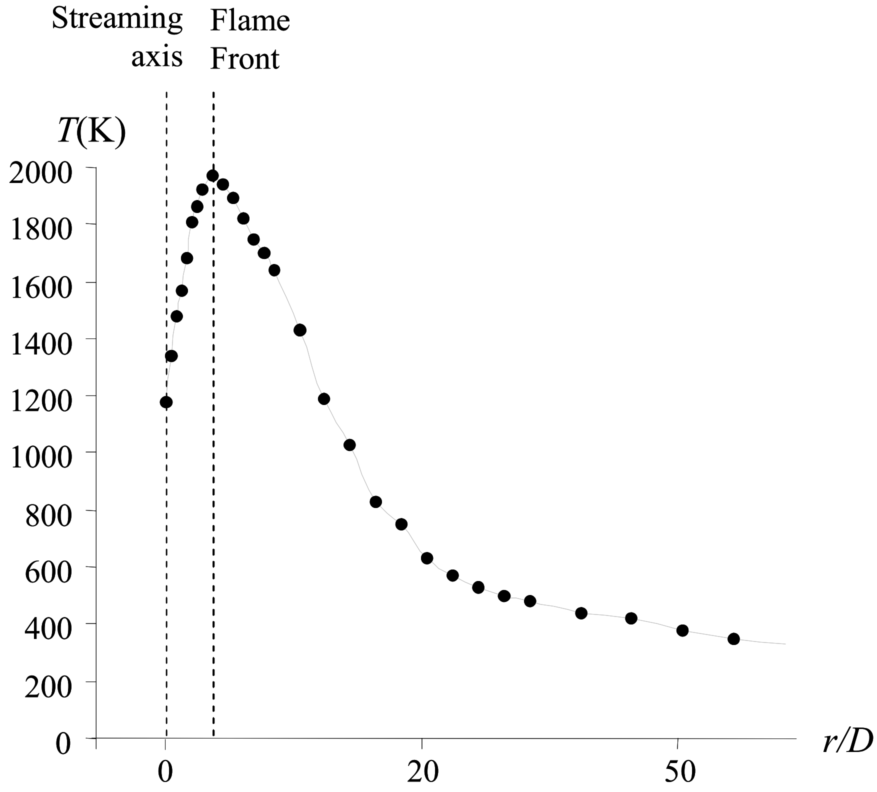

Figure 5.1.2 Radial profile of the gas temperature in the flame

When dealing with combusting droplets, the ambient temperature, used to estimate the convective heat transfers, is taken on the flame axis where the moving droplets are mainly located. The effects of the distance parameter (*C*) (that defined as ratio of the distance between droplets and their diameters) on the flame temperature were investigated in detail with the help of this technique. Data referring to four droplet streams with different droplet spacing are shown in Figure 5.1.3 for a time 3.2 ms after droplets left the injector and for droplet diameters of about 200 μm. It can be noticed that the temperature on the flame axis and at the flame front increase slightly with the initial distance parameter.

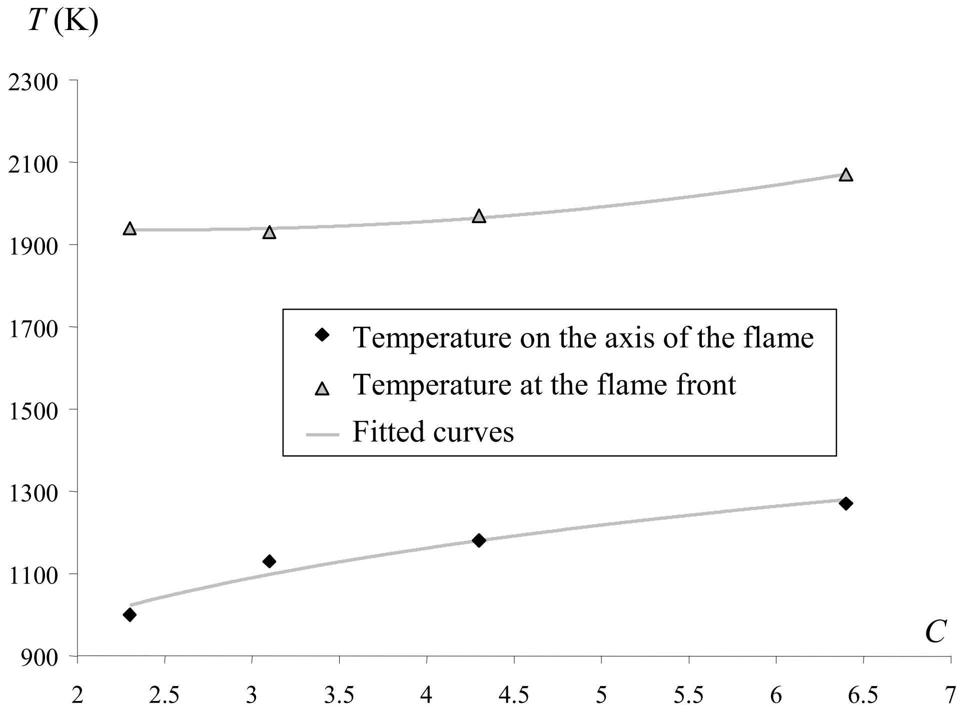

Figure 5.1.3 Temperature in the flame as a function of the distance parameter

5.1.3 Velocity and size measurements

Phase Doppler Anemometry (PDA) in the refraction mode was used to measure droplet velocities and diameters at various distances from the injector. The main problem with the size measurements arises from the trajectory ambiguity. When the droplet size is of the order or larger than the laser beam, the Doppler signal may be altered by unwanted scattering modes which may lead to an error of measurements. The risk of error is very high in the case of linear monodispersed droplet streams since the trajectory of the droplets is very stable and the droplets are rather large compared to the width of the laser beam in the probe volume. To reduce as much as possible the trajectory effects, the position of the stream axis in the probe volume can be adjusted so that the contribution of the refractive mode is strengthened compared to the reflection mode in the direction of the receiving optics. A calibration of the PDA is required to achieve accurate size measurements. Both the positioning of the droplet streams and the calibration process were performed as described by Castanet et al. (2005). The discrepancy is about 1µm for droplet diameters around 100µm. The droplet velocity is measured concomitantly by processing the Doppler frequency of the bursts at ± 1%. Size measurements are performed only for combusting droplets, since the size reduction of droplets evaporating within the hot air plume is too small to be captured with a sufficient accuracy by this technique.

5.1.4 Two-colour laser induced fluorescence thermometry

Only the main outlines of the two-colour laser-induced fluorescence technique are described in this section. Further technical details can be found in Lavieille et al. (2001, 2002). The fuel is seeded with a low concentration (a few mg/l) of rhodamine B, which is an organic dye usually used as a fluorescent temperature sensor. Furthermore, the fluorescence of rhodamine B can be easily induced by the green line (λ=514.5 nm) of the argon ion laser. The technique requires two spectral bands of detection with highly different temperature sensitivities. The ratio of the fluorescence signal measured on the two spectral bands of detection appears to be only temperature dependent and the dependencies in tracer concentration, probe volume dimensions, laser intensity and optical layout are totally removed Lavieille et al. (2001). If the probe volume is sufficiently large to provide a global excitation of all the droplet volume and if the signal is averaged for the entire droplet transit in the probe volume, a volume averaged droplet temperature can be obtained. The two crossing laser beams of the PDA system are also used to induce the fluorescence.

The emitted photons are collected by a doublet located at 90 degrees to the incident beams and the optical signal is transmitted to an optical fibre. The incident laser light scattered by the droplets is removed by means of a high-pass optical filter to enable the collection of the fluorescence emission only. The remaining fluorescence is separated in the two spectral bands by means of interference filters. Finally, the photon flux is converted into an electrical signal by photomultiplier tubes.

The layout of this setup, however, differs slightly depending on whether the experiment is focused on combusting or purely evaporating droplets. For combusting droplets, the PDA is used concomitantly to perform size and velocity measurements. To avoid the ambiguity effects described in Section 5.1.3, a relatively large probe volume is formed, the dimensions of which are 4000 μm along the laser beam axis and 243 μm for the transverse dimension. In the case of the droplets that evaporate in the hot air plume, the probe volume is smaller, i.e. 1200 μm long and 150 μm large since only the droplet velocity is measured. Regarding the collection optics, in the focus plane of the collection front lens, the image of the core of the optical fibre extends roughly over 200 μm (this image is however slightly reduced in the presence of a droplet within the probe due to the refraction processes at the air-liquid interface).

Regions located near the droplet surface may have a rather limited contribution to the fluorescence signal depending on the optical arrangement, the size and the trajectory of the droplets. This comes essentially from the Gaussian distribution of the energy in the laser beams and the refraction at the droplet surface as explained in Maqua et al. (2006). This effect can safely be ignored in the case of droplets significantly smaller than the probe volume. Regarding the probe volume size in the case of the purely evaporating droplets, this implies that the measured temperature is more likely to be close to the temperature at the droplet centre instead of the volume averaged temperature when the droplet diameter becomes larger than 150μm.

Note that the droplet detection is based on the initial determination of the thresholds for each spectral band (Lavieille et al., 2001). Each threshold is fixed at high level, so that only the droplets well centred within the probe volume contribute to the temperature measurement. Multiple measurements carried out at the same location show a ± 1 K dispersion of the averaged temperature.

5.2 Model

The heating and evaporation models discussed in Chapters 2, 3 and Chapter 4 have been used in this analysis. Namely on the liquid phase, the model based on the analytical solution of heat conduction equation (see Equation 2.1.22) have been used. The recirculation inside droplets is considered via the introduction of the effective thermal conductivity of droplets (ETC model). In the gas phase, the model takes into account the effect of finite thickness of the thermal boundary layer around droplets (Model 4) (see Equations 2.2.50 and 2.2.51 on Chapter 2).

The radiative heating of droplets is calculated considering the semi-transparency of droplets. The main obstacle in doing this, however, is that the spectra of ethanol and acetone are not known to us. To estimate possible contribution of thermal radiation, the ethanol and acetone droplets were considered with iso-octane radiative properties. It was shown that the predicted temperatures and pressures in the presence and absence of thermal radiation differ by not more than about 2% in most case, even if the radiation temperature was assumed to be equal to the maximal temperature in the flame (this is true only when gas is totally transparent to thermal radiation). Since this error can be tolerated in our analysis, we believe that the effect of thermal radiation can be ignored as the first step in the modelling of the process.

This model has been further developed to capture the effect of finite distance parameter. In the case of droplet streams, Castanet et al. (2002) suggested the following correction to take into account the finite distance parameter C (ratio of the distance between droplets and their diameters)

$$\frac{Nu}{Nu_{iso}}=\frac{Sh}{Sh_{iso}}=\eta\left(C\right), \tag{5.2.1}$$

where

$\eta\left(C\right)=\tanh\left(0.36C-0.82\right)$ and $C>3$.

Hence the Nusselt number and Sherwood number can be written as:

$$Sh=2\eta(C)\frac{\ln(1+B_{\mathrm{M}})}{B_{\mathrm{M}}}\left[1+\frac{(1+Sc_{\mathrm{d}}\,Re_{\mathrm{d}})^{1/3}f(Re)-1}{2F(B_{\mathrm{M}})}\right] \tag{5.2.2}$$

$$Nu=2\eta(C)\frac{\ln(1+B_{\mathrm{T}})}{B_{\mathrm{T}}}\left[1+\frac{(1+Pr_{\mathrm{d}}\,Re_{\mathrm{d}})^{1/3}f(Re)-1}{2F(B_{\mathrm{T}})}\right]. \tag{5.2.3}$$

To evaluate the Reynolds number Re_{d} in calculation of Sherwood number and Nusselt number, the droplet velocity relative to the gas is required. Although the droplet deceleration could have been modelled, the droplet velocity was fixed to its experimental value in the simulation. This choice enabled us to avoid errors due to the estimation of the droplet drag coefficients and to focus exclusively on heating and evaporation processes. All transport coefficients for air, alongside with its density and specific heat capacity were calculated similarly to Sazhin et al. (2006) (see Appendix C). Temperature dependence of all physical properties of air was taken into account. For the comparison with experimental data the following temperatures will be used: temperature at the surface of the droplet T_{s}, temperature at the centre of the droplet T_{c}, and the average droplet temperature.

5.3 Results

As mentioned in the introduction, the comparison between experimental data and predictions of the model will be performed for two cases: droplet heating and evaporating in air flow with prescribed temperatures, and their heating and evaporation in a flame produced by combustion of the previously injected droplets. These will be discussed separately in the following subsections. The measurements of the droplet velocities and the hot air temperature on the droplet axis are used as inputs in our simulations. In contrast to Chapters 3 and 4, the physical properties of fuel were evaluated based on temperature not normalized temperature due to lower operation temperature.

5.3.1 Droplet heating and evaporation in a hot air flow

In the first experiment, ethanol droplets with initial radii 65 μm, initial temperature 298.75 K and the initial distance parameter C = 6.72 were considered. The time dependence of the droplet velocity (m/s) and droplet temperature (^{o}C) were measured experimentally and the result were approximated by the following correlations:

$$v_d(m/s) = 0.0024t^3 - 0.0268t^2 - 0.1940t + 8.5744 \tag{5.3.1}$$

$$T(°C) = 0.0361t^4 - 1.3536t^3 + 20.905t^2 - 160.6t + 631.62 \tag{5.3.2}$$

Based on Equations (5.2.2)-(5.2.3) and (5.3.1)-(5.3.2), the Nusselt and Sherwood numbers were calculated. The values of droplet radii calculated at the previous time step were used to calculate these numbers. Then the droplet radii and temperatures were calculated as described in Section 5.2.

The measured and calculated values of droplet temperatures versus time elapsed from droplet injection are shown in Figure 5.3.1. In the same figure, the time dependence of gas temperature at droplet locations is shown. The predicted values of droplet radii are not shown, as they were not measured in our experiment. As follows from this figure, temperatures at the surface and centre of the droplets, and droplet average temperatures differ considerably one from another, especially at the initial stage of droplet heating and evaporation.

The best agreement with experimental data is observed for the droplet average temperatures up to 2 ms. The maximum droplet temperature, observed experimentally and predicted by the model, is related to a decrease in gas temperature. In this case, after about 2.5 ms, droplet cooling due to evaporation has a greater effect than droplet heating by the surrounding gas. This effect is not related to maximum droplet temperature during the evaporation due to the contribution of thermal radiation (see Abramzon and Sazhin, 2005, 2006 for the details). The model clearly overestimates the measurements in the case of ethanol droplets: the observed deviations between the experimental results and the predictions of the model can reach 4 K and can be attributed to a number of experimental factors, including random motions of the droplets, especially when the distance from the nozzle increases.

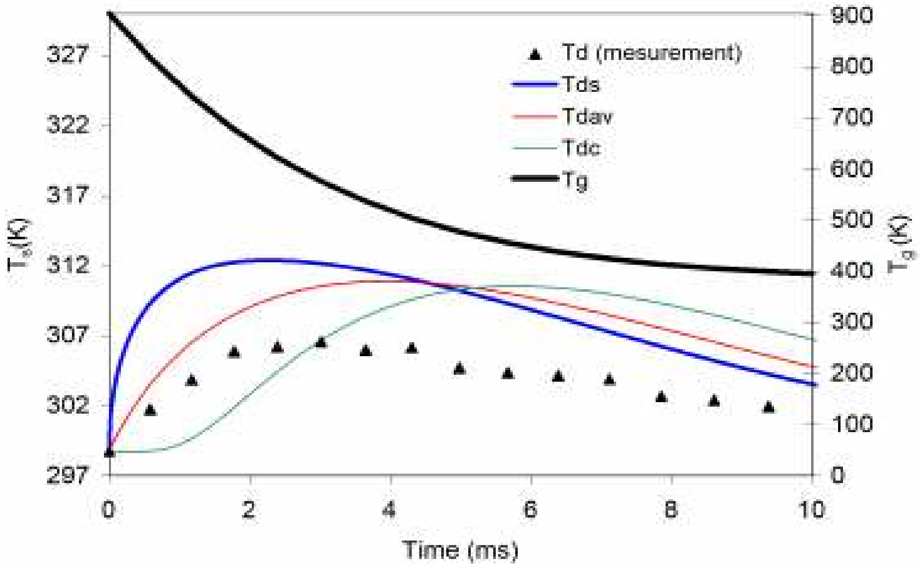

Figure 5.3.1 Plot of ethanol droplet temperature T_d, measured experimentally (solid triangles) and predicted by the model (T_{ds} droplet temperatures at the surface of the droplet, T_{dav} average droplet temperature, and T_{dc} droplet temperature at the centre of the droplet) and gas temperature T_g for the initial conditions R_{do}= 65 µm, T_{do}=298.75 K, C=6.72

In the second experiment, ethanol droplets with initial radii 118.65 µm, initial temperature 294 K and initial distance parameter C=3.97 were considered. The time dependence of the ambient gas temperature was described by Equation (5.3.4) (Note the dependencies of the ambient gas temperatures on z are identical for experiments 1 and 2, but their dependencies on t vary due to different droplet velocities). The observed time dependence of droplet relative velocities has been approximated by Equation (5.3.3).

$$v_d(m/s) = 0.00294t^2 - 0.1383t + 9.154 \qquad (5.3.3)$$

$$T(^oC) = 0.0264t^4 - 1.2121t^3 + 21.113t^2 - 167.75t + 630.86 \qquad (5.3.4)$$

The Nusselt and Sherwood numbers were calculated similarly to the first experiment. The plots referring to the second experiment are shown in Figure 5.3.2. As in the case of Figure 5.3.1, temperatures at the surface and centre of the droplets, and droplet average temperatures differ considerably from one another, especially at the initial stage of droplet heating and evaporation.

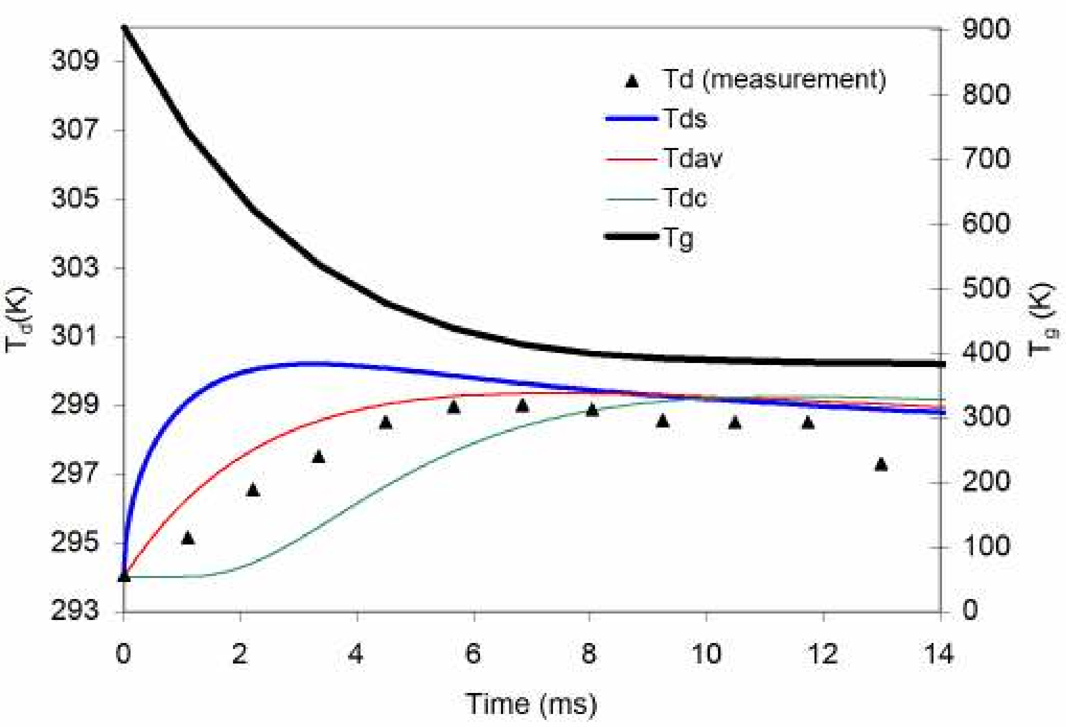

Figure 5.3.2 Plot of ethanol droplet temperature T_d, measured experimentally (solid triangles) and predicted by the model (T_{ds} droplet temperatures at the surface of the droplet, T_{dav} average droplet temperature, and T_{dc} droplet temperature at the centre of the droplet) and gas temperature T_g for the initial conditions R_{do}= 118.65 μm, T_{do}=294 K, C=3.97

The best agreement with experimental data in the case shown in Figure 5.3.2 is observed not for droplet average temperature but for the temperature between the average temperature and the temperature at the centre of the droplet. This can be related to the fact that the measurement volume in this case is noticeably less than the droplet volume. As in the case shown in Figure 5.3.1, the maximum droplet temperature, observed experimentally and predicted by the model is related to a decrease in gas temperature. This maximum for the second experiment is observed at later times (about 6 ms).

In the third experiment, acetone droplets with initial radii 63.2 μm, initial temperature 300 K and the initial distance parameter C=7.56 were considered. The approximations of the observed time dependence of the droplet relative velocities and ambient gas temperature are given by Equations (5.3.5)-(5.3.6). In the fourth experiment, acetone droplets with initial radii 116.2 μm, initial temperature 296 K and the initial distance parameter C=3.52 were considered (see Equations (5.3.7) and (5.3.8) for the time dependence of the relative droplet velocity and the ambient gas temperature).

$$v_{\mathrm{d}}(m/s) = 0.0004701t^3 - 0.014067t^2 - 0.18347t + 9.7742 \tag{5.3.5}$$

$$T(^oC) = 0.0597t^4 - 1.9605t^3 + 26.634t^2 - 180.4t + 631.08 \tag{5.3.6}$$

$$v_{\mathrm{d}}(m/s) = 0.0001461t^2 - 0.05631t + 8.561. \tag{5.3.7}$$

$$T(^oC) = 0.0207t^4 - 1.0108t^3 + 18.779t^2 - 158.7t + 631. \tag{5.3.8}$$

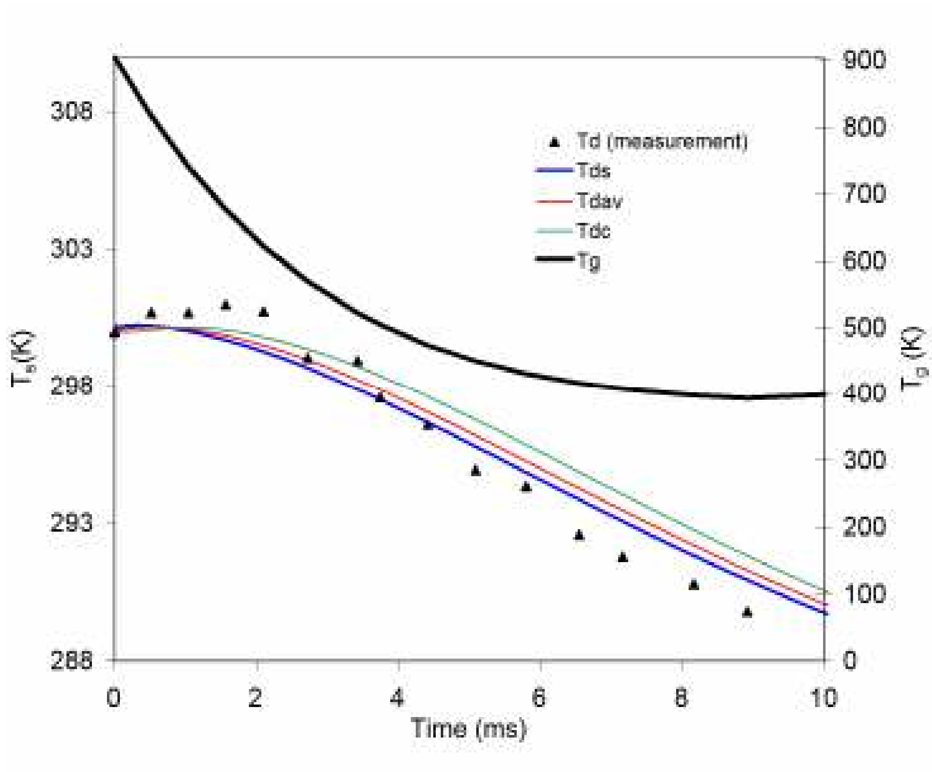

Figure 5.3.3 Plot of acetone droplet temperature T_d, measured experimentally (solid triangles) and predicted by the model (T_{ds} droplet temperatures at the surface of the droplet, T_{dav} average droplet temperature, and T_{dc} droplet temperature at the centre of the droplet) and gas temperature T_g for the initial conditions R_{do}= 63.2 μm, T_{do}=300 K, C=7.56

The plots similar to those shown in Figures 5.3.1 and 5.3.2, but for the third and fourth experiments, are shown in Figures 5.3.3 and 5.3.4 respectively. In contrast to the case of heating and evaporation of ethanol droplets, the initial heating of acetone droplets is hardly visible, while the temperature drop of acetone droplets is much more pronounced than in the case of ethanol droplets. This can be attributed to higher volatility of acetone compared with ethanol. The initial heating of acetone droplets is almost completely compensated by their cooling due to evaporation. In the case shown in Figure 5.3.3, the predicted temperatures at the centre and the surface of the droplets and the droplet average temperature turned out to be rather close.

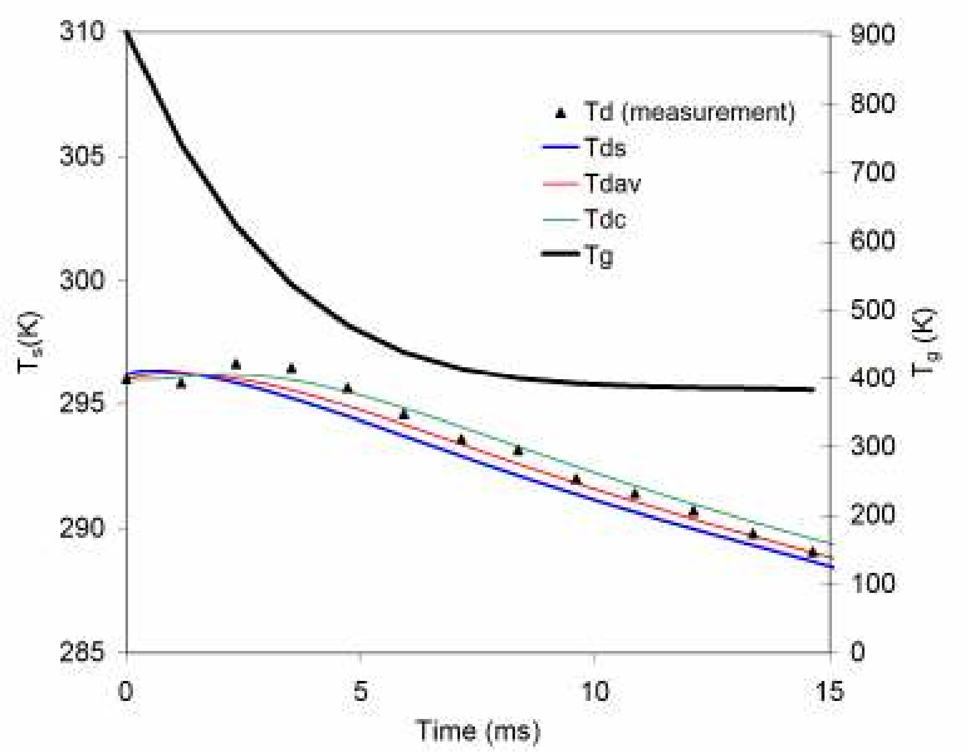

Figure 5.3.4 Plot of acetone droplet temperature T_d, measured experimentally (solid triangles) and predicted by the model (T_{ds} droplet temperatures at the surface of the droplet, T_{dav} average droplet temperature, and T_{dc} droplet temperature at the centre of the droplet) and gas temperature T_g for the initial conditions R_{do}= 116.2 μm, T_{do}=296 K, C=3.52

The best agreement with experimental data can be seen for the droplet average temperature, as in the case shown in Figure 5.3.1. In the case shown in Figure 5.3.4, the best agreement with experimental data can be observed for the temperature at the centre of the droplets.

5.3.2 Droplet heating and evaporation inside a flame

The experiments focused on heating and evaporation of droplets injected into a flame produced by previously injected combusting droplets allow us to investigate these processes in a much wider range of temperature. Also, in these experiments, the time evolution of droplet radii was measured. The values of both droplet temperatures and radii will be compared with the predictions of the model described in Section 5.2. In contrast to the cases considered in Section 5.3.1, however, only the measurements of the average gas temperature at a single location of the droplets could be performed in the case of the experiments discussed in this section. The ambient temperature is assumed to be constant and its value is obtained from Figure 5.1.3 for the given initial distance parameter *C*. As in the cases considered in Section 5.3.1, droplet velocities were not calculated, but measured.

In the first experiment, ethanol droplets with initial radii 52.25 μm, initial temperatures 309 K and the initial distance parameter *C*= 3.4 were considered. The average gas temperature at the location of the droplets was 1140 K. and the droplet velocity evolves as described by:

$$v_d(m/s) = -0.0021t^3 + 0.0332t^2 - 0.3221t + 6.9956 \qquad (5.3.9)$$

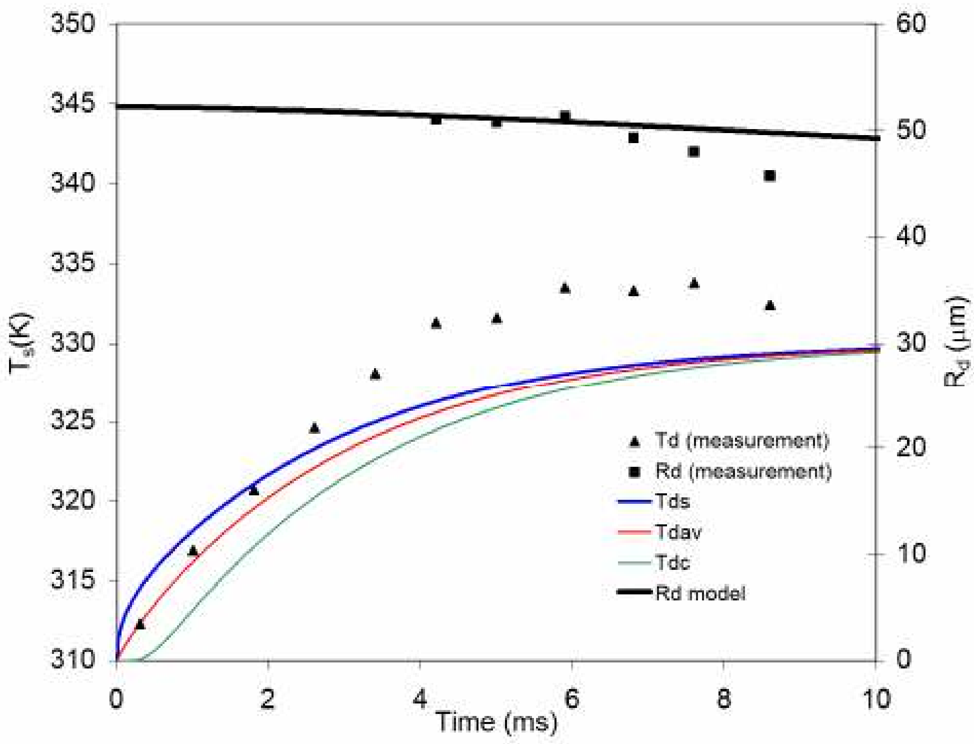

Figure 5.3.5 Plot of ethanol droplet temperature T_d radius R_d, measured experimentally (solid triangles and squares) and predicted by the model (T_{ds} droplet temperatures at the surface of the droplet, T_{dav} average droplet temperature, and T_{dc} droplet temperature at the centre of the droplet) and droplet radii R_d for gas average temperature T_g equal to 1140 K for the initial conditions R_{do}= 52.25 μm, T_{do}=309 K, *C*=3.4

The measured and calculated values of droplet radii and temperatures (at the centre and the surface of the droplet, and average droplet temperature) versus time are shown in Figure 5.3.5. As in the cases shown in Figures 5.3.1 and 5.3.3, the best agreement with experimental data is observed for the droplet average temperatures.

The agreement between the results of modelling and experimental results both for droplet temperatures and radii seems to be reasonably good, although it is marginally worse in the cases shown in Figure 5.3.5 than in the cases considered in Section 5.3.1.

In the second and the third experiments, ethanol droplets with the same initial radii and temperatures as in the first experiment, but with the initial distance parameters C=6.0 and C=10.5, respectively, gas temperatures 1260 K and 1270 K respectively, and the droplet velocities were considered as Equations (5.3.10) and (5.3.11) respectively.

$$v_d(m/s) = -0.0052t^3 + 0.0943t^2 - 0.7238t + 6.9138 \tag{5.3.10}$$

$$v_d(m/s) = 0.005t^3 + 0.1145t^2 - 0.9830t + 6.8877 \tag{5.3.11}$$

The measured and calculated values of droplet radii and temperatures (at the centre and the surface of the droplet, and average droplet temperature) versus time for these experiments are shown in Figures 5.3.6 and 5.3.7 respectively. As in the cases shown in Figure 5.3.5, the best agreement with experimental data is observed for the droplet average temperatures.

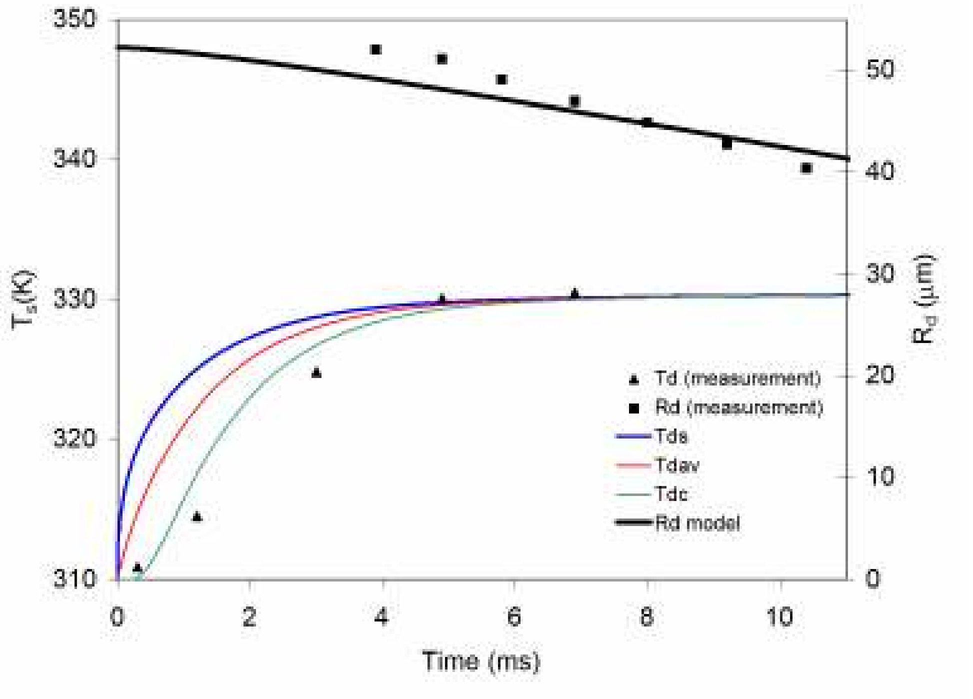

Figure 5.3.6 The same as Figure 5.3.5 but for gas average temperature T_g equal to 1260 K for the initial conditions R_{do}= 52.25 μm, T_{do}=309 K, C=6.0

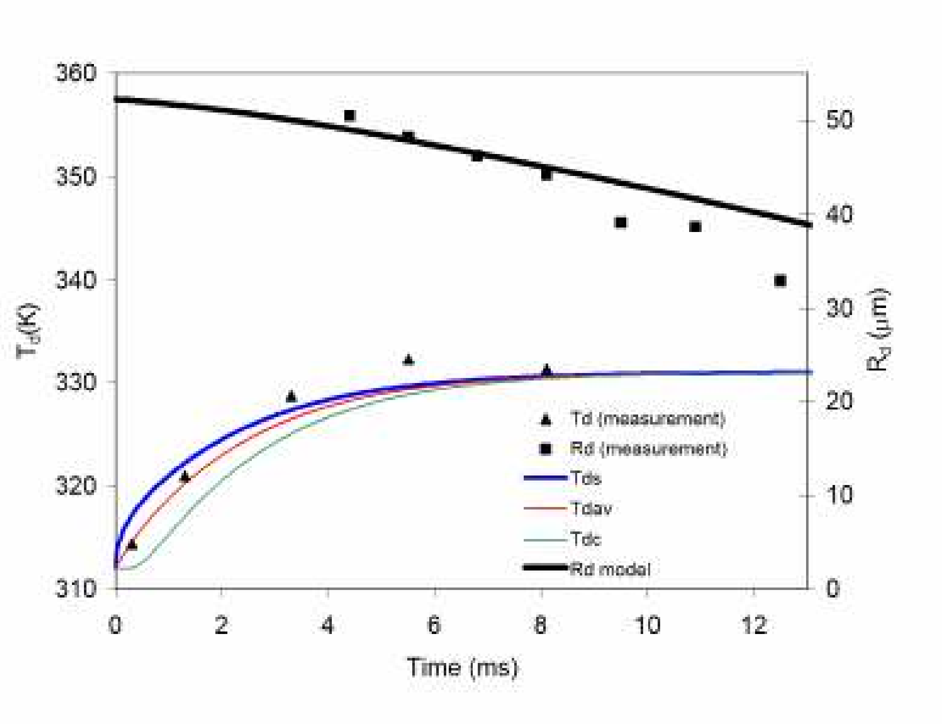

Figure 5.3.7 The same as Figure 5.3.5 but for gas average temperature T_g equal to 1270 K and for the initial conditions R_{do}= 52.25 μm, T_{do}=309 K, C=10.5

In the fourth experiments, ethanol droplets with the initial radii 55.2 μm and temperatures 312 K was considered. In this experiments initial distance parameters C=4.4, gas temperatures 1150 K, and the droplet velocities considered as Equation (5.3.12) were used. The measured and calculated values of droplet radii and temperatures versus time for these experiments are shown in Figure 5.3.8.

$$v_d(m/s) = -0.0022t^3 + 0.0175t^2 - 0.1078t + 6.7633 \qquad (5.3.12)$$

In the fifth experiments, ethanol droplets with the initial radii 54 μm and temperatures 318 K was considered. In this experiments initial distance parameters C= 4.0, gas temperatures 1150 K, and the droplet velocities considered as Equation (5.3.13) were used. The measured and calculated values of droplet radii and temperatures versus time for these experiments are shown in Figure 5.3.9.

$$v_d(m/s) = -0.0022t^3 - 0.0333t^2 + 0.0515t + 4.4892 \qquad (5.3.13)$$

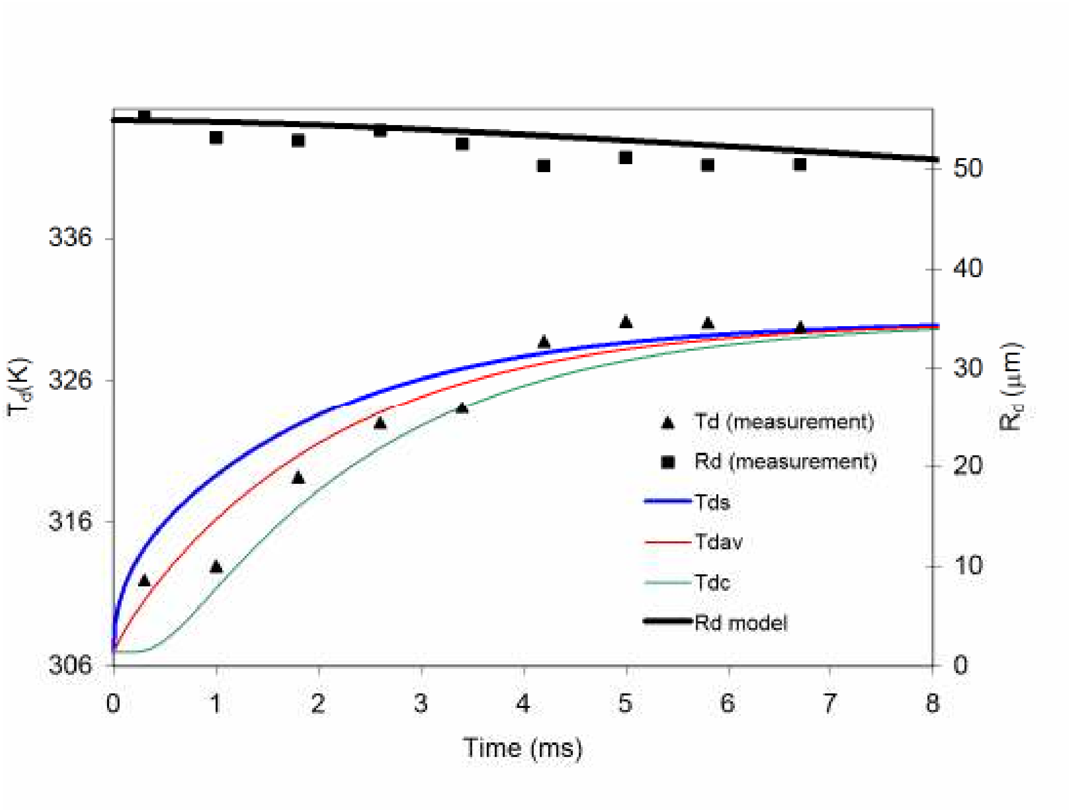

Figure 5.3.8 The same as Figure 5.3.5 but for gas average temperature T_g equal to 1150 K and for the initial conditions R_{do}= 55.2 µm, T_{do}=312 K, C=4.4

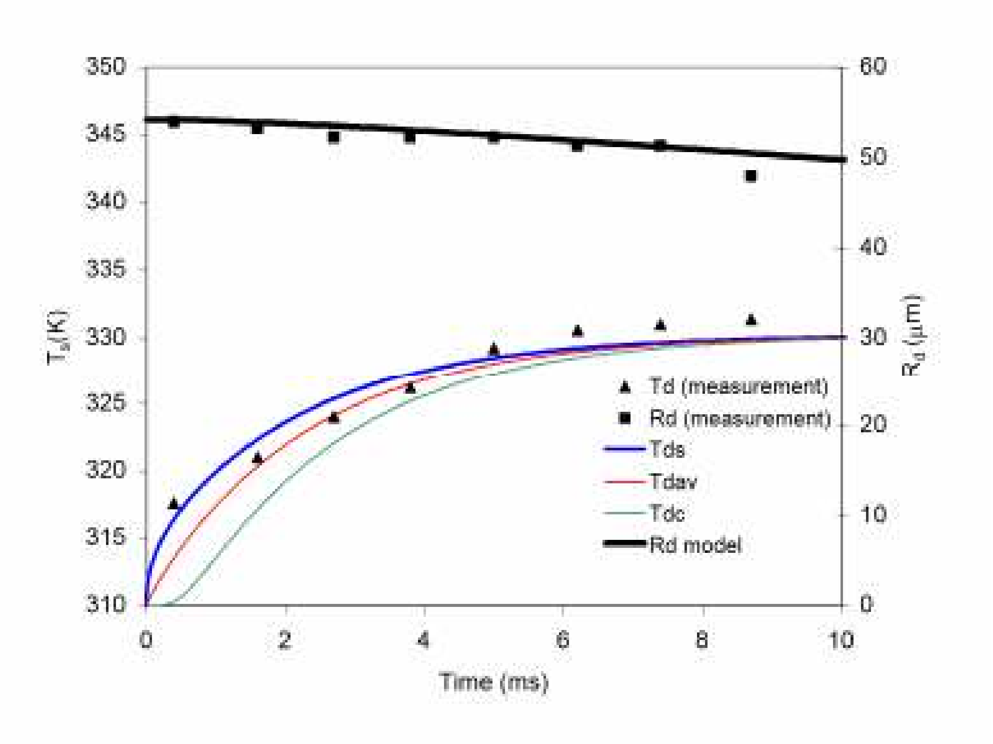

Figure 5.3.9 The same as Figure 5.3.5 but for gas average temperature T_g equal to 1150 K and for the initial conditions R_{do} = 54.0 µm, T_{do} =318 K, C=4

5.4 Conclusions to Chapter 5

Heating and evaporation of monodisperse ethanol and acetone droplets has been studied in two regimes: pure heating and evaporation of droplets in a flow of air of prescribed temperature, and droplet heating and evaporation in flame produced by previously injected combusting droplets. Two colour laser induced fluorescence thermometry has been used for the estimate of droplet temperatures, while their sizes and velocities have been characterized by Phase Doppler Anemometry. In the flames, CARS technique has made it possible to estimate the gas temperature. The experiments have been performed for various distances between droplets and various initial droplet radii and velocities. The experimental data have been compared with the results of modelling, based on given gas temperatures, and Nusselt and Sherwood numbers calculated using measured values of droplet relative velocities. When estimating the latter numbers the finite distance between droplets was taken into account. The model has been based on the assumption that droplets are spherically symmetric with a radial distribution of temperature inside droplets is taken into account. This model considers the recirculation inside droplets via the introduction of the effective thermal conductivity of droplets (effective thermal conductivity model). In the gas phase, it takes into account the effect of finite thickness of the thermal boundary layer around droplets. The radiative heating of droplets has been calculated taking into account the semi-transparency of droplets. The radiative effects, however, have been shown to be small and ignored in most of the analysis. It has been pointed out that for relatively small droplets (initial radii about 65 μm) the experimentally measured droplet temperatures are close to the predicted average droplet temperatures, while they are closer to the temperatures predicted at the centre of the droplets when the droplet diameter becomes larger than the probe volume size of the two-colour LIF thermometry.

6. THE IMPLEMENTATION OF THE NEW MODELS INTO THE KIVA-2 CFD CODE

The effects of temperature gradient inside droplets, described by the ETC liquid phase model based on the analytical solution of the heat conduction Equation (2.1.5), on the heating, evaporation and ignition of Diesel fuel droplets were discussed in Chapter 3. This analysis was based on the zero dimensional code that takes into account the coupling between liquid and gas phases, droplet breakup and uses the Shell autoignition model. In this code all values of gas parameters (velocity, temperature, fuel vapour concentration) were assumed to be homogeneous.

This chapter is focused on the implementation of the ETC model and the new gas model (Model 4) into the KIVA-2 CFD code and application of this code to study the effects of the liquid and gas models of droplet heating and evaporation on Diesel engine processes. These models are coupled with breakup, collision/coalescence, turbulence and autoignition models. The turbulence and collision/coalescence models, used in the original KIVA-2 CFD code, were not changed. We used three breakup models: TAB model, originally used in KIVA-2, the conventional and modified WAVE models. The autoignition was modelled using the Shell autoignition model. The results of calculations are compared with in house experimental data.

A brief description of the experimental results is presented in Section 6.1. In Section 6.2 the spray model implemented earlier in the KIVA-2 code is briefly described. The implementation of the ETC model and gas phase Model 4 into KIVA-2 are described in Section 6.3. In Section 6.4 the results of calculations using the new customised version of the KIVA-2 CFD code and the comparison of these results with experimental data are discussed. The main results of this chapter are summarised in Section 6.5.

6.1 Experimental setup

High speed Diesel sprays have been studied experimentally at University of Brighton using various optical diagnostic techniques (Crua, 2002). These studies were conducted in a rapid compression machine based on a single cylinder Ricardo Proteus test engine which was converted to two-stroke cycle. The engine had a bore of 135 mm, a stroke of 150 mm and a displacement of 2.2 litres. The Proteus rig was coupled to a DC dynamometer via reduction belts (6:1). An optical chamber 80 mm in length and 50 mm in diameter was fitted on the cylinder head to investigate the spray development. This allowed a fuel spray to be injected vertically without any impingement on the walls or the windows. A second generation Bosch common rail fuel injection system was used to generate the high pressure required to maintain injection pressure ranging from 60 to 160 MPa. The fuel pump was driven externally via an electrical motor running at 1400 rpm to maintain the required high pressure in the fuel rail with minimum fluctuation (Crua, 2002).

The main parameters which were studied using this setup were spray penetration and autoignition delay. To investigate the spray visualisation a Kodak Ektapro HS Motion Analyser was used, with a recording rate adjustable up to 4500 frames per second at maximum resolution. The processing of the video images for measurement of the spray penetration was performed by purpose-developed software. Suitable pixel thresholding was carried out in order to pick out the unbroken portion of the spay outline, furthest from the nozzle on the spray axis. The maximum spray penetration was calculated by finding the spray pixel furthest from the nozzle (Crua, 2002).

In order to record the autoignition processes, two high-speed CCD video cameras were placed at 90^o to each other. The cameras had a resolution of 128x64 pixels x 256 grey levels, with a sensitivity equivalent to 3,000 ISO and recording speed up to 27000 frames per second. Both cameras were triggered by the same dedicated signal emitted by the custom-built FIE controller. In order to further maximise the sensitivity of the recordings, the lens was set to its widest aperture (f/1.9). The time at which the first fuel droplets were seen leaving the nozzle was measured to be 0.37 ms after the start of the recording for an injection pressure of 160 MPa. The data were adjusted to compensate for this delay. This method was supplemented by in-cylinder pressure trace measurement. Both methods were used simultaneously in order to assess the complementary nature of both techniques (Crua, 2002).

The test cases chosen for the analysis were based on the measurements of sprays under realistic conditions of operation for a light-duty Diesel engine with a single-hole injector of 0.2 mm in diameter, located on the axis at the top centre of a cylindrical combustion chamber. The fuel injection pressure was 160 MPa, the monitored in-cylinder pressures at top dead centre (TDC) were 5.6, 6.2, and 6.9 MPa. The rate of injection was measured as a function of time using a Lucas rate tube. The ignition delay time was defined as the time from the start of injection to the first appearance of a visible flame on the video recordings (Crua, 2002).

At the start of injection, the gas pressure was assumed to be equal to experimentally measured pressure at TDC, while the temperature was estimated based on the intake gas pressure and temperature, and the air compression ratio. The polytropic law was used with the polytropic coefficient calculated based on the plots log p versus log V for each individual pressure at TDC (Lacoste, 2005). The comparison was performed for initial gas pressures in the range from about 2.5 to 8.5 MPa. The values of temperature for various pressures, obtained using this method are indicated as filled circles in Figure 6.4.4. The solid lines on the same figure were used for the estimate of temperature at other pressures, including those in the test cases. The values of temperature, calculated using this procedure are shown in Table 6.1. The errors of calculations were estimated to be about ±50 K. The values of autoignition delay time, defined as the time from the start of injection to the first appearance of a visible flame on the video recordings (Crua, 2002) are presented in Table 6.1.

In-cylinder pressure (MPa)	Temperature (K)	Autoignition delay time (ms)
5.6	832	2.37
6.2	847	2.04
6.9	852	1.78

Table 6.1 The values of the measured autoignition delay times and calculated initial in-cylinder gas temperatures for various in-cylinder pressure.

6.2 Spray models in the KIVA-2 CFD code

6.2.1 Droplet breakup models

6.2.1.1 TAB model

The Taylor Analogy Breakup (TAB) model is based on the analogy between an oscillating and distorting droplet and a spring mass system (O'Rourke and Amsden, 1987). In this model the droplet motion is governed by a linier differential equation for a forced, damped harmonic oscillator. The external force is analogues to the aerodynamic force; the spring restoring force is related to the liquid surface tension and the damping force corresponds to the liquid viscosity force. Droplet breakup is thus due to the amplification of droplet deformation caused by vibrational resonance of the surface. The governing equation of such a system is based on the forced harmonic oscillator equation:

$$m\ddot{x} = F - kx - d\dot{x} \tag{6.2.1}$$

where:

$$\frac{F}{m} = C_F \frac{\rho_g \left(\mathrm{v_d} - \mathrm{v_g}\right)^2}{\rho_l R_d},$$

$$\frac{k}{m} = C_k \frac{\sigma_s}{\rho_l R_d^3}, \tag{6.2.2}$$

$$\frac{d}{m} = C_d \frac{\mu_l}{\rho_l R_d^2},$$

ρ_g and ρ_l are the gas and liquid densities, $\left(\mathrm{v_d} - \mathrm{v_g}\right)$ is the relative velocity between the gas and droplet, R_d is the droplet radius, σ_s is the gas-liquid surface tension coefficient and μ_l is the liquid viscosity. C_F, C_k and C_d are dimensionless constants. Introducing non-dimensional parameter $y = 2x/R_d$ and substituting Equation (6.2.2) into Equation (6.2.1) gives:

$$\ddot{y} = 2C_F \frac{\rho_g}{\rho_l} \frac{\left(\mathrm{v_d} - \mathrm{v_g}\right)^2}{R_d^2} - \frac{C_k \sigma_l}{\rho_l R_d^3} y - \frac{C_d \mu_l}{\rho_l R_d^2} \dot{y}, \tag{6.2.3}$$

with breakup occurring if, and only if, $y > 1$ ($y_{cr} = 1$).

For constant ($\mathrm{v_d}$-$\mathrm{v_g}$) the solution of Equation (6.2.3) can be written as (O'Rourke, 1987):

$$y(t) = \frac{2C_F}{C_k}We + e^{-t/t_d}\left[\left(y(0) - \frac{2C_F}{C_k}We\right)\cos\omega t + \frac{1}{\omega}\left(\dot{y}(0) + \frac{y(0) - \frac{2C_F}{C_k}We}{t_d}\right)\sin\omega t\right] \tag{6.2.4}$$

where $We = \rho_g u^2 R_d/\sigma$ is the Weber number, $\frac{1}{t_d} = C_d \frac{\mu_l}{2\rho_l R_d^2}$, $\omega^2 = C_k \frac{\sigma}{\rho_l R_d^3} - \frac{1}{t_d^2}$ is the square of the oscillation frequency.

For each droplet, firstly We, t_d and ω^2 are calculated. If $\omega^2 \le 0$ Equation (6.2.4) does not describe oscillatory processes. This occurs only for very small droplets. If $\omega^2 > 0$, the amplitude A of the un-damped oscillation is calculated as (O'Rourke, 1987):

$$A^2 = \left(y^n - \frac{2C_F}{C_k}We\right)^2 + \left(\frac{\dot{y}^n}{\omega}\right)^2 \tag{6.2.5}$$

where superscript n refers to the time step.

If $\frac{2C_F}{C_k}We + A \le 1$, then according to Equation (6.2.4), the value of y will never exceed unity and breakup will not occur. If $\frac{2C_F}{C_k}We + A > 1$ the updated values of y and $\dot{y}$ are obtained for the next time step using Equation (6.2.4). In the later case, breakup is possible and breakup time t_{bu} is calculated as the smallest root greater than t^n of the equation:

$$\frac{2C_F}{C_k}We + A\cos\left[\omega\left(t - t^n\right) + \phi\right] = 1, \tag{6.2.6}$$

where $\cos\phi = \frac{\left(y^n - \frac{2C_F}{C_k}We\right)}{A}$ and $\sin\phi = \frac{-\dot{y}^n}{(A\omega)}$

If time t^n+1 is less than t_{bu} the no breakup occurs on the current time step, and y and $\dot{y}$ are obtained for the next time step using Equation (6.2.4).

The dimensionless terms C_F, C_k and C_d need to be adjusted to reproduce the experimental data. O'Rourke and Amsden (1987) suggested that the values of C_F, C_k and C_d are 1/3, 8 and 5 respectively.

6.2.1.2 Conventional WAVE model

The model is based on the first-order theory of stability analysis (Kelvin-Helmholtz instability) of a stationary, round liquid jet immersed into a quiescent and incompressible gas (Reitz, 1987). The theory considers a cylindrical liquid jet issuing from a circular orifice of radius a into a stationary, incompressible infinitely large gas medium. The atomisation is the result of aerodynamic interaction between the liquid and gas that induces unstable wave growth on the liquid jet surface.

The model determines how and when droplets breakup by calculating the wavelength of the fastest growing disturbances on the surface of a liquid jet due to aerodynamic instabilities. The model assumes that aerodynamic forces at a liquid-gas interface and the resulting surface waves are responsible for atomisation. The rate of change of the droplet radius and the resulting child droplet size are related to the frequency (Ω) and wavelength (Λ) of the fastest growing surface wave, determined by the following expressions:

$$\Lambda = \frac{9.02 R_\mathrm{d}\left(1+0.45\sqrt{Z}\right)\left(1+0.4T^{0.7}\right)}{\left(1+0.865We^{1.67}\right)^{0.6}} \tag{6.2.7}$$

$$\Omega = \frac{0.34+0.385We^{1.5}}{\left(1+Z\right)\left(1+1.4T^{0.6}\right)}\sqrt{\frac{\sigma}{\rho_1 R_\mathrm{d}^3}} \tag{6.2.8}$$

where We is Weber number for gas. The Ohnesorge number Z is defined as $Z=\sqrt{We_1/Re_1}$ where Re_1 is liquid Reynolds number, We_1 is the liquid Weber number which is similar to We, except that liquid density is used to replace gas density in We. The Taylor number T is defined as $T = Z\sqrt{We}$.

In the conventional WAVE model a new droplet with radius of equilibrium R_{eq} is eventually formed from a parent droplet with radius R_d. R_{eq} is defined by the following equation (Reitz, 1987):

$$R_{eq} = \begin{cases} B_o\Lambda, & B_o\Lambda \le R_{\mathrm{d}} \\ \min\begin{pmatrix} \left(3\pi R_{\mathrm{d}}^2 \left|\mathrm{v}_{\mathrm{d}} - \mathrm{v}_{\mathrm{g}}\right| / 2\Omega\right)^{0.33} \\ \left(3R_{\mathrm{d}}^2\Lambda/4\right)^{0.33} \end{pmatrix}, & B_o\Lambda > R_{\mathrm{d}}, \end{cases} \tag{6.2.9}$$

where $B_{\mathrm{o}} = 0.61$ is the model constant. The rate of change of droplet radius in a parent parcel due to droplet breakup is described using the following expression (Reitz, 1987):

$$\frac{dR}{dt} = -\frac{R_{\mathrm{d}} - R_{eq}}{\tau_{bu}}, \tag{6.2.10}$$

where

$$\tau_{bu} = 3.726 B_1 \frac{R_{\mathrm{d}}}{\Lambda\Omega} \tag{6.2.11}$$

is the characteristic breakup time. The breakup time constant B_1 is the model constant depending on the injector characteristics and is assumed to be related to initial disturbance levels originating within the injector nozzle. Reitz (1987) used B_1=10 based on the results of measurements of quasi-steady-state Diesel spray penetration at relatively low injection pressure (Hiroyasu and Kadota, 1974).

Patterson and Reitz (1998) developed this model further in order to account for the effect of the Rayleigh-Taylor (RT) instability of droplets. When the wave length corresponding to the maximum increment of this instability

$$\Lambda_{RT} = 2\pi\sqrt{\frac{3\sigma}{a\rho_1}}, \tag{6.2.12}$$

is less than the diameter of a droplet, the bag breakup of the droplet is expected to take place. In this case R_{eq} was calculated as $R_{eq} = C_{RT}\Lambda_{RT}$, where $C_{RT} = 2.5$ is the model constant (Patterson and Reitz, 1998). The breakup time was estimated as:

$$\tau_{bu(RT)} = \sqrt{\frac{3}{2a}\sqrt{\frac{3\sigma}{a\rho_1}}}, \tag{6.2.13}$$

where $a = \frac{3}{8} C_D \frac{\rho_g \left|\mathrm{v}_{\mathrm{d}} - \mathrm{v}_{\mathrm{g}}\right|^2}{\rho_1 R_{\mathrm{d}}}$ is the deceleration of the droplet due to the drag force.

6.2.1.3 Modified WAVE model

A modified WAVE breakup model was suggested by Martynov et al. (2007). This model takes into account the effect of injection acceleration. This effect was accounted for by modifying the expression for B_1 based on the following expression (Martynov et al., 2007):

$$B_1 = B_{1,st} + c_1 \left(a^+\right)^{c_2}, \tag{6.2.14}$$

where $a^+ = \sqrt{Re} \dfrac{D}{U_{inj}^2} \dfrac{dU_{inj}}{dt}$ is the parameter taking into account the effect of flow acceleration, c_1 and c_2 are adjustable constants. In the steady-state limit a^+ is zero and $B_1 = B_{1,st}$. Following Reitz (1987), it was assumed that $B_{1,st} = 10$. The values of c_1 and c_2 were obtained by curve fitting. Martynov et al. (2007) recommended the following values $c_1=0.6$ and $c_2=0.2$. This modified WAVE model was shown to be more accurate than the conventional WAVE model especially at the initial stage of injection where acceleration effects need to be taken into account.

6.2.2 Heating and evaporation models

6.2.2.1 Spalding model

In the original KIVA-2 CFD code a classic droplet heating and evaporation model, the so called Spalding model, is used (Spalding, 1971). This model is based on the following simplifying assumptions: the gas boundary layer is assumed to be quasi-steady; the droplet is assumed to be spherical; thermal radiation is neglected; air and fuel vapour are assumed to behave as ideal gases; vapour/liquid phases are in equilibrium at the fuel surface; the 1/3 rule is used for gas properties; and both circulation and temperature gradient inside the droplets are neglected (Spalding, 1971).

The energy balance for the droplet is presented as:

$$\frac{4}{3}\pi R_{\mathrm{d}}^3 \rho_1 c_1 \frac{dT}{dt} - 4\pi R_{\mathrm{d}}^2 \dot{R}_{\mathrm{d}} \rho_1 L = 4\pi R_{\mathrm{d}}^2 Q_1, \tag{6.2.15}$$

where Q_1 is the convective heat flux to the surface of the droplet (W/m^2). It is calculated based on the Ranz-Marshall correlation (Faeth, 1977):

$$Q_1 = Nu \frac{k_{\mathrm{air}}\left(T_{ref}\right)\left(T_{\mathrm{g}} - T_{\mathrm{d}}\right)}{2R_{\mathrm{d}}}, \tag{6.2.16}$$

Nu is calculated based on Equation (2.2.31) with B_{T} is replaced by B_{M} (called as model 0), $Pr = \frac{\mu_{\text{air}}\left(T_{ref}\right)c_{\text{air}}\left(T_{ref}\right)}{k_{\text{air}}\left(T_{ref}\right)}$, $k_{\text{air}}\left(T_{ref}\right) = \frac{K_1 T_{ref}^{3/2}}{T_{ref} + K_2}$, $\mu_{\text{air}} = \frac{A_1 T_{ref}^{3/2}}{T_{ref} + A_2}$, K_1=252 g cm/(s^{3}K$^{3/2}$), K_2=200 K, A_1 =1.457E-5 g/(s.cm K$^{1/2}$), A_2 = 110 K, k_{air} is the air thermal conductivity at T_{ref}, c_{air} is air specific heat capacity at constant pressure at T_{ref} and μ_{air} is air viscosity (Amsden et al., 1989).

The mass vaporisation rate from the droplet surface is described by Equation (2.2.15); presented in the following form (Faeth, 1977):

$$\dot{m}_f = 2\pi\overline{\rho}_{\text{air}}\overline{D}_{\text{air}}R_{\text{d}}B_{\text{M}}Sh, \tag{6.2.17}$$

where Sh is calculated from Equation (2.2.30) (Model 0), $Sc = \frac{\mu_{\text{air}}\left(T_{ref}\right)}{\rho_{\text{air}}D_{\text{air}}}$, $\overline{\rho}_{\text{air}}$ and $\overline{D}_{\text{air}}$ are the average air density and binary diffusion coefficient of the fuel vapour in air. Amsden et al. (1985) suggested the following empirical correlation:

$$\overline{\rho}_{\text{air}}\overline{D}_{\text{air}} = D_1 T_{ref}^{D_2}, \tag{6.2.18}$$

where D_2= 0.6, D_1 is a constant based on the fuel type. Equation (6.2.18) is implemented in the KIVA-2 code.

6.2.2.2 ETC model

In a typical internal combustion engine environment, the duration of transient droplet heating is comparable with droplet vaporisation time. Therefore the temperature gradient inside droplets cannot be ignored in CFD calculations (Bertoli and Migliaccio, 1999). In order to introduce a more realistic transient heating of droplets, the ETC model, described in Chapter 2, was suggested. This model allows for the calculation of internal temperature distribution in the droplet taking into account the circulation inside it (ETC) and the effects of thermal radiation. This model was successfully implemented into a zero dimensional code. Analysis presented in Chapter 3 showed that application of the ETC model is important for accurate prediction of the autoignition delay time. Hence the ETC model needs to be taken into account in calculations based on multi dimensional CFD codes, including the KIVA-2 code.

In the gas phase analysis, it was pointed out that a model taking into account the finite thickness of the thermal boundary layer around the droplet predicts the evaporation time closest to the one based on the approximation of experimental data (see Chapter 3). This model is based on Equations (2.2.50) and (2.2.51) and is called Model 4 in our analysis. It will be used in calculations based on the KIVA-2 code.

6.2.3 Ignition model

The ignition process in the conventional KIVA-2 code is described in terms of the chemical reactions in a system which are generally symbolised as (Amsden et al.,1989):

$$\sum_m a_{mr} X_m \rightleftarrows \sum_m b_{mr} X_m , \tag{6.2.19}$$

where X_m represents one mole of species m and a_{mr} and b_{mr} are integral stoichiometric coefficients for reaction r. The stoichiometric coefficients must satisfy the following equation:

$$\sum_m (a_{mr} - b_{mr}) W_m = 0 , \tag{6.2.20}$$

so that mass is conserved in the chemical reaction. Chemical reactions are divided into two classes: those that proceed kinetically and those that are assumed to be in equilibrium.

In the KIVA-2 CFD code the kinetic reaction is presented in CHEM subroutine. Kinetic reaction r proceeds at a rate $\dot{\omega}_r$ given by Amsden et al. (1989):

$$\dot{\omega}_r = k_{fr} \prod_m (\rho_m / W_m) a'_{mr} - k_{br} \prod_m (\rho_m / W_m) b'_{mr} \tag{6.2.21}$$

Here, the reaction orders a'_{mr} and b'_{mr} need not to be to equal to a_{mr} and b_{mr}, so that empirical reaction orders can be used. The coefficients k_{fr} and k_{br} are assumed to be of a generalised Arrhenius form (Amsden et al., 1989):

$$k_{fr} = A_{fr} T^n \, exp\left(- E_{fr} / T\right), \tag{6.2.22}$$

and

$$k_{br} = A_{br} T^n \, exp\left(- E_{br} / T\right), \tag{6.2.23}$$

where E_{fr} and E_{br} are activation temperatures.

These rate expressions are evaluated by a partially implicit procedure (Amsden et al., 1989). The autoignition in the customised version of the KIVA-2 code is modelled based on the customised version of the Shell model (see Chapter 2).

6.3 Numerical simulation

In this section a brief description of the implementation of various liquid and gas phase models of droplet heating and evaporation into the customised version of the KIVA-2 CFD code is presented. The ETC and ITC liquid models based on the analytical solution and gas Models 0 and 4, described in Chapter 2, were implemented in the KIVA-2 CFD code via the EVAP subroutine. These replaced the Spalding model in the original KIVA-2. The effects of various breakup models were investigated using the TAB model, the conventional and modified WAVE models. These models were implemented in the BREAK subroutine. To investigate the effect of the ETC model on the autoignition delay time, the customised version of the Shell autoignition model was implemented in the CHEM subroutine to replace the original KIVA-2 kinetic reaction model.

The block diagram of the subroutines related to droplets in the KIVA-2 code is presented in Figure 6.3.1 (Amsden et al., 1989). The names of subroutines which calculate the related processes are written in brackets.

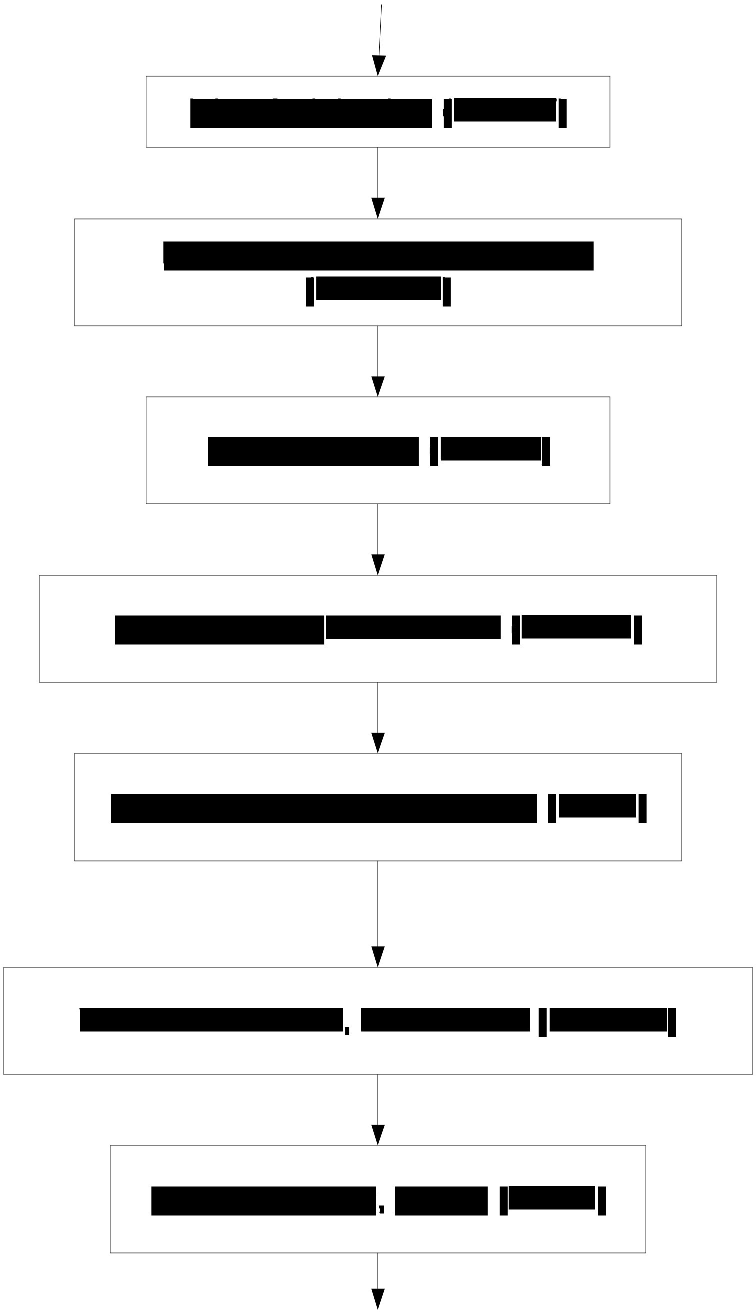

Figure 6.3.1 Block diagram for the subroutines related to droplets in the KIVA-2 code

Some other modifications have been implemented. The droplet surface tension, latent heat of vaporisation and vapour pressure were calculated based on droplet surface temperature while the liquid heat capacity at constant pressure and liquid viscosity were calculated based on droplet average temperature. T_{ref} was calculated based on the droplet surface temperature and gas temperature.

6.4 Result and discussions

6.4.1 Spray penetration in a 'cold' air

The droplet breakup models, described in the previous section, are expected to have an effect on spray heating and evaporation processes, and ultimately on the timing of the fuel vapour/air mixture autoignition. This will be discussed in Section 6.4.2. In a realistic Diesel engine-like environment the effect of these models is obscured by the contribution of other models, including those of droplet heating/evaporation and chemical autoignition. Hence, to identify the most suitable droplet breakup model we found appropriate to perform the testing of these models in a 'cold' gas environment, before considering realistic Diesel engine-like conditions. The predictions of the models described in Section 6.2 have been compared with the results of in-house measurements of Diesel fuel sprays. These were performed for sprays injected through a single-hole nozzle of 0.2 mm in diameter into compressed air at temperature 572 K and pressure 4 MPa. Spray penetration data were obtained from the analysis of video recordings, combined with mass flow rate measurements (Karimi et al., 2006). Based on the measured mass flow rate, the average velocity of injection has been calculated. The results are shown in Figure 6.4.1. As can be seen from this figure, the observed spray is highly transient and we anticipate that the modified WAVE model, described in Section 6.2.1.2, is the most appropriate one for its analysis.

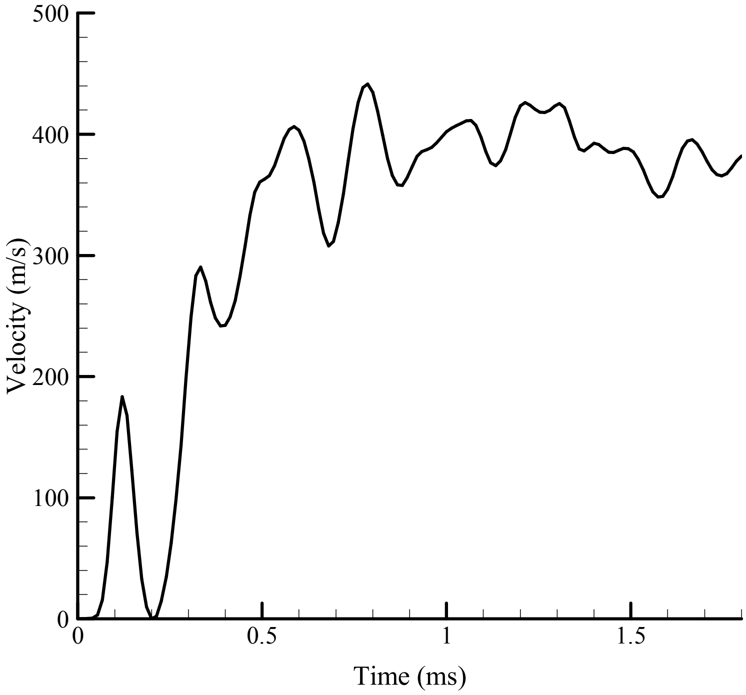

Figure 6.4.1 Calculated instantaneous jet injection velocities. A single-hole injector with a nozzle of diameter 0.2 mm was used. The injector and in-cylinder pressures were 160 MPa and 4 MPa respectively. The ambient gas temperature was 572 K (Karimi et. al., 2006)

Spray computations were performed using the KIVA-2 code, in which the models described in Section 6.2 were implemented (Amsden et al., 1989). Droplet parcels were injected into a cylindrical gas-filled domain using the blob injection method. Spray computations were performed in two dimensions, taking into account axial symmetry of the flow. The flow domain was represented by a constant volume gas chamber of 2 cm in radius and 10 cm in length, neglecting the piston motion during the injection pulse. The domain was covered by a uniform 2-dimensional grid, typically with 20 cells in the radial and 48 cells in the axial direction (the effects of the grid on the results will be discussed later in Section 6.4.2). The calculations were performed using all three droplet breakup models described in Section 6.2.

The results of calculations of spray tip penetration and the corresponding experimental data are shown in Figure 6.4.2. The spray tip penetration length is defined as the distance from the nozzle exit to the leading droplet of the spray. As follows from this figure, the conventional WAVE and TAB models under-predict significantly the penetration at the initial stage of this process. The increase in the parameter B_1 from 10 to 60 leads to some improvement in the accuracy of the prediction of this model. At the same time, the modified version of WAVE model, described in Section 6.2.1.2, gives much better agreement between the prediction of the model and experimental data, as expected, remembering a highly transient nature of the spray under consideration.

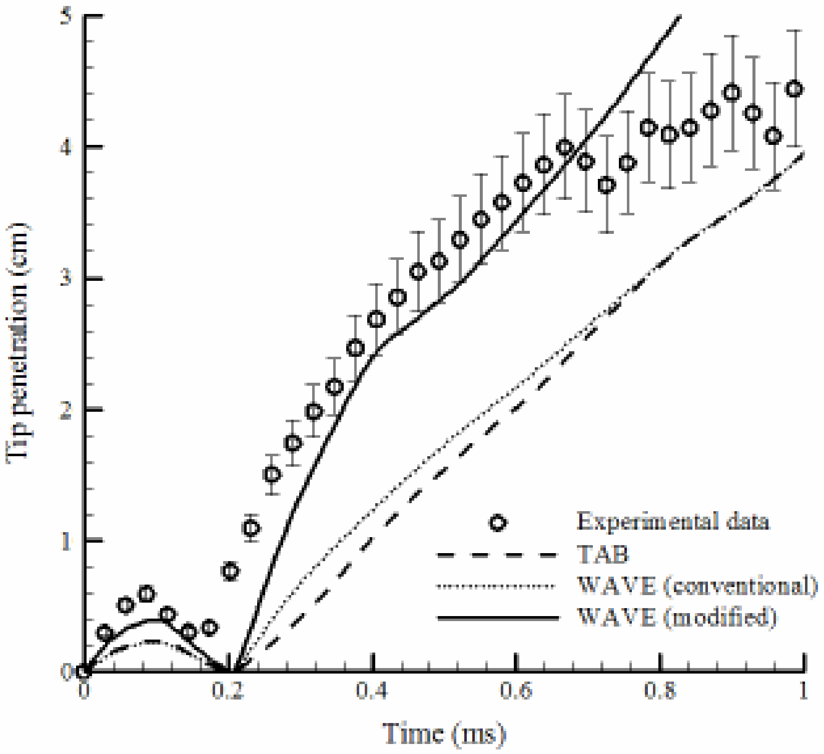

Figure 6.4.2 Experimentally observed and computed spray tip penetration (defined as the distance from the nozzle exit to the leading droplet of the spray) (Karimi et. al., 2006). The experimental conditions were the same as described in Figure 6.4.1. The computations were performed using the customised version of the KIVA-2 CFD code in which various droplet breakup models were implemented. These include the TAB model, conventional WAVE model and the modified WAVE model

At a later stage of injection the cluster shedding from the tip of the spray was observed experimentally. This led to the fluctuation of the tip penetration length around 4 cm (see Figure 6.4.2). This phenomenon has not been addressed in the present study. In our computations, the spray penetration length was identified with the distance from the nozzle to the leading droplet parcel. This leads to the deviation between the predictions of all models and experimental data at times greater than about 0.6 ms. We anticipate that the actual tip penetration length is larger than that shown in Figure 6.4.2, as the spray at distances greater than about 4 cm from the nozzle is not actually detected by the available equipment due to very low droplet volume fraction. Note that in the case of spray injected into 'hot' air, the ignition takes place typically at about 2 ms after the start of injection (Crua, 2002). For this late stage of injection, measurements of droplet sizes were performed for the same spray by Lacoste (2005). Figure 6.4.3 shows the experimentally observed evolution of the Sauter Mean Radius (SMR) of droplets on the spray axis (a) and its periphery (b) at a distance of 3 cm downstream from the nozzle (Lacoste, 2005). On the same figure, the results of calculation of SMR at the same locations, using the models described in Section 6.2, are shown.

As follows from this figure, the modified WAVE model leads to the best agreement between calculated and experimental results. Although these results were obtained for 'cold' sprays, we anticipate that they will remain valid for more realistic 'hot' sprays. Hence, we can recommend this model for modelling of highly transient sprays.

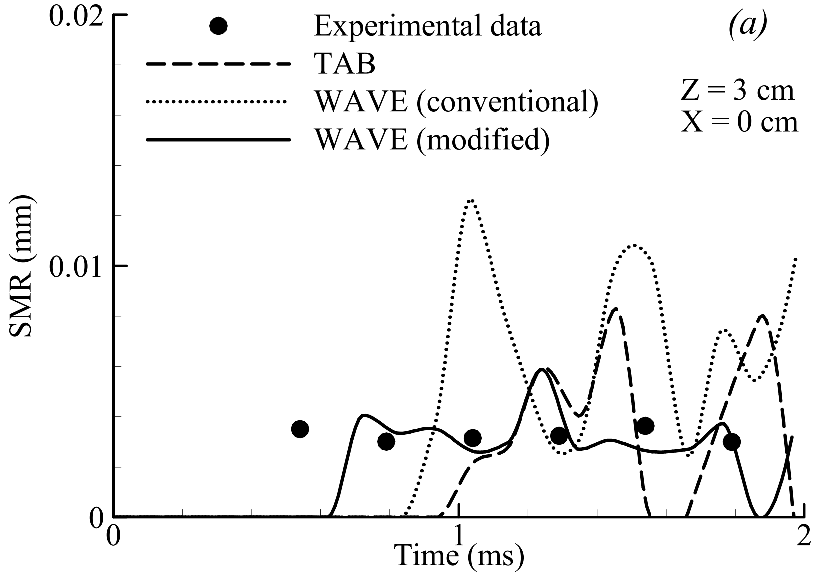

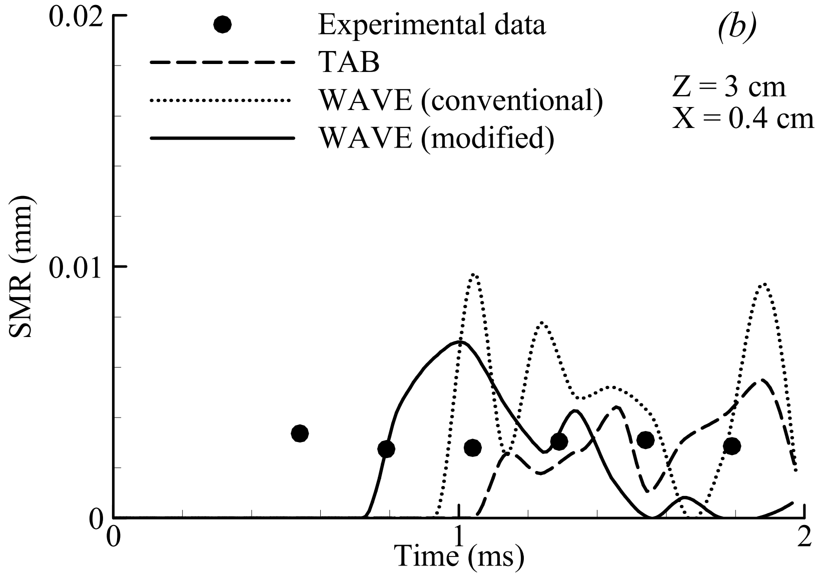

Figure 6.4.3 Experimentally observed and computed Sauter Mean Radii (SMR) of droplets at two different locations in the spray (Lacoste, 2005). The models used and the experimental conditions were the same as in the case shown in Figure 6.4.2

6.4.2 Spray in a ‘hot’ air

For the chosen test cases computations were performed assuming axial symmetry of the flow. Variations in the volume of the combustion chamber caused by piston motion during the injection pulse were small and, therefore, were ignored in the computations. The domain was covered by a uniform 2-dimensional grid, typically with 20 cells in the radial and 48 cells is the axial direction. In computations, the liquid spray penetration is defined as the distance from the nozzle to the leading droplet parcel in the spray. The ignition delay is defined as the moment after the start of injection when the local gas temperature rises above the critical threshold of 1100 K. Injection velocities were calculated from the measured rate of injection (Karimi et al., 2006) (see Figure 6.4.1).

The fuel injector could be heated up to 350 – 400 K. In most cases the temperature of the droplet parcels emerging from the injector was set to 375 K. A special study was undertaken to determine the sensitivity of the results to variations in the liquid fuel temperature. It was assumed that the chamber was filled with dry air (79% nitrogen and 21% oxygen by volume).

The following analysis is subdivided into two parts. The analysis of the autoignition delay characteristics is presented in Section 6.4.2.1, and the analysis of the pre-ignition spray characteristic is presented in Section 6.4.2.2.

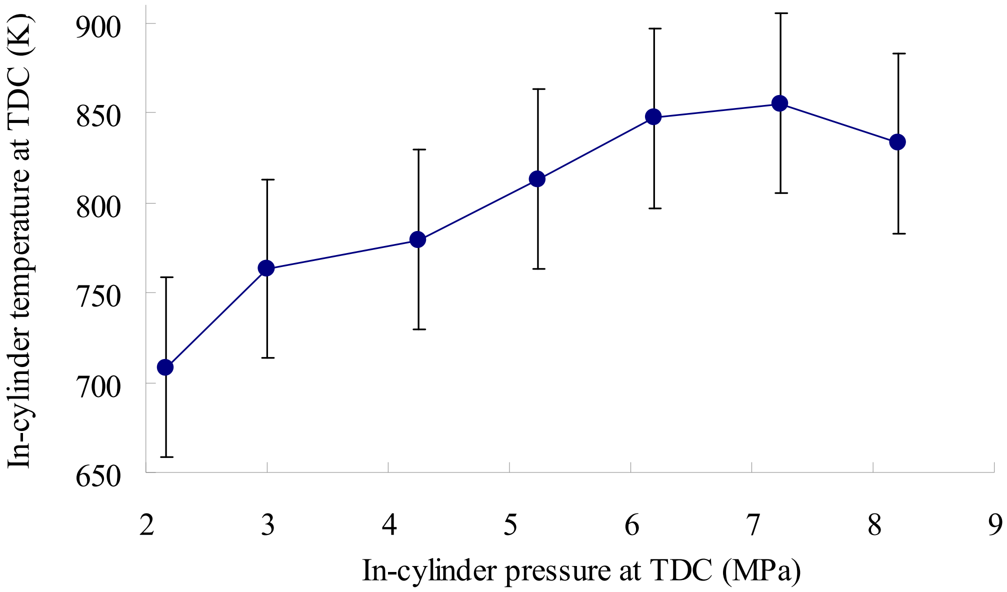

Figure 6.4.4 The initial in-cylinder gas temperatures at the top dead centre (TDC) as a function of the initial gas pressure at TDC. Filled circles refer to the values of this temperature calculated using the polytropic law

6.4.2.1 Autoignition delay

At first the modified WAVE breakup model was used and the parameter A_{f4} in the Shell model was assumed equal to 3 x 10^6. The predictions of the KIVA-2 code with two liquid phase models (ITC and ETC) and two gas phase models (Model 0 and Model 4) were compared with experimental data. The results are shown in Figure 6.4.5.

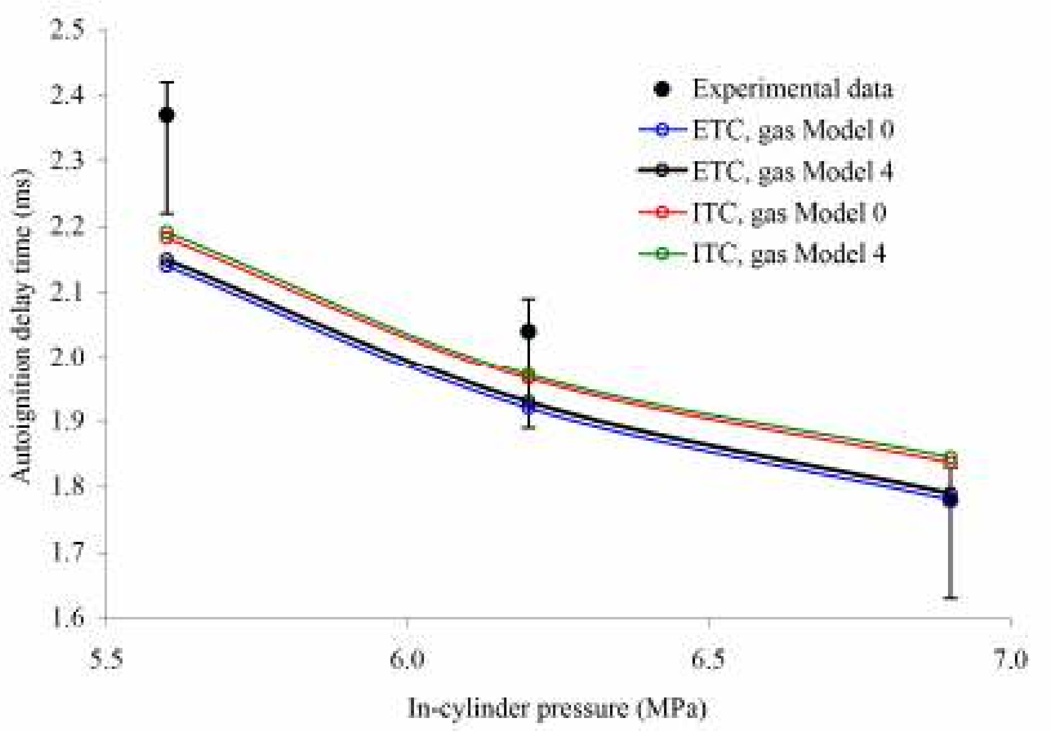

Figure 6.4.5 The total autoignition delay times observed experimentally (Crua, 2002) and computed using the customised version of the KIVA-2 CFD code at three initial in-cylinder pressures. The values of the initial gas temperature were obtained from Figure 6.4.4. The initial injected liquid fuel temperature was assumed equal to 375 K. The injection pressure was equal to 160 MPa. The modified WAVE model, two liquid phase models (ETC and ITC) and two gas phase models (Model 0 and Model 4) were used for computations

As follows from the figure, the choice of the liquid phase model leads to a much stronger effect on the autoignition delay compared with the gas phase model. This agrees with the previously reported results based on the zero dimensional code (see Chapter 3). This provides an additional support for recommendation made in Chapter 3, that the more accurate ETC model, rather than the ITC model, should be used for the prediction of autoignition delay. All models predict correctly the decrease in autoignition delay with increasing in-cylinder pressure. However, there is a noticeable (up to about 10%) deviation between experimental data and the predictions of all models, especially at relatively low pressure. This can be attributed to uncertainty over the choice of other parameters used in modelling, as discussed later in this section. A similar decrease of the autoignition delay with increasing in-cylinder pressure was observed for injection pressure 100 MPa. However, we could not compare the results for this injection pressure with the prediction of the model as measurements of fuel injection rate were not performed for this case. At higher in-cylinder gas pressures (more than about 7 MPa for 160 MPa injection pressure, and 8 MPa for 100 MPa injection pressure), the measurements have shown an increase in the ignition delay time with the gas pressure (Crua, 2002). However this trend is not reproduced by the model. This can be attributed to the limitations of the ideal-gas approximations for the fuel air mixture at high in-cylinder pressures. Possible other explanations of this trend were discussed by Crua et al. (2004). Note that error bars referring to experimental data are not symmetric.

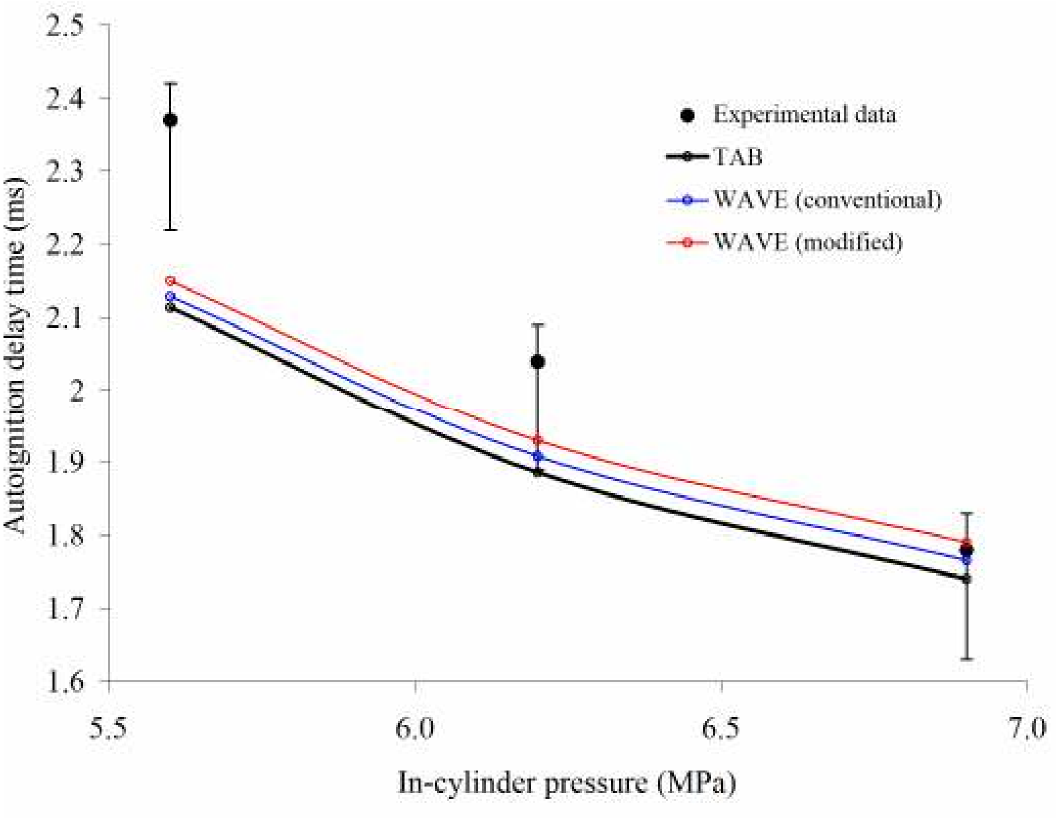

Figure 6.4.6 The same as Figure 6.4.5, but the computations were based on the ETC liquid phase model, the gas phase Model 4 and various droplet breakup models

Figure 6.4.6 shows the effect of breakup models on the autoignition delay in a Diesel spray using the ETC liquid phase model and gas phase Model 4. As can be seen from this figure, the variations in the autoignition delay time caused by the choice of breakup model are less than about 2.5%, which is within the accuracy of the experimental data. Strong injection accelerations during the first 0.2 ms after the injection, which affect the spray breakup at the initial stage of injection (during about 1 ms), have little effect on spray properties at the time of autoignition (about 2 ms after injection). This explains the relatively small difference between the ignition delays calculated using conventional and modified WAVE breakup models. The fact that the TAB breakup model predicts slightly shorter ignition delays than the WAVE models can be explained by the fact that the TAB model predicts the generation of larger amount of smaller droplets which evaporate faster (see Figure 6.4.3).

As follows from Figure 6.4.4, an uncertainty of estimation of the initial gas temperature in the combustion chamber is about ± 50 K. The sensitivity analysis of the results with respect to the choice of the initial gas temperature is shown in Figure 6.4.7. The ETC liquid phase model, the gas phase Model 4 and the modified WAVE model were used for calculations. The results of computations based on the initial gas temperatures, estimated from the measurements (reference temperature as shown in Table 6.1), are presented by the solid curve. Thick and thin dashed curves show the autoignition delays predicted based on the assumption that the initial gas temperature is 20 K higher and 20 K lower than the reference temperature respectively. As follows from Figure 6.4.7, the effect of the initial gas temperature on the predicted autoignition delay is rather strong (up to about 20%). The autoignition delay decreases with increasing gas temperature as expected. The best agreement with experimental data is achieved when using an initial gas temperature 20 K below the reference one.

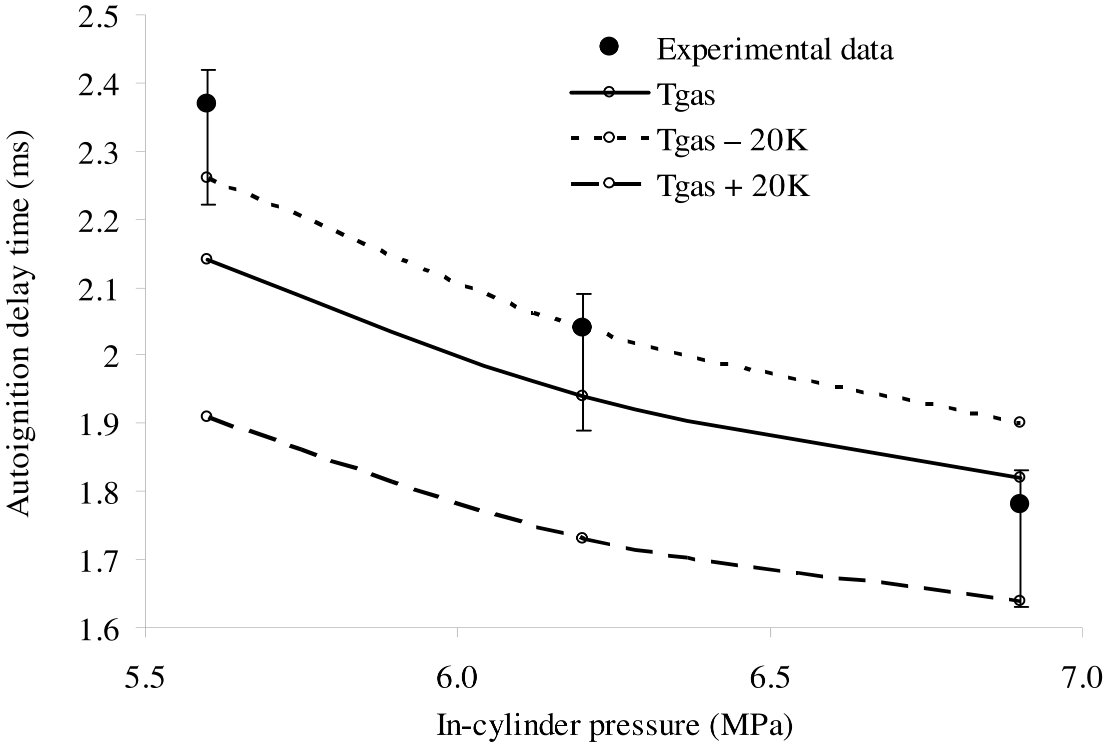

Figure 6.4.7 The same as Figures 6.4.5 and 6.4.6, but the computations were based on the ETC liquid phase model, the gas phase Model 4, the modified WAVE model and three values of the initial gas temperature. Firstly, the initial gas temperature was taken equal to the one predicted by Figure 6.4.4; secondly, this temperature was taken equal to the one predicted by this figure minus 20 K; thirdly, this temperature was taken equal to the one predicted by this figure plus 20 K.

Figure 6.4.8 shows the effect of the temperature of injected fuel on the autoignition delay. As is the case of Figure 6.4.7, the ETC liquid phase model, the gas phase Model 4 and the modified WAVE model were used for calculations. The initial gas temperature was calculated based on Figure 6.4.4. As follows from Figure 6.4.8 the decrease in injection fuel temperature from 375 K to 350 K leads to a very small increase in autoignition delay. However, increases in this temperature from 375 K to 400 K lead to a quite significant decrease in the delay, especially for in-cylinder pressure of 6.2 MPa. Since this increase in the injected fuel pressure leads to considerable deviation between the experimental and computed results, it seems unlikely that the value of this temperature can reach 400 K.

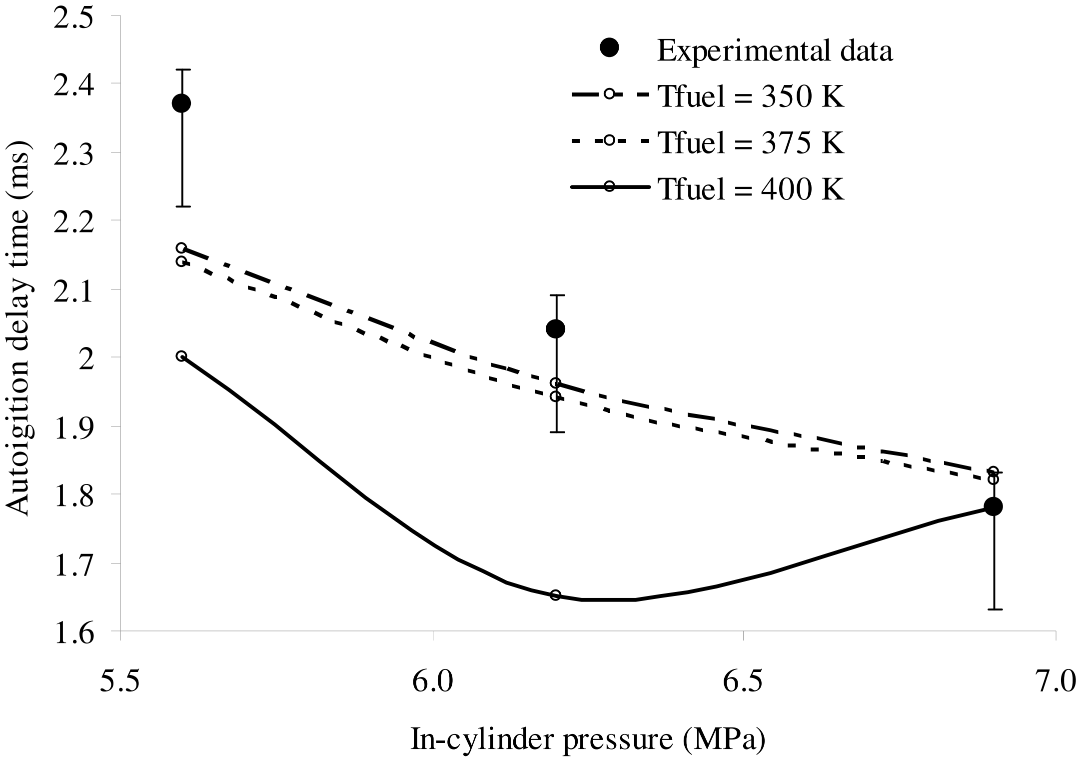

Figure 6.4.8 The same as Figure 6.4.7, but the computations were based on three injected fuel temperatures: 350 K, 375 K and 400 K.

As shown by Sazhina et al. (2000), increases in parameter A_{f4} lead to a decrease in the chemical autoignition delay time. At the next stage in the analysis the sensitivity of predicted autoignition delay to the value of A_{f4} was investigated. The results for the same models and values of parameters as in Figures 6.4.5-6.4.8, but for various A_{f4} are shown in Figure 6.4.9. Following Sazhina et al. (2000), the analysis was focused on A_{f4} in the range 3 x 10^6 to 6 x 10^6 (see Chapter 2). As follows from this figure, the values of the autoignition delay decrease with increasing A_{f4} in agreement with Sazhina et al. (2000). This decrease could up to about 20% which indicates a non-negligible role of the chemical ignition delay compared with the total ignition delay in this particular case. In fact the parameter A_{f4} could be the fitting parameter of the model if we are able to specify accurately both the initial gas temperature and injection fuel temperature.

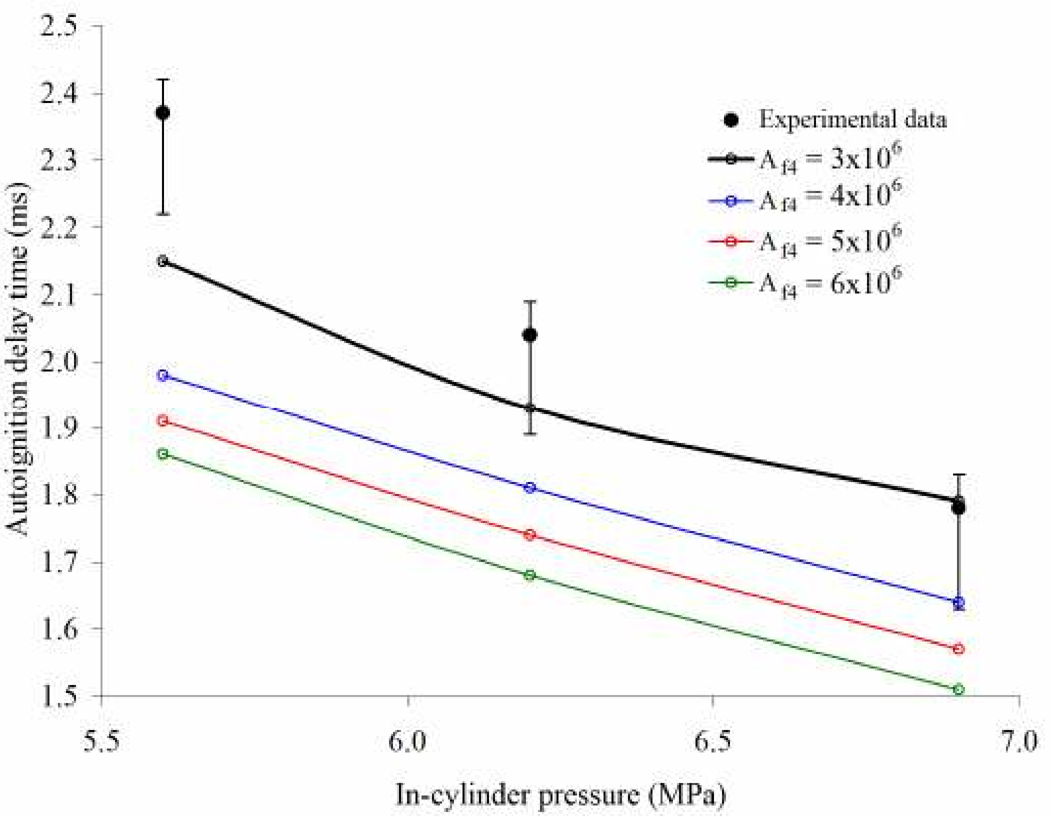

Figure 6.4.9 The same as Figure 6.4.8 for the injected fuel temperature 375 K, but the computations were based on four values of the coefficient A_{f4} in the Shell model, as indicated in the figure

Finally the grid sensitivity of the result shown in Figures 6.4.5 – 6.4.9 was investigated. The results are shown in Figure 6.4.10. The same models as in Figures 6.4.5 - 6.4.9 were used with injection temperature equal to 375 and A_{f4}=3x10^6. As follows from this figure, the difference between the delay times predicted by computations based on various grids does not exceed about 3 %. This is well below the experimental errors and allows us to conclude that mesh resolution, as used in this computation, is sufficient to achieve accurate results.

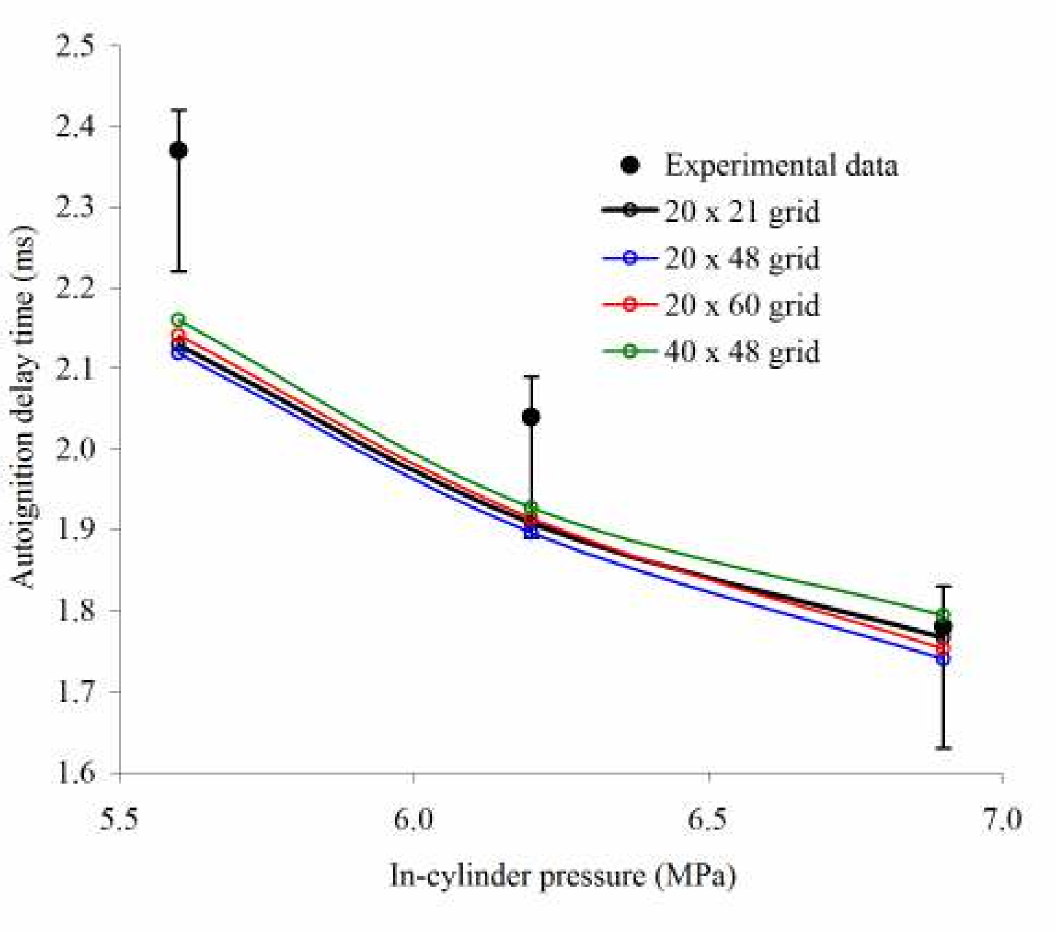

Figure 6.4.10 The same as Figure 6.4.9 for $A_{f4} = 3x10^6$, but the computations were based on four grid arrangements as indicated in the figure

6.4.2.2 Pre-ignition spray characteristics

In this subsection a number of spray characteristics, mainly at the pre-ignition stage are discussed. No direct experimental verification of the results will be available in most cases, but these results are expected to allow us to get better understanding of the processes which cannot be directly observed at the moment.

Figure 6.4.11 shows the time dependence of the maximum Sauter Mean Radius (SMR) of droplets and maximal in-cylinder pressure predicted by the KIVA-2 CFD code with the modified WAVE model, the ETC liquid phase model and the gas phase Model 4. The injection pressure was taken to 160 MPa, the initial gas pressure was equal to 6.2 MPa, and the injection temperature was taken to be equal to 375 K. The same grid as in Section 6.4.2.1 was used. As follows from Figure 6.4.11, the SMR of droplets rapidly reduces to about 10 μm, due to the breakup processes, which are of the same order of magnitude as observed experimentally. The initial peak of the maximal in-cylinder pressure is related to compression of air during the injection process.

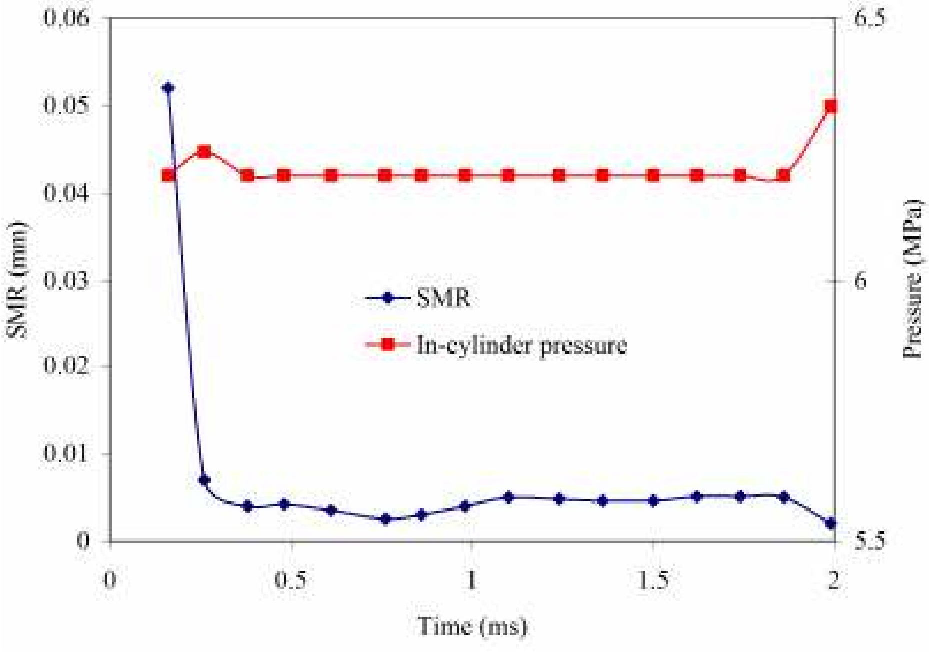

Figure 6.4.11 The time evolution of the maximal Sauter Mean Radii (SMR) of droplets and in-cylinder gas pressure in the combustion chamber for the initial gas pressure 6.2 MPa and initial gas temperature 850 K. The modified WAVE model, the ETC liquid phase model and the gas phase Model 4 were used for computations

Figure 6.4.12 shows the time dependence of the maximal and minimal gas temperatures in the combustion chamber and the maximal temperature at the surface of the droplet for the same models and initial values of parameters as in Figure 6.4.11. The autoignition process at times greater than about 1.8 ms, accompanied by a rapid increase of the maximal gas temperature, is clearly seen in this figure. The predicted initial decrease of the minimal gas temperature is clearly linked with the evaporation of the freshly injected droplets. At times greater than about 0.4 ms, heat supplied by the chemical reactions seems to exceed the heat consumed for the evaporation process and the minimal gas temperature slowly begin to increase. The increase of the maximal droplet surface temperature during approximately the first 0.3 ms after the injection corresponds to the droplet heat-up period. After that, this temperature remains at a nearly constant level, close to the critical temperature of Diesel fuel (but always below it).

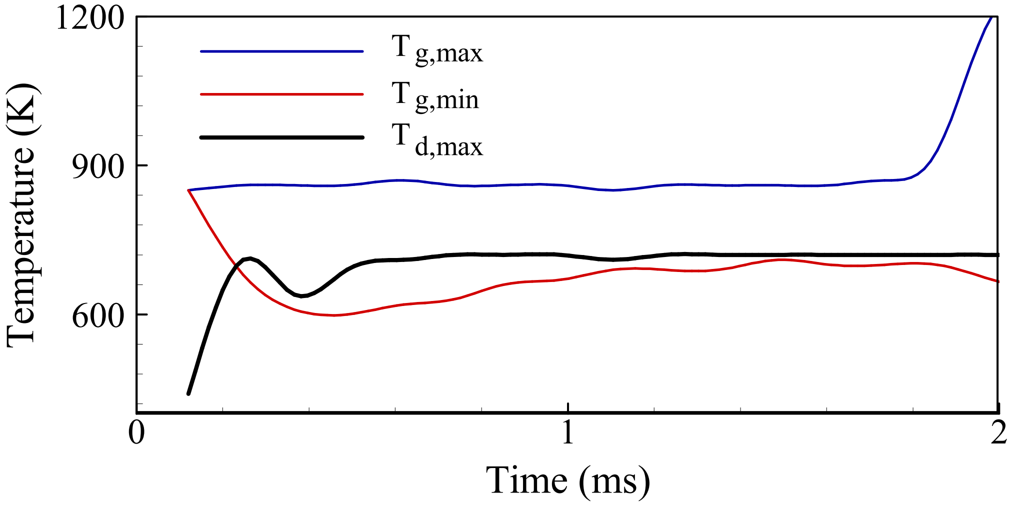

Figure 6.4.12 The same as Figure 6.4.11 but for maximal and minimal gas temperatures and maximal droplet surface temperature

Figure 6.4.13 shows the time dependence of the maximal mass fractions of fuel vapour and the species described by the Shell model (the radical (*R*), branching agent (*B*) and intermediate agent (*Q*)), and the minimal mass fraction of oxygen for the same models and the initial values of parameters as in Figures 6.4.11-6.4.12. The initial increase in the fuel vapour mass fraction is related to the evaporation of liquid Diesel fuel. The autoignition stage is preceded by a slow decrease in fuel vapour and oxygen mass fractions. This is accompanied by the corresponding increase in mass fractions of radicals, branching and intermediate agents. Immediately before the onset of autoignition, the increase in the mass fractions of radicals, branching and intermediate agents is visibly accelerated. This is accompanied by an acceleration of decrease in mass fraction of oxygen, while the maximal concentration of fuel vapour remains practically unchanged.

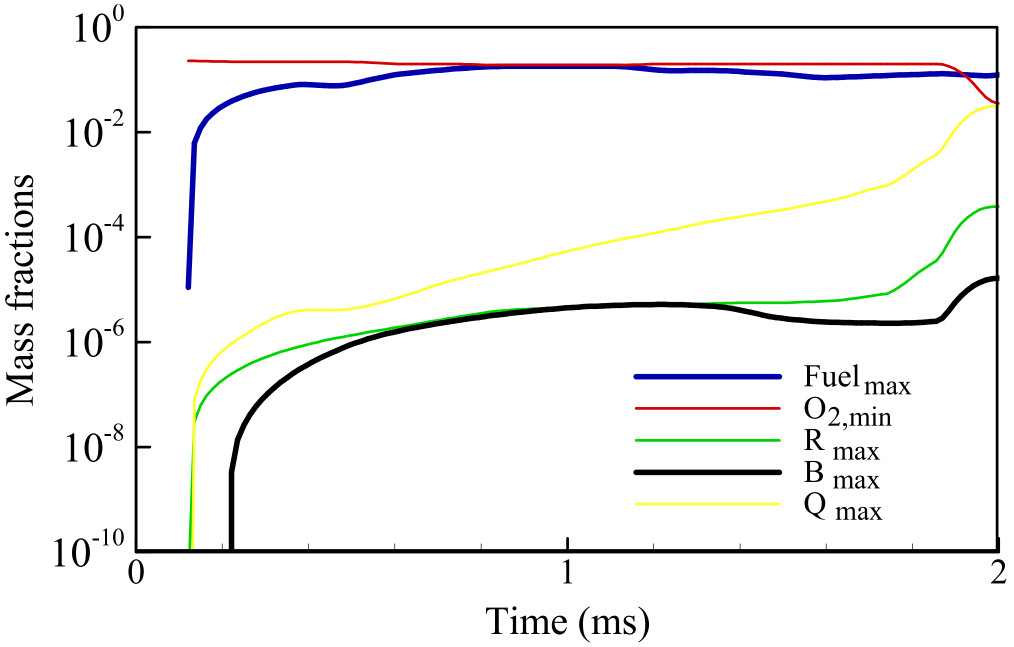

Figure 6.4.13 The same as Figures 6.4.11-6.4.12 but for the maximal mass fractions of fuel vapour and the species described by the Shell model (the radicals (*R*), branching agent (*B*), and intermediate agent (*Q*)), and the minimal mass fraction of oxygen

Figure 6.4.14 shows the spatial distribution of droplets in the spray at four moments of time after the start of injection. These moments correspond to the three stages in the spray evolution: (a) breakup and heating of the liquid droplets (b) and (c) breakup, heating, and evaporation of droplet, (d) ignition stage. The same models and initial values of parameters as in Figures 6.4.11-6.4.13 were used for computations. The circles in this figure show the SMR of droplets magnified 500 times. At the injector, the radii of droplets were specified based on the radius of the injector, taking into account the effects of flow cavitation in the nozzle: R_{d0}=R_{nozzle}. C_{contr}, where C_{contr} = 0.62 if the cavitation number CN is greater than or equal to 1, and C_{contr} =1 if this number is less than 1. Then the droplet radii rapidly decrease due to breakup processes.

At the moment of time 0.98 ms no droplets are observed beyond Z equal about 4.5 cm. This is due to limitation of the penetration length at this moment. At t = 1.49 ms the droplets are observed over whole range of Z. At t = 1.73 ms the number of droplets beyond Z = 4.5 cm is visibly reduced alongside with SMR. This is related to droplet evaporation processes. These reductions are even more clearly visible at t = 1.98 when autoignition took place, and the increased gas temperature led to still more rapid droplet evaporation.

The spatial distribution of gas temperatures, SMRs, mass fractions of fuel vapour, oxygen, branching agent, radicals and intermediate agent for the same moments of time as in Figure 6.4.14 are shown in Figure 6.4.15. The same models and initial values of parameters as in Figures 6.4.11-6.4.14 were used for computations. As follows from Figure 6.4.15a, before autoignition the slow increase in gas temperature takes place in the area away from the spray. In the immediate vicinity of the spray, gas is cooled down due to the evaporation process. After autoignition, a rapid increase of gas temperature takes place mainly at the periphery of the spray in agreement with the early results reported by Flynn et al. (1999) and Sazhina et al. (2000). The distribution of the SMRs shown in Figure 6.4.15a is generally consistent with the distribution of droplets shown in Figure 6.4.14.

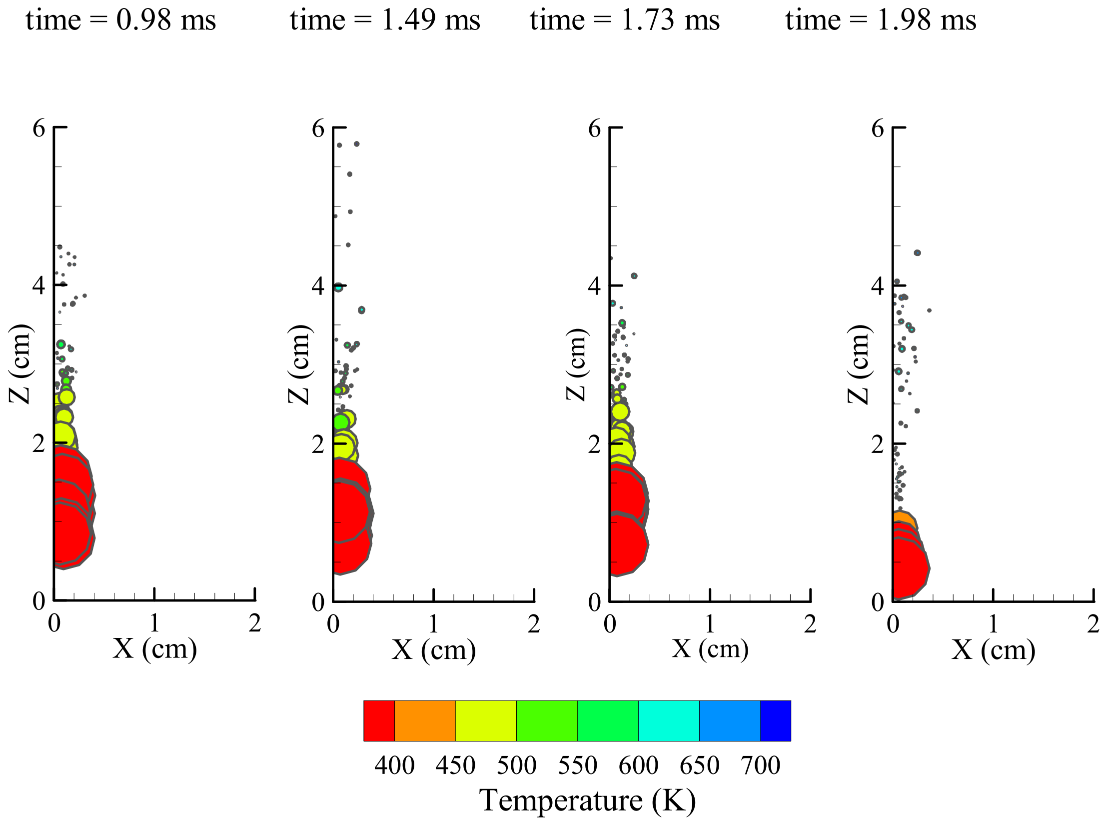

Figure 6.4.14 Spatial distribution of droplets at four moments of time for the same values of the initial parameters and models as in Figures 6.4.11-6.4.13. The circles show SMR of droplets magnified 500 times

As follows from Figure 6.4.15b, for *t* between 0.98 ms and 1.73 ms, the fuel vapour mass fraction gradually increases and this vapour spreads from the vicinity of the spray to the ambient gas, while the maximal fuel vapour mass fraction remains practically unchanged (see Figure 6.4.13). At *t* =1.98 ms a visible decrease in fuel vapour mass fraction can be seen at spray periphery where the autoignition took place. The decrease in oxygen mass fraction at the same time and location can be clearly seen in Figure 6.4.15b. Visible increase in the mass fractions of the branching agent, radicals and intermediate agent at *t* =1.98 ms near the periphery of the spray can be clearly seen in Figure 6.4.15c.

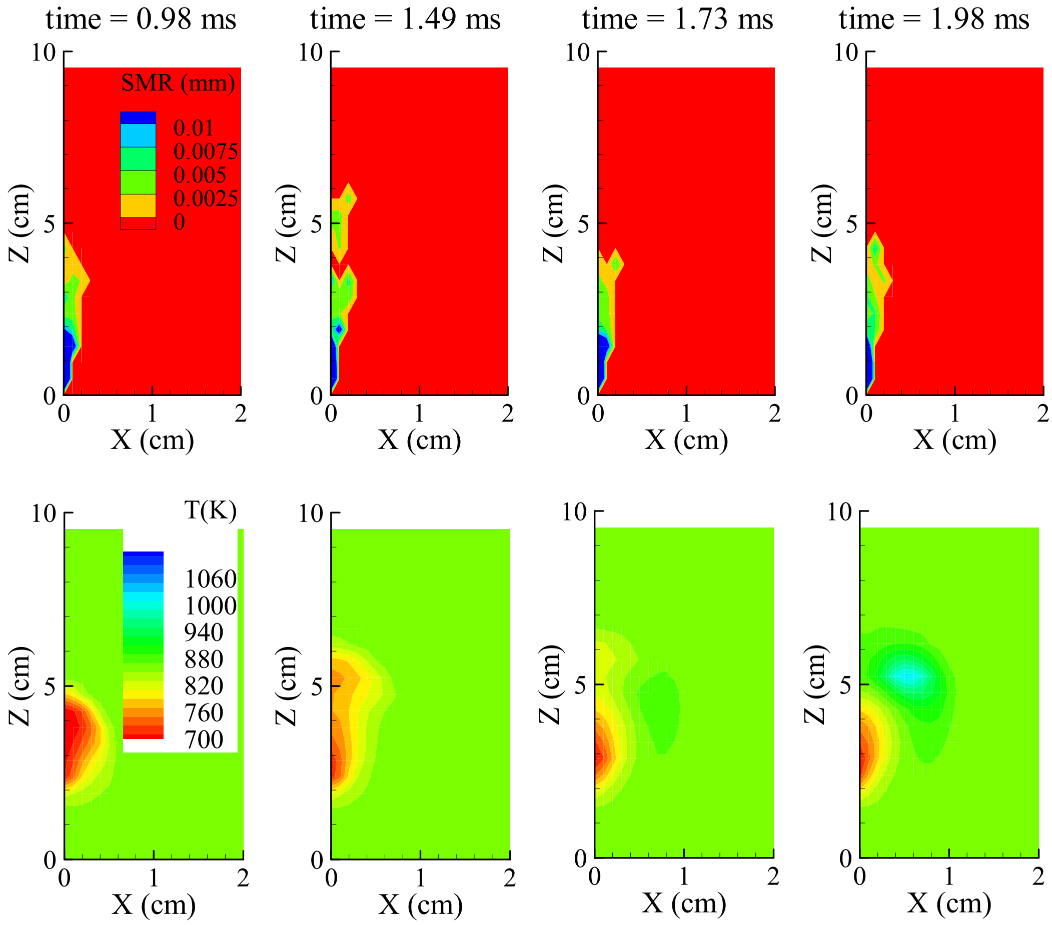

Figure 6.4.15a Spatial distributions of SMRs of droplets and gas temperature for the same moments of time, values of the initial parameters and models as in Figure 6.4.14

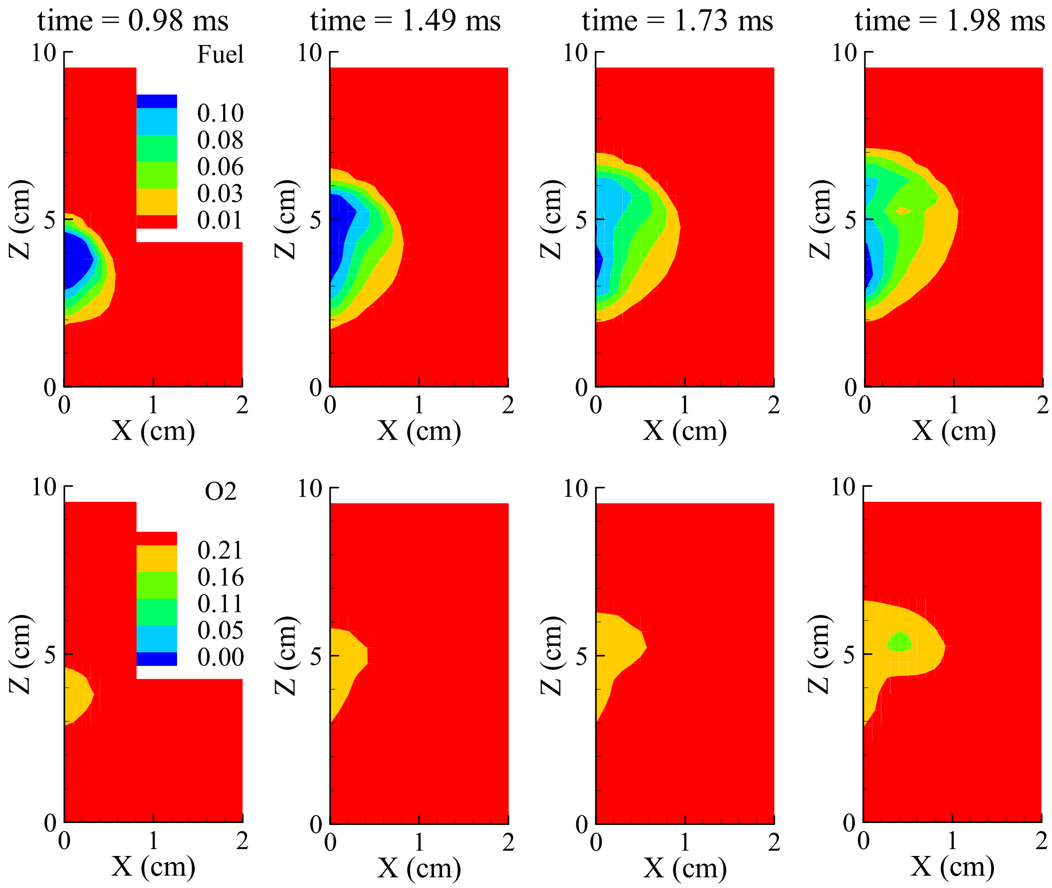

Figure 6.4.15b The same as Figure 6.4.15a, but for the fuel vapour and oxygen relative mass fractions

Figure 6.4.16 shows the evolution of droplet parameters at various ranges of radii at the same moments of time as in Figures 6.4.14 and 6.4.15. Eight bands were considered:

band 1 for droplets of radius less than 1.32 μm,

band 2 for droplets of radius from 1.32 to 4.44 μm,

band 3 for droplets of radius from 4.44 to 10.5 μm,

band 4 for droplets of radius from 10.5 to 20.6 μm,

band 5 for droplets of radius from 20.6 to 35.6 μm,

band 6 for droplets of radius from 35.6 to 56.5 μm,

band 7 for droplets of radius from 56.5 to 82.0 μm,

band 8 for droplets of radius larger than 82.0 μm.

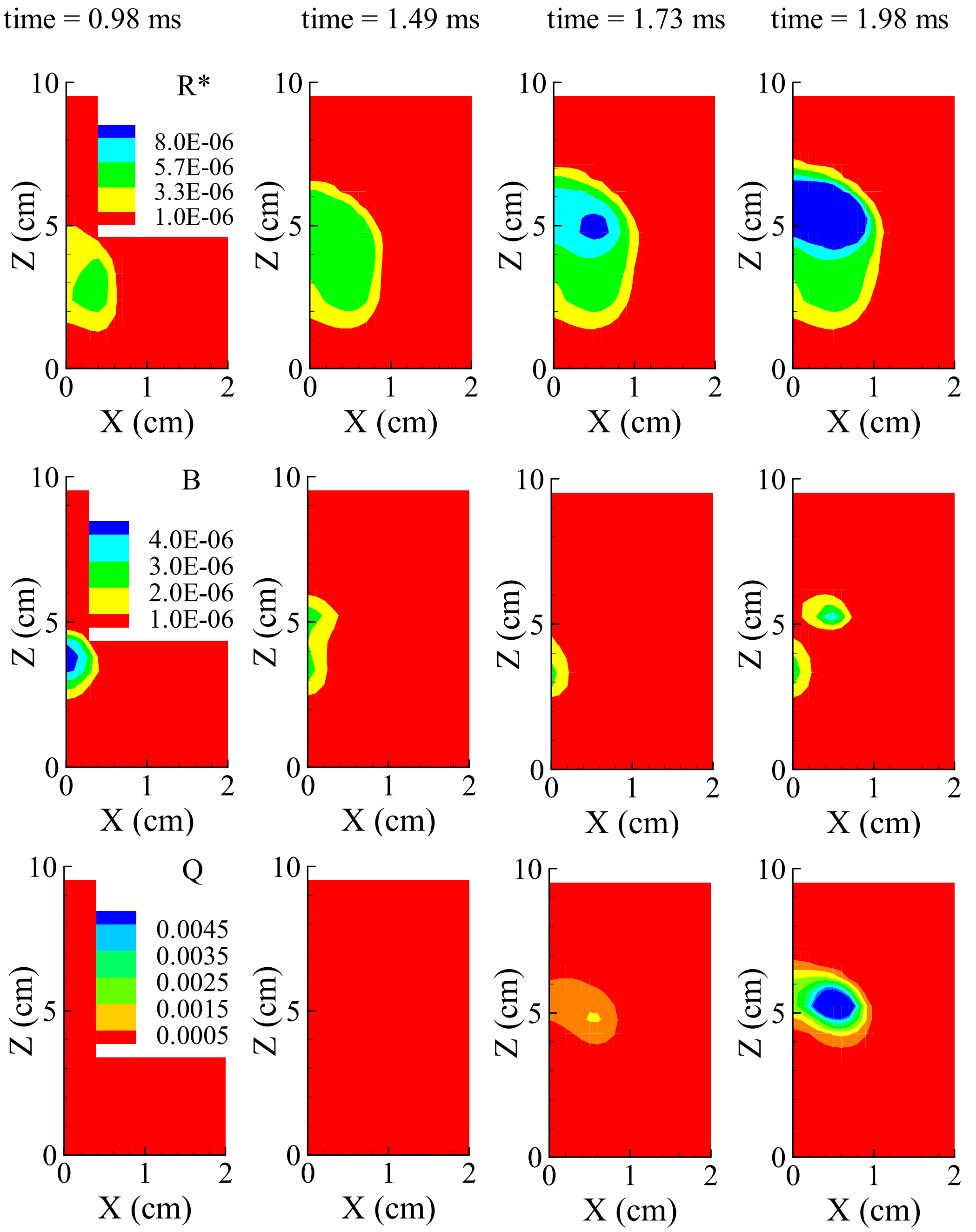

Figure 6.4.15c The same as Figures 6.4.15a,b, but for the radicals, branching agent and intermediate agent relative mass fractions

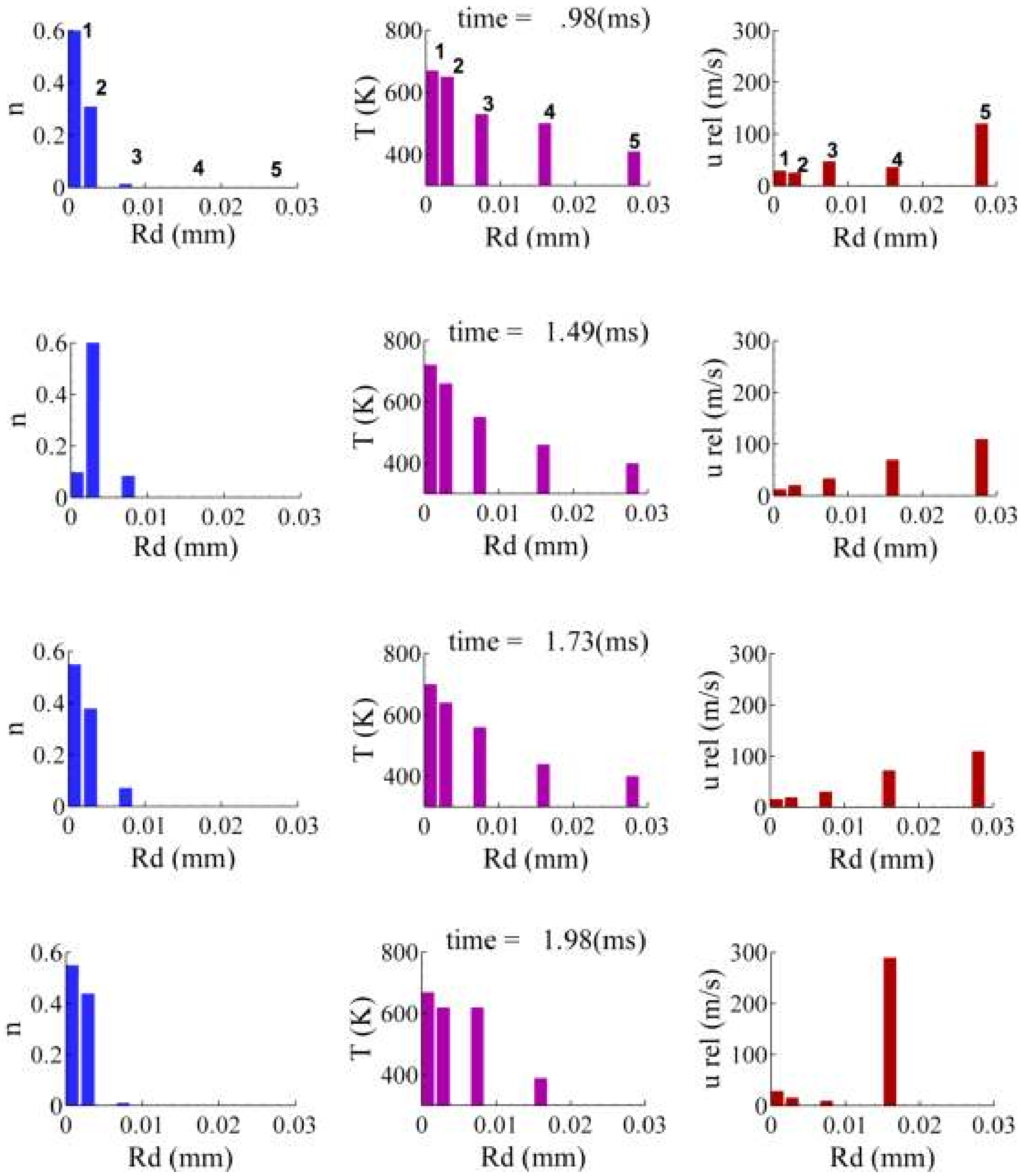

Figure 6.4.16 Relative number density, temperature and relative speeds of droplets at four moments of time (the same as in Figures 6.4.14 and 6.4.15) and various radii bands. The same values of the initial parameters and models as in Figures 6.4.14-6.4.15 were used.

In Figure 6.4.16 bands 1-5 are shown, as these are the most representative for the presentation of the evolution of spray parameters. Droplets with radii greater than about 30 μm (bands 6-8) disappear from the system due to the breakup process. As follows from this figure, at *t*=0.98 ms, those with radii up to about 30 μm are present in the system. By *t*=1.98, the droplets with radii greater than about 20 μm practically disappear from the system due to breakup and evaporation processes. At all stages the surface temperatures of larger droplets are always smaller than those of smaller droplets. This is explained by the fact that larger droplets require more time to heat-up compared with smaller droplets and fresh large droplets are continuously injected into the system. The relative speed of larger droplets is always greater than that of smaller ones, as smaller droplets are more easily entrained by the ambient air.

6.5 Conclusions to Chapter 6

A number of new models have been implemented into the customised version of the KIVA-2 CFD code. These are the modified WAVE droplet breakup model, the effective thermal conductivity (ETC) liquid phase model, the gas phase model suggested by Abramzon and Sirignano (Model 4), and the customised version of the Shell autoignition model. The predictions of the updated KIVA-2 code have been compared with the results of the in-house experimental studies of Diesel sprays where appropriate. The measurable spray parameters include spray penetration length, the time evolution of the Sauter Mean Radius (SMR) of droplets and the autoignition delay times. Both spray injection into a relatively ‘cold’ gas, not leading to the autoignition process, and ‘hot’ gas, leading to this process have been considered.

It has been pointed out that in the case of spray injection into a ‘cold’ gas, the observed spray tip penetration agrees much better with the prediction of the modified WAVE model compared with other droplet breakup models widely used in computer simulation of quasi-steady-state spray dynamics. A similar conclusion is applied to the predicted and observed SMR of droplets.

The prediction of the total autoignition delay by gas phase Model 4 have been compared with the prediction of this delay by a more basic gas phase model, based on a number of simplifying assumptions. It has been shown that the choice of the gas phase model has only a minor effect on the predicted autoignition delay, which can be safely ignored in practical engineering computations. The autoignition delays predicted by the infinite thermal conductivity (ITC) and effective thermal conductivity (ETC) liquid phase models have also been compared. The ITC model is a default one used in the conventional KIVA-2 code. The ETC model is the new model implemented into this code. The implementation of the latter model was based on the analytical solution of the heat conduction equation in a spherical droplet applied at each time step. It has been pointed out that the difference in the autoignition delay times predicted by the ITC and ETC models is noticeable and needs to be taken into account in practical computations. The application of the ETC model is recommended as a more physical one.

It has been pointed out that the predicted decrease in the autoignition delay with increasing in-cylinder gas pressure, ranging between about 5.5 MPa and 7 MPa, agrees with experimental observations. However, the predicted values of this delay are up to approximately 10% less than the experimentally observed ones. This level of agreement between experimental and computational results is considered acceptable remembering the uncertainty of both experimental data and values of the input parameters in the model. Uncertainty over the model values of parameters refers primarily to the initial gas temperature (calculated based on the observed in-cylinder gas pressure), the injected liquid temperature, and the parameters of the Shell autoignition model. It has been shown that the grid dependence of the results is relatively weak and can be ignored in the analysis.

A detailed analysis of time evolution of various Diesel parameters has been presented. These include gas pressure and temperature, the SMRs of droplets, mass fractions of various gas components, droplet temperatures and speeds relative to the ambient gas. The results turned out to be consistent with the physical background of the processes involved. In agreement with the previously reported results, it has been shown that autoignition takes place at the periphery of the fuel spray.

7. CONCLUSIONS

7.1 Comparative analysis of liquid and gas phase model of heating and evaporation

A comparative analysis of liquid and gas phase models of fuel droplet heating and evaporation is conducted using a zero dimensional code. The analysis is focused on the liquid phase model based on the assumption that the liquid thermal conductivity is infinitely large (infinite thermal conductivity (ITC) model), and the so called effective thermal conductivity (ETC) model suggested by Abramzon and Sirignano (1989). Seven gas phase models are compared. These are six semi-theoretical models based on various assumptions and a model based on the approximation of experimental data. It is pointed out that the gas phase model, taking into account the finite thickness of the thermal boundary layer around the droplet, in the form suggested by Abramzon and Sirignano (1989), predicts the evaporation time closest to the one based on the approximation of experimental data. This gas phase model is recommended for practical applications in CFD codes. The evaporation times predicted by both the ETC and ITC models are coincide, however a noticeable difference in temperature was observed at the initial stage of droplet heating and evaporation.

In agreement with Sazhin et al. (2005a), for sufficiently small time steps, predictions of the numerical algorithms based on the analytical solution of the heat conduction equation and its numerical solution practically coincide. At larger time steps the numerical algorithms based on the analytical solution of the heat conduction equation is more accurate and less CPU intensive than the algorithm based on the numerical solution of this equation.

7.2 Radiative heating

The values of absorption coefficients of gasoline fuel (BP Pump Grade 95 RON ULG), 2,2,4-trimethylpentane (iso-octane) and 3-pentanone have been measured experimentally in the range of wavelengths 0.2 μm – 4 μm. The values of the indices of absorption calculated based on these coefficients are shown to be similar to those obtained earlier for low sulphur ESSO AF1313 Diesel fuel. The values of this index tend to be lower for pure substances (for example, iso-octane and 3-pentanone) than for Diesel and gasoline fuels. It is shown that the main contribution to the average absorption efficiency factor is expected to come from radiation at wavelengths less than 4 μm for the range of external temperatures between 1000 K and 3000 K. The value of this factor is approximated by a power function aR_{d}^{b}, where R_{d} is the droplet radius. Coefficients a and b are approximated by piecewise quadratic functions of the radiation temperature, with the coefficients calculated separately in the ranges of radii 2 μm – 5 μm, 5 μm – 50 μm, 50 μm – 100 μm and 100 μm – 200 μm for all fuels. This new approximation is shown to be more accurate when compared with the case when a and b are approximated by quadratic functions or fourth power polynomials of the radiation temperature, with the coefficients calculated over the entire range 2 μm – 200 μm. This difference in the approximations of a and b, however, is shown to have little effect on the modelling of fuel droplet heating and evaporation in conditions typical for internal combustion engines, especially in the case of Diesel fuel and 3-pentanone.

7.3 Models and experimental data

Validation of the droplet heating and evaporation models against experimental data was performed based on a zero dimensional code and the KIVA 2 CFD code.

Zero dimensional code

The direct comparison of the predictions of various gas models with experimental data for droplet evaporation in the absence of break-up reported by Belardini et al. (1992) and Nomura et al. (1996) leads to inconclusive results. None of the gas phase models under consideration can be supported by all experimental data presented. The ETC model leads to a marginally better agreement with experimental data than the ITC model.

Several liquid and gas phase models have been used for modelling droplet heating and evaporation, together with the autoignition of the mixture of air and fuel vapour produced by evaporating droplets. The chemical part of the autoignition process has been modelled based on the Shell model in the form suggested by Sazhina et al. (1999). The results have been compared with experimental data reported by Tanabe et al. (1995). It is pointed out that the total ignition delay (physical and chemical delays) depends weakly on the choice of the gas phase model for the values of parameters used by Tanabe et al. (1995). Its dependence on the choice of the liquid phase model turned out to be strong, in agreement with the earlier results presented by Sazhin et al. (2005b). In the presence of droplet break-up processes, the evaporation time and the total ignition delay depend on the choice of both gas and liquid phase models.

The model based on the analytical solution of the heat conduction equation taking into account effect of recirculation inside the droplet (ETC model) has been validated against experimental data for ethanol and acetone droplets. Heating and evaporation of monodisperse ethanol and acetone droplets has been studied in two regimes: pure heating and evaporation of droplets in a flow of air of prescribed temperature, and droplet heating and evaporation in a flame produced by previously injected combusting droplets. The model was combined with a gas phase model that took into account the effect of finite distance parameter. It has been pointed out that for relatively small droplets (initial radii about 65 μm) the experimentally measured droplet temperatures are close to the predicted average droplet temperatures. They are closer to the temperatures predicted at the centre of the droplets when the droplet diameter becomes larger than the probe volume size of the two-colour LIF thermometry.

The KIVA-2 CFD code

The ETC and ITC liquid phase models, Abramzon and Sirignano (1989) and simplified gas phase models, conventional and modified WAVE breakup models and the customised version of the Shell autoignition models have been implemented into KIVA-2 CFD code. This new customized version of the KIVA-2 code has been used for modelling the processes is Diesel engine-like environment. The results of calculations have been compared with in-house experimental data where appropriate. It has been pointed out that in the case of spray injection into a ‘cold’ gas, the observed spray tip penetration agrees much better with the prediction of the modified WAVE models compared with other droplet breakup models, widely used in computer simulation of quasi-steady-state sprays. A similar conclusion is applied to the predicted and observed SMR of droplets.

The predictions of the total autoignition delay by the Abramzon and Sirignano model (the gas phase Model 4) have been compared with the predictions of this delay by a more basic gas phase model (Model 0). It has been shown that the choice of gas phase model produces only minor effects on the predicted autoignition delay, which can be safely ignored in practical engineering computations. The difference in the autoignition delay times predicted by the ITC and ETC models is noticeable and needs to be taken into account in practical computations. The application of the ETC model is recommended as a more physical one.

7.4 Recommendations for further work

- The measurement of the index of absorption of various fuels in the range of wave length 4 μm – 10 μm is recommended.
- This thesis was focused on the hydrodynamic models for evaporation, while the effects of kinetic processes have been neglected. Further analysis using the kinetic model would be helpful for understanding of the underlying physics of the processes and more accurate modelling.

References:

Abramzon B., Sirignano W.A. (1989), *Droplet vaporization model for spray combustion calculation*, Int. J. Heat and Mass Transfer 32, 1605-1618.

Abramzon B., Sazhin S.S. (2005), *Droplet Vaporization Model in The Presence of Thermal Radiation*, Int. J. Heat Mass Transfer 48, 1868 – 1873.

Abramzon B., Sazhin S.S. (2006), *Convective Vaporization of Fuel Droplet with Thermal Radiation Absorption*, Fuel 85, 32-46.

Aggarwal S.K. (1998), *A review of spray ignition phenomena: present status and future research*, Progress in Energy and Combustion Science 24, 565-600

Amsden A.A., O'Rourke P.J., Ramshaw J.D., Dukowics J.K. (1985), *KIVA: A Computer Program for Two and Three Dimensional Fluid Flows with Chemically Reactions and Fuel Sprays,* Los Alamos Nat. Laboratory, New Mexico.

Amsden A.A., O'Rourke P.J., Butler T.D. (1989), *KIVA II: A Computer Program for Chemically Reactive Flows with Sprays*, Los Alamos Nat. Laboratory, New Mexico.

Amsden A.A. (1993), *KIVA-3: A KIVA Program with Block-Structured Mesh for Complex Geometries*, Los Alamos Nat. Laboratory, New Mexico.

Amsden A.A. (1997), *KIVA-3V: A Block-Structured KIVA program for Engines with Vertical or Canted Valves*, Los Alamos Nat. Laboratory, New Mexico.

Arcoumanis C., Gaivaises M., French B. (1997), *Effect of Fuel Injection Processes on the Structure of Diesel Spray*, SAE paper, 970799

Assanis D.N and Jung D. (2001), *Multizone DI Diesel Spray Combustion Model for Cycle Simulation Studies of Engine Performance and Emissions*, SAE paper, 011246.

Bachalo W.D and Houser M.J. (1984), *Development of Phase dopller Spray Analyser for Liquid Drop Size and velocity characterisations*, proc. AIIA 20th Joint Propulsion Conference, Ohio.

Belardini P., Bertoli C., Lazzaro M., Massoli P. (1992), *Single droplet evaporation rate: experimental and numerical investigations,* in: Proceedings of the Second International Conference on Fluid-mechanics, Combustion, Emissions and Reliability in Reciprocating Engines, Capri, Italy, 265-270.

Benson S.W. (1981) *The Kinetics and Themochemistry of Chemical Oxidation with Application to Combustion and Flames*, Prog. Energy Combustion Science 7, 125-134

Benson R.S., Winterbone D.E. (1982), *The Thermodynamic and Gas Dynamics of Internal Combustion Engine*, Claredon Press, Oxford.

Bertoli C., Migliaccio M. (1999), *A finite conductivity model for diesel spray evaporation and computations*, Int.J. Heat and Fluid Flow 20, 552-561.

Bird R.B., Steward W.E., Lightfoot E.N. (2002), *Transport Phenomena*, Chichester: Wiley.

Bonamy J., Bonamy L., Robert D. (1977) *Overlapping effects and motional narrowing in molecular band shapes – Application to Q branch of HD*, J. Chem. Phys. 67, 4441-4453.

Borman L.G. and Ragland K.W. (1998), *Combustion Engineering*, McGraw-Hill, Singapore.

Brady R.N. (1996), *Modern Diesel Technology*, Prentice-Hall, New Jersey.

Brower G., Chang S.K, Corradini M.L., Martin J.K (1988), *Physical Mechanism for Atomization of a Jet Spray: A Comparison of Models and Experiments*, SAE paper, 881318.

Brzustowaki T.A., Twardus E.M., Wojcicki S., Sobiesiak A. (1979), *Interaction of Two Burning Fuel Droplet of Arbitrary Size*, AIAA journal 17, 1234

Carslaw H.S., Jaeger J.C. (1986), *Conduction of Heat in Solids*, Clarendon Press, Oxford.

Castanet G., Lavieille P., Lemoine F., Lebounce M., Atthasit A., Biscos Y., Lavergne G. (2002), *Energetic Budget on an Evaporating Monodisperse Droplet Stream Using Combined Optical Methods. Evaluation of The Convective Heat Transfer*, Int. J. Heat and Mass Transfer 45, 5053-5067.

Castanet G, Lebouché M., Lemoine F. (2005), *Heat and mass transfer of combusting monodisperse droplets in a linear stream*, Int. J. Heat Mass Transfer 48, 3261–3275.

Charles F.T. (1985), *The Internal Combustion Engine in The Theory and Practice*, The MIT Press.

Chiang C.H., Sirignano W.A. (1993a), *Interacting, convecting, vaporizing fuel droplets with variable properties*, Int. J. Heat Mass Transfer 36, 875.

Chiang C.H., Sirignano W.A. (1993b), *Axisymmetric calculations of three droplet interactions*, Atomization and Sprays 3, 91-107.

Chin J.S., Lefebvre A.H. (1985), *The role of the heat-up period in fuel drop evaporation*, Int. J. of Turbo and Jet Engines 2, 315-325.

Chryssakis A.C., Assanis D.N., Lee J.K., Nishida K. (2003), *Fuel Spray Simulation of High Pressure Swirl injector for DISI Engines and Comparison with Laser Diagnostic Measurements*, SAE paper, 030007.

Cox R.A. and Cole J.A. (1985), *Chemical Aspects of The Autoignition of Hydrocarbon Air Mixture*, Combustion and Flame 60, 109-123

CRC Handbook of Chemistry and Physics, 86th edition (2005), CRC Taylor & Francis, Boca Raton FL, 6-35 – 6-90.

Crua C. (2002), *Combustion Processes in a Diesel Engine*, Ph.D Thesis, University of Brighton.

Dec J.E., Espey C. (1998), *Chemiluminescence Imaging of Autoignition in a Diesel Engine*, SAE paper, 982685

Dombrovsky L.A.(1996), *Radiation Heat Transfer in Disperse System*, Begel House, New York.

Dombrovsky L.A. (2000), *Thermal Radiation from Nonisothermal Spherical Particles a Semitransparent Material*, Int. J. Heat and Mass Transfer 43, 1661-1672.

Dombrovsky L.A. (2002), *A Spectral Model of Absorption and Scattering of Thermal radiation by diesel fuel droplets*, High Temp. 40 (2), 242-248

Dombrovsky L.A. and Sazhin S.S. (2003a), *A parabolic Temperature Profile Model for Heating of Droplets*, ASME J. Heat Transfer 125, 535-537.

Dombrovsky L.A. and Sazhin S.S. (2003b), *A Simplified Non-isothermal Model for Droplet Heating and Evaporation*, Int. Communications Heat and Mass Transfer 30 (6), 787-796.

Dombrovsky L.A. and Sazhin S.S. (2003c), *Absorption of Thermal Radiation in a Semi-transparent Spherical Droplet: a Simplified Model*, Int. J. Heat and Fluid Flow 24 (6), 919-927.

Dombrovsky L.A. and Sazhin S.S. (2004), *Absorption of External Thermal Radiation in Asymmetrically Illuminated Droplets*, J. Quantitative Spectroscopy and Radiation Transfer 87, 119-135.

Dombrovsky L.A., Sazhin S.S., Sazhina E.M., Feng G., Heikal M.R., Bardsley M.E.A., Mikhalovsky S.V. (2001), *Heating and Evaporation of Semi Transparent Diesel Fuel Droplets in Presence of Thermal Radiation*, Fuel 80 (11), 1535-1544.

Douglas J.F., Gasorek J.M., Swaffield (1995), *Fluid Mechanics*, Longman, 3rd Edition.

Druet S., Taran J.P. (1981), *CARS Spectroscopy*, Prog. Quant. Electr 7, 1-72
Durret R.P., Oren D.C., Ferguson C.R. (1987), *A Multidimensional Data Set for Diesel Combustion Model Validation: I. Initial Conditions, Pressure History and Spray Shapes*, SAE Technical Report, 872087.

Dust F., Melling A., Whitelaw J.H. (1981), *Principle and Practice of Laser Doppler Anemometry*, Academic Press, London.

Dwyer H.A, Stapf P., Maly R (2000), *Unsteady vaporization and ignition of a three-dimensional droplet array*, Combustion and Flame 121, 181-94.

El Wakil M.M., Uyehara O.A., Myers P.S. (1954), A *Theoretical Investigation of The Heating-up Period of Injected Fuel Droplets Vaporizing in Air*, NACA Technical Note, 3179.

Eckbreth A.C. (1996), *Laser Diagnostics for Combustion Temperature and Species*, Second Edition, Gordon and Breach, Amsterdam.

Faeth G.M. (1977), *Current Status of Droplet and Liquid Combustion,* Prog. Energy Combustion Science 3, 191-224.

Feng Z.G., Michaelidies E.E. (2000), *A numerical Study of The Transient Heat Transfer from a Sphere at High Reynolds and Peclet Numbers,* Int. Journal Heat and Mass Transfer 43, 219-229.

Fermeglia M., Lapasin R., Torriano G. (1990), *Excess Volumes and Viscosities of Binary Systems Containing 4-methyl 3 pentanone* J. Chem. Eng. Data 35, p. 260-265

Flynn P.F., Durrett R.P., Hunter G.L., Zur Loye A.O., Akinyemi O.C., Dec J.E., Westbrook C.K. (1999), *Diesel combustion: an integrated view combining laser diagnostics, chemical kinetics, and empirical validation*, SAE report, 1999-01-0509.

Frohn A., Roth N. (2000) *Dynamics of Droplets*, Springer-Verlag Berlin and Heidelberg GmbH

Fuchs N.A. (1959), *Evaporation and Droplets Growth in Gaseous Media*, Pergamon Press, London.

Gold M.R., Arcoumanis C., Whitelaw, Gaade J. (2000), *Mixture Preparation Strategy in an Optical Four Valve Engine*, Int. J. Engine Res.

Goldfarb I., Sazhin S.S., Zinoviev A. (2004), *Delayed Thermal Explosion in Flammable Gas Containing Fuel Droplets: Asymptotic Analysis*, Int. J. Engineering Mathematics 50, 399-414

Griffiths J.F. and Barnard J.A. (1995), *Flame and Combustion*, Glasgow: Blackie.

Grisch F., Bouchardy P., Vingert L., Clauss W., Oschwald M., Stel'mack O.M., Smirnov V.V. (2004) *Coherent Anti-Stokes Raman Scattering Measurements at High Pressure in Cryogenic LOX/*GH_2 *Jet Flames, in Liquid Rocket Thrust Chambers: Aspects of Modeling, Analysis and Design*, Progress in Astronautics and Aeronautics 200 (10) 369-404.

Hales J.L., (1967) *Thermodynamic Properties of Organic Oxygen Compounds. Part 18. Vapour heat capacities and heat of vaporization of ethyl ketone, ethyl propyl ketone, methyl isopropyl kethone and methyl phenyl ether,* Trans. Faraday Soc. 63, 1876-1879

Halstead M.R, Kirsch L.J, Quinn C.P., (1977), *The autoicnition of hydrocarbon fuels at high temperature and pressures- fitting of a mathematical model,* Combustion and Flame 30, 45-60.

Handbook of Aviation Fuel Properties (1984), SAE CRC Technical Report No. 530.

Harstad K., Bellan J. (1999), *The Lewis number under supercritical conditions*, Int. J. of Heat Mass Transfer 42, 961-970.

Harstad K., Bellan J. (2001) *Evaluation of commonly used assumptions for isolated and cluster heptane drops in nitrogen at all pressures*, Combustion and Flame 127 ,1861-1879.

Hay N. and Jones P.L. (1972), *Comparison of the Various Correlation for Spray Penetration*, SAE Paper, 720776

Haywood R.J., Nafziger R., Renksizbulut M. (1989), *Detailed Examination of Gas and Liquid Transient Processes in Convection and Evaporation*, ASME J Heat Transfer 111, 495-502.

Heywood J.B. (1988), *Internal Combustion Engine Fundamentals*, McGraw Hill, Singapore.

Hiroyasu H., Kadota T., Arai (1980), *Fuel Spray Characterization in Diesel Engine, Combustion Modelling in Reciprocating Engine*, Plenum Press.

Hiroyasu H., Kadota T. (1974), *Fuel Droplet Size Distribution in Diesel Combustion Chamber*, SAE paper 740715.

Hirschfelder J.O., Curtiss C.F., Bird R.B. (1967), *Molecular theory of gases and liquids,* 4th Edition, John Wiley & Sons, New York/ Chichester.

Holman J.P. (2002), *Heat Transfer*, McGraw-Hill, London

Hoyt C.H., Adel F.S. (1967), *Radiative Transfer*, McGraw-Hill, London.

Huh K., Gosman A.D. (1991), *A phenomenological Model of Diesel Spray Atomization,* Proceeding of the International Conference on Multiphase Flow, Tsukuba, Japan.

Ibrahim E.A., Yang H.Q., Przekwas A.J. (1993), *Modelling of Spray Droplet Deformation and Break-up*, AIAA J. Propulsion and Power 9, 651-654.

Incropera F.P, de Witt D. (1996), *Fundamentals of Heat and Mass Transfer*, Wiley, New York.

Jeffrey A. (1976), *Problems of Laser Velocimeter Application to Combustion System and Combustion Measurement*, Academic Press, London.

Kang S.H., Baek S.W., Choi J.H. (2001), *Autoignition of Sprays in a Cylindrical Combustor*, Int. J. Heat and Mass Transfer 44, 2413-1422.

Karimi K., Sazhina E.M, Abdelghaffar W.A., Crua C., Heikal M.R, Gold M. (2006), *Development in Diesel Spray Characterisation and Modelling,* In: Proceedings of THIESEL-2006, Valencia, Spain.

Kreith F. (1988), *Principles of Heat Transfer,* McGraw Hill, New York

Kryukov A.P., Levashov V.Y., Sazhin S.S. (2004), *Evaporation of Diesel Fuel Droplets: Kinetic versus Hydrodynamic Models,* Int. J. Heat Mass Transfer 47, 2541-2549.

Labowsky M. (1980), *Calculation of the Burning Rate of Interacting Fuel Droplets*, Combustion Science and Technology 22, 217

Lacoste J. (2005) *Characteristics of Diesel Sprays at High Temperatures and Pressures,* PhD thesis, University of Brighton, 2005.

Lacoste J., Crua C., Heikal M.R., Kennaird D.A., Gold M. (2003), *PDA Characterisation of Dense Spray Using a Common-rail Injection System*, SAE International, 2003-01-3085.

Lavieille P., Lemoine F., Lebouché M. (2001), *Evaporating and Combusting Droplet Temperature Measurements using Two Color Laser Induced Fluorescence*, Exp. Fluids 31, 45.

Lavieille P., Lemoine F., Lebouché M. (2002), *Investigation on Temperature of Evaporating Droplets in Linear Stream using Two Color Laser Induced Fluorescence*, Combust. Science Technology. 174, 117.

Lefebvre A.H. (1989), *Atomization and Sprays*, Taylor & Francis.

Liu A.B., Mather D., Reitz R.D. (1993), *Modelling the Effect of Droplet Drag and Break-Up on Fuel Spray*, SAE Paper, 930072.

Lee L., Chuang M. (1997), *Excess volumes of cyclohexane with 2-propanone, 2-butanone, 3-pentanone, 4-methyl-2-pentanone, 1-propanol, and 2-propanol and ethanoic acid + 1-propanol systems*, J. Chem. Eng. Data 42, p. 850-853

Luikov A.V. (1968), *Analytical Heat Transfer Theory*, Academic Press, London.

Maqua C., Castanet G., Doué N., Lavergne G., Lemoine F. (2006), *Temperature measurements of binary droplets using three color laser-induced fluorescence*, Experiments in Fluid 40 786-797.

Maran D.F., Long M.B., Studzinki W.M., Swindal J.C. (1998), *Planar Laser Induced Fluorescene Imaging of Crevice Hydrocarbon Emission*, 27th Symposium on Combustion, The Combustion Institute Pittsburgh.

Marberry M., Ray A.k., Leung K. (1984), *Effect of Multiple Particle Interactions on Burning Droplets*, Combustion and Flame 57, 237

Martynov S, Sazhin S.S., Gorokhovski M., Chtab A., Karimi K., Crua C, Heikal M., (2007) *A modified WAVE model for transient liquid spray*, Int. Journal of Heat and Fluid Flow (submitted)

Mason E.A., Saxena C.S. (1958), *Approximate formula for the thermal conductivity of gas mixtures*, Physics of Fluids 1, 361-369.

Maxwell J.B. (1950), *Data Book on Hydrocarbons: Application to Process Engineering,* D. van Nostrand Company INC., New York.

Melissari B., Agyropoulos S.A. (2005), *Development of a Heat Transfer Dimensionless Correlation for Sphere Immersed in a Wide Range Prandtl Number Fluids*, Int. Journal Heat and Mass Transfer 48, 4333-4341

Michaelides E.E. (2003), *Hydrodynamic force and heat/mass transfer from particles, bubbles, and drops* - the Freeman scholar lecture, ASME J Fluid Engineering 125, 209-238.

Modest M.F. (1993), *Radiative Heat Transfer*, McGraw-Hill.

Morgan R., Gold M., Wray J., and Whelan S. (2001), *A Study of The Formation and Break Up of a Diesel Spray for HSDI Diesel engine Combustion System*, The fifth International Symposium on Diagnostic and Modelling of Combustion in IC Engine, Nagoya.

Nomura J., Ujiie Y., Rath H.J., Sato J., Kono M. (1996), *Experimental Study on High Pressure Droplet Evaporation Using Microgravity Conditions*, 26th Symposium (International) on Combustion, The Combustion Institute, 1267-1273
O'Rourke P.J, and Amsden A.A. (1987), *The TAB Method for Numerical Calculation of Spray Droplet Break-up*, SAE paper, 872089.

Panton R.L. (1996), *Incompressible Flow*, Wiley, New York.

Paredes M.L.L., Nobrega R., Tavares F.W. (2000), *A completely analytical equation of state for mixture of square-well chain fluid of variable well width*, In 'XIX Inter American Congress of Chemical Engineering', Agios de Sao Pedro, Brazil, 24-27 September 2000, paper No. 396.

Patankar S.V. (1980), *Numerical Heat Transfer and Fluid Flow*, McGraw-Hill Book Company, New York.

Patterson M.A and Reitz R.D. (1998), *Modelling the Effects of Fuel Spray Characteristic on Diesel Engine Combustion and Emission*, SAE paper 980131

Poling B.E., Prausnitz J.M., O'Connell J. (2000), *The Properties of Gases and Liquids,* McGraw- Hill, New York, Chichester.

Pozorski J., Sazhin S.S., Waclawczyk M., Crua C., Kennaird D.A., Heikal M.R. (2002), *Spray Penetration in Turbulent Flow*, Flow, Turbulence and Combustion, 68, 153-165.

Raznjevic K. (1976), *Handbook of Thermodynamic Tables and Charts*, McGraw Hill, London

Reitz R.D. (1987), *Modelling Atomisation Process in High-Pressure Vaporizing Spray*, Atomisation and Spray Technology 3, 309-337.

Reitz R.D, Kong S.C., Senecal P.K. (1999), *Developments in Spray Modelling in Diesel and Direct Injection Gasoline Engine*, Oil & Gas Science and Technology 4, 197-204.

Renksizbulut M., Yuen M.C. (1983), *Experimental Study of Droplet Evaporation in a High Temperature Air Stream,* ASME J Heat Transfer 105, 384-388.

Rotondi R., Bella G., Grimaldi C., Postrioti L. (2001), *Atomization of High-Pressure Diesel Spray: Experimental Validation of New Breakup Model*, SAE paper, 2001011070.

Sangiovanni J.J., Labowski M. (1982), *Burning Times of Linear Fuel Droplet Arrays: A comparison of Experiment and Theory*, Combustion and Flame 45, 15

Sangiovanni J.J., Kesten A.S. (1976), *Effect of droplet interaction on ignition in monodispersed droplet stream*, Sixteenth International Symposium on Combustion, The Combustion Institute

Sazhin S.S. (2006), *Advanced Models of Fuel Droplet Heating and Evaporation,* Progress in Energy and Combustion Science 32, 162-214.

Sazhin S.S, Sazhina, E.M., Faltsi-Saravelou O., Wild P. (1996), *The P-1 Model for Thermal Radiation Transfer: Advantages and Limitations*, Fuel 75, 289-294.

Sazhina E.M., Sazhin S.S., Heikal M.R., Marooney C.J. (1999), *The Shell Autoignition Model: Applications to Gasoline and Diesel Fuels*, Fuel 78, 389-401.

Sazhin S.S., Heikal M.R., Marooney C.J., Mikhalovsky S.V. (1999), *The Shell Autoignition Model: A New Mathematical Formulation*, Combustion and Flame 117, 529-540

Sazhina E.M., Sazhin S.S., Heikal M.R., Babushok V.I., Johns R.J.R. (2000), *A Detailed Modelling of the Spray Ignition Process in Diesel Engines*, Combustion Science and Technology 160, 317-344.

Sazhin S.S., Feng G., Heikal M.R., Goldfarb I., Goldshtein V. and Kuzmenko G. (2001a), *Thermal Ignition Analysis of a Monodisperse Spray with Radiation.* Combustion and Flame 124 (4), 684-701.

Sazhin S.S., Feng G., Heikal M.R. (2001b), *A Model for Fuel Spray Penetration*, Fuel 80, 2171-2180.

Sazhin S.S., Gol'dshtein V.A., Heikal M.R. (2001c), *A Transient Formulation of Newton's Cooling Law for Spherical Bodies*, ASME Journal of Heat Transfer 123, 63-64

Sazhin S.S., Crua C., Kennaird D., Heikal M.R. (2003), *The Initial Stage of Fuel Spray Penetration*, Fuel 82, 875-885.

Sazhin S.S., Abdelghaffar W.A., Sazhina E.M., Mikhalovsky S.V., Meikle S.T., Bai C. (2004a), *Radiative Heating of Semi-transparent Diesel Fuel Droplets*, ASME J. Heat Transfer 126, 105-109; Erratum 126, 490-491

Sazhin S.S., Krutitskii P.A., Abdelghaffar W.A., Mikhalovsky S.V., Meikle S.T., Heikal M.R. (2004b), *Transient Heating of Diesel Fuel Droplets*, Int. J. Heat Mass Transfer 47, 3327-3340 .

Sazhin S.S., Abdelghaffar W.A., Krutitskii P.A., Sazhina E.M., Heikal M.R. (2005a)*, New Approaches to Numerical Modelling of Droplet Transient Heating and Evaporation*, Int. Journal of Heat and Mass Transfer 48, 4215-4228.

Sazhin S.S., Abdelghaffar W.A., Sazhina E.M., Heikal M.R. (2005b), *Models for Droplet Transient Heating: Effects on Droplet Evaporation, Ignition, and Break-up*, Int. J. Thermal Science 44, 610-622

Sazhin S.S., Kristyadi T., Abdelghaffar W.A., Heikal M.R. (2006), *Models for Fuel Droplet Heating and Evaporation: Comparative Analysis*, Fuel 85, 1613-1630.

Sazhin S.S., Kristyadi T., Abdelghaffar W.A., Begg S., Heikal M.R., Mikhalovsky S.V., Meikle S.T., Al-Hanbali O. (2007) *Approximate Analysis of Thermal Radiation Absorption in Fuel Droplets*, ASME Journal of Heat Transfer 129, 1246-1255.

Schäpertöns H. and Lee W. (1985), *Multidimensional Modelling of Knocking Combustion in SI Engine*, SAE paper no. 850502

Siegel R. and Howell Jr.J.P. (1992), *Thermal Radiation Heat Transfer*, Hemisphere Publishing Corporation.

Silverstein M. and Webster F.X. (2005), *Spectrometric Identification of Organic Compounds*, Wiley, Chichester, 7th Edition.

Sirignano W.A. (1999), *Fluid Dynamics and Transport of Droplets and Sprays*, Cambridge University press.

Sirignano W.A., Law C.K. (1978), *Transient Heating and Liquid Phase Mass Diffusion in Droplet Vaporization*, Advances in Chemistry Series, American Chemical Society 166, 1-26.

Spalding D.B. (1971) *Concentration Fluctuations in a Round Turbulent Free Jet*, Chemical Engineering Science 26, 95-107

Tabaczyski R.J. (1982), *Effect of Inlet and Exhaust System Design on Engine Performance*, SAE paper, 821577.

Tanabe M., Kono M., Sato J., Koeing J., Eigenbrod C., Dinkelacker F., Rath H.J. (1995), *Two Stage Ignition of n-Heptane Isolated Droplets,* Combustion Science and Technology 108, 103-119

Tanner F.X. (1997), *Liquid Jet Atomization and Droplet Break-up Modelling of Non-Evaporating Diesel Fuel Sprays*, SAE paper, 970050.

Theobald M.A. (1986), *Numerical Simulation of Diesel Autoignition*, PhD thesis, MIT

Touloukian T.S., Makita T. (1970), *Specific Heat Non Metallic Liquid and Gases*, IFI/Plenum, New York

Versteeg H.K., Malalasekera W. (1999), *An Introduction to Computational Fluid Dynamics*, Longman, Harlow.

Wakisaka (1988), *Induction Swirl in a Multiple Intake Valve Engine Three Dimensional numerical analysis*, Proceeding of the Institution of Mechanical Engineers.

Watrasiewicz B.M. and Rudd M.J. (1977), Laser *Doppler Measurements*, Butterworths & CO Ltd.

Yao G.F., Abdel-Khalik S.I., Ghiaasiaan S.M. (2003), *An Investigation of Simple Evaporation Models Used in Spray Simulations*, ASME Journal of Heat Transfer 125, 179-182.

Zhao H. and Ladommatos (1998), *Optical Diagnostics For in Cylinder Mixture Formation measurement in IC Engine*, Prog. Energy Combustion Sci 24, 221-225.

Papers published by the author

International refereed journals

Sazhin S.S., Kristyadi T., Abdelghaffar W.A., Heikal M.R. (2006), *Models for Fuel Droplet Heating and Evaporation: Comparative Analysis*, Fuel 85, 1613-1630.

Sazhin S.S., Kristyadi T., Abdelghaffar W.A., Begg S., Heikal M.R., Mikhalovsky S.V., Meikle S.T., Al-Hanbali O. (2007) *Approximate Analysis of Thermal Radiation Absorption in Fuel Droplets*, ASME Journal of Heat Transfer 129, 1246-1255.

Maqua C., Castanet G., Grish F., Lemoine F., Kristyadi T., Sazhin S.S. (2007), *Monodisperse Droplet Heating and Evaporation: Experimental Study and Modelling*, Int. Journal Heat and Mass Transfer (submitted).

Sazhin S.S., Martynov S.B., Kristyadi T., Crua C., Heikal M.R. (2007), *Diesel Fuel Spray Penetration, Heating, Evaporation and Ignition: Modelling Versus Experimentation,* Int. Journal of Engineering Modelling and Simulation (submitted)

Refereed international conferences proceeding

Sazhin S.S., Kristyadi T., Heikal M.R., Abdelghaffar W.A., Shishkova I.N. (2007), *Fuel Droplet Heating and Evaporation: Analysis of Liquid and Gas Phase Models*, SAE paper 07SFL-18 - 2007-01-0019

Sazhin S.S., Crua C., Martynov S.B., Kristyadi T. and Heikal M.R. (2007), *Advanced Models for Droplet Heating and Evaporation: Effect on the Autoignition of Diesel Fuel Sprays*, Proceedings of the Third European Combustion Meeting ECM 2007, paper 15-2.

Sazhin S.S., Martynov S.B., Kristyadi T., Crua C., and Heikal, M.R (2007), *Models for Droplet Heating and Evaporation: Application to the Autoignition Process in Diesel Engines,* Proceedings of the PTNSS Congress (Krakow, Poland 20-23 May 2007) pp. 246-257, Published in Combustion engines V.2 Mixture Formation, Ignition & Combustion, by 'Polskie Towarzystwo Naukowe Solnikow Spalinowych'

Sazhin S.S., Shishkova I.N, Kristyadi T., Martynov S.B., Heikal M.R. (2007), *Droplet Heating and Evaporation : Hydrodynamic and Kinetic Models*, Proceedings of the Baltic Heat Transfer Conference (St. Petersburg, September 19-21, 2007) pp. 405-414, In ‘Advanced in Heat Transfer’, Publishing House of Polytechnical University (St. Petersburg, Rusia).

Internal conferences

Kristyadi T. (2005), *Modelling of Droplet Heating and Evaporation*, Engineering Research in Action, Internal Conference, University of Brighton.

Kristyadi T. (2006), *Models of Droplet Heating and Evaporation*, Engineering Research in Action, Internal Conference, University of Brighton.

Appendix A

Physical properties of fuel based on normalised temperature

Some of physical properties of fuels used in this thesis (e.g : n-heptane, tetradecane, n-dodecane and Diesel fuel) are given in Appendix A of Sazhin et al. (2005b), where in most cases they are approximated as polynomials of the absolute temperature T. This presentation, however, has a major drawback. For realistic temperatures high powers of T lead to rather large numbers. Hence, to get required values of these properties these large numbers are often multiplied by very small numbers and this potentially can lead to errors in calculations. To minimise these errors, rather large numbers of digits (up to 11) were needed to be retained in these formulae. Also, this approximation of properties made it rather difficult to infer their values for widely used temperatures (say room temperature 300 K).

These factors were the main driving force behind our intention to look for an alternative approximation of physical properties given in the abovementioned Appendix. We presented these properties not as polynomials of T, but as polynomials of the normalised temperature:

$$\widetilde{T} = \frac{T - T_0}{T_0},$$

where $T_0 = 300$ K. There are at least two main advantages of this approximation of physical properties. Firstly, in contrast to T, the values of $\widetilde{T}$ vary in a rather narrow range (between 0 and 3 in most cases). Hence, the coefficients of the polynomials are expected to be comparable with the values of the properties in most cases. Also, the number of digits in the coefficients required can be relatively small (about 3-4 in most cases). Secondly, the zeroth term of the polynomials automatically gives the values of properties at room temperature. For consistency, even if the approximations different from polynomials are used, the properties are still presented as functions of $\widetilde{T}$. The values of parameters, obtained using new formulae, are very close to the ones based on the formulae given in Sazhin et al. (2005b), the corresponding plots are indistinguishable. Some relevant plots are shown at Figure A.1 to Figure A.12. In these figures, plots 1 refer to the approximations of properties based on temperatures as used by Sazhin et al. (2005b), and plots 2 refer to the new approximations based on the normalised temperatures.

Physical properties of tetradecane

Latent heat of evaporation:

Using data presented in Maxwell (1950), the latent heat of evaporation is approximated as:

$$L = 3.60 \text{ x } 10^5 - 1.17 \text{ x } 10^5 \tilde{T} + 4.40 \text{ x } 10^3 \tilde{T}^2 - 2.93 \text{ x } 10^4 \tilde{T}^3 - 5.77 \text{ x } 10^4 \tilde{T}^4 - 1.15 \text{ x } 10^4 \tilde{T}^5 + 1.57 \text{ x } 10^4 \tilde{T}^6 \text{ J/kg}$$

when $\tilde{T} < \tilde{T}_{\mathrm{cr}} = 1.31$ (normalised critical temperature) and zero otherwise (Poling et al., 2000)

Specific heat capacity of liquid:

Using data presented in Maxwell (1950), the specific heat capacity of liquid is approximated as:

$$c_{\mathrm{l}} = 2220.30 \exp\left(0.42\tilde{T}\right) \text{ J/(kg·K)}$$

The specific heat capacity of vapour at constant pressure:

The specific heat capacity of vapour at constant pressure is approximated as (Poling et al., 2000):

$$c_{\mathrm{pF}} = 1.66 \text{ x } 10^3 + 1.39 \text{ x } 10^2 \tilde{T} - 2.51 \text{ x } 10^2 \tilde{T}^2 + 15.11\tilde{T}^3 + 0.69\tilde{T}^4 \text{ J/(kg.K)}$$

Saturated vapour pressure

The saturated vapour pressure is approximated as:

$$p_{\mathrm{s}} = 10^5 \left(9.00 \text{ x } 10^{-5} + 7.50 \text{ x } 10^{-3} \tilde{T} - 0.23\tilde{T}^2 + 2.08\tilde{T}^3 - 6.86\tilde{T}^4 + 12.86\tilde{T}^5 - 3.71\tilde{T}^6\right) \text{ Pa}$$

when $\tilde{T} < \tilde{T}_{\mathrm{cr}}$, and zero otherwise (Poling et al., 2000).

The density of liquid:

Using data presented in Maxwell (1950), the density of liquid is approximated as:

$$\rho_{\mathrm{l}} = 762.94 - 194.21\tilde{T} - 42.13\tilde{T}^2 \text{ kg/m}^3$$

and the thermal conductivity of liquid is approximated as

$$k_1 = 0.14 - 5.47 \text{ x } 10^{-2}\tilde{T} - 2.05 \text{ x } 10^{-2}\tilde{T}^2 + 1.61 \text{ x } 10^{-2}\tilde{T}^3 \text{ W/(m· K)}$$

when $\tilde{T} < \tilde{T}_{\rm cr}$, and zero otherwise.

Comparison of two approximations of physical properties of tetradecane

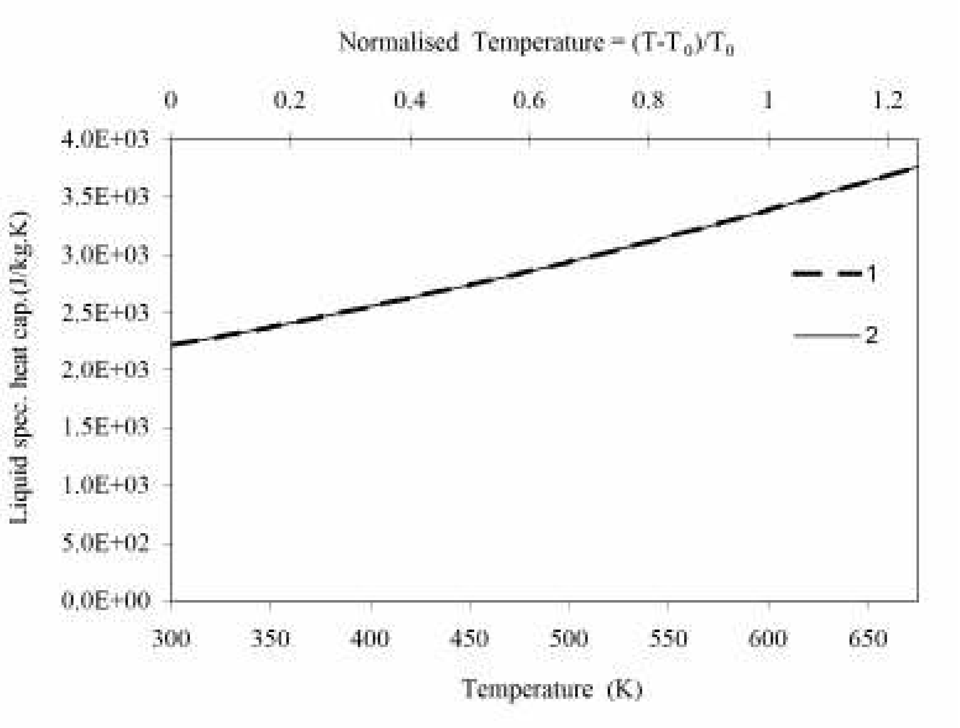

Figure A.1 The liquid specific heat capacity of tetradecane as predicted by Sazhin et al. (2005b) (plot 1) and the present approximation (plot 2)

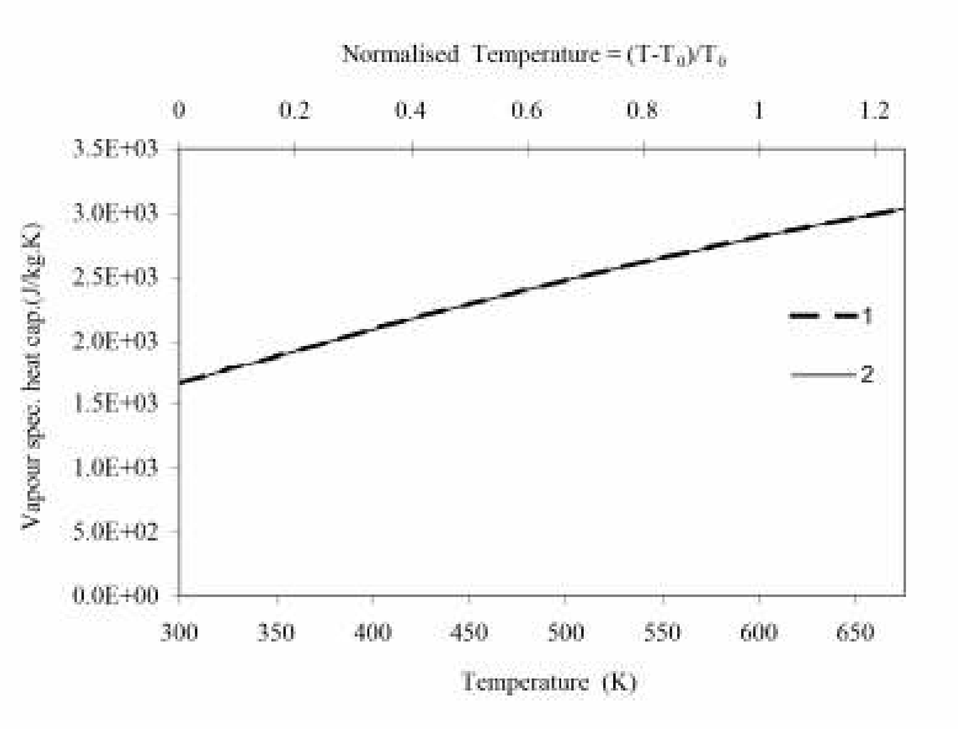

Figure A.2 The same as Figure A.1 but for vapour specific heat capacity

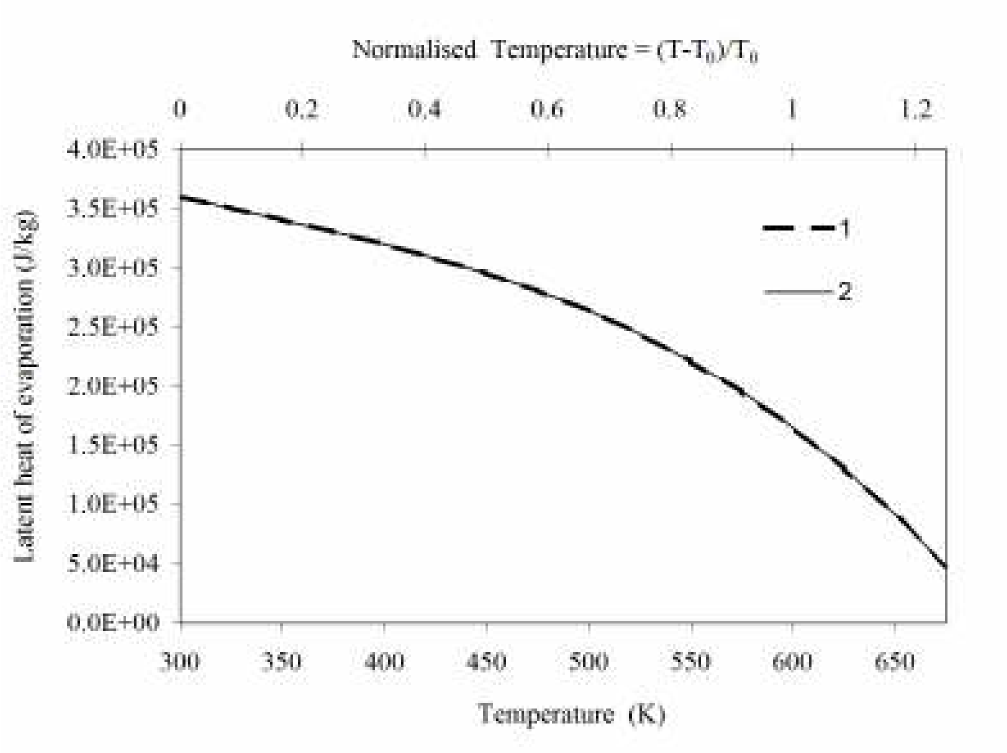

Figure A.3 The same as Figures A.1-A.2 but for latent heat of evaporation.

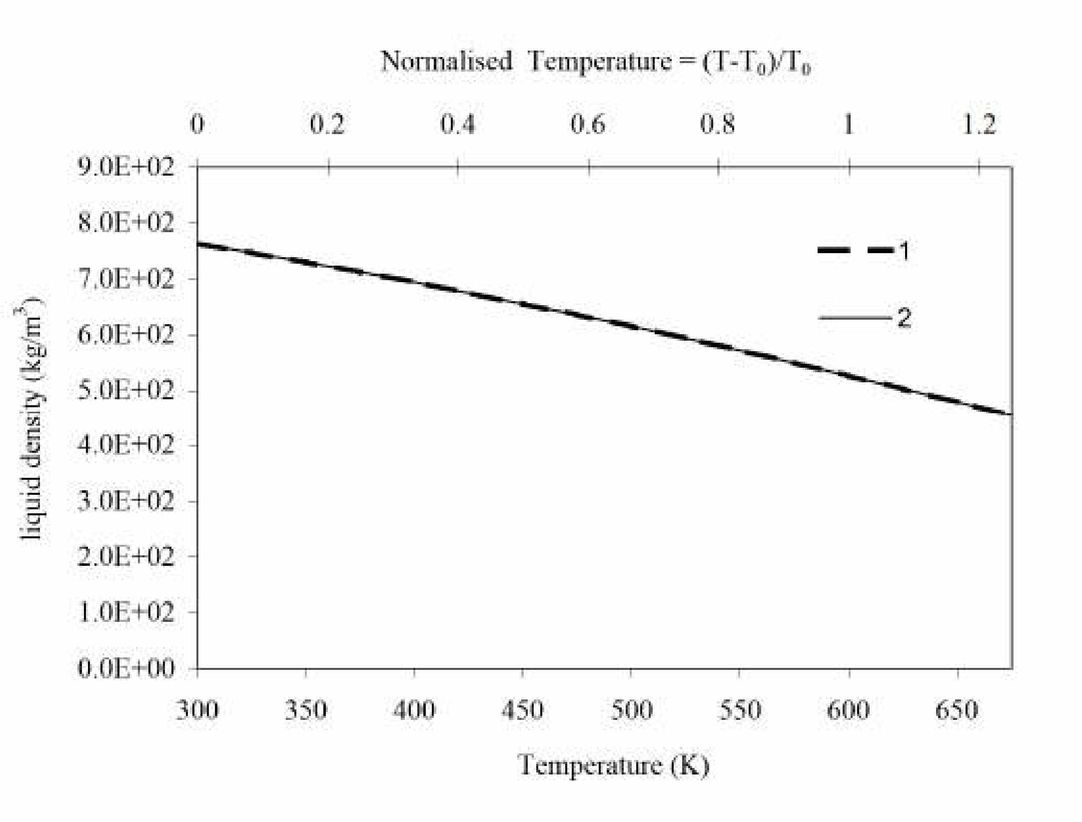

Figure A.4 The same as Figures A.1-A.3 but for liquid density

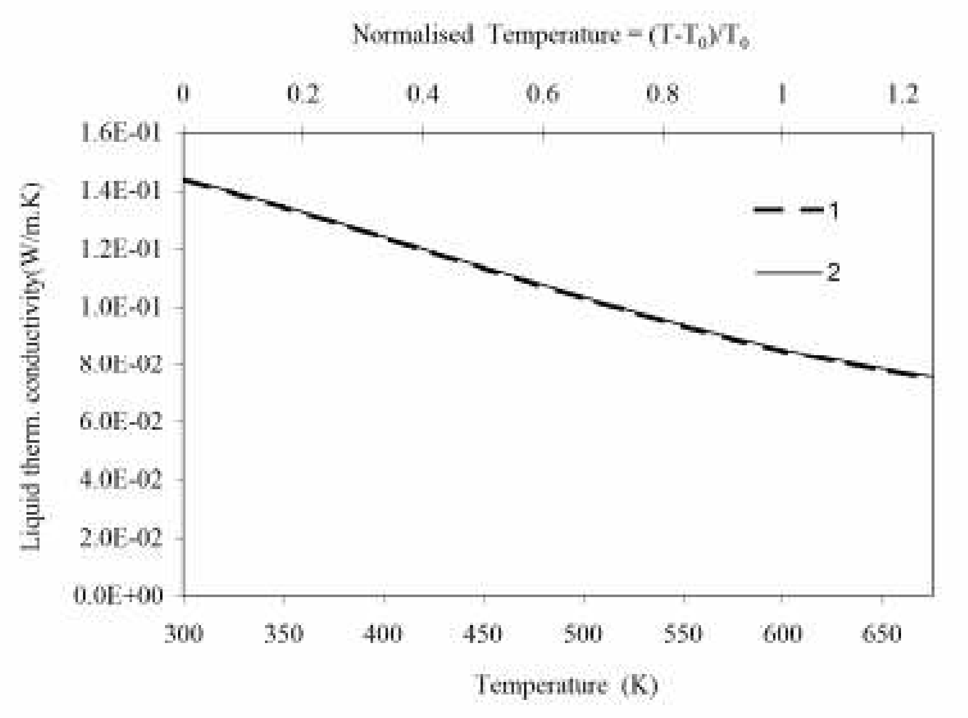

Figure A.5 The same as Figures A.1-A.4 but for liquid thermal conductivity

Physical Properties of n-heptane

Latent heat of evaporation:

Latent heat of evaporation is approximated as (Chin et al., 1985)

$$L = 317.8x10^3\left(\frac{\tilde{T}_{\mathrm{cr}} - \tilde{T}}{\tilde{T}_{\mathrm{cr}} - \tilde{T}_{\mathrm{b}}}\right)^{0.38} \text{ J/kg,}$$

when $\tilde{T} < \tilde{T}_{\mathrm{cr}}$ and zero otherwise, where $\tilde{T}_{\mathrm{cr}} = 0.800$ and $\tilde{T}_{\mathrm{b}} = 0.238$

Specific heat capacity of liquid:

Specific heat capacity of liquid is approximated as (Maxwell, 1950):

$$c_{\mathrm{l}} = 2.25\,\mathrm{x}\,10^3 + 1.11\,\mathrm{x}\,10^3\tilde{T} + 1.87\,\mathrm{x}\,10^3\tilde{T}^2 - 4.89\,\mathrm{x}\,10^3\tilde{T}^3 + 5.16\,\mathrm{x}\,10^3\tilde{T}^4 \text{ J/(kg· K)}$$

Specific heat capacity of vapour at constant pressure:

The specific heat capacity of vapour at constant pressure is approximated as (Poling et al., 2000):

$$c_{\mathrm{pF}} = 1662.50 + 1.28\,\mathrm{x}\,10^3\tilde{T} + 121.75\tilde{T}^2 - 240.64\tilde{T}^3 + 52.22\tilde{T}^4 \text{ J/(kg.K)}$$

The saturated vapour pressure is assumed to be equal to (Poling et al., 2000):

$$p_{\mathrm{s}} = 10^5\left(0.082 + 1.078\tilde{T} + 8.707\tilde{T}^2 + 11.030\tilde{T}^3 + 64.967\tilde{T}^4 - 40.802\tilde{T}^5 + 7.740\tilde{T}^6\right) \text{ Pa}$$

when $\tilde{T} < \tilde{T}_{\mathrm{cr}}$ and zero otherwise.

The density of Liquid:

Using data presented in Maxwell (1950), the density of liquid is approximated as:

$$\rho_{\mathrm{l}} = 678.93 - 248.73\tilde{T} - 251.16\tilde{T}^2 + 735.16\tilde{T}^3 - 882.37\tilde{T}^4 \text{ kg/m}^3$$

when $\tilde{T} \leq 0.793$,

$$\rho_{\mathrm{l}} = -3.16x10^5 + 8.04x10^5\tilde{T} - 5.10x10^5\tilde{T}^2 \text{ kg/m}^3$$

when $\tilde{T} > 0.793$.

Liquid thermal conductivity:

Using data presented in Maxwell (1950), the thermal conductivity of liquid is approximated as:

$$k_{\mathrm{l}} = 0.122 - 0.137\tilde{T} \text{ W/(m·K)}$$

when $\widetilde{T} < \widetilde{T}_{cr}$, and zero otherwise.

Comparison of two approximations of physical properties of n-heptane

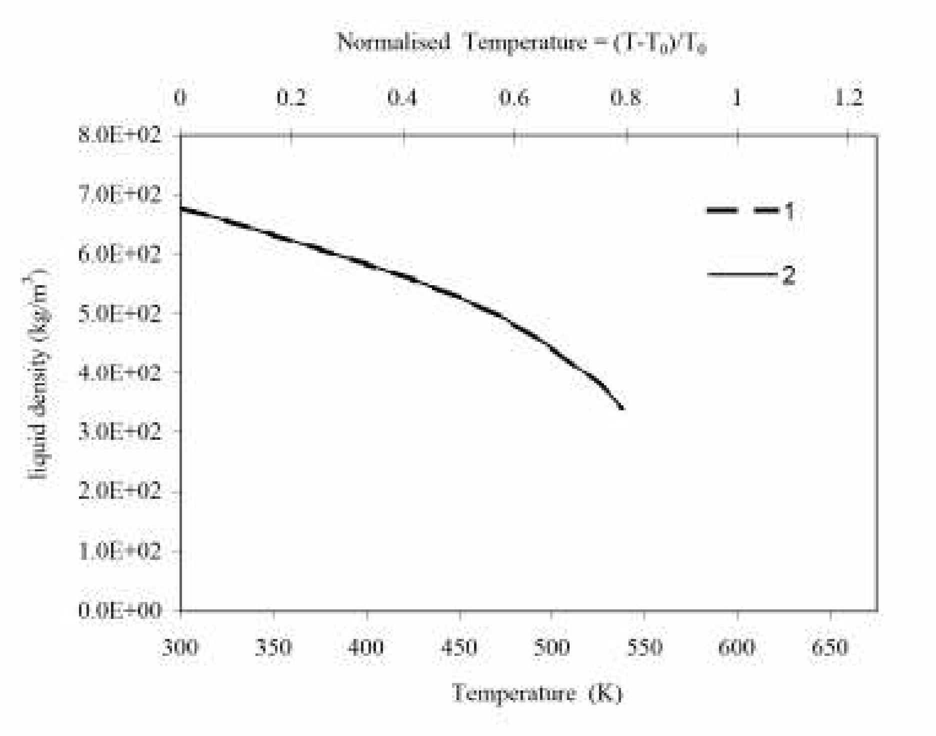

Figure A.6 The liquid density of n-heptane as predicted by Sazhin et al. (2005b) (plot 1) and the present approximation (plot 2)

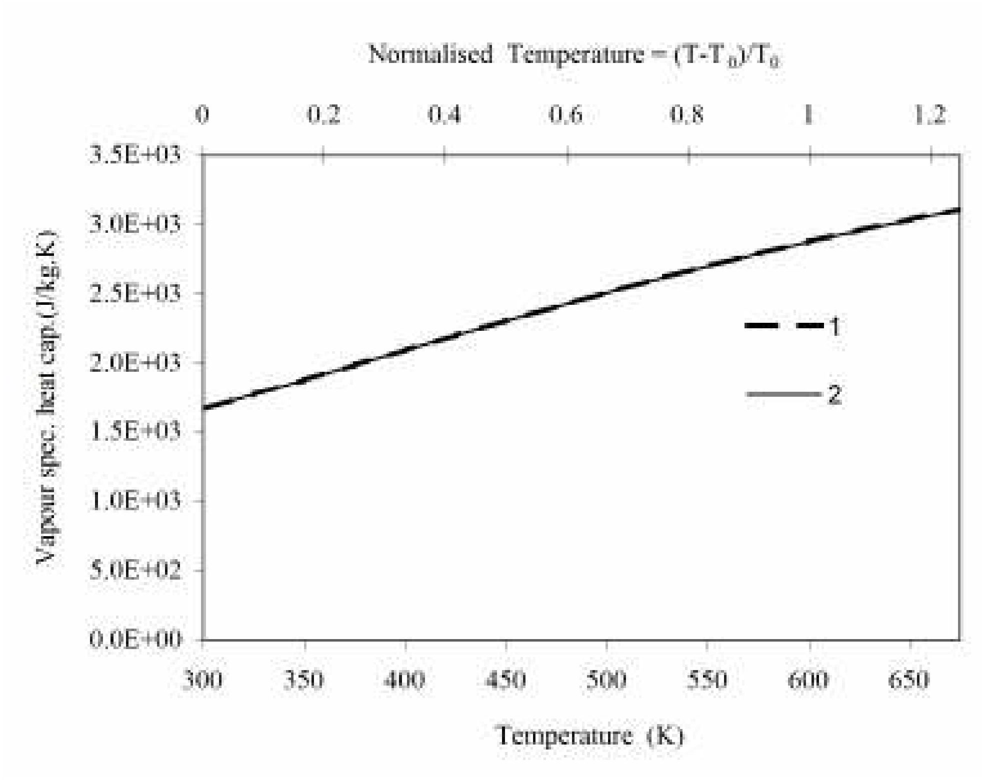

Figure A.7 The same as Figure A.6 but for vapour specific heat capacity

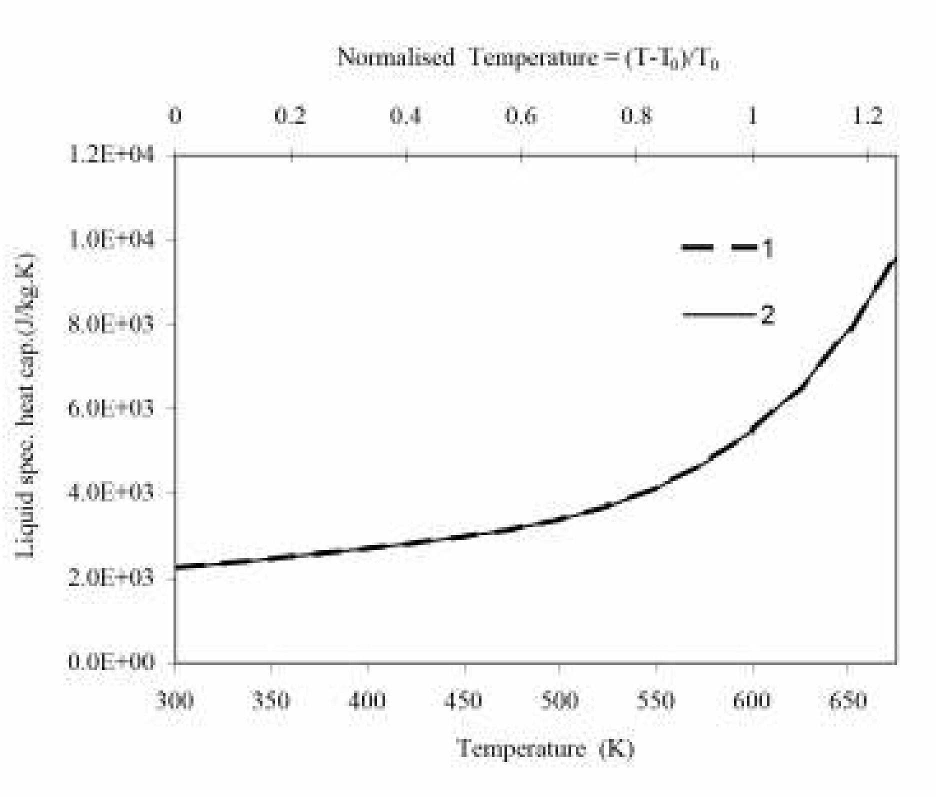

Figure A.8 The as Figures A.6-A.7 but for liquid specific heat capacity

Physical properties of n-dodecane:

Latent heat of evaporation:

Latent heat of evaporation is approximated as (Poling et al., 2000; Borman et al., 1962):

$$L = 4.45 \text{ x } 10^5 + 334.92\tilde{T} + 1.01 \text{ x } 10^5 \tilde{T}^2 + 9.96 \text{ x } 10^4 \tilde{T}^3 - 1.17 \text{ x } 10^5 \tilde{T}^4 \text{ J/kg,}$$

when $\tilde{T} < \tilde{T}_{\mathrm{cr}} = 1.1967$ and zero otherwise.

Specific heat capacity of liquid:

Using data presented in Maxwell (1950), the specific heat capacity of liquid is approximated as:

$$c_{\mathrm{l}} = 2172.50 + 1260.50\tilde{T} - 63.38\tilde{T}^2 + 45.17\tilde{T}^3 \text{ J/(kg·K)}$$

Specific heat capacity of vapour:

The specific heat capacity of vapour at constant pressure is approximated as (Durret et al., 1987):

$$c_{\mathrm{pF}} = 1594.60 + 1.15\tilde{T} - 100.56\tilde{T}^2 - 28.56\tilde{T}^3 + 5.07\tilde{T}^4 - 0.25\tilde{T}^5 \text{ J/(kg.K)}$$

The saturated vapour pressure is assumed to be equal to

$$p_{\mathrm{s}} = 6894.76 \text{ x } \exp\left[12.13 - 3743.84/\left(300\tilde{T} + 207\right)\right] \text{ Pa}$$

when $\tilde{T} < \tilde{T}_{\mathrm{cr}} = 1.1967$ and zero otherwise

Density of liquid:

The density of liquid is approximated as (Handbook of Aviation Fuel Prop., 1984):

$$\rho_{\mathrm{l}} = 744.96 - 230.42\tilde{T} + 40.90\tilde{T}^2 - 88.70\tilde{T}^3 \text{ kg/m}^3$$

Thermal conductivity of liquid:

The thermal conductivity of liquid n-dodecane and liquid diesel fuel in W/(m· K) was used in the table form (see table A 1: (Poling et al., 2000))

Surface tension:

The surface tension is approximated as (Duret et al., 1987):

$$\sigma_s = 0.0528\left(1 - \frac{\widetilde{T}+1}{\widetilde{T}_{cr}+1}\right)^{0.121} \text{ N/m}$$

Comparison of two approximations of physical properties of n-dodecane

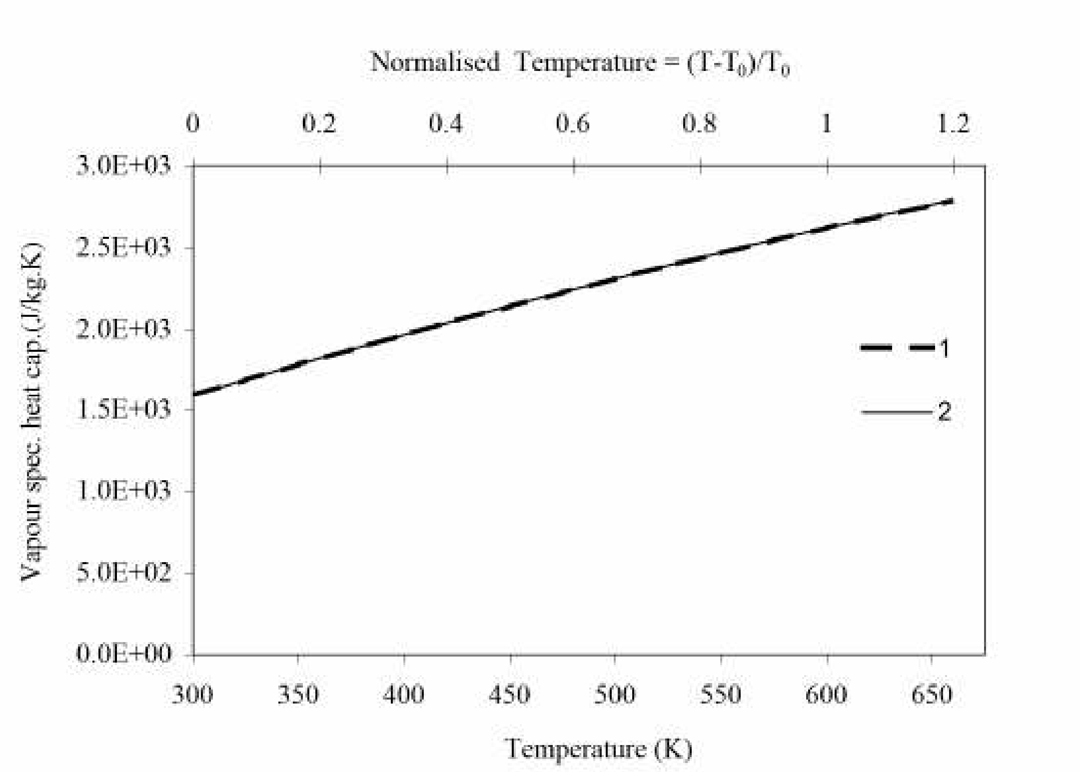

Figure A.9 The vapour specific heat capacity of n-dodecane as predicted by Sazhin et al. (2005b) (plot 1) and the present approximation (plot 2)

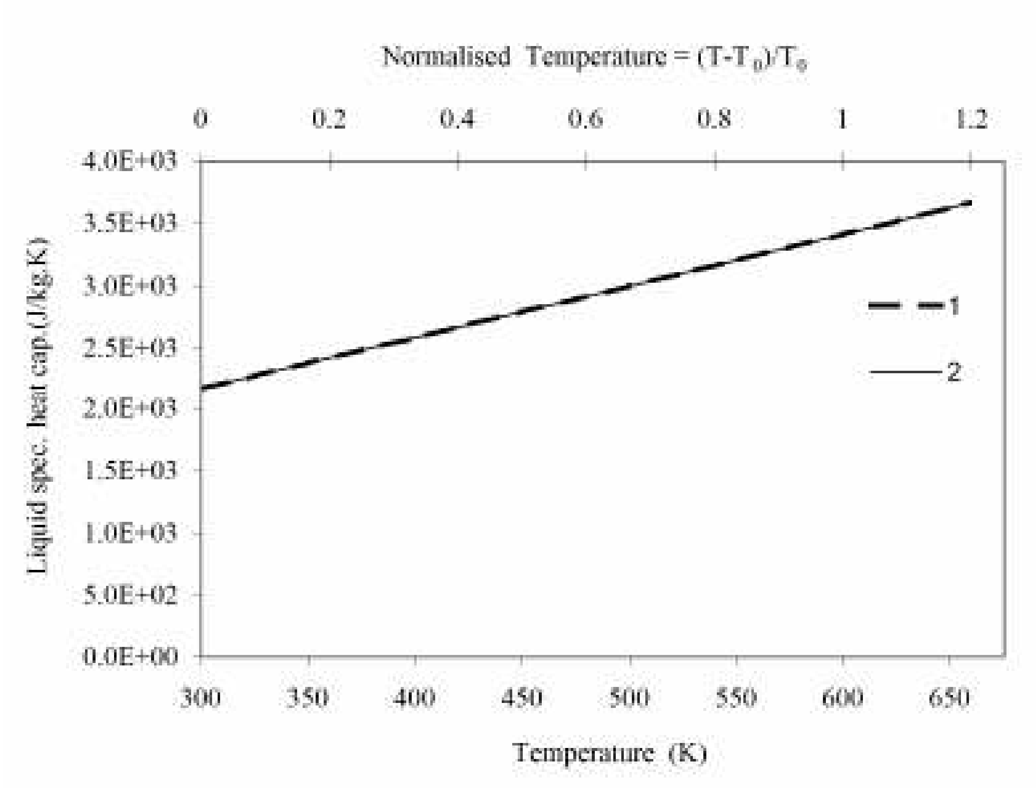

Figure A.10 The same as Figure A.9 but for liquid heat capacity

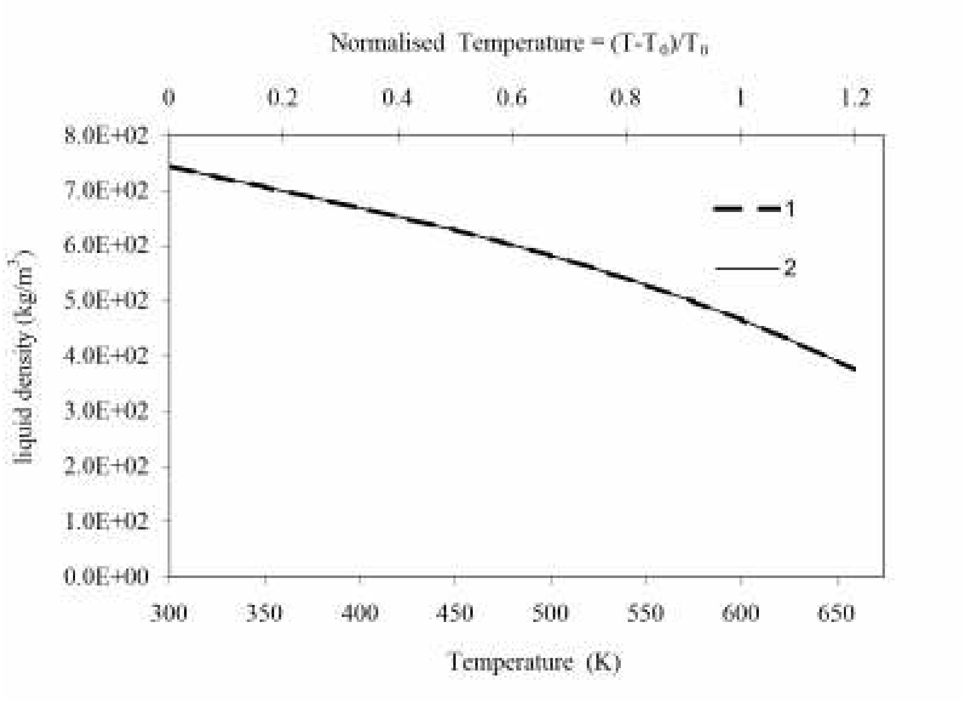

Figure A.11 The same as Figures A.9-A.10 but for liquid density.

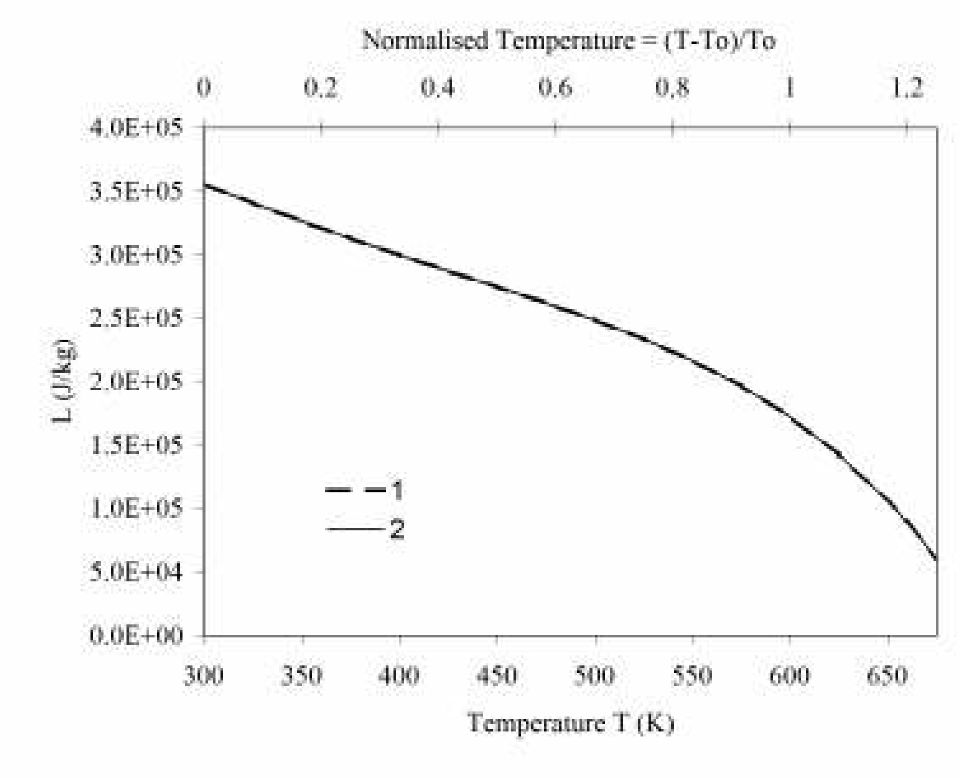

Figure A.12 The same as Figures A.9-A.11 but for latent heat of evaporation

Physical properties of Diesel fuel

In this section a compilation of physical properties of a 'typical' Diesel fuel is given. These are expected to differ slightly from any particular Diesel fuel.

Latent heat of evaporation:

Latent heat of evaporation is approximated as (Chin et al., 1987):

$$L = 254 \text{ x } 10^3 \left(\frac{\tilde{T}_{\mathrm{cr}} - \tilde{T}}{\tilde{T}_{\mathrm{cr}} - \tilde{T}_{\mathrm{b}}} \right)^{0.38} \text{ J/kg}$$

when $\tilde{T} < \tilde{T}_{\mathrm{cr}} = 1.419$, and zero otherwise, where $\tilde{T}_{\mathrm{b}} = 0.788$.

Specific heat capacity of liquid:

The specific heat capacity of liquid is approximated as (Duret et al., 1987):

$$c_{\mathrm{l}} = 1896.60 + 1366.20\tilde{T} - 266.40\tilde{T}^2 \text{ J/(kg.K)}$$

The specific heat capacity of vapour at constant pressure is assumed to be equal to that of n-dodecane (Duret et al., 1987).

Saturated vapour pressure

The saturated vapour pressure (in Pa) is assumed to be equal to (Chin et al., 1985):

$$p_s = \begin{cases} 1000\ \exp\left[8.59 - 2591.52/\left(257 + 300\tilde{T}\right)\right] & \text{when } \tilde{T} < 0.267 \\ 1000\ \exp\left[14.06 - 4436.10/\left(257 + 300\tilde{T}\right)\right] & \text{when } 0.267 \le \tilde{T} < 0.667 \\ 1000\ \exp\left[12.93 - 3922.51/\left(257 + 300\tilde{T}\right)\right] & \text{when } 0.667 \le \tilde{T} < 1.067 \\ 1000\ \exp\left[16.20 - 5810.82/\left(257 + 300\tilde{T}\right)\right] & \text{when } 1.067 \le \tilde{T} < \tilde{T}_{\mathrm{cr}} \end{cases}$$

Density of liquid:

The density of liquid is approximated as (Handbook of Aviation Fuel Properties, 1984):

$$\rho_l = 840/(1.008 + 0.201\tilde{T})\ \text{kg/m}^3$$

Surface tension:

The surface tension is approximated as (Duret et al., 1987):

$$\sigma_s = 0.059\left(1 - \frac{\tilde{T} + 1}{\tilde{T}_{\mathrm{cr}} + 1}\right)^{0.121}\ \text{N/m}$$

Thermal conductivity

Thermal conductivities of Diesel fuel are shown in Table A 1 (Poling et al., 2000)

Table A1. The liquid thermal conductivities of Diesel fuel and n-dodecane

$\tilde{T}$	k_l (W/mK)	
	Diesel fuel	n-dodecane
0	0.145	0.139
0.033	0.143	0.136
0.067	0.141	0.134
0.100	0.139	0.132
0.133	0.137	0.13
0.167	0.135	0.128
0.200	0.133	0.126
0.233	0.131	0.123
0.267	0.129	0.121
0.300	0.127	0.119

0.333	0.125	0.117
0.367	0.123	0.115
0.400	0.121	0.112
0.433	0.119	0.11
0.467	0.117	0.108
0.500	0.115	0.106
0.533	0.113	0.103
0.567	0.111	0.101
0.600	0.109	0.098
0.633	0.107	0.096
0.667	0.104	0.093
0.700	0.102	0.091
0.733	0.1	0.088
0.767	0.098	0.086
0.800	0.096	0.083
0.833	0.094	0.08
0.867	0.091	0.077
0.900	0.089	0.073
0.933	0.086	0.07
0.967	0.084	0.066
1.000	0.081	0.062
1.033	0.078	0.058
1.067	0.076	0.053
1.100	0.073	0.047
1.133	0.069	0.04
1.167	0.066	0.03
1.200	0.062	
1.233	0.059	
1.267	0.054	
1.300	0.049	
1.333	0.043	
1.367	0.036	
1.400	0.025	

Properties of 3-pentanone

Latent heat of evaporation:
Using data presented in (CRC Handbook, 2005), the latent heat of evaporation is approximated as:

$$L = -3.845 \text{ x } 10^4 \tilde{T}^4 + 1.764 \text{ x } 10^5 \tilde{T}^3 - 1.896 \text{ x } 10^4 \tilde{T}^2 - 65.22\tilde{T} + 3.889 \text{ x } 10^5 \text{ J/kg}$$

when $\tilde{T} < \tilde{T}_{cr}$=0.87 and zero otherwise.

Saturated vapour pressure:
The saturated vapour pressure is approximated as (CRC Handbook, 2005):

$$p_s = 10^5 (0.154\tilde{T}^4 + 1.056\tilde{T}^3 + 2.156\tilde{T}^2 - 0.205\tilde{T} + 0.110) \text{ N/m}^2$$

Liquid densities:
Using data presented by Lee et al. (1997), the density of liquid is approximated as:

$$\rho_1 = -26.112\tilde{T}^4 + 91.16\tilde{T}^3 - 88.184\tilde{T}^2 - 61.341\tilde{T} + 815.17 \text{ kg/m}^3$$

Liquid viscosities:
Using data presented in (CRC Handbook, 2005), the liquid viscosities is approximated as:

$$\mu_1 = (15.0\tilde{T}^2 - 5.56\tilde{T} + 4.44)10^{-4} \text{ Ns/m}^2$$

Vapour viscosities:
Vapour dynamic viscosity is taken at room temperature $\tilde{T} = 0$ (effect of temperature is ignored (Fermeglia et al., 1990):

$$\mu_F = 9.16.10^{-6} \text{ Ns/m}^2$$

Specific heat capacity of liquid:
Specific heat capacity of liquid is taken from CRC Handbook (2005) at room temperature $\tilde{T} = 0$

$$c_1 = 2219.86 \text{ J/(kg.K)}$$

Liquid thermal conductivity:
Using data presented in CRC Handbook (2005), the liquid thermal conductivity is approximated as:

$$k_1 = -0.00019\tilde{T}^2 - 0.0467\tilde{T} + 0.144 \text{ W/(m.K)}$$

when $\tilde{T} < \tilde{T}_{cr}$ and zero otherwise.

Specific heat capacity of vapour:
Using data presented by Hales (1967), the vapour specific heat capacity is approximated as:

$$c_F = -68.16\tilde{T}^2 + 972.88\tilde{T} + 1486.16 \text{ J/(kg.K)}$$

Physical properties of n-octane

Latent heat of evaporation:

The latent heat of evaporation is approximated as (Maxwell, 1950):

$$L = -5.23\,\mathrm{x}10^{3}\,\tilde{T}^{4} + 2.72\,\mathrm{x}\,10^{4}\tilde{T}^{3} - 5.64\,\mathrm{x}\,10^{4}\,\tilde{T}^{2} + 4.37\,\mathrm{x}\,10^{3}\tilde{T} + 3.49\,\mathrm{x}\,10^{5}\ \text{J/kg}$$

when $\tilde{T} < \tilde{T}_{cr}$=0.888 and zero otherwise.

The saturated vapour pressure:

The saturated vapour pressure is approximated as (Reid and Sherwood, 1958):

$$p_s = 10^{5}(\,0.34\tilde{T}^{4} - 0.82\tilde{T}^{3}3 + 0.99\tilde{T}^{2} - 0.09\tilde{T} + 0.03)\ \text{N/m}^2$$

Liquid densities:

Using data presented by Raznjevic (1976) the liquid densities is approximated as:

$$\rho_{\mathrm{l}} = -5.61\tilde{T}^{4} + 28.33\tilde{T}^{3} - 56.16\tilde{T}^{2} - 33.12\tilde{T} + 725.56\ \text{kg/m}^3$$

when $\tilde{T} < \tilde{T}_{cr}$

Viscosities:

The liquid and vapour viscosities is approximated as (Raznjevic, 1976)

$$\mu_{\mathrm{l}} = (-78.75\tilde{T}^{3} + 67.613\tilde{T}^{2} - 24.791\tilde{T} + 5.6137)10^{-4}\ \ \text{Ns/m}^2$$

$$\mu_{\mathrm{F}} = (-6.93\tilde{T}^{3} + 10.761\tilde{T}^{2} + 0.88\tilde{T} + 6.4)10^{-6}\ \ \text{Ns/m}^2$$

Specific heat capacity:

The liquid and vapour viscosities are approximated as (Touloukian et al., 1970):

$$c_{\mathrm{l}} = -311.12\tilde{T}^{3} + 602.23\tilde{T}^{3} + 930.43\tilde{T} + 2224.12\ \ \text{J/(kg.K)}$$

$$c_{\mathrm{pF}} = -18.85\tilde{T}^{3} - 162.68\tilde{T}^{2} + 1339.81\tilde{T} + 1697.61\ \text{J/(kg.K)}$$

Liquid thermal conductivity:

Using data presented by Raznjevic (1976) the liquid thermal conductivity is approximated as:

$$k_{\mathrm{l}} = -0.027\tilde{T}^{2} - 0.042\tilde{T} + 0.1413\ \ \text{W/(m.K)}$$

when $\tilde{T} < \tilde{T}_{cr}$ and zero otherwise

Physical properties of gasoline fuel

Liquid density:

The liquid density is taken from Handbook of Aviation Fuel Properties (1984) and approximated as:

$$\rho_{\mathrm{l}} = -\,222.22\tilde{T} + 720.02\ \text{kg/m}^3$$

Latent heat of evaporation:
Using data presented by Chin et al. (1985), the latent heat of evaporation is approximated as:

$L = -1.61 \; x\, 10^5 \; \tilde{T}^3 + 2.88 \; x \; 10^4 \tilde{T}^2 - 1.64\, x\, 10^5 \tilde{T} + 3.48\, x\, 10^5$ J/kg

when $\tilde{T} < \tilde{T}_{cr} = 0.883$

Saturated vapour pressure:
Using data presented by Chin et al. (1985), the saturated vapour pressure is approximated as:

$p_{\mathrm{s}} = (178.985\, \tilde{T}^4 - 164.867 \tilde{T}^3 + 72.812\, \tilde{T}^2 - 4.051 \tilde{T} + 0.353) 10^5$ N/m^2

Liquid heat capacity:
Using data presented in CRC Handbook (2005), the liquid heat capacity is approximated as: $c_{\mathrm{l}} = 1200\, \tilde{T} + 2058$ J/(kg.K)

Vapour heat capacity:
Using data presented by Chin et al. (1985), the vapour heat capacity is approximated as:

$c_{\mathrm{pF}} = 2.111 \tilde{T}^3 - 13.841\, \tilde{T}^2 + 720.76 \tilde{T} + 2507.70$ J/(kg.K)

Liquid thermal conductivity:
The liquid thermal conductivity is taken from Reid and Sherwood (1958) and is approximated as:

$k_{\mathrm{l}} = -0.3579\, \tilde{T}^4 + 0.4575\, \tilde{T}^3 - 0.2047 \tilde{T}^2 - 0.0462 \tilde{T} + 0.1251$ W/(m.K)

when $\tilde{T} < \tilde{T}_{cr}$ zero otherwise.

Liquid viscosities:
Using data presented in Handbook of Aviation Fuel Properties (1984), the liquid viscosities is approximated as:

$\mu_{\mathrm{l}} = (-8.8431 \tilde{T}^3 + 16.449 \tilde{T}^2 - 14.848 \tilde{T} + 4.5048) 10^{-4}$ Ns/m^2

Vapour viscosity:
The vapour viscosity is taken from Hirschfelder et al. (1967) and is approximated as:

$\mu_{\mathrm{F}} = (0.0014 \tilde{T}^3 - 0.6356 \tilde{T}^2 + 6.0455 \tilde{T} + 5.0555) 10^{-6}$ Ns/m^2

Appendix B

Physical properties of a mixture of fuel vapour and air

Density and specific heat capacity of the mixture are calculated using the following simple formulae:

$$\rho_{\mathrm{mix}} = \frac{p_{\mathrm{mix}}}{R_{\mathrm{mix}} T_{\mathrm{mix}}} \tag{B.1}$$

$$c_{p\mathrm{mix}} = (1 - Y_{\mathrm{F}}) c_{\mathrm{pa}} + Y_{\mathrm{F}}\, c_{\mathrm{pF}}\,, \tag{B.2}$$

where p_{mix}, R_{mix} and T_{mix} are the pressure, gas constant, and temperature of the mixture of fuel vapour and air, Y_{F} is the mass fraction of fuel vapour, subscripts a and F refer to air and fuel vapour respectively.

Dynamic viscosity of the mixture is calculated from the following general semi empirical formula (Bird et al.,2002):

$$\mu_{\mathrm{mix}} = \sum_{i=1}^{N} \frac{X_{\mathrm{i}} \mu_{\mathrm{i}}}{\sum_{j=1}^{N} X_{\mathrm{j}} \Phi_{\mathrm{ij}}} \tag{B.3}$$

where

$$\Phi_{\mathrm{ij}} = \frac{1}{\sqrt{8}} \left(1 + \frac{M_{\mathrm{i}}}{M_{\mathrm{j}}}\right)^{-1/2} \left[1 + \left(\frac{\mu_{\mathrm{i}}}{\mu_{\mathrm{j}}}\right)^{1/2} \left(\frac{M_{\mathrm{j}}}{M_{\mathrm{i}}}\right)^{1/4}\right]^2$$

X_{i} are molar fractions of species i, M_{i} are molar masses (kg/kmol), the summation is performed over all N species.

Similarly, the thermal conductivity of the mixture is calculated from the following general semi empirical formula (Mason and Saxena, 1958; Bird et al., 2002):

$$k_{\mathrm{mix}} = \sum_{i=1}^{N} \frac{X_{\mathrm{i}} k_{\mathrm{i}}}{\sum_{j=1}^{N} X_{\mathrm{j}} \Phi_{\mathrm{ij}}} \tag{B.4}$$

where Φ_{ij} is the same as in Equation (B.3).

The binary diffusion coefficient was estimated using the following equation (Bird et al., 2002):

$$D_{\mathrm{Fa}} = 1.8583 \,\mathrm{x}\, 10^{-7} \sqrt{T^3 \left(\frac{1}{M_{\mathrm{F}}} + \frac{1}{M_{\mathrm{a}}}\right)} \frac{1}{p \sigma_{\mathrm{Fa}}^2 \Omega_{\mathrm{Fa}} (T^*)} \tag{B.5}$$

where D_{Fa} is in m^2/s, p is in atm (1 atm = 0.101 MPa), T is in K, $\sigma_{Fa} = 0.5(\sigma_F + \sigma_a)$ is the minimal distance between molecules in Angstroms (1 Angstrom = 10^{-10} m), Ω_{Fa} is the collision integral, the value of which depends on the normalised temperature $T^* = Tk_B/\varepsilon$, k_B is the Boltzmann constant, $\varepsilon_{Fa} = (\varepsilon_F.\varepsilon_a)^{0.5}$.

The values of σ_a and ε_a/k_B can be obtained from Table E.1 in Bird et al. (2002): $\sigma_a = 3.617$ Angstrom, $\varepsilon_a/k_B = 97.0$ K.

There is some controversy regarding the values of these parameters for various fuels. The values σ_F (in Angstrom) and ε_F/k_B (in K) for tetradecane, n-heptane, gasoline, n-octane, 3-pentanone and n-dodecane reported by Hirschfelder et al. (1967) and Paredes et al. (2000) are shown in the Table B.1:

Fuel	**Reference**	**σ_F (Angstrom)**	**ε_F/k_B (K)**
Tetradecane	Hirschfelder et al. (1967)	9.800	244.0
Tetradecane	Paredes et al. (2000)	6.55	454.38
n-heptane	Hirschfelder et al. (1967)	5.949	399.3
n-heptane	Paredes et al. (2000)	6.498	455.04
n-dodecane	Hirschfelder et al. (1967)	9.37	245.0
n-dodecane	Paredes et al. (2000)	6.5972	454.6768
n-octane	Paredes et al. (2000)	6.52	456.627
Gasoline	Hirschfelder et al. (1967)	7.451	320.00
3-pentanone	Hirschfelder et al. (1967)	4.22	351.562

Table B.1 The values σ_F (in Angstrom) and ε_F/k_B (in K) for various fuel

Once the value of T^* has been found, the collision integral Ω_{Fa} could be obtained from Table E.2 (Bird et al., 2002). Following Bird et al., 2002, these values of Ω_{Fa} are approximated as:

$$\Omega_{Fa} = \frac{1.06036}{T^{*0.15610}} + \frac{0.19300}{\exp(0.47635T^*)} + \frac{1.03587}{\exp(1.52996T^*)} + \frac{1.76474}{\exp(3.89411T^*)} \quad (B.6)$$

The plots of D_{Fa} for the diffusion of n-dodecane in air versus temperature for $p = 3$ MPa and the values of σ_{F} and $\varepsilon_a/k_{\mathrm{B}}$ recommended by Hirschfelder et al. (1967) and Paredes et al. (2000) given in the above table, are shown in Figure B.1.

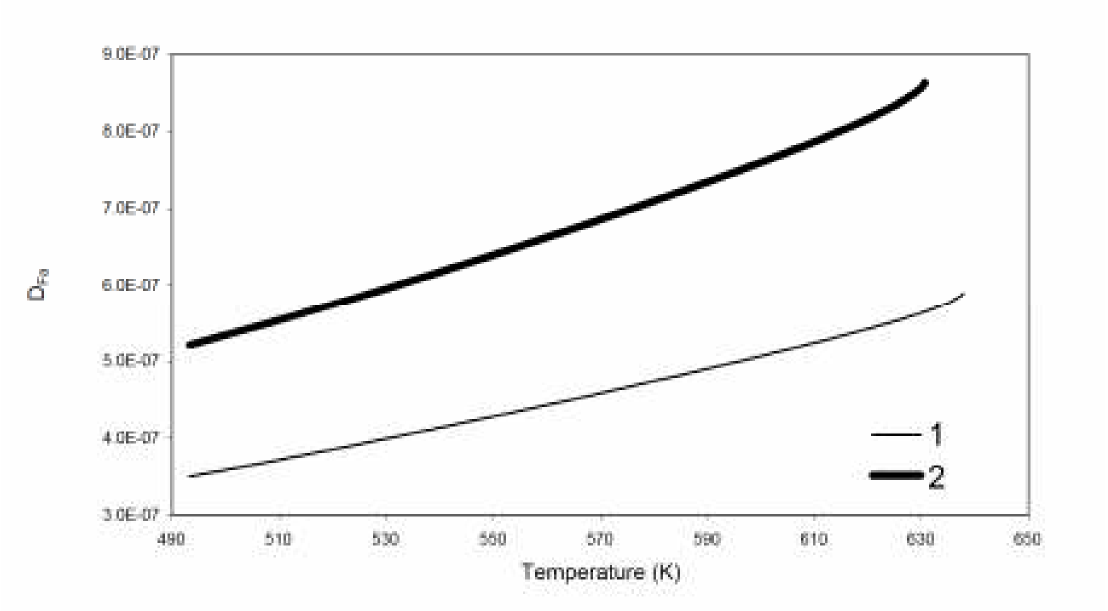

Figure B.1 The plots of D_{Fa} for diffusion of n-dodecane in air versus temperature for $p = 3$ MPa and the values of σ_{F} and $\varepsilon_a/k_{\mathrm{B}}$ given by Hirschfelder et al. (1967) (Curve 1) and Paredes et al. (2000) (Curve 2).

As can be seen from this figure, the values of D_{Fa} based on the parameters recommended by Paredes et al. (2000) are noticeably larger than those based on the parameters recommended by Hirschfelder at al. (1967) The analysis of this paper is based on data obtained by Paredes et al. (2000). They are more recent ones and they lead to more realistic values of *Le*, which in the case of gases are assumed to be of the order of 1 ($Le = O(1)$) (Harstad et al., 1999).

Alternatively we could use approximation of Ω_{Fa} was suggested by Hirschfelder et al. (1967):

$$\Omega_{\mathrm{Fa}} = \frac{-0.0080997}{T^{*3}} - \frac{0.028472}{T^{*2}} + \frac{0.76871}{T^{*}} + 0.71062 - 0.0048976T^{*} + 0.00004572T^{*2} - 1.6844 * 10^{-7} T^{*3} \qquad \text{(B.7)}$$

The plots of D_{Fa} using different approximation of Ω_{Fa} are presented in Figure B.2. Curve 1 refer to D_{Fa} using approximation of Ω_{Fa} suggested by Bird et al. (2002) and curve 2 refer to D_{Fa} using approximation of Ω_{Fa} suggested by Hirschfelder et al. (1967). As one can see from this figure, the predictions of both approximations almost coincide. In this analysis we use approximation of Ω_{Fa} that suggested by Bird et al. (2002).

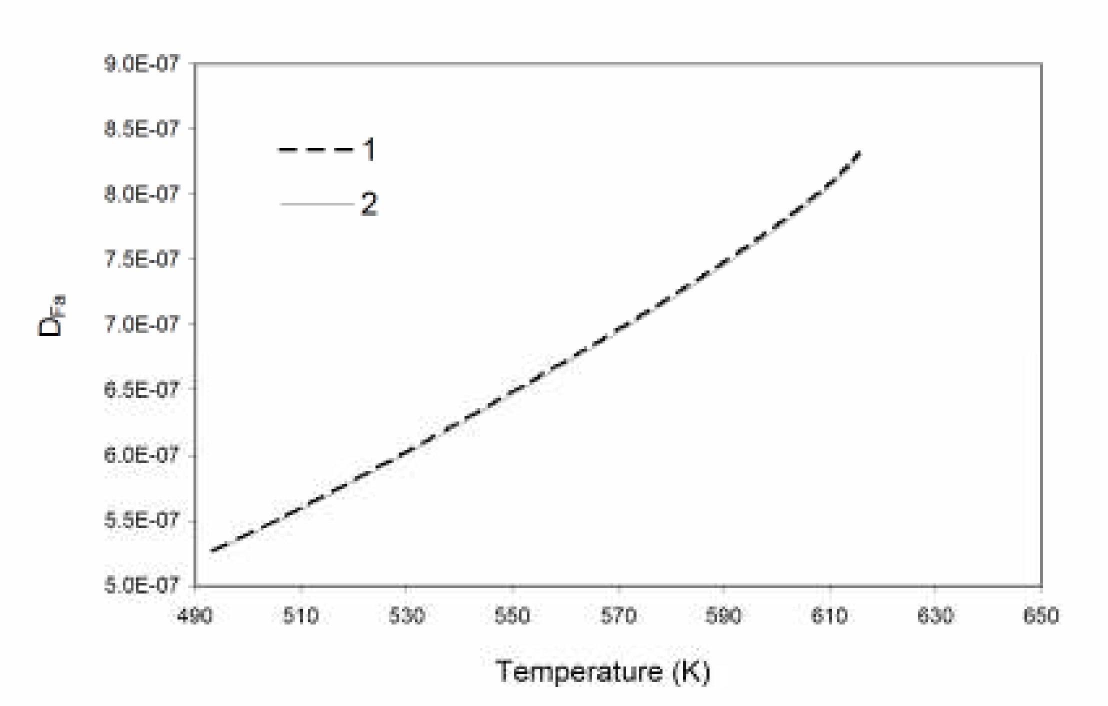

Figure B.2 The plots of D_{Fa} for the diffusion of n-dodecane in air versus temperature for $p = 3$ MPa and the values of Ω_{Fa} given by Bird et al. (2002) (Curve 1) and Hirschfelder et al. (1967) (Curve 2).

Appendix C

Numerical procedure of the zero dimensional code

This Appendix is focused on the implementation of the model of convective and radiative heating of a semi-transparent fuel droplet, based on the analytical solution of the heat conduction equation inside the droplet into a zero dimensional code (see Chapter 2).

A number of processes in Diesel engines (swelling, evaporation, internal circulation inside the droplets, dynamics of the droplets, effects of the droplets on gas phase, droplet break-up and the autoignition) have been into account. Effects of turbulence and coalescence processes have been ignored.

As the first step it is assume that the temperature of gas T_{g} (t=0) and initial droplet velocity $\mathbf{v}_{\mathrm{d}}$ (t=0) are given. The values of the convection heat transfer coefficient depend on gas properties (thermal conductivity and viscosity) and droplet radii. For stationary droplet the later is calculated using the equation:

$$\frac{dR_{\mathrm{d}}}{dt} = -\frac{\rho_{\mathrm{g}} D_{\mathrm{g}} \ln\left(1 + B_{\mathrm{M}}\right)}{\rho_{\mathrm{l}} R_{\mathrm{d}}}, \tag{C.1}$$

and taking into account swelling due to the decrease of liquid density with increasing temperature. Under these assumptions the calculation of the droplet temperature reduces to the solution of Equation (2.1.21) subject to appropriate initial and boundary conditions. When calculating droplet radius we took into account the conservation of mass of liquid droplets during their swelling.

The analytical solution (2.1.22) enables us to get the temperature distribution inside the droplets $T(R,t)$ as a function of radius R at the end of each time step. For the first time step the initial conditions $T_{\mathrm{d0}}(R,t\text{=}0)$ are used. The solution at the end of the first time step is used as the initial condition for the second time step etc. If the time step over which the droplet temperature and radius are calculated is small, it can be assumed that $h(t)$ = const over time step. In this case $\dot{m}_{\mathrm{d}}(t\text{=}0)$ is calculated using the equation:

$$\dot{m}_d = -2\pi R_{\mathrm{d}} \rho_{\mathrm{g}} D_{\mathrm{g}} Sh B_{\mathrm{M}} \tag{C.2}$$

where Sh is calculated from Equation (2.2.30) for Model 0, Equation (2.2.30) for Model 1, Equation (2.2.46) for Model 2, Equation (2.2.35) for Model 3, Equation (2.2.50) for model 4, Equation (2.2.48) for Model 5 and Equation (2.2.9) for Model 6.

The change of droplet radius $\dot{R}_{\mathrm{d}}$ (t=0) is calculated as:

$$\frac{dR_d}{dt}=\frac{\dot{m}_d}{4\pi R_d^2\rho_l}-\frac{R_d}{3\rho_l}\frac{d\rho_l}{dt} \tag{C.3}$$

T_{eff} (t=0) is calculated from Equation (2.2.56). Then the initial condition at t=0 allowed us to calculate $T(R,t)$ at the end of the first time step ($T(R,t_1)$) using Equation (2.1.22). The heat transfer coefficient is calculated as $h(t)=\mathrm{Nu}\, k_{\mathrm{g}}/2R_{\mathrm{d}}(t)$. The Nusselt number obtained using Equation (2.2.31) with B_{T} is replaced by B_{M} for Model 0, Equation (2.2.31) for Model 1, Equation (2.2.47) for Model 2, Equation (2.2.34) for Model 3, Equation (2.2.51) for Model 4, Equation (2.2.49) for Model 5 and Equation (2.2.5) for Model 6. Regarding the effect of film thickness (Model 2, Model 4 and Model 5), the calculation of B_{T} and $F(B_{\mathrm{T}})$ should be performed simultaneously using the iteration procedure (see Figure C.1).

The effect of internal circulation inside the droplet is taken into account by multiplying the liquid thermal conductivity by the factor χ, which is calculated using Equation (2.1.11).

The velocity of droplets injected from a nozzle are initially much greater than the velocity of the gas (air) stream, but they are slowed down due to the drag force, while gas is accelerated. In this case, the dynamic of droplet is taken into account using the following equation (Abramzon & Sirignano, 1989):

$$m_{\mathrm{d}}\frac{d\mathrm{v}_{\mathrm{d}}}{dt}=-\frac{C_{D0}}{2}\rho_{\mathrm{g}}\left(\mathrm{v}_{\mathrm{g}}-\mathrm{v}_{\mathrm{d}}\right)\left|\mathrm{v}_{\mathrm{d}}-\mathrm{v}_{\mathrm{g}}\right|A_{\mathrm{d}} \tag{C.4}$$

where A_{d} is the cross-sectional area of droplets, C_{D0} is the drag coefficient for non-evaporating droplets, depending on Re_{d}. In this analysis, C_{D0} is calculated based on the following approximation (Panton, 1996):

$$C_{D0}=\begin{cases}\dfrac{24}{Re_{\mathrm{d}}}\left(1+\dfrac{1}{6}Re_{\mathrm{d}}^{2/3}\right) & \text{when } Re_{\mathrm{d}}\le 1000\\ 0.424 & \text{when } Re_{\mathrm{d}}>1000\end{cases} \tag{C.5}$$

The effect of evaporation is taken into account via replacing C_{D0} by (Abramzon & Sirignano, 1989):

$$C_D = -\frac{C_{D0}}{\left(1+B_{\mathrm{M}}\right)^{\alpha}}, \tag{C.6}$$

where

$$\alpha = \begin{cases} 1 & \text{when } B_{\mathrm{M}} < 0.78 \\ 0.75 & \text{when } B_{\mathrm{M}} \geq 0.78 \end{cases}$$

The system of Equations (C.4) and (C.2) is solved using the Runge-Kutta method with adaptive step size control to obtained the droplet mass and velocity at $t=t_1$. The fuel vapour mass is calculated as:

$$\Delta m_v = n_0 m_{\mathrm{d}}(t=0) - n_0 m_{\mathrm{dv}}(t=t_1), \tag{C.7}$$

where m_{dv} is the droplet mass obtained by solving Equation (C.2) and n is the number of droplets. The momentum transferred from gas to droplets has the same value but the opposite sign to the momentum transferred from droplets to gas. Gas velocity is calculated from the momentum conservation equation, which can be presented in the form:

$$\frac{d\left(m_{\mathrm{g}} \mathrm{v}_{\mathrm{g}}\right)}{dt} = -\sum_i \frac{d\left(m_{\mathrm{d}i} \mathrm{v}_{\mathrm{d}i}\right)}{dt}, \tag{C.8}$$

where subscript i indicates individual droplets and summation is performed over all droplets.

It was checked that the second term in Equation (C.3) is relatively small and can be neglected if errors less than 0.1 % in evaporation time calculation can be tolerated.

In break-up models, two types of stresses acting on the moving droplets are taken into account. These are normal stresses, leading to droplet 'bag' break-up, and tangential stresses, leading to droplet 'stripping' break-up (Sazhin et al., 2003). In both cases, the reduction of droplet radii is described by the equation:

$$\frac{dR_{\mathrm{d}}}{dt} = \begin{cases} 0 & \text{when } R_{\mathrm{d}} \leq R_{\mathrm{d}b(s)} \\ -\dfrac{\left(R_{\mathrm{d}} - R_{\mathrm{d}b(s)}\right)}{t_{\mathrm{b}(s)}} & \text{when } R_{\mathrm{d}} > R_{\mathrm{d}b(s)} \end{cases} \tag{C.9}$$

where $R_{\mathrm{d}b(s)}$ are threshold radii marginally stable droplet with respect to bag (stripping) break-up, $t_{\mathrm{b}(s)}$ are the characteristic times of the development of these break-ups (Sazhin et al., 2003):

$$R_{\mathrm{d}b} = \frac{6\sigma_{\mathrm{s}}}{\bar{\rho}_{\mathrm{g}}\left|\mathrm{v}_{\mathrm{g}} - \mathrm{v}_{\mathrm{d}}\right|^2}, \quad R_{\mathrm{d}b} = \frac{0.5\sigma_{\mathrm{s}}^2}{\bar{\rho}_{\mathrm{g}}^2\left|\mathrm{v}_{\mathrm{g}} - \mathrm{v}_{\mathrm{d}}\right|^3 \upsilon_{\mathrm{g}}}, \tag{C.10}$$

$$t_{\mathrm{b}} = \pi\left[\frac{\rho_{\mathrm{d}} R_{\mathrm{d}}^3}{2\sigma_{\mathrm{s}}}\right]^{1/2}, \quad t_{\mathrm{s}} = \frac{13R_{\mathrm{d}}}{\left|\mathrm{v}_{\mathrm{g}} - \mathrm{v}_{\mathrm{d}}\right|}\sqrt{\frac{\rho_{\mathrm{d}}}{\bar{\rho}_{\mathrm{g}}}}, \tag{C.11}$$

σ_{s} is the surface tension coefficient, $\bar{\rho}_{\mathrm{g}}$ is the average gas density.

The threshold value of R_{db} and R_{ds} follow from the following criteria for bag and stripping break-up (Reitz and Diwakar, 1986):

$We \equiv \frac{\bar{\rho}_g\left|v_g - v_d\right|^2 R_d}{\sigma} > 6$ (bag break-up), and $\frac{We}{\sqrt{Re}} > 0.5$ (stripping break-up), where We is the Weber number. These criteria were checked for each droplet parcel at each time step. If either of the two criteria is met for the time equal to the corresponding time defined in Equations (C.11), the stable droplet size for the parcel was obtained from Equation (C.10). The size of an unstable droplet was allowed to change continuously with time following the rate Equation (C.9). This approach was used for the analysis of breakup in a zero dimensional code. (the models used in the KIVA-2 code are described in Chapter 6)

As evaporation and breakup processes can happened simultaneously, the mass of liquid droplet was calculated as:

$$m_{\mathrm{d}}(t_1) = \left(n_0 m_{\mathrm{d}}(0) - \Delta m_{\mathrm{v}}\right)/n_{\mathrm{n}} \tag{C.13}$$

$R_{\mathrm{d}}(t_1)$ is calculated as:

$$R_{\mathrm{d}}(t_1) = \left(3m_{\mathrm{d}}(t_1)/4\pi\rho\left(\bar{T}(t_1)\right)\right)^{1/3} \tag{C.14}$$

The gas temperature $T_{\mathrm{g}}(t_1)$ was obtained from the following equation:

$$\frac{dT_{\mathrm{g}}}{dt} = -2\pi\frac{k_{\mathrm{g}}}{m_{\mathrm{g}}c_{\mathrm{pg}}}\sum_i Nu_{0i}R_{\mathrm{d}i}\left(T_{\mathrm{g}} - T_{si}\right). \tag{C.15}$$

If the equivalence ratio (actual fuel /air ratio divided by stoichiometric fuel/air ratio) reaches the lower flammability range of the fuel, the Shell model is activated in the calculation of gas temperature and new concentrations of the fuel vapour, oxygen and the inert gas mass fractions in the surrounding gas.

For the second time step, the values of variables obtained at the end of the first time step ($t=t_1$) $T(r,t_1)$,$R_{\mathrm{d}}(t_1)$, $T_{\mathrm{g}}(\mathrm{t}_1)$, $\mathbf{v}_{\mathrm{d}}(t_1)$, $\mathbf{v}_{\mathrm{g}}(t_1)$, $\mathrm{m}_{\mathrm{d}}(t_1)$, $n(t_1)$ and concentration of the fuel vapour, oxygen and inert gas in surrounding gas are used as initial conditions to integrate the equation in the range (t_1,t_2). The previous calculations are repeated based on the new initial conditions to get the result at t=t_2.

The same procedure is repeated for all subsequent time steps until the autoignition starts at T_g= 1100 K (Sazhina et al., 1999). The number of terms in the series in Equation (2.1.22), which needs to be taken into account, depends on the timing of the starts of droplet heating and time when the value of droplet temperature is calculated. For parameters relevant to Diesel engines environment just three terms in the series can be safely used with possible errors of not more than about 1% (Sazhin et al. 2004a).

The gradients of temperature and fuel vapour concentration in the gas phase are ignored. This has been introduced with view to the future implementation of the algorithm into a multidimensional computational fluid dynamics (CFD) code, where this assumption refers to individual computational cells. The number of droplets in the enclosure can be arbitrary, but the direct interaction between droplets is not taken into account at this stage. All transport coefficients for the gas phase for Model 0- 5 were calculated at the reference temperature, $T_{\rm ref}$ defined as (Lefebvre, 1989):

$$T_{\rm ref} = \frac{T_{\rm g} + 2T_{\rm s}}{3}$$

and

$$T_{\rm ref} = \frac{T_{\rm g} + T_{\rm s}}{2}$$

for Model 6 (Haywood et al., 1989).

The concentration of fuel vapour is assumed to be so small that its effect on transport coefficients can be ignored. This effect could be taken into account as described in Appendix 3 of Sazhin et al. (1993). It was taken into account when calculating gas density and average specific heat capacity. The ignition of fuel vapour/air mixture is based on the customised version of the Shell autoignition model in which the autoignition process is reduced to eight-step chain branching reaction scheme with A_{f4} in the range between 3 x 10^6 and 6 x 10^6 (Sazhina et al., 1999, 2000).

The flow chart of the zero dimensional code is shown in Figure (C.2)

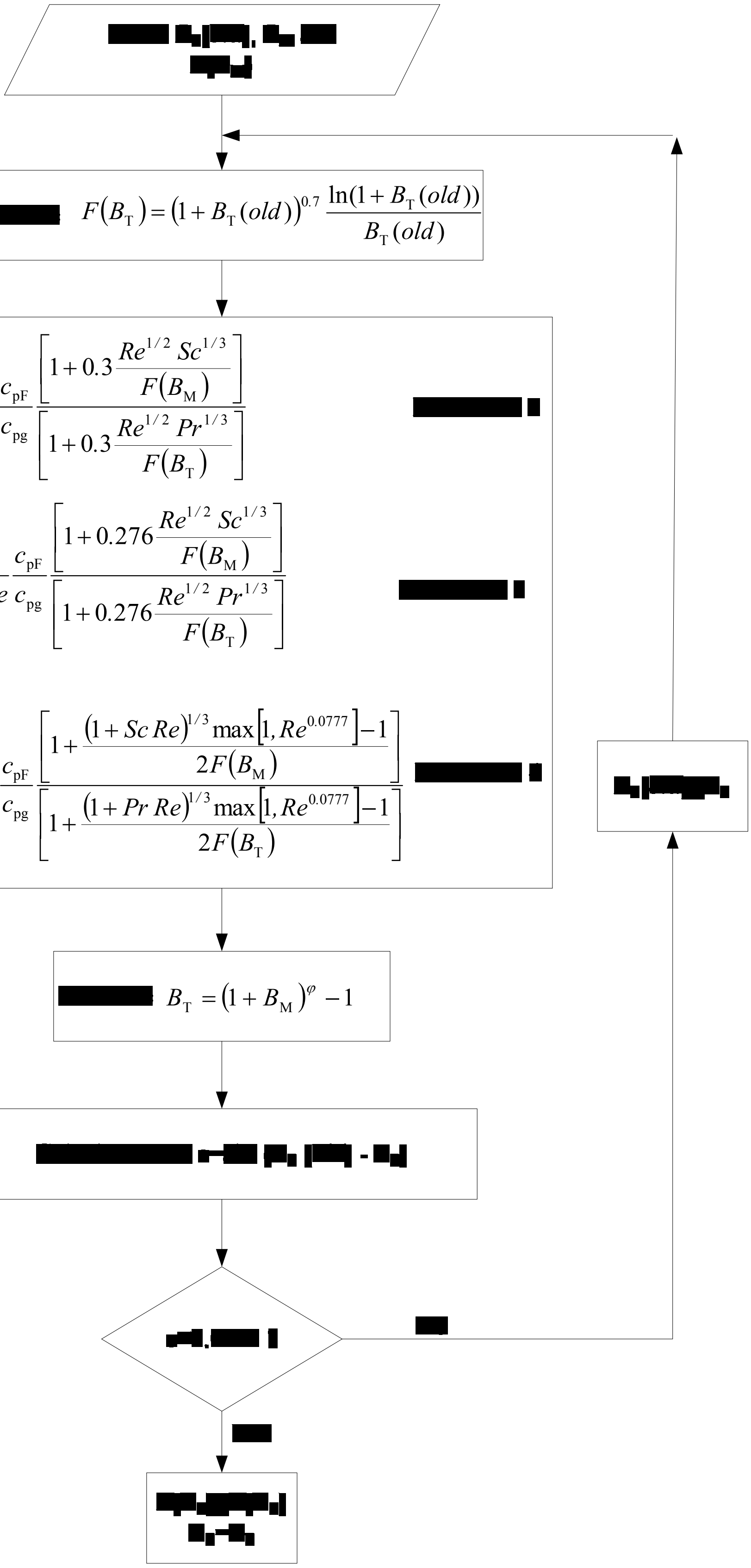

Figure C.1 The iteration procedure to calculate B_{T} and $F(B_{\mathrm{T}})$ for gas Models 2, 4 and 5.

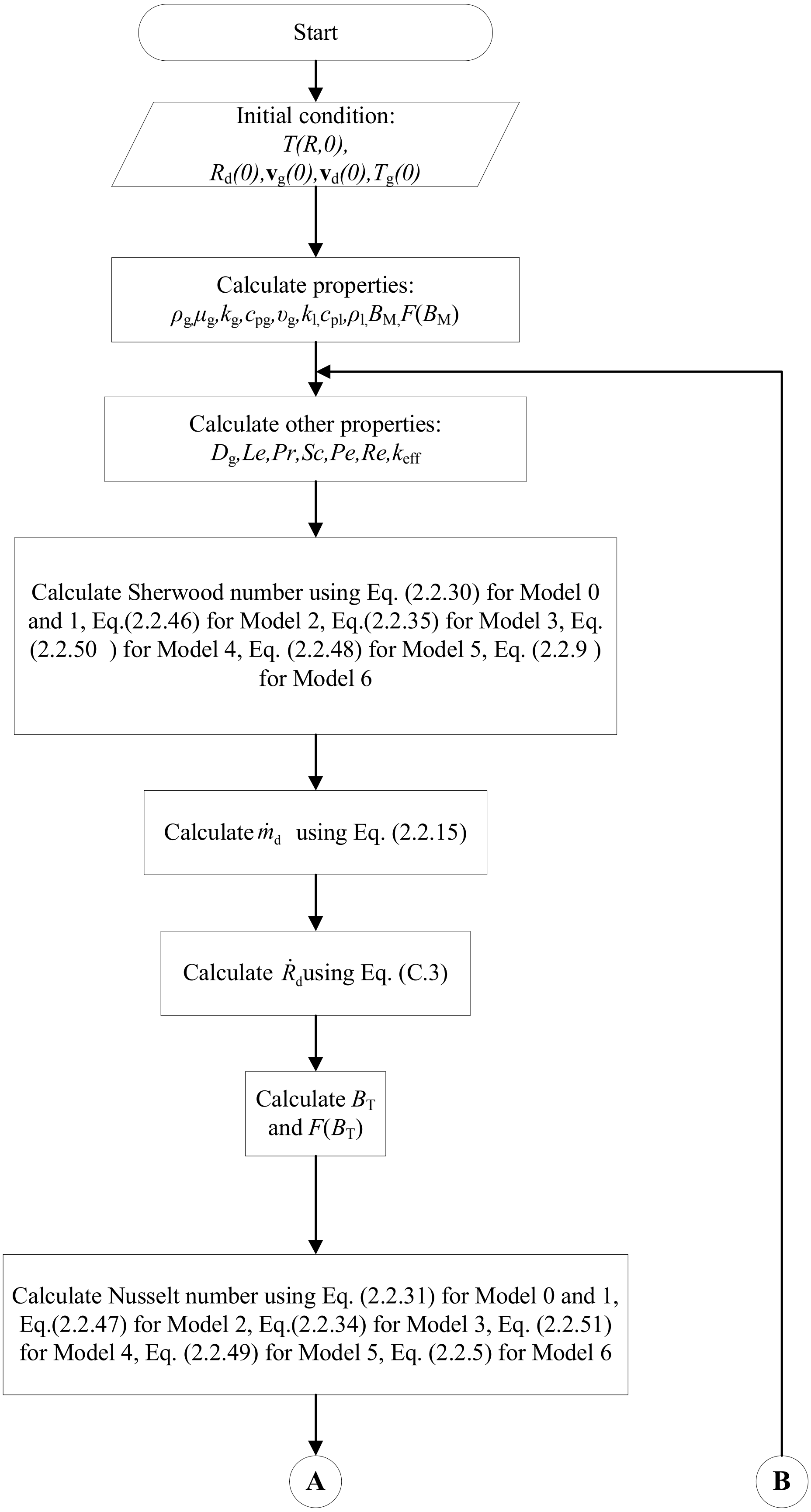

Figure C.2 The flow chart of the zero-dimensional code

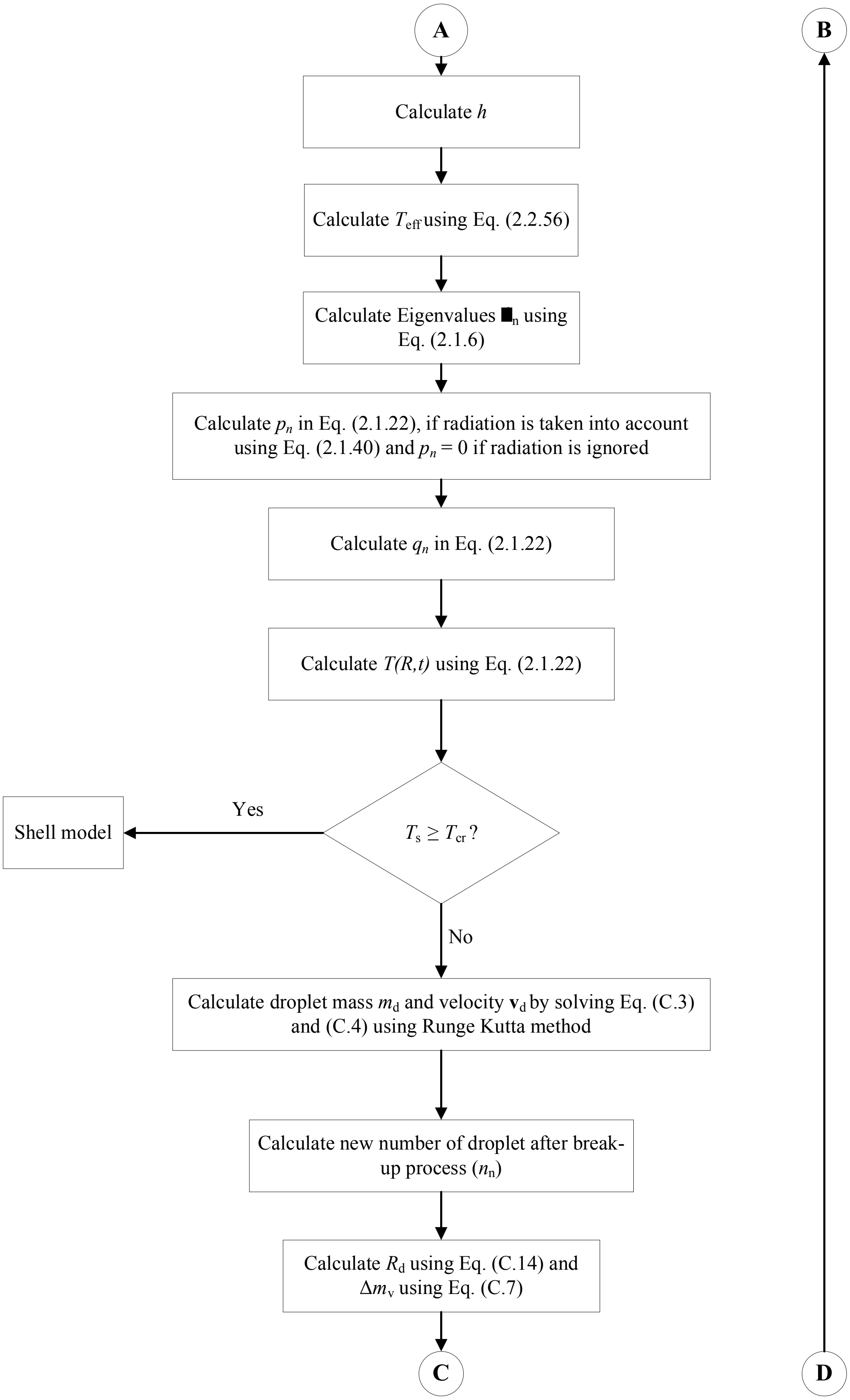

Figure C.2 The flow chart of the zero-dimensional code (continued)

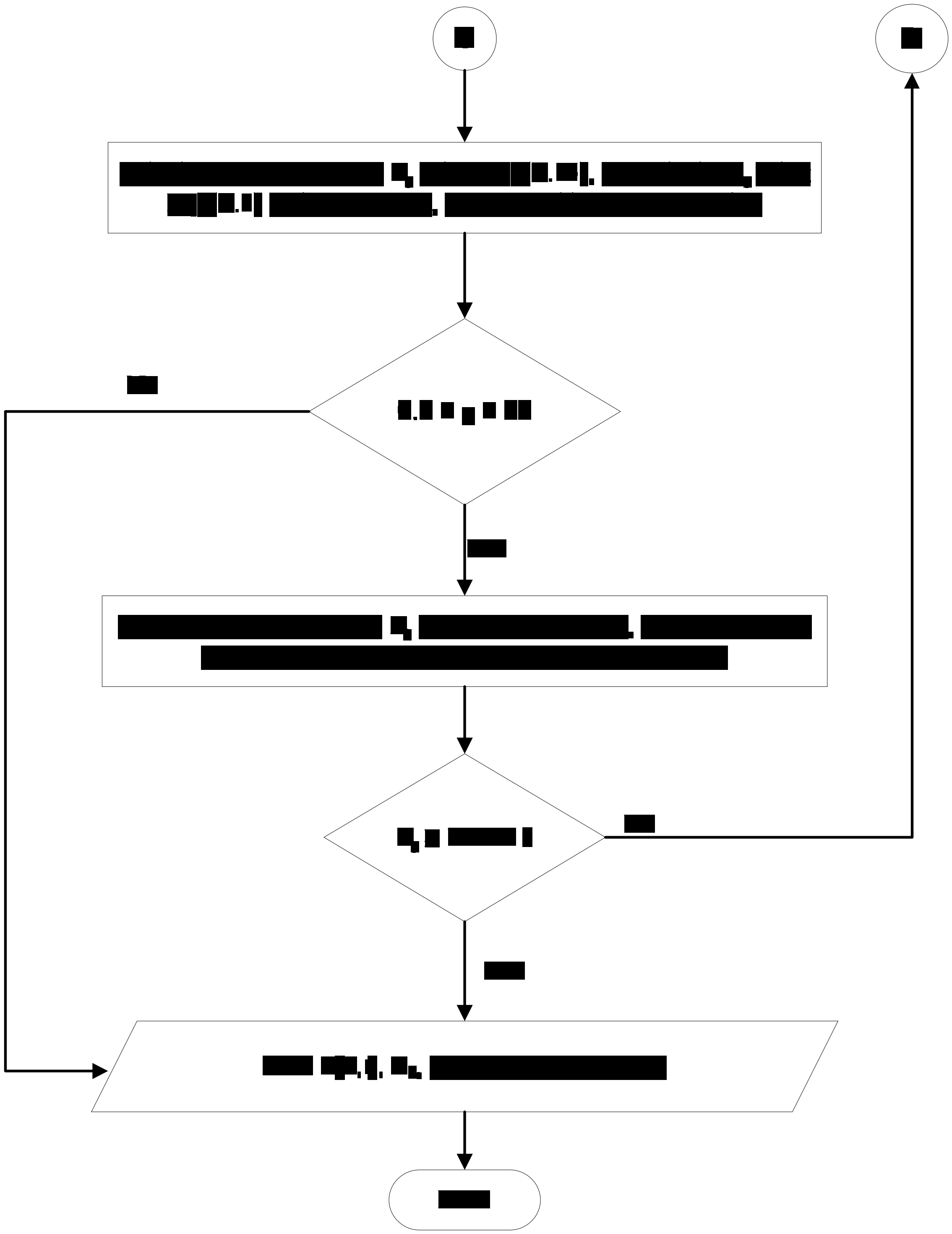

Figure C.2 The flow chart of the zero-dimensional code (continued)

APPENDIX D
Numerical solution of the discretised heat conduction equation

The one-dimensional unsteady state heat conduction equation in Cartesian coordinate (2.1.21) can be solved numerically as follows (Versteg and Malalasekera, 1995):

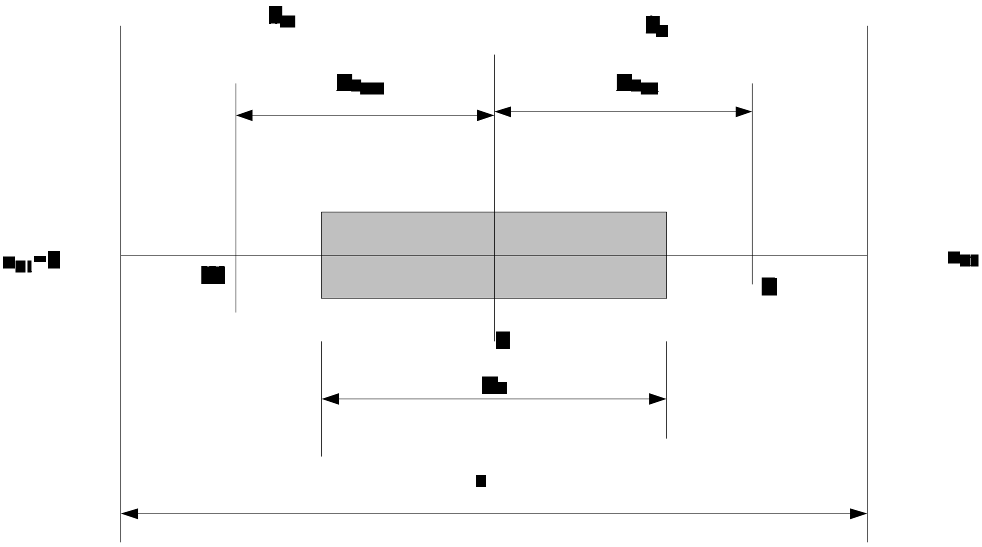

Figure D.1 The grid used for NSDE

Introducing a new variable $u = TR$, Equation (2.1.21) become (Sazhin et al., 2004b):

$$\frac{\partial u}{\partial t} = K\frac{\partial^2 u}{\partial R^2} + \tilde{P}(R), \tag{D.1}$$

with the following boundary and initial conditions :

$$\begin{aligned} &\frac{\partial u}{\partial R} + H(t)u = M(t) && \text{when } R = 1 \\ &u = 0 && \text{when } R = 0 \\ &u(t=0) = RT_0(RR_d) \equiv \tilde{T}_0(R) && \text{when } 0 \le R \le 1 \end{aligned} \tag{D.2}$$

Consider the one-dimensional control volume shown in Figure D.1. Integration of Equation (D.1) over the control volume and over a time interval from t to $t + \Delta t$ gives:

$$\int_t^{t+\Delta t}\int_{CV}\frac{\partial u}{\partial t}dVdt = \int_t^{t+\Delta t}\int_{CV}\frac{\partial}{\partial r}\left(k\frac{\partial u}{\partial r}\right)dVdt + \int_t^{t+\Delta t}\int_{CV} SdVdt \tag{D.3}$$

This may be written as:

$$A\int_{w}^{e}\left[\int_{t}^{t+\Delta t}\frac{\partial u}{\partial t}dt\right]dr=\int_{t}^{t+\Delta t}\left[\left(kA\frac{\partial u}{\partial r}\right)_{e}-\left(kA\frac{\partial u}{\partial r}\right)_{w}\right]dt+\int_{t}^{t+\Delta t}\bar{S}\Delta V dt \qquad \text{(D.4)}$$

In Equation (D.4), A is the face area of the control volume, ΔV is its volume and $\bar{S}$ is the average source strength. The left hand side can be written as:

$$A\int_{w}^{e}\left[\int_{t}^{t+\Delta t}\frac{\partial u}{\partial t}dt\right]dr=\left(u_{p}-u_{p}^{0}\right)\Delta V, \qquad \text{(D.5)}$$

where ΔV is equal to $A\Delta r$ where Δr is the width of the control volume, superscript '0' refers to u at time t; u at the level $t+\Delta t$ are not superscripted.

If the central differencing to the diffusion term on the right hand side is applied, Equation (D. 4) can be written as:

$$\left(u_{P}-u_{P}^{0}\right)\Delta V=\int_{t}^{t+\Delta t}\left[\left(k_{e}A\frac{u_{E}-u_{P}}{\Delta r_{PE}}\right)-\left(k_{w}A\frac{u_{P}-u_{W}}{\Delta r_{WP}}\right)\right]dt+\int_{t}^{t+\Delta t}\bar{S}\Delta V dt \qquad \text{(D.6)}$$

To evaluate the right hand side of this equation we need to make an assumption about the moments of time when the values of u_{P}, u_{E} and u_{W} are taken. We introduce a weighting parameter θ between 0 and 1 and write the integral I_{T} of u_{P} with respect to time as:

$$I_{T}=\int_{t}^{t+\Delta t}u_{P}dt=\left[\theta u_{P}+(1-\theta)u_{P}^{0}\right]\Delta t \qquad \text{(D.7)}$$

Using formula (D.7) for u_{W} and u_{E} in Equation (D.6) and dividing by $A\Delta t$ throughout, we have:

$$\left(\frac{u_{P}-u_{P}^{0}}{\Delta t}\right)\Delta r=\theta\left[\frac{k_{e}\left(u_{E}-u_{P}\right)}{\Delta r_{PE}}-\frac{k_{W}\left(u_{P}-u_{W}\right)}{\Delta r_{WP}}\right]+ (1-\theta)\left[\frac{k_{e}\left(u_{E}^{0}-u_{P}^{0}\right)}{\Delta r_{PE}}-\frac{k_{W}\left(u_{P}^{0}-u_{W}^{0}\right)}{\Delta r_{WP}}\right]+\bar{S}\Delta r \qquad \text{(D.8)}$$

Assuming that $k_e = k_w = k$ and $\Delta r_{PE} = \Delta r_{Wp} = \Delta r$, Equation (D.8) can be rearranged to :

$$\left[\frac{\Delta r}{\Delta t} + \frac{2\theta k}{\Delta r}\right]u_P = \frac{k}{\Delta r}\left[\theta u_E + (1-\theta)u_E^0\right] + \frac{k}{\Delta r}\left[\theta u_W + (1-\theta)u_W^0\right] + \left[\frac{\Delta r}{\Delta t} - 2(1-\theta)\frac{2\theta k}{\Delta r}\right]u_P^0 + \bar{S}\Delta r \tag{D.9}$$

We divided the domain into n control volumes. Equation (D.9) is the discretised equation for value of u_P at the centre of control volume. The control volumes 1 and n have to be modified to take into account the boundary conditions. The discretised equation for the control volume 1 can be written as:

$$\left(\frac{u_P - u_P^0}{\Delta t}\right)\Delta r = \theta\left[\frac{k(u_E - u_P)}{\Delta r} - \frac{2k(u_P - u_{B1})}{\Delta r}\right] + (1-\theta)\left[\frac{k(u_E^0 - u_P^0)}{\Delta r} - \frac{2k(u_P^0 - u_{B1}^0)}{\Delta r}\right] + \bar{S}\Delta r, \tag{D.10}$$

where $u_{B1}=0$. Equation (D.10) can be rearranged as:

$$\left[\frac{\Delta r}{\Delta t} + \frac{3\theta k}{\Delta r}\right]u_P = \frac{k}{\Delta r}\left[\theta u_E + (1-\theta)u_E^0\right] + \frac{k}{\Delta r}\left[\theta u_W + (1-\theta)u_W^0\right] + \left[\frac{\Delta r}{\Delta t} - 3(1-\theta)\frac{2\theta k}{\Delta r}\right]u_P^0 + \bar{S}\Delta r \tag{D.11}$$

The discretised equation for the control volume n can be modified as:

$$\left(\frac{u_P - u_P^0}{\Delta t}\right)\Delta r = \theta\left[\frac{2k(u_{B2} - u_P)}{\Delta r} - \frac{k(u_P - u_w)}{\Delta r}\right] + (1-\theta)\left[\frac{2k(u_{B2}^0 - u_P^0)}{\Delta r} - \frac{k(u_P^0 - u_w^0)}{\Delta r}\right] + \bar{S}\Delta r \tag{D.12}$$

where the value of u_{B2} can be obtained from the boundary condition in Equation (D.2) as:

$$u_{B2} = \frac{M(t) + \frac{2}{\Delta r}u_P}{H(t) + \frac{2}{\Delta r}} \tag{D.13}$$

Substituting Equation (D.13) into Equation (D.12) we obtain :

$$\left[\frac{\Delta r}{\Delta t}+\frac{3\theta k}{\Delta r}-\frac{4k}{\Delta r^{2}\left(H(t)+\frac{2}{\Delta r}\right)}\right]u_{P}=$$

$$\frac{\theta k}{\Delta r}u_{W}+\frac{(1-\theta)k}{\Delta r}u_{W}^{0}+\left(\frac{\Delta r}{\Delta t}-\frac{3(1-\theta)k}{\Delta r}\right)u_{P}^{0}+\frac{2kM(t)}{\Delta r\left(H(t)+\frac{2}{\Delta r}\right)}+\overline{S}\Delta r \tag{D.14}$$

The exact form of the final discretised equations depends on the value of θ. When θ is zero, we use u_{P}^{0}, u_{W}^{0} and u_{E}^{0} at the previous time level t on the right hand side of the Equations (D.9), (D.11) and (D.14) to evaluate u_P at the new time level. The resulting algorithm is called explicit. When $0<\theta<1$, u at the new time level are used on both sides of equation. The resulting algorithm is called implicit. The algorithm based on the assumption $\theta=1$ is called fully implicit and algorithm corresponding to $\theta=1/2$ is called the Crank-Nicholson algorithm (Versteeg and Malalasekera, 1995). For implicit algorithm the solution of discretization equation was obtained by Thomas algorithm or the TDMA (TriDiagonal Matrix Algorithm) (Patankar, 1980)